



ÓBUDA UNIVERSITY

Doctoral School of Materials Sciences and Technologies

**Surface Chemistry and Catalysis Department
Centre for Energy Research**

Sahir M. Alzuraji

(Ph. D.) dissertation

**“Application of Water-Insoluble Iron Complexes in Water
Oxidation”**

Supervisor:

Dr. József Sandor Pap

2022 Budapest

“Application of Water-Insoluble Iron Complexes in Water Oxidation”

Ph.D. Dissertation

Sahir M. Alzurairji

“This dissertation is presented as a partial requirement for the Doctor of Philosophy Degree award at the Doctoral School of Materials Science and Technologies.”

ÓBUDA UNIVERSITY

**Experimental work was done at Surface Chemistry and Catalysis Department,
Centre for Energy Research**

Budapest 2022

Public Defense Committee

President: Telegdi Lászlóné, professor emerita, DSc, ÓE

Secretary: Kovács Tünde Anna, PhD, egyetemi docens, ÓE

Committee Members: Zámbó Dániel, PhD, tud. munkatárs, ELKH EK MFA

Endrődi Balázs, PhD, egy. adjunktus, SZTE

Opponents: Balácsi Csaba, DSc, tud. tanácsadó, ELKH EK MFA

London Gábor, PhD, tud. munkatárs, MTA TTK

Public Defense date: 2022. 06.

Declaration

Ph. D. dissertation is submitted to Materials Science and Technologies, Ph.D. School of ***Óbuda University***, under the supervision of ***Dr. József Sandor Pap***, as part of the requirements for the Doctor of Philosophy degree award requirements.

The dissertation is original and has never been previously submitted, neither in part nor in full, for any other degree. I declare that the research carried out herein is my work. The references chapter lists the sources used in writing this document.

M. S.A.
Mohammed

Sahir M. Alzuraji

Acknowledgements

First, my heartfelt gratitude goes to my supervisor **Dr. József S. Pap**, for his supervision during my Ph.D. studies and his unlimited assistance, motivation, immense knowledge, and support throughout my journey.

He was my instructor and mentor, guiding me and giving me the proper steps to be a successful researcher in the field. I want to thank him and be grateful for his friendship and my scientific achievements due to his helpfulness despite all the obstacles we faced together.

Secondly, besides my supervisor, I am grateful to **Dr. Judit Borsa** for her professional advice and support throughout my research journey. All the staff members of Óbuda University have provided me with expansive personal help and trained me a great deal in my Ph.D. study course.

My sincere thanks go to the group work and colleagues, **Tamás Ollár, Tímea Benkó, Krisztina Frey, Miklós László Németh, Horváth Anita, Dávid Lukács, Anna Szuja**, for the social and scientific assistance through my work at *Surface Chemistry and Catalysis Department (Centre for Energy Research)*. I am thankful to **Noémi Szász** and **Levente Illés** in SEM-EDX for technical support.

My appreciation to all *my family members and friends*; without their support, I would not be at this stage. Special thanks to the Dean of the College of Engineering (Al-nahrian University), **Dr. Basim O. Hassan**, for guidance and support throughout my study journey.

Ultimately, thankful for the J. Bolyai Research Scholarship from the Hungarian Academy of Sciences. This work is financed by the NKFI-128841 grant and the VEKOP-2.3.2-16-2016-00011 grant supported by the European Structural and Investment Funds.

Table of Contents

Declaration

Acknowledgements

Abbreviations

Abstract

	i
	iv
	vii
1. Literature background	1
1.1. Today's energy world (an outlook)	1
1.2. Renewable Energy	2
1.3. Energy storage problems	2
1.4. Natural photosynthesis	3
1.5. Artificial photosynthesis (AP)	7
1.6. Hydrogen Production	9
1.7. Principles of Electrochemical Water Splitting	11
1.8. Water electrolysis via photoelectrochemical (PEC) devices	13
1.9. A brief overview of water oxidation catalysts	16
1.10. Mechanistic pathways for water oxidation catalysts, initial steps, and O-O bond formation	18
1.10.1. Mechanistic pathways for water oxidation materials	19
1.11. Iron-based molecular catalysts for water oxidation (WO)	23
1.11.1. Homogeneous catalysts	23
1.11.2. Immobilization of molecular catalysts (heterogeneous catalysis)	29
2. Aim of the work	34
2.1. Motivation and preliminary considerations	34
2.2. Aim of the work	34
3. Experimental	35
3.1. Solvents and materials	35
3.2. Ligands and complexes	35
3.3. Electrodes, semiconductor substrates and electrochemical techniques	36
3.4. Electrocatalytic investigations	41
3.4.1. Homogeneous electrocatalysis	41
3.4.2. Heterogeneous electrocatalysis	42
3.5. Physical characterization	45

3.5.1.	Scanning electron microscopy (SEM) and energy-dispersive X-ray spectroscopy (EDX)	45
3.5.2.	X-ray photoelectron spectroscopy (XPS)	45
3.5.3.	Ultraviolet-visible spectrophotometry	46
3.6.	Quantitative analysis of O ₂	46
3.6.1.	Optical oxygen sensor	46
3.6.2.	Gas chromatography analysis of the headspace gas	46
4.	Results and discussion	48
4.1.	Immobilization and characterization of water-insoluble Fe(II) complexes as water oxidation catalysts utilizing hydrophobic NN' bidentate ligands	49
4.1.1.	Selection of the complexes based on preliminary examples	49
4.1.2.	Synthesis of complexes 1 and 2 and their redox properties in homogeneous water/acetonitrile mixture	51
4.1.3.	Immobilization of complexes 1 and 2 on ITO	60
4.2.	Immobilization and characterization of water-insoluble Fe(III) complexes as water oxidation catalysts using hydrophobic pincer ligand	71
4.2.1.	Selection of the complex based on preliminary results	71
4.2.2.	Structural properties of [Fe ^{III} Cl ₂ (tia-BAI)] (3) and its behavior in acetone	72
4.2.3.	Addition of water to the solution of [Fe ^{III} Cl ₂ (tia-BAI)] in acetone	74
4.2.4.	Electrocatalytic water oxidation in water/acetone with [Fe ^{III} Cl ₂ (tia-BAI)]	77
4.2.5.	Drop-casting and characterization of 3 as a solid ad-layer on ITO	80
4.2.6.	Utilization of 3 in water oxidation electrocatalysis as a solid ad-layer on ITO anode	85
4.3.	Electrodeposition of water-insoluble Fe(III) complexes with pincer ligands as WOCs	90
4.3.1.	Strategies to enhance the performance of immobilized molecular catalysts	90
4.3.2.	Structural properties of complexes 3 and 4 and electrodeposition in DCM	91
4.3.3.	Comparison of the differently immobilized complexes 3 and 4 in water oxidation	96
4.3.4.	Post-catalytic analysis of the ED samples by SEM-EDX	100
5.	Conclusions and outlook	103
6.	Scientific results and thesis points	107
7.	List of publications	110
8.	Conference presentations	111
9.	References	112
	Appendix (A)	A.1
	Appendix (B)	B.1

Abbreviations

AP	Artificial Photosynthesis
OER	Oxygen Evolution Reaction
HER	Hydrogen Evolution Reaction
TMs	Transition Metals
WOCs	Water oxidation Catalysts
OEC	Oxygen Evolving Complex
PS-I	Photosystem I
PS-II	Photosystem II
NADPH	Nicotinamide Adenine Dinucleotide Phosphate
ATP	Adenosine triphosphate
PCET	Proton-Coupled Electron Transfer
SMR	Steam Methane Reforming
CG	Coal Gasification
PEM	Proton Exchange Membrane
PEC	Photoelectrochemical Cell
WNA	Water nucleophilic attack
I2M	Interaction of two M–O units
DFT	Density functional theory
RDS	Rate-determining Step
LDHs	Layered Double hydroxides
CAN	Cerium Ammonium Nitrate
HPLC	High Performance Liquid Chromatography
BDD	Boron Doped Diamond
GC	Glassy Carbon
ITO	Indium Tin Oxide

FTO	Fluorine doped tin oxide
TBAP	Tetrabutylammonium perchlorate
DCM	Dichloromethane
KIE	Kinetic Isotope Effect
CV	Cyclic Voltammtry
LSV	Linear Swep Voltammetry
SWV	Square Wave Voltammetry
CPE	Controlled Potential Electrolysis
NHE	Normal Hydrogen Electrode
EIS	Electrochemical Impedance Spectroscopy
SEM	Scanning Electron Microscopy
EDX	Energy-Dispersive X-ray Spectroscopy
XPS	X-ray photoelectron Specroscopy
UV-vis	Ultraviolet-visible Spectroscopy
GC	Gas chromatography
FID	Flame-ionization detector
TCD	Thermal-conductivity detector
BID	Barrier ionization discharge detector
NMR	Nuclear Magnetic Resonance
FTIR	Fourier-transform infrared spectroscopy
DC	Drop-Casting
DIP	Dip-Coating
ED	Electrodeposition
EASA	Electrochemically Active Surface Area
FE	Faradaic Efficiency
TON	Turnover Number
TOF	Turnover Frequency
MLCT	Metal to Ligand Charge Transfer
HAT	Hydrogen Atom Transfer

ILCT	Intra-ligand Charge Transfer
LMCT	Ligand to Metal Charge Transfer
TAML	Tetra-amido macrocyclic ligand
PBI	2-(2'-pyridyl) benzimidazole
BPO	2-(2'-pyridyl) benzoxazole

Abstract

Artificial photosynthesis (AP) is a promising concept to generate clean and renewable chemical energy carriers, including H₂ by sunlight (Solar Energy). To achieve this objective, developing inexpensive, highly active, and stable catalysts for hydrogen production (Hydrogen Evolution Reaction, HER) and water oxidation (Oxygen Evolution Reaction, OER) in the first place is a fundamental challenge since, nowadays, the catalysts in practice utilize noble metals.

According to the above objective, many recent studies focus on molecular systems based on transition metals (TMs) suitable as water oxidation catalysts (WOCs) due to their structural versatility, clear catalytic mechanisms, and highest atomic efficiency with respect to catalytic centers. Among these TMs, Iron is an abundant and less toxic element in Earth's crust, having rich redox chemistry for the activation of O₂ in biological systems and versatile catalytic applications. Fe-based compounds can be envisioned as efficient electrocatalysts for the OER, too. Indeed, (electro)chemical OER by efficient Fe-based catalysts have been published, and factors were pointed out to control their performance. A brief yet, in-depth review of the recent progress in this field is provided as part of the dissertation.

However, from the overview, it will be apparent that there is room for further studies to improve the performance and durability of Fe-based WOCs. With this in mind, I investigated new electrocatalytic systems based on Fe complexes that were presumed to form immobilized catalytic films on electrodes. The activity of the electrocatalysts is discussed based on essential parameters such as overpotential, Tafel slope, stability, Faradaic efficiency, and turnover frequency determined by electrochemical techniques. A part of this work is devoted to the electrochemical behavior of water-insoluble Fe complexes in homogeneous water/organic mixtures to reveal their intrinsic molecular properties. Furthermore, water-insolubility of Fe complexes aided in to apply of simple methods (dip-coating and drop-casting) to immobilize these catalysts on model semiconductors (indium tin oxide and fluorine-doped tin oxide) to be applied in controlled potential electrolysis in borate buffer at pH ~ 8.3. I found that water-insolubility presents a viable strategy for designing new molecular catalyst/(photo)anode hybrids. An unforeseen but beneficial outcome of these studies was that a fruitful immobilization method (electrodeposition) had been explored to reduce the amount of the complex required for good operando stability. This method will be discussed at the end of this work.

1. Literature background

1.1. Today's energy world (an outlook)

There is a growing global energy demand, and clean energy production is highly desirable for several reasons. Approximately 84% of the world's energy supply (Chart 1.1) relies on fossil fuels, including **coal**, **natural gas**, and **oil**, due to the suitable energy density of these carriers that fulfill our needs [1]. Fossil fuels made industry growth possible for a long time because of their apparent inexpensiveness and availability [2]. Over the past half-century, fossil fuel consumption has increased dramatically, around eight-fold since 1950 and roughly doubling since 1980.

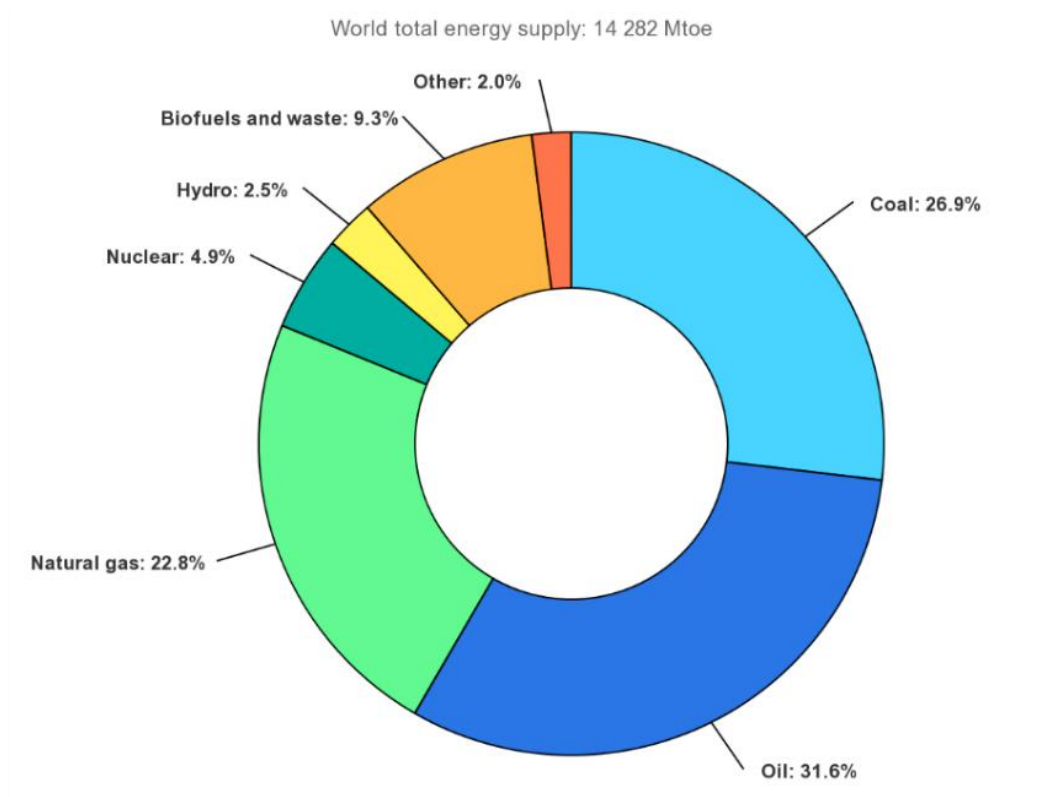


Chart 1.1. The World's total energy supply in 2018, *Mtoe= mega tonnes of oil [1].

Meanwhile, a clear shift towards oil and gas can also be observed with time [3]. Based on current expectations, global energy consumption will increase to 20 TW or more by 2030, double and triple by 2050, and by the end of the century, respectively [4,5]. The combustion of fossil fuels has fundamental adverse effects on the global climate, which is well known to be the major contributor to global warming. Nuclear power could be an excellent alternative to generate electricity with a low impact on CO₂ production but generate radioactive waste that should be put away (storage).

After witnessing nuclear disasters, human society faces a fundamental challenge (Three Mile Island, Chernobyl, and Fukushima) [6]. Therefore, a clean, abundant, sustainable, and safe energy source is the real challenge for establishing an economy in continuous development.

1.2. Renewable Energy

Substitution of fossil fuels requires enormous efforts to find energy carriers that are cheap, renewable, and not harmful to the environment [7]. Renewable energy is derived from resources capable of renewal at a reasonable timescale without depleting the planet's (local or global) capabilities, including carbon-neutral sources such as **sunlight, wind, rain, tides, waves, and geothermal heat**. These resources are available in one form or another nearly everywhere. Several technologies have already been introduced, such as **wind power, hydropower, biomass, and solar power** (solar panel). Among these, solar energy constitutes the most prominent and invaluable source of producing electricity/fuel. Roughly 4.3×10^{20} J of energy reaches the Earth's surface every hour, comparable to what humankind uses every year. In other words, although the total amount of solar energy is large, the energy density (reaching any given square meter of the planet's surface) over time is diffuse (low) and intermittent [5]. Since solar energy means a clean and sustainable alternative, several technologies, such as photovoltaic, have been developed to convert sunlight into electricity [8].

1.3. Energy storage problems

It is not easy to store the energy on a large scale and utilize it when sunlight is unavailable, limiting its application. The production is strongly dependent on sunlight power stability, *i.e.*, seasonal, weather-based, and nighttime-daytime fluctuations require balancing and production on different timescales. Two electrochemical methods are available to convert and store electrical energy: batteries and chemical carrier production by electrolysis. Among batteries, lead-acid and lithium are the most popular and currently make up over 81% of new energy storage installations globally; the lithium-ion battery is considered one of the most efficient batteries nowadays [9]. Primary challenges are the low availability and relatively expensive of some components, environmental hazards, limited charge-discharge lifetime, and low gravimetric energy density. Since batteries also experience discharge losses with time, alternative methods for longer-term energy storage should be explored.

The energy storage in chemical bonds would be a widely applicable solution to store surplus harvested (but not readily used) renewable electrical energy [10]. Caching solar energy in the form

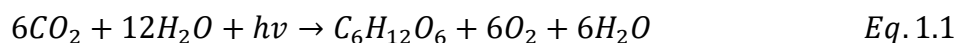
of hydrogen (H_2) is a good alternative for a valid reason; H_2 has a much higher gravimetric energy density than the utmost fossil fuels [9]. The most self-evident solution is H_2 gas derived from water electrolysis, for which the fuel cell technology to re-generate electricity is mature, but the energy loss associated with storage and the conversion steps is considerable. However, solar to hydrogen (STH) is a suitable carrier to replace fossil fuels in many ways (see section 1.5). However, a straightforward and complete substitution of fossil fuels is not viable [11]. Water splitting is extensively considered the most viable option for renewable energy storage. One reason is that many obstacles made electricity unsuitable for some industries or long-distance transportation [12], calling for a renewable chemical energy carrier.

There are three STH conversion ways: **thermal splitting** based on solar heat (see section 1.6.), **electrolysis**, and **photo(electro)lysis**. The latter system involves an energy harvesting unit (light absorber) that undergoes charge separation (i.e., electrons and holes = excitons are generated) to create potential and current as in photovoltaics [11,13], but it is considered suitable rather for small-scale devices. Solar cells can be a delegated source for solar energy conversion to produce electricity for electrolysis, but energy storage capacity on a large scale has practical limitations [2,12].

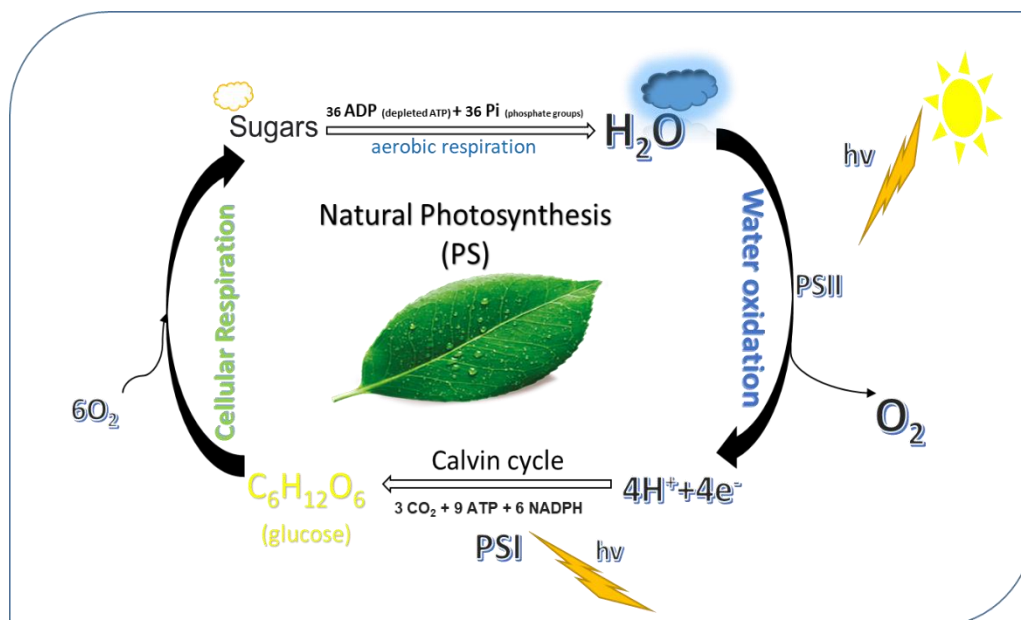
To our luck, Nature serves with an instance of renewable energy production, storage, and use: *photosynthesis*. The photosynthetic system is appealing to imitate its principles and thus achieve *artificial photosynthesis*. The photosynthetic process stores energy in the form of chemical bonds, and the products are carbohydrates that act as energy carriers or structural polymers made by CO_2 fixation [14]. Thus, Nature's system guides researchers on how solar energy can be converted by a photosynthetic machinery system sustainably [15].

1.4. Natural photosynthesis

Photosynthesis is a fundamental biological process that runs life on Earth. For more than 2 billion years, plants, algae, and other organisms have been converting solar into chemical energy in the broadest sense; thus, solar energy could be captured in the bonds of organic molecules. The chemical energy is stored in carbohydrate molecules (sugars, $C_6H_{12}O_6$) as shown in Equation (1.1) and their polymers, synthesized from CO_2 in the dark (photosystem I, or PS-I). Light absorption occurs in photosystem II (PS-II) to oxidize the ubiquitous electron source H_2O to O_2 byproduct (that is later consumed to generate energy during respiration by aerobic life forms or consumed by plants) [16].



Scheme 1.1. illustrates two processes, natural photosynthesis and cellular respiration in plants. Harvesting solar energy and CO₂ fixation into carbohydrates using H₂O are further discussed in the next section.



Scheme 1.1. The process of natural photosynthesis and cellular respiration in plants.

Plants harvest solar energy in PS-II, produce O₂ from water molecules, and convert CO₂ into carbohydrates in PS-I (Fig.1.1) [17]. These two processes have a determinant role in the trafficking of O₂ and CO₂ between living organisms and the environment [18].

Chlorophyll units in PS-I absorb light at 700 nm (introduced as P₇₀₀), while those in PS-II, at 680 nm (introduced as P₆₈₀) [19]. More accurately, photons are absorbed by the organic (porphyrin-containing) antenna system in the thylakoid membrane furnishing PS-II with very high efficiency (>97%). The excited state molecule P680 gives electrons to an external quinone (Q), reducing it to hydroquinone (HQ). Electron vacancies are filled by H₂O oxidation carried out by the oxygen-evolving complex (OEC), which contains an oxo-bridged tetramanganese-calcium cluster (Mn₄CaO₅) [20].

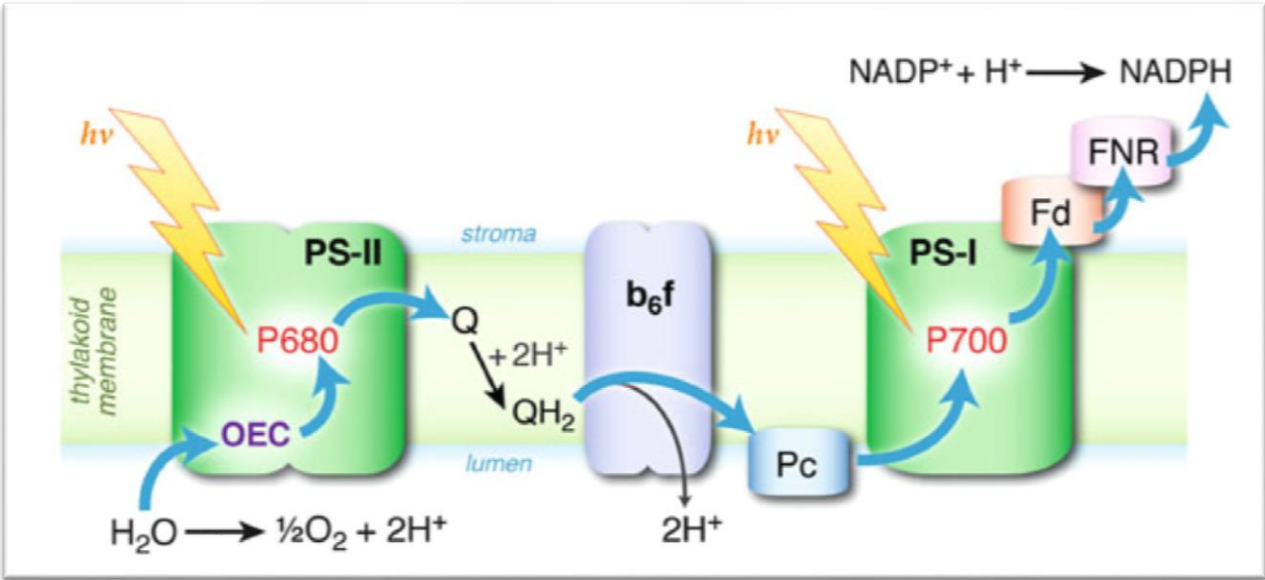
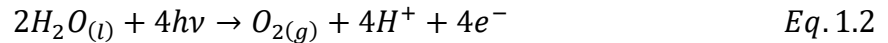
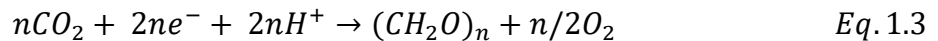


Figure 1.1. Overview of the oxygenic photosynthesis, including the light-dependent reactions and electron transfer in the thylakoid membrane. Electrons flow from H_2O to other components NADPH (blue arrows). Q: plastoquinone, Pc: plastocyanin, Fd: ferredoxin, FNR: ferredoxin– NADP^+ reductase [20].

A multiple-step charge transfer process leads to oxidized water Equation (1.2), and O_2 is released into the atmosphere as a byproduct.



In the Mn-cluster, protons and electrons accumulate four oxidative charge equivalents transferred to the PS-I by the Q/HQ system [21]. The electrons and protons are employed in the light-independent reactions for reducing CO_2 directly to generate carbohydrates within the Calvin Cycle, a dark reaction utilizing nicotinamide adenine dinucleotide phosphate (NADPH) and adenosine triphosphate (ATP) in the course of the reduction steps [22] (see Equation (1.3)). Cellular respiration involves breaking down glucose, producing ATP, and releasing energy [23]. Note that carbohydrates are beneficial to humans for direct use or ethanol production, while lipids are useful for biodiesel production [20].



The light absorption, energy transfer to the reaction center, charge separation, and stabilization are carried out by PS-II, driving water oxidation and reducing plastoquinone [20]. PS-II is a large protein complex located in the thylakoid membranes of oxygenic photosynthetic organisms that

involves a catalytic center where the OEC that contains the μ -oxido- Mn_4Ca - cluster catalyzes the water oxidation. Detailed structural investigations revealed that the Mn_4Ca cluster consists of three Mn ions, and the Ca ion forms a cubane-like structure with the four metal ions linked by oxo-bridges (Fig. 1.2a) [24]. Two water molecules are oxidized by sequentially removing four electrons to generate one molecule of O_2 and 4H^+ , where electrons pass from water to P_{680} *via* the OEC. The oxidized P_{680+} cation radical is the most oxidizing redox cofactor in nature, with an oxidation potential of *ca.* 1.25 V *vs* NHE, which recovers the electron from a Mn_4Ca -cluster in the OEC [25]. Several amino acid residues surround the OEC that either provide ligands to the metal ions or facilitate hydrogen-bonding networks that almost certainly play a vital role in the deprotonation of the substrate water molecules [26]. The kinetic activation barrier to water oxidation requires a highly active metal center to support the multiple electron transfer steps. Indeed, proton-coupled electron transfer (PCET) contributes to biological processes, as electron transfer in many proteins and enzymes is supported along pathways exhibiting hydrogen-bond contact between amino acid residues and polypeptide chains [27]. In 1975, Kok and Joliot systematized the stepwise oxidation mechanism by the OEC. Experiments conducted independently revealed that the oxidation of H_2O to O_2 is a four-stage process, each step termed as S_i ($i = 1-4$) starting from the resting state S_0 (see Fig. 1.2b) [41]. Each oxidation state of the OEC is known as the “S-state,” S_0 is considered the most reduced. At the same time, S_4 is the most oxidized state in the catalytic cycle, produced by a repeatedly photo-oxidized chlorophyll center, P_{680} , which converts collected light energy into oxidizing potential energy [42,43]. Four photons are needed to trigger the $S_0 \rightarrow S_1 \rightarrow S_2 \rightarrow S_3 \rightarrow S_4$ transitions. The last step is a chemical reaction ($S_4 \rightarrow S_0$) where the dioxygen molecule is evolved [23,44].

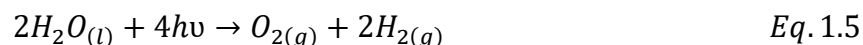
The two water molecules are coordinatively bound to the Mn centers of the OEC in the various S_i states; there is a general agreement that the dark-stable S_I state of the OEC has two Mn(III) and two Mn(IV) centers [28]. The most oxidized cluster state, S_4 , returns to the most reduced state, S_0 a four-electron reduction process and O_2 evolution. There is an ongoing debate in the literature about the mechanism of O–O bond formation, as it could involve either the nucleophilic attack of a water molecule (WNA mechanism) coordinated to the Ca ion at an Mn(V)=O moiety or that of an Mn(IV)–O•– radical at a neighboring Mn(IV)–O–Mn(IV) oxo-bridge (for catalytic systems, these mechanisms will be discussed in section 1.9.1).

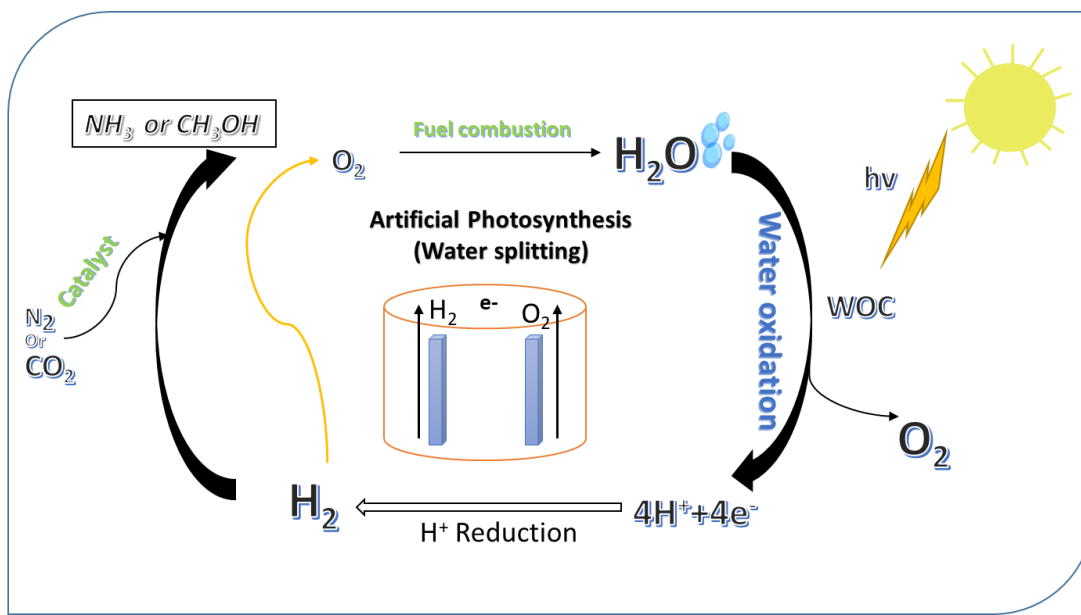
rise everywhere; inside of these will take place the photochemical processes that hitherto have been the guarded secret of the plants, but that will have been mastered by human industry which will know how to make them bear even more abundant fruit than Nature, for Nature is not in a hurry and humankind is. Furthermore, suppose in the distant future, the supply of coal becomes completely exhausted. In that case, civilization will not be checked by that, for life and civilization will continue as long as the Sun shines!' , Ciamician has envisaged an AP process that will have been created successfully based on the principle of natural photosynthesis by chemists [30,31].

In the past decade, enormous efforts at elucidating AP machinery have significantly expanded. Developments are encouraging, but substantial efforts are still required until functional prototypes are realized [32]. Converting sunlight into valuable energy for daily life and our civilization's development is an important goal [33,34]. In the broader perspective, AP systems must produce solar fuels that are economically and environmentally attractive from abundant, inexpensive raw materials such as water and carbon dioxide [35].

Rather than being collected for electricity, in certain areas, the photo-generated electrons and holes can be used to drive chemical reactions directly, converted into chemical energy (solar fuel) stored in the form of chemical bonds [11]. In Scheme 1.2, the multiple-step of AP process, which mimics the function of natural photosynthesis, is presented: splitting water (H₂O) into O₂ and releasing 4e⁻ and 4H⁺ involve sequential proton-coupled electron transfer (PCET) steps [36]. Equation 1.5 shows the general water-splitting reaction using solar energy [37,38].

Nature is devised to bypass the unavoidable long-term oxidative degradation of organic molecules, which has been that of continuous replacement and repair of the molecular machinery of the OEC [28]. The OEC reaches harshly oxidizing states and demands high chemical resistance of the molecular components. Thus, creating artificial water oxidation catalysts (WOCs) inspired by Nature is still a fundamental challenge [28]. Effective strategies are hard to apply to artificial systems as plants do in the chloroplast, as the OEC must be re-synthesized under surrounding sunlight every thirty minutes to indemnify the oxidation damage it suffers from producing O₂ [39].





Scheme 1.2. The general concept of artificial photosynthesis systems.

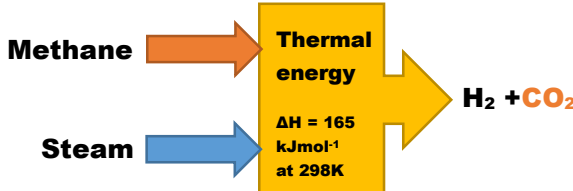
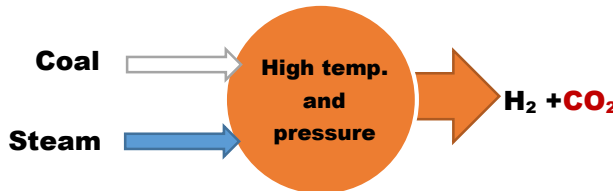
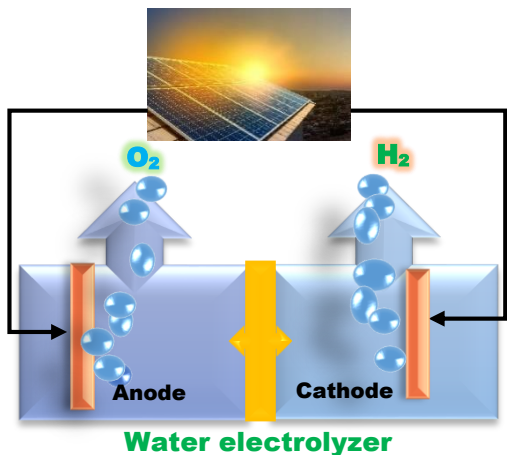
Therefore, the design and preparation of robust artificial molecular components require special considerations [28,39]. *Before I go into a detailed analysis of these special considerations and the state-of-the-art scientific achievements with Fe-based systems (that is the focus of my dissertation) in sections 1.9-1.11, let us discuss the technical aspects of hydrogen usage and modern production systems that can be applied at different scales, because these represent the receiving medium for any new scientific achievements.*

1.6. Hydrogen Production

More than 44.5 Mt of hydrogen gas is produced and utilized for industrial purposes every year, and thus various techniques have been developed for its production [40,41]. Currently, 95% is produced from fossil fuels by two principal technologies, steam methane reforming (SMR) and coal gasification (CG) (Table 1.1). In comparison, only 4% of the H₂ is produced using solar energy for water electrolysis (PV-WE), a sustainable way for which the feedstock is solely water - an abundant and renewable hydrogen source [41,42].

Many studies agreed that H₂ is the only fuel to overcome energy-related environmental problems by utilizing renewable resources [43–45]. Water electrolysis is considered a system that can serve our requirements; however, the high-cost make of the process makes it limited to applying this technique in comprehensive practice [41–43].

Table 1.1. Three principal technologies for industrial H₂ production.

Technology	Reaction	Side prod.	Proc. eff.	Price of H ₂ [46]
SMR	$CH_4 + 2H_2O \rightarrow 4H_2 + CO_2$ 	CO ₂ emission	65-85%	1.4 \$/Kg
CG	$C + 2H_2O \rightarrow 2H_2 + CO_2$ 	CO ₂ emission	~ 50%	-
PV-WE	$2H_2O + \text{energy (e.g. PV)} \rightarrow 2H_2 + O_2$ 	O ₂ (Zero CO ₂ emission)	>85% (in progress)	5.6 \$/Kg

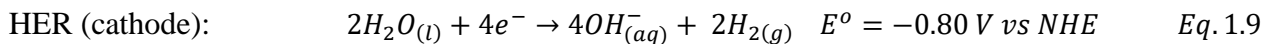
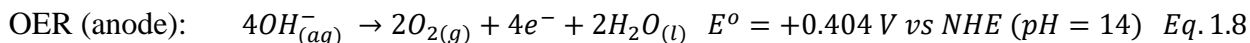
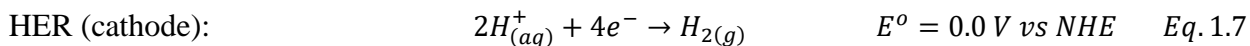
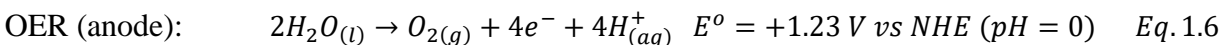
H₂ has the advantages such as high combustion value and zero-emission of CO₂, and most importantly, it can be converted to many energy-rich materials for storage or transport, e.g., with CO₂ to methane, methanol or formic acid, with molecular nitrogen to ammonia, or synthetic hydrocarbons using the Fischer–Tropsch process [47]. A further attractive advantage of H₂ as fuel for transportation applications is the advanced technology to produce fuel cell electric vehicles (FCEVs). Various methods are available for solar-to-hydrogen conversions, such as photovoltaic-water electrolysis (PV-WE), photoelectrochemical (PEC), photochemical (PC), photobiological,

and hybrid methods [9]. Herein, we will review the principles of WE and PEC systems since these are relevant to my research thesis (section 1.8).

1.7. Principles of Electrochemical Water Splitting

Overall, water splitting consists of two half-reactions: hydrogen-evolution reaction (HER) and oxygen-evolution reaction (OER). The water splitting is an endothermic chemical reaction with an associated increase in the Gibbs free energy ($\Delta G^\circ = 237 \text{ kJ mol}^{-1}$).

In acidic electrolytes, the OER releases protons and electrons, and evolving oxygen gas, as shown in Equation (1.6), where the charges generated ($4e^-$ and $4H^+$) by the anodic OER are used up for the respective formation of H_2 by the cathodic HER Equation (1.7). In alkaline electrolytes, the process follows Equations (1.8) and (1.9) [48].



In the OER, the removal of four electrons and protons, the breakage of four O-H bonds, and the formation of an O-O bond forms a mechanistic complexity, and this half-reaction is currently the bottleneck for developing efficient and sustainable artificial water-splitting devices. Notably, a large overpotential is required by the sluggish, sequential multi-step OER [49]; thus, sufficient applied voltage is needed to overcome the overpotential aggregate of the anode (and cathode) and reach high enough current density (the goal for practically useful devices should be in the 0.5-1 A/cm² range). Consequently, careful selection of superior electrocatalysts for HER and OER reactions plays a crucial role in lowering voltage consumption. A result of the complexity and the high oxidation potential required by the OER means an enormous challenge for chemists seeking efficient and robust electrocatalysts (as a minimum, a potential more positive than $\sim 1.23\text{V}$ vs. normal hydrogen electrode (NHE) is required) [11,15,49–51].

The OER requires a higher overpotential (η) than the HER, which follows the two-step Volmer-Tafel, or the Volmer-Heyrovsky mechanism. This means that most η results from the OER (i.e., $\eta_a > \eta_c$).

When uncatalyzed, the removal of 4H^+ and 4e^- from two water molecules, which undergo O-O bond formation to produce O_2 as the final step demands considerable energy to overcome the kinetic barrier [25,52,53]. An *electrocatalyst* is a catalyst that lowers the activation energy needed for an electrochemical reaction without being consumed [54]. In other words, it opens a new, energetically favorable mechanistic route toward the products. Electrocatalysts are unique, as they operate near to or on the electrode surface only. The activation energy is provided by the electrical energy (electric field or potential) set on the electrode.

Consequently, electrocatalysts usually change the potential at which oxidation (OER, see Equation 1.6) or reduction processes (HER) occur [55]. Electrocatalysts can be heterogeneous (e.g., a solid surface catalyzing a reaction in solution) or homogeneous (molecular catalysts), soluble, and aid the transfer of electrons within the diffusion layer near the electrode. The current commercial electrocatalysts rely on valuable and rare noble metals, such as Pt for HER [56,57] and Ir and Ru for OER [58,59]. **Due to their preciousness and rarity, these catalysts** are a severe obstacle to using electrolyzers at immense scale production of H_2 with affordable price per unit volume [60]. Thus, massive efforts have focused on investigating inexpensive and highly abundant elements in robust and efficient catalysts for water oxidation, including homogeneous and heterogeneous catalysts.

Three well-known vital technologies of water electrolysis as shown in (Fig. 1.3): **1**) alkaline electrolyzers with a liquid electrolyte (NaOH , or KOH) and a diaphragm to separate chambers of the electrodes, **2**) proton exchange membrane (PEM) electrolyzers, the electrodes are separated by a proton-conducting polymeric solid membrane, and **3**) solid oxide high-temperature electrolyzers, the electrode chambers are separated by the ceramic solid [61]. In the alkaline electrolyzer process, the water reacts at the cathode into H_2 and OH^- ; at the anode, OH^- is transformed into O_2 and H_2O , as shown in Fig. 1.3. Inexpensive materials such as Ni and its alloys are used to increase the efficiencies of electrodes in alkaline electrolytes. Different electrocatalysts in the acidic and basic electrolytes are employed for HER and the highly irreversible OER. Nevertheless, water-alkaline electrolyzers with Ni nanowires electrodes covered by different electrocatalysts have affordable and durable performance at room temperature[62].

In contrast, in PEM cells, the water decomposition at the anode produces O_2 , and protons pass through the proton-conducting membrane to the cathodic side, where H_2 production occurs. In solid oxide (high-temperature) electrolysis, water vapor reacts at the cathode into hydrogen gas, and O^{2-}

ions are passed to the anode through the ceramic solid electrolyte, where they are oxidized to O₂ gas at an operating temperature of *ca.* 700–1000°C (Fig. 1.3).

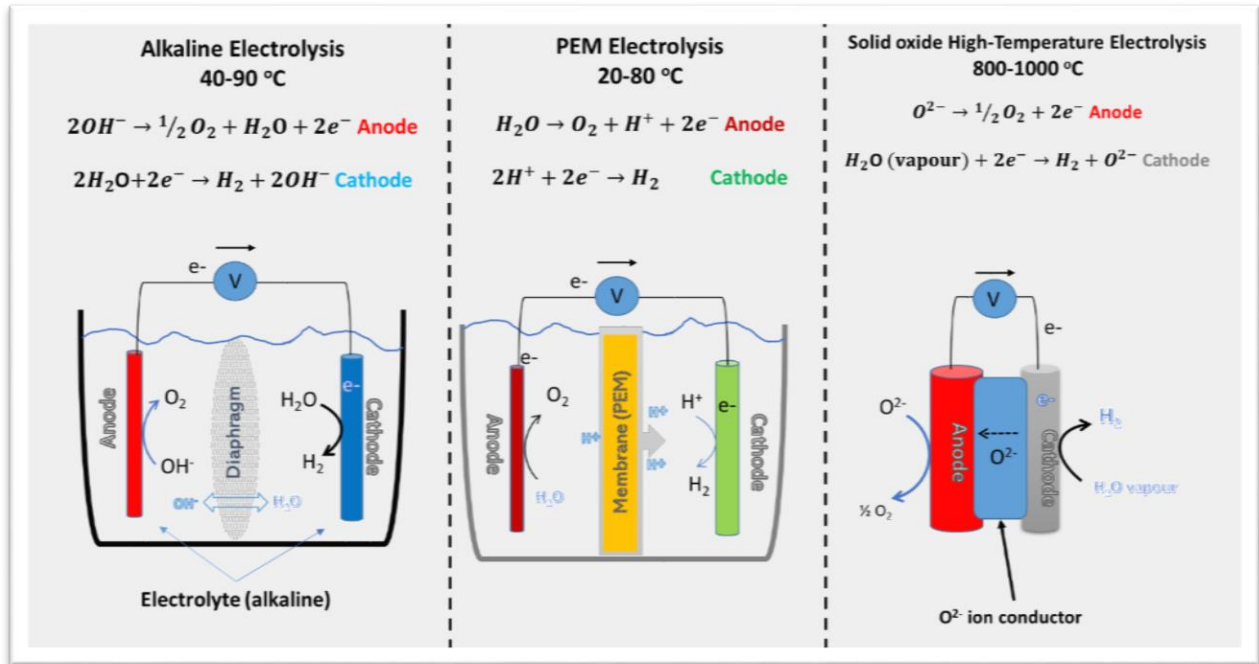


Figure 1.3. Schematic view of the three types of water electrolysis (alkaline, PEM, and solid oxide).

1.8. Water electrolysis via photoelectrochemical (PEC) devices

According to nonconservative estimates, 173,000 TW of solar power reaches the Earth continuously, while our consumption is *ca.* 15-17 TW and no more than 30 TW by 2050 [63,64]. It is a free and infinite energy source on the timescale of human history. The energy of solar irradiation at the Earth’s surface constitutes in small part high energy ultraviolet (3-5% below 380 nm), 42-43% of visible (380 nm – 700 nm), and 52-55% of infrared and far-infrared light (above 700 nm) [9,65].

From this perspective, if only the ultraviolet region is utilized, it could only employ a maximum of 10% of the total incident solar energy. While, if it worked in the visible and near-infrared area, potentially 50% of the whole incident solar power would be available [9]. In the most evident setup, photovoltaic devices (PVs, or solar cells) transforming solar energy into electric power can be connected to stacks of water electrolyzers (WEs) to supply them with renewable electricity to accomplish water electrolysis. Both PVs and WEs are well developed; thus, their combination is readily available [66], as shown in Table 1.1. (PV-WE). While the PV-WE technique is suitable

for a somewhat centralized green H₂ production [67], small-scale, decentralized, or mobile applications may require better-fitted options. In addition, the PV technology is still relatively high-priced, the utilization of visible light is still minimal, and the PV panels occupy a large area; thus, extended pieces of research are demanded in this field [68].

The above reasons motivate research on photoelectrochemical (PEC) cells based on a semiconductor-liquid junction that provides direct photon-to-chemical energy conversion. This can be done efficiently by connecting or integrating light-harvesting and catalytic sub-units into one system in different ways [69]. There are various encouraging entrances to solar water splitting, including photochemical (PC) and, most importantly, PEC systems. Herein, I shortly describe the solar-assisted PEC of H₂ production, although it has to be mentioned that modern studies were all inspired by Fujishima's and Honda's pioneering work (1972), who successfully demonstrated the concept of PEC water splitting for H₂ production [70]. However, no practical PEC device ultimately producing solar hydrogen is in use because this would require an overall highly durable, simplistic, and cost-effective design [71].

The least complicated draft of a PEC cell that concurrently performs both OER and HER is shown in Fig. 1.4. PEC is based on photoelectrodes made of semiconducting materials coated, or combined with catalysts, as shown in Figure 1.4a. The working electrode, ordinarily a semiconductor, is also described as the photoelectrode (it can be a photocathode or photoanode, too) because of the light-induced chemical reactions admitted at its surface. A PEC cell consists of an n-type electrode immersed in an electrolyte for the OER studies, as shown in Figure 1.4b. A membrane separates the (photo-)cathode, where H⁺ ions and electrons are combined to produce H₂, as shown in Fig. 1.4a [11,13]. The OER reaction involves intermediate species on the bare photoanode surfaces with a huge energy barrier; thus, an overpotential is required to overcome the kinetically rate-limiting multistep reactions [72–74]. To suppress surface recombination, a common way is to combine the photoanodes surface with proper water oxidation catalysts [75]. As for the catalysts, cost-efficient and robust compounds are sought. In the case of the anodic OER, a catalyst unit serves as a hole trap and ensures chemical selectivity so that the highest possible proportion of captured holes are consumed in OER while parasitic (side-)reactions are suppressed. The generated holes and electrons by illumination should be moved immediately to the catalysts immobilized on the semiconductor's surface [11].

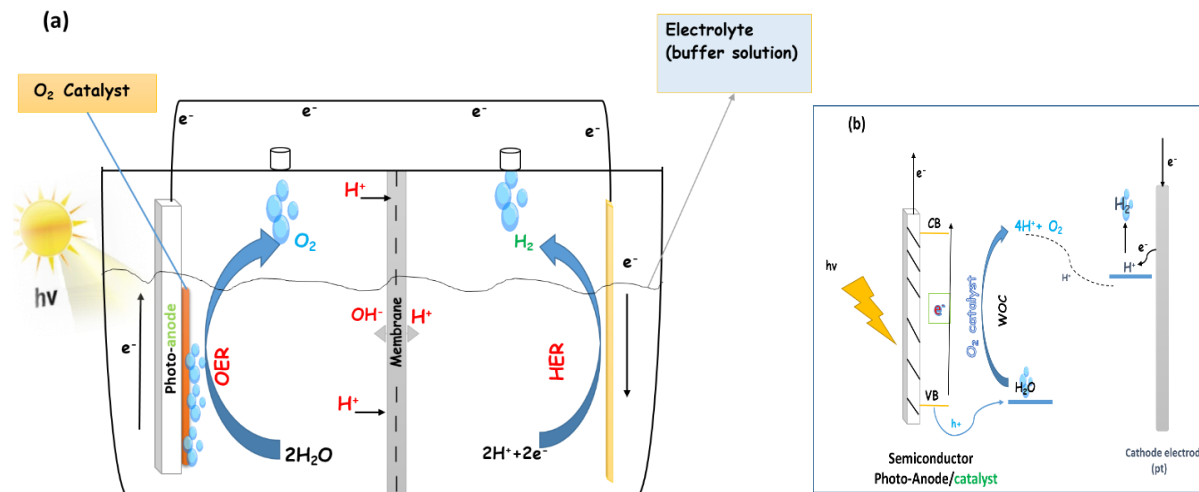


Figure 1.4. a) PEC cell for water splitting, illustrating two half-reactions, OER and HER; b) the anodic half-cell reaction (OER) on a photoanode and the water oxidation catalyst (WOC) located on its surface.

The effective extraction of carriers at the interfaces of both H₂ and O₂ evolving electrode surfaces requires surface modifications to enhance catalysis [72]. Overcoming reaction barriers and hastening the reactions by developing efficient catalysts with low overpotential, high intrinsic activity, stability, and a high catalytic rate is the essential criteria for each half-reaction and a crucial step in making highly efficient water splitting devices [11,15,49,72]. In this respect, WEs and PECs have the exact requirements for catalysts (as detailed above), but in the case of PECs, photo-degradation and the light-attenuating effect of the catalyst must be avoided (i.e., when the catalyst absorbs light in the same range where the semiconductor is excited). One of the recent developments in PEC water-splitting utilizes pairing tungsten oxide (WO₃) and bismuth vanadate (BiVO₄) to form heterojunction photoanode. In WO₃/BiVO₄ heterojunction, BiVO₄ serves as an excellent visible-light absorber (~30% sunlight), and WO₃ functions as an active electron conductor. In this study, the substantial efforts and impressive milestones showed the highest photocurrent value of about 6.72 mA cm⁻² (at 1.23 V vs. reversible hydrogen electrode (RHE)) with an incident photon to current efficiency of 90% (at 1.23 V vs. RHE)[76].

Additionally, a practical strategy can be electrocatalysts on semiconductor photoelectrodes that play an influential role in accelerating the HER/OER kinetics, repressing surface recombination, overcoming the sluggish interfacial kinetics, and boosting the functional lifetime of semiconductors[77]. Different techniques include spin coating, electrodeposition, and drop-casting to immobilize catalysts on semiconductors; for instance, Spurgeon et al. sputter-coated IrO₂ on

WO₃ photoanodes and compared their PEC water oxidation performance was the effective adequate method of coupling IrO₂ to WO₃ given that it allowed for a higher degree of surface coverage of catalysts[78]. Importantly, PEC water splitting should be performed using electrolytes in the near-neutral range rather than under strongly acidic or basic conditions to avoid corrosion issues [79]. Therefore, future directions should consider the development of electrocatalysts of OER and HER operating in neutral or near-neutral conditions that are more environmentally friendly with cause fewer corrosion problems.

1.9. A brief overview of water oxidation catalysts

As previously introduced, OER is arguably the most challenging process of overall water splitting. Due to the transfer of four electrons and the formation of O-O bond to produce O₂, and this transformation required harsh oxidizing conditions and significant overpotentials [25,80,81]. Thus, efficient water oxidation catalysis (WOCs) is indispensable through design catalysts that minimize the overpotential and achieve high turnover frequencies (TOFs)[82]. Typically, Turnover number (TON) = number of moles of O₂/(mole of catalyst), and Turnover frequency (TOF) = TON/time of reaction. The WOCs can be classified into two groups: **catalytic materials** (typically metal oxides/hydroxides) [83–87] and **molecular complexes** [88–91][25,92,93]. As far back as 1903, Cohen and Glazer reported cobalt oxides to produce dioxygen electrocatalytically [94]. Cobalt-based metal oxides have been publicized as the most promising electrocatalysts for water splitting[95].

For molecular complexes, the natural Mn–Ca cluster serves as inspiration which is operated as a catalyst for water oxidation and exhibits a turnover frequency (TOF) of 100~300 s⁻¹ through multiple proton-coupled electron-transfers (PCETs) with a photogenerated bias. On the other hand, artificial systems like electrolyzers generally utilize noble metal-based materials that are robust in all pH values combined with their considerable activity towards OER. The pioneering discovery of the Ru “blue dimer” reported by T. J. Meyer in 1982 [96], ruthenium-based complexes have primarily been studied as candidates for WOC. Therefore, enormous studies showed excellent catalytic activities of ruthenium-based complexes. At the same time, these complexes are not suitable for potential large-scale practical applications due to their rare and expensive compared to first-row transition metals (TMs) [97,98]. For instance, the rare metals ruthenium (Ru) and iridium (Ir) demonstrated efficient performance in WOCs at low overpotentials with high activity (TOF 10³ s⁻¹) and stability (Turnover number (TON) > 10⁶) [99,100]. However, their low abundance,

relatively expensive, and scalability obstructions impeded intensified research on earth-abundant first-row TMs and their complexes as potential WOCs [101]. Efforts have resulted in promising findings by applying different first-row TM-based electrocatalysts that can help develop catalysts suitable for industrial and practical applications to replace noble metal-based materials.

Molecular systems have certain advantages over bulk materials from clarifying fundamental questions regarding the structure-activity relationships at an atomic level. These catalysts can be investigated by advanced molecular spectroscopic methods in combination with electrochemical ones, providing details on the nature of the high valence active species in a redox process at a given pH, OER kinetics, kinetic isotope effects, electronic structure of the catalytic intermediates, the role of secondary interactions in catalysis, and secondary (parasitic or degradation) reactions, to name only the most important ones. For example, it was possible to fine-tune Ru-polypyridyl complexes to obtain a record high TOF of $7,700 \text{ s}^{-1}$ and $50,000 \text{ s}^{-1}$ at $\text{pH} = 7$ and 10 , respectively, by ligand adjustments [102]. Organometallic Ir complexes also provided essential knowledge on the effect of the ancillary ligand structure on stability [103]. More recently, a similar evolution of some first row TM complexes can be witnessed [104]. Proton-coupled electron transfer (PCET) reactions can also be investigated in high detail using molecular systems that are of great importance since PCETs are essential in biological processes, including nitrogen fixation, photosynthesis, respiration, enzymatic reactions, and activation of small molecules in conversion and storage of solar energy, mainly water oxidation and carbon dioxide reduction [105].

However, designing active and robust molecular electrocatalysts and immobilizing them on conductive substrates remains a significant challenge. Catalytic materials are not discussed in detail since my dissertation focuses on *molecular catalysts*. Herein, I would like to highlight a few points that I find relevant in context to molecular catalysis and immobilization. In (photo)electrocatalysis, heterogeneous catalysts indicate materials layered on a support electrode, typically various aggregates of metal atoms, or compounds, only a part of those exposed to reactants [106]. These can be generated by standard solvothermal, bottom-up methods, epitaxial growth of nanocrystallites, drop-casting of suspensions, etc.

In the particular case of OER, the severe conditions required to drive the reaction may also degrade and convert molecular complexes to form metal oxide particles *in situ* [25]. In this case, a derived heterogeneous film will be responsible for sustained catalysis, and the initial complex acts as a

precursor. Consequently, various difficulties have to be defeated in designating the mechanistic aspects of water oxidation in a homogeneous system.

A complementary mix of electrochemical analyses (e.g., electrolysis, impedance spectroscopy), detection techniques (e.g., spectroscopy), and other specific detection procedures have been applied to distinguish between real homogeneous and heterogeneous catalysts. Wherever the *in situ* occurrences of metal-based nanoparticles on electrodes are suspected, a sequence of tests can be accomplished before and after bulk electrolysis by scanning electron microscopy (SEM), energy-dispersive X-ray spectroscopy (EDX), and X-ray photoelectron spectroscopy (XPS) to address this question [101,107]. Last but not least, the borderline between heterogeneous and homogeneous may be indefinite, as there are examples of tandem equilibrium systems where the catalysis involves different phases in equilibrium [108].

Heterogeneous catalysts possess some flexibility in structural features, the composition of combined materials, doping, and surface morphology that all affect long-term stability and activity [109,110]. McCrory *et al.* have presented a flow chart of the practical steps of evaluating the electrocatalytic performances of electrodeposited oxygen-evolving electrocatalysts by proposed a protocol for measuring the electrochemically active surface area, catalytic activity, stability, and Faradaic efficiency, which includes electrochemical studies, and morphological investigations [111].

Finally, molecular catalysts were reported immobilized on the electrode surface and act as heterogeneous catalysts without mineralization, but the number of examples is scarce, and there is room for further research in this field. The importance and the advantage of immobilization starting from molecular compounds can be summarized in several summonses, including the possibility of better characterizing the so derived heterogeneous species, the variability of the produced catalytic sites, and better defining the number of active sites, which has a crucial role in determining TOF, as uncertainty about the number of active sites frequently occur in materials [112].

1.10. Mechanistic pathways for water oxidation catalysts, initial steps, and O-O bond formation

It was mentioned that the role of a catalyst is to open new mechanistic routes with lower kinetic energy barriers. Concerning the OER, the formation of O₂ involves much more complicated kinetics than that of H₂; therefore, it is regarded as the most critical process in WEs or PECs. Besides the electron transfer steps, a purely chemical step also occurs in most of the cases that is

the formation of the O–O bond. Generally, this is energetically the most demanding step, and different mechanisms have been proposed for the construction of the O–O bond by WOCs. We also must distinguish **molecular catalysts** (homogeneous or immobilized) from **catalytic materials** (inherently heterogeneous); therefore, we discuss their mechanistic routes separately.

1.10.1 Mechanistic pathways for molecular water oxidation catalysts.

Two significant types of mechanistic pathways have to be distinguished based on the nature of the O–O bond formation step, depending on whether an external water molecule is involved [113].

Water nucleophilic attack (WNA): the nucleophilic attack of H₂O or HO⁻ at the L–M⁽ⁿ⁺¹⁾⁺–O⁻¹ or L–M⁽ⁿ⁺²⁾⁺–O⁻² species' electrophilic center that leads to the formation of a metal-peroxide bond. The ancillary ligands should favor the occurrence of the oxo form, i.e., M=O (Fig. 1.5), which is the highest obtained oxidation state of the catalyst, usually generated by a 2×1e⁻ withdrawal from the resting state, exhibiting high redox potential, thus capable of WNA (see the Kok cycle, S4).

Interaction of two M–O units (I₂M): two M–O units is involved in forming the O–O bond, as shown in Fig.1.5. In both pathways, the formation of the O=O bond constitutes the rate-determining step (RDS) of the whole process. Thus, understanding this step must be considered during the rational design of new catalysts.

Following the O–O bond formation, the rest of the electron and proton transfer steps occur rapidly since the peroxidic intermediates have considerably lower redox potential than the applied electric potential (WE), or electric potential plus photon energy (PEC). Consequently, the most crucial aspect of catalyst design is to find ancillary ligands/chemical environments capable of supporting high oxidation states of transition metals.

1.10.1. Mechanistic pathways for water oxidation materials

Generally, heterogeneous catalysts do not show high-density catalytic sites in a well-defined single crystalline surface or unique catalytic sites in a complex polycrystalline surface [114]. Concerning water oxidation, a multiphase chemical reaction system exists entirely determined by the surface cooperation between these phases. For illustration, many factors impact the activity of a catalyst: the porosity, point defects in bulk materials and surface, the exposed structure facets, the bridge sites, terrace kinks, edge structures, and water coordination [115]. Water oxidation on a heterogeneous surface based on the fact that adsorbed/bound water molecules or hydroxyl groups

partially cover the surface, likely combined in the surface reaction kinetics when the electrode is contacted with H₂O in the electrolyte utilized bias or applied photon irradiation [115].

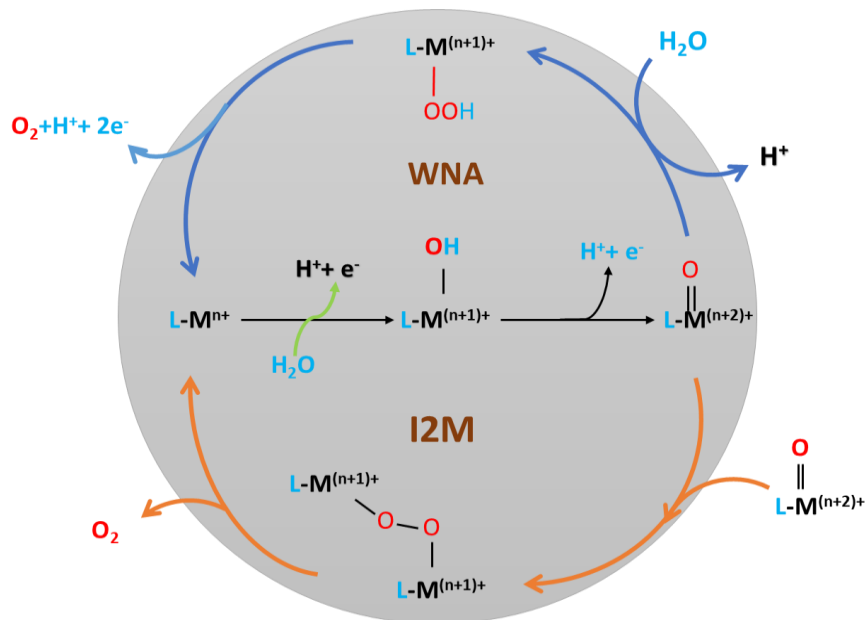
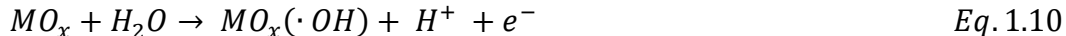


Figure 1.5. The two major types of the O-O bond formation pathways in molecular WOCs.

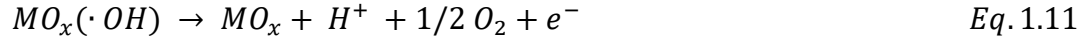
The OER may involve several surfaces adsorbed intermediates. Studies on mechanistic principles and hypotheses of the series of elementary steps relying on atomic-scale investigations remained limited. A few proposed mechanisms, conclusions about the rate-determining step (RDS), and experimental methods have been developed.

RuO₂, IrO₂, SnO₂, and PbO₂-based anodes are commonly employed in acidic media for OER [116]. Over the past decade, models have been proposed for the OER on these metal oxide electrodes. Fig. 1.6 shows the scheme of the mechanism, including two parallel reaction paths. The first primary step is forming adsorbed hydroxyl radicals by discharging H₂O molecules at the metal oxide surface, MO_x, Equation (1.10) [116].



The subsequent steps rely on cooperation between the electro-generated hydroxyl radicals and oxide anode. Based on a couple of restricted states, oxygen evolution *via* physisorbed hydroxyl radicals and chemisorbed intermediates will occur. As can be described in Equations (1.11-1.12) [116]:

- The physically adsorbed hydroxyl radicals are electrochemically oxidized to oxygen,



- The chemisorbed hydroxyl radicals interact with the oxide forming the higher oxide,



- The final O₂ evolving step and the decomposition of the higher oxide re-forming the lower oxidation state oxide, Equation (1.13),



Density functional theory (DFT) calculations revealed that routes b and d on metal-oxide surfaces, as it is illustrated in Fig. 1.6, may be interconnected and become dominant (depending on the catalyst and conditions) because the -OH and the -OOH groups link in an identical way to the catalyst [117]. The peroxidic M-OOH intermediate's rapid degradation is high energy (instability) [118].

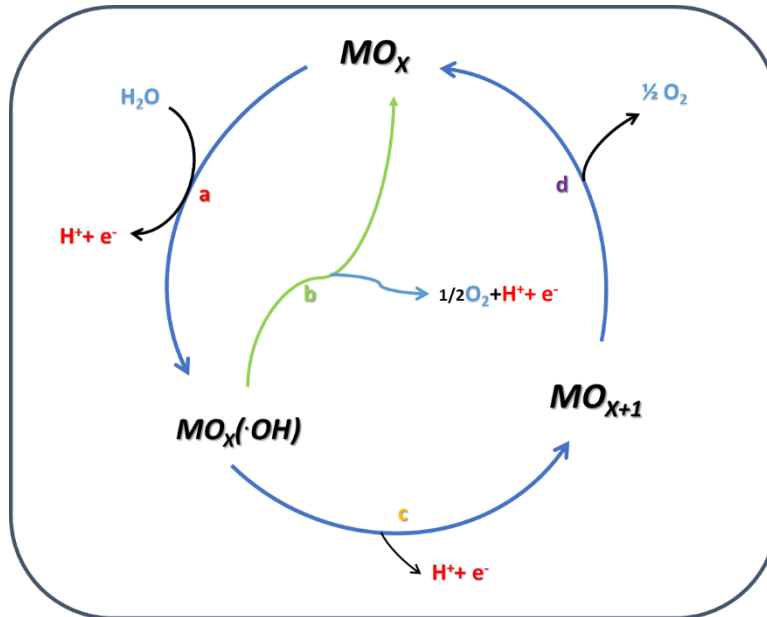


Figure 1.6. Scheme of OER on conductive metal oxide anodes: (a) generation of adsorbed OH radicals by water discharge, (b) O₂ evolution *via* electrochemical oxidation of physisorbed hydroxyl radicals, (c) generation of higher metal oxide *via* chemisorbed hydroxyl radicals, and (d) O₂ by chemical decomposition of the higher oxide [116].

S. Trasatti *et al.* proposed a multi-step mechanism after studying ternary mixed oxide electrodes $Ru_{0.3}Ti_{(0.7-x)}Ce_xO_2$ catalyzes OER in acidic environments [119]. Comparable to the homogeneous processes, the first step is the same as the absorption of a hydroxide group (Equation (1.14)),

accompanied by the formation of a metal oxide species, either through a second electron transfer Equation (1.15) or a recombination step (Equation (1.16)) [120]:



*denotes the catalytically active surface sites.

The final step, the O=O bond formation Equation (1.17), allows the active catalyst species to regenerate. Indication of the catalytic activity of an electrocatalyst can be gained from the Tafel slopes. The Tafel slope could be didact precise details on the rate-determining steps concerned in electrocatalysis, and it can be associated with the reaction mechanism of electrocatalysts (in case the whole kinetics is known). Therefore, Tafel slops provide an understanding of reaction mechanisms. Before the foundation of electron transfer kinetics theory was established, The Tafel equation ($\eta = a + b \log j$, where η is the overpotential, (a) constantly provides information about the electrocatalytic activity of the electrodes, and (b) is the Tafel slope) was extrapolated experimentally, (η vs. $\log j$) carried out information regarding the electrode reaction mechanisms (More details, Appendix B). The experimentally estimated Tafel slopes could be associated with the reaction mechanism for OER on the metal oxide surface. Thus, based on the available mechanistic models, a slope of 40 mVdec^{-1} suggests a mechanism where the second electron transfer is rate-limiting and Equations (1.14 or 1.15), and the slope of 30 mVdec^{-1} is characteristic for systems where the rate-determining step is the recombination reaction Equation (1.16). Accordingly, measuring the Tafel slope is required to inspect the reaction mechanism and helps in finding the rate-determining step [121].

Transition-metal oxides are the most investigated materials for OER, mainly due to their worthy activity and stability. For instance, many promising non-noble metal oxides often contain 3d elements (Mn, Fe, Ni, and Co). It should be noted that Layered double hydroxides (LDHs) have been used in a variety of areas and widely studied for OER due to the development of electrocatalysts. The LDH structure has been enormously researched in OER catalysts since NiFe-LDHs found the most efficient catalytic performances toward OER [122]. Rational design, studies

on active sites for OER, and a fundamental understanding of the structural characteristics of LDHs led to advanced LDH OER electrocatalysts [123,124]. Porous Ni-coated anodes were initially soaked with nickel hydroxide *via* electrochemical precipitation methods to produce α -Ni(OH)₂, the first metal hydroxide distinguished to show OER electrocatalytic activity [125]. Doping it with other metal cations with variable oxidation states such as a NiFe-LDH phase was realized to be critical for high OER activity [126,127]. In line with this, CoFe- and CoNi-LDHs were also employed as water oxidation electrocatalysts by other researchers [128,129].

A pioneering work by Kanan and Nocera showed that cobalt is also suitable for *in situ* formations of catalytic films on electrodes at neutral pH in phosphate [130]. Since then, this catalyst has been applied in combination with several semiconductors in PEC systems. Similarly, a Ni catalyst was also shown to form under benign conditions in the presence of borate [131]. The Ni-borate films could be prepared with precise thickness control and operated at modest overpotential, providing an alternative to the Co catalyst. These encouraging examples clearly demonstrated life beyond utilizing noble metals in OER electrocatalysis.

1.11. Iron-based molecular catalysts for water oxidation (WO)

1.11.1. Homogeneous catalysts

Lately, massive efforts have been made to develop efficient water oxidation catalysts (WOCs) composed of more abundant metals, homogeneous catalysts, and electrocatalysts based on metals such as manganese [130,131], iron [132–134], cobalt [135,136], nickel [137,138], and copper [139,140] received significant attention. Iron (Fe) deserves distinguished attention among these metals since it is the 4th most abundant element on Earth and an environmentally friendly metal. Several Ru- and Ir-based WOCs have been published to connect efficiency with robustness, and these noble metal complexes gave the incentive to explore other transition metals (TMs) in the field of WOCs [100,129]. However, instead of noble metals, first-row TMs might mean the real solution if we aim to utilize water splitting on a broader scale.

Among first-row TMs, Fe is a vital element (co-factor) in a family of enzymes and presents rich chemistry in synthetic catalysis due to its redox properties [132]. From low coordinate Fe(II) complexes to compounds that furnish high oxidation states like Fe(IV), Fe(V), or in a few cases, Fe(VI) are known, no wonder that Fe complexes represent a desirable choice as reactant/catalyst in a variety of redox reactions. Thus, Fe appears fully suitable for using artificial WOCs [133].

High-valent iron-oxygen species are strong oxidants, effective for substrate oxidation in enzymes [134–136], organic synthesis, and catalytic applications [137,138]. In addition to the selection of the conditions [133], the activity of Fe complexes is highly susceptible to electronic and geometric features, too, due to the occurrence of different oxidation and spin states. Therefore, designing precise ligand architectures that favor the formation and stabilization of high-valent Fe species sufficiently stable to promote water oxidation is still a challenge [133,139]. In the past decade, Fe-based molecular catalysts have confirmed the capability for water oxidation. Furthermore, Fe can catalyze different reactions, water oxidation, H₂ evolution, and CO₂ reduction because the electronic structures of the Fe cores are precisely adjusted by the particular coordination environments created by the ligands [11,140].

In 1980, the story of high-valent Fe-oxygen complexes as catalysts originated with Collins's work developing robust tetraamido macrocyclic ligands (TAMLs) for Fe [141]. Earlier, TAMLs were identified as perfect ligand structures to support TMs in high oxidation states, as considerably robust versus oxidation, and proved an efficient activation of O₂ to form Fe-oxo species. The work revealed that using donor deprotonated amide ligands firmly allows access to high oxidation state Fe and the thorough, stepwise elimination of oxidatively unsteady substructures in the TAML, which is topping in a series of highly robust macrocycles[25].

In 2010, Bernhard and Collins presented the first single-site Fe complexes catalyst for the OER [142]. Different Fe^{III}-TAML complexes (1-5) with substituents of varying electronic properties were synthesized as well-defined homogeneous (see Fig. 1.7a). Computational study on the WNA mechanism using an excess amount of cerium(IV) ammonium nitrate (CAN) as the chemical oxidant at pH =0.7. No activity was considered with complex 1; oxidatively stable TAML catalyst was ineffective because of ligand oxidation or maybe due to its lower stability in the acidic environment. The acidity caused fast deactivation allowing only 16 TONs (note that sacrificial chemical oxidants like CAN are often applied instead of electrochemical activation to explore the kinetics of WOCs). While complexes 2-5 show fast oxygen liberation at a varying rate (Fig. 1.7b), correlating with the addition of the electro-withdrawing group to the ligand. Thus, increasingly electron-withdrawing substituents on the TAML have influenced the catalyst performance. Complex 5 with Cl⁻ and F⁻ substituents showed the highest activity as an initial TOF > 1.3 s⁻¹, even though a slower phase takes a few seconds, and the rate of OER was first-order in complex concentration [5], as shown in (Fig. 1.7c). Correspondingly, the more uncomplicated iron

prototypes, such as $\text{Fe}(\text{acac})_3$ (acetylacetonate (acac) ligands), Fe_2O_3 , $[\text{Fe}(\text{bpy})_3](\text{NO}_3)_2$, and $\text{Fe}(\text{NO}_3)_3$, both with and without the TAML, showed no O_2 evolving, therefore assuring the remarkable reactivity of the Fe-TAML complexes. Established on these results, the oxygen evolution performances of the Fe-TAMLS catalysts are dramatically controlled by the electronic structure of derivative complexes because of the adjusted reactivity of the high valent iron-oxo intermediated[143].

The first model of a light-driven OER using a Fe complex was published by Dhar and co-workers, who studied two biuret-modified Fe-TAML complexes using CAN at pH=1 and 25°C in the dark, and under illumination in 10 mM acetonitrile-borate buffer at pH 8.7, where $[\text{Ru}(\text{bipy})_3]^{2+}$ served as a photosensitizer and $\text{Na}_2\text{S}_2\text{O}_8$ as electron acceptor. The experiments showed that a $\text{Fe}^{\text{V}}(\text{O})$ intermediate was photochemically produced as the active intermediate for the oxidation of H_2O to O_2 , leading to the formation of $\text{Fe}^{\text{III}}\text{-OOH}$ via WNA [144]. The demetallation reaction under acidic conditions was evidenced to cease catalysis. However, the initial OER rates were proportionate to the complex concentration, showing that the rate-determining step is the WNA on the $\text{Fe}^{\text{V}}=\text{O}$ species rather than I2M [142,144]. Thus, a single-site mechanism and a monomeric Fe^{III} -hydroperoxo species were responsible for OER [145].

Hoffert and coworkers summarized the catalytic activities of new complexes with pendant bases. Specifically, $[\text{Fe}(\text{L})(\text{CH}_3\text{CN})_2]^{2+}$ [L = N,N'-dimethyl-N,N'-bis(pyridazin-3-yl-methyl)ethane-1,2-diamine] was a robust catalyst using CAN at pH 0.7. This study demonstrated that incorporating pendant bases into molecular catalysts to aid PCETs might be an effective strategy in constructing new catalysts for the OER [143]. In other studies, robust ancillary ligands and *cis*-coordination of two water molecules were shown to favor catalytic OER. For instance, Randolph *et al.* reported a Fe^{III} complex with the tetradentate ligand, 2-(pyrid-2'-yl)-8-(1'',10''-phenanthroline-2''-yl)-quinoline (ppq), and a bis-phenanthroline amine ligand (dpa) by the presence of the potent chemical oxidant CAN work at pH 1 (Fig. 1.7d-e). The $\text{Fe}^{\text{III}}(\text{dpa})$ complex exhibited two reversible electrochemical, one-electron oxidations, whereas the dimeric $\text{Fe}^{\text{III}}(\text{ppq})$ complex, apparent two-electron oxidation associated with the process $\text{H}_2\text{O}-\text{Fe}^{\text{III}}\text{OFe}^{\text{III}} \rightarrow \text{H}_2\text{O}-\text{Fe}^{\text{IV}}\text{OFe}^{\text{IV}} \rightarrow \text{O}=\text{Fe}^{\text{V}}\text{OFe}^{\text{III}}$. The latter complex shows a fast initial rate of TOF = 2.2 s^{-1} but loses most of its activity after 1 h. The slower dpa complex displays TOF = 0.23 s^{-1} but proceeds to give activity after 1 h [146]. An exciting extension of neutral tetradentate ligands is the dedication of an anionic coordinating moiety since ligand basicity would be supposed to facilitate the high oxidation state

$\text{Fe}^{\text{V}}(\text{O})$. In this characteristic, Meyer and co-workers published that a six-coordinate Fe^{III} -aqua complex $[\text{Fe}^{\text{III}}(\text{dpaq})(\text{H}_2\text{O})]^{2+}$ (dpaq is 2-[bis(pyridine-2-ylmethyl)]amino-N-quinolin-8-yl-acetamido), (Fig. 1.7f), was an active electrocatalyst for WO in propylene carbonate/ H_2O mixture. After 15 h electrocatalysis at 1.58 V vs NHE, 29 μmol of O_2 was produced at 45% Faradaic efficiency. Under experimental conditions, the catalyst was stable and did not decompose in a PC/ H_2O mixture [147].

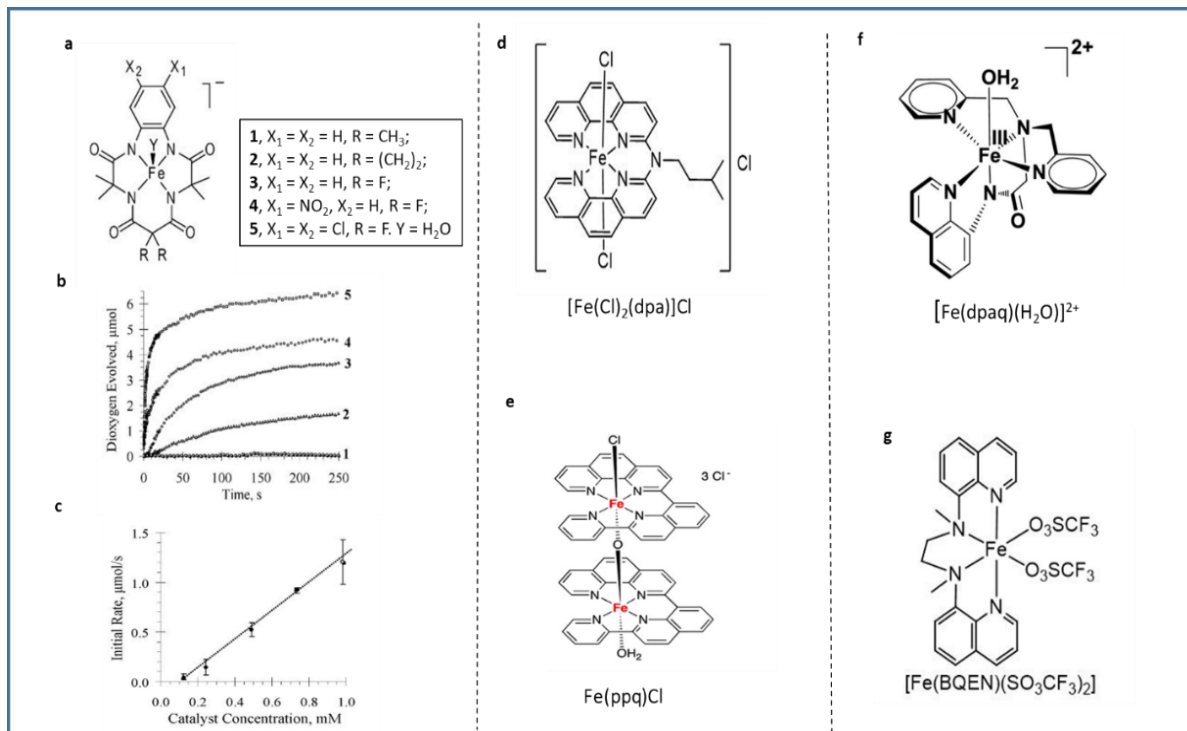


Figure 1.7. a) Molecular structure of Fe^{III} -TAMLs used as WOCs; b) evolution of O_2 using the different complexes upon addition of CAN in unbuffered water; c) initial rates of the O_2 plotted vs [complex], taken from [142]; d-e) structure of $[\text{Fe}^{\text{III}}(\text{Cl})_2(\text{dpa})]\text{Cl}$ and $\text{Fe}^{\text{III}}(\text{ppq})\text{Cl}$; f) the $[\text{Fe}^{\text{III}}(\text{dpaq})(\text{H}_2\text{O})]^{2+}$ complex, and g) the $[\text{Fe}^{\text{III}}(\text{BQEN})(\text{SO}_3\text{CF}_3)_2]$ catalyst.

The stability of complexes by the selection of the ligands is the core to obtaining robust WOC, as shown by $\text{Fe}(\text{BQEN})(\text{OTf})_2$ and $\text{Fe}(\text{BQCN})(\text{SO}_3\text{CF}_3)_2$ (BQEN = N, N'-dimethyl-N, N'-bis(8-quinolyl)-ethane-1,2-diamine(Fig.1.7g), and BQCN = N, N'-dimethyl-N, N'-bis(8quinolyl) cyclohexanediamine) which are evaluated in chemical and photochemical water oxidation. These two complexes catalyzed water oxidation using CAN under an acidic condition. The $\text{Fe}^{\text{IV}}=\text{O}$ species formed by two-electron oxidation in rivalry with ligand oxidation. The characteristics of catalysis varied depending on pH and the oxidizing agent; the result implied that ligand dissociation

and oxidation happen under acidic conditions by CAN, producing the O₂, which is mixed with the yield of CO₂ [148].

In contrast, in light-driven water oxidation by Fe(BQEN)(OTF)₂ using [Ru(bpy)₃]²⁺ as photosensitizer and S₂O₈²⁻ as a sacrificial electron acceptor, the real catalyst was Fe(OH)₂ nanoparticles. The earliest Fe(II) complexes based on aminopyridyl ligands published in 2011 were highly active for WO by using chemical oxidants.

Non-heme iron complexes are regarded to be explored as the activity for WO. Consequently, this triggered new developments in the field. Fillol and Costas et al. [104] illustrated that mononuclear Fe complexes of N tetradentate neutral organic ligands (N,N'-dimethyl-N,N'-bis(2-pyridylmethyl)-cyclohexane-1,2-diamine (mcp), N,N'-dimethyl-N,N'-bis-(2-pyridylmethyl)-ethane-1,2-diamine (mep) (Fig 1.8). These catalysts hold readily available and modular tetradentate ligands that differ in solidity and basicity. Still, the typical fundamental structure resembles the presence of two free cis-coordination sites occupied by weakly binding ligands. Two complexes exhibited high catalytic activity at low pH using CAN, TON > 350 (mcp), and TON > 145 (mep), respectively. Under catalytic conditions, high valent reaction intermediates gather, allowing mechanistic studies but also cooperating in ligand oxidation. Nevertheless, Fe^{IV}(O) species was presented as the reactive intermediate for the O–O bond formation in WNA was recognized through UV-vis spectroscopy and electrospray ionization mass spectrometry (ESI-MS). Furthermore, techniques DLS (Dynamic Light Scattering) and NTA (Nanoparticle Tracking Analysis) examinations indicated no iron oxide formation nanoparticles appearance in situ, indicating the experimental catalysis stemmed from the molecular water oxidation catalyst. This outcome extended a new development of Fe-based WOCs. Hence, numerous investigations have been accomplished to demonstrate the catalytic mechanism, analyze the structure-activity relations of catalysts, and develop devices with molecular Fe-based WOCs.

Tai-Chu Lau *et al.* also investigated the complex *cis*-Fe(mcp)Cl₂, beside other complexes such as [Fe(bpy)₂Cl₂]Cl, [Fe(tpy)₂]Cl₂ (tpy = 2,2':6',2''-terpyridine), *cis*-[Fe(cyclen)Cl₂]Cl (cyclen = 1,4,7,10-tetraazacyclododecane) and *trans*-Fe(TMC)Br₂ (TMC = 1,4,8,11-tetramethyl-1,4,8,11-tetraazacyclotetradecane). These were employed as light-driven catalysts by [Ru(bpy)₃]³⁺ for evolving oxygen [149] (see Table 1.2 on details). All studies confirmed an Fe^{IV}=O species as the reactive intermediate for the O–O bond formation in the initial phase of catalysis, however, all Fe

complexes underwent hydrolysis, followed by the ligand oxidation to produce Fe_2O_3 , the true catalyst for the sustained catalytic WOC at high pH [149,150].

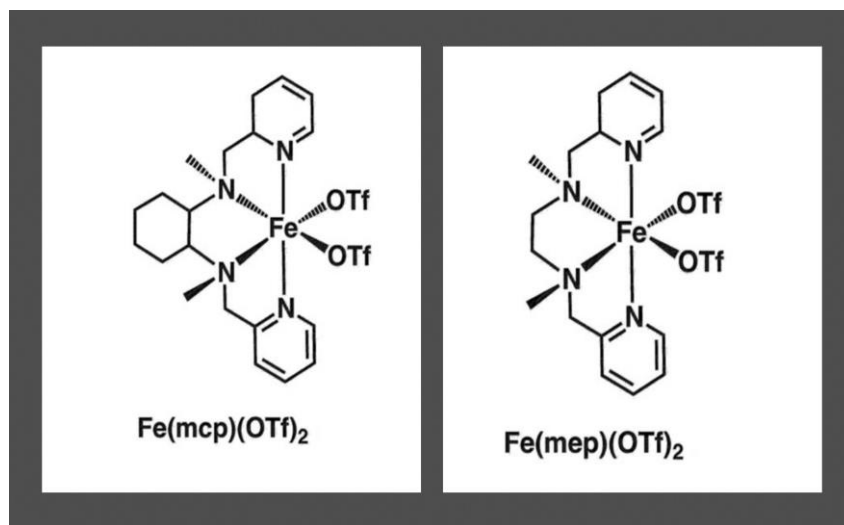


Figure 1.8. Fe(II) complexes with tetradentate N donor ligands were employed for WOCs [104].

Li-Zhu *et al.* replaced one of the three pyridines of TPA in $\text{Fe}(\text{TPA})\text{Cl}_2$ (TPA = tris(2-pyridylmethyl)amine) with quinoline in $\text{Fe}(\text{Lq})\text{Cl}_2$ (Lq = 1-(pyridin-2-yl)-*N*-(pyridin-2-ylmethyl)-*N*-(quinolin-8-ylmethyl)methanamine) to expand the ligand space as shown Fig. 1.9. The catalyst presented a more active production of the high valence $\text{Fe}^{\text{IV}}(\text{O})$ species and higher activity in catalytic OER than $\text{Fe}(\text{TPA})\text{Cl}_2$ [151].

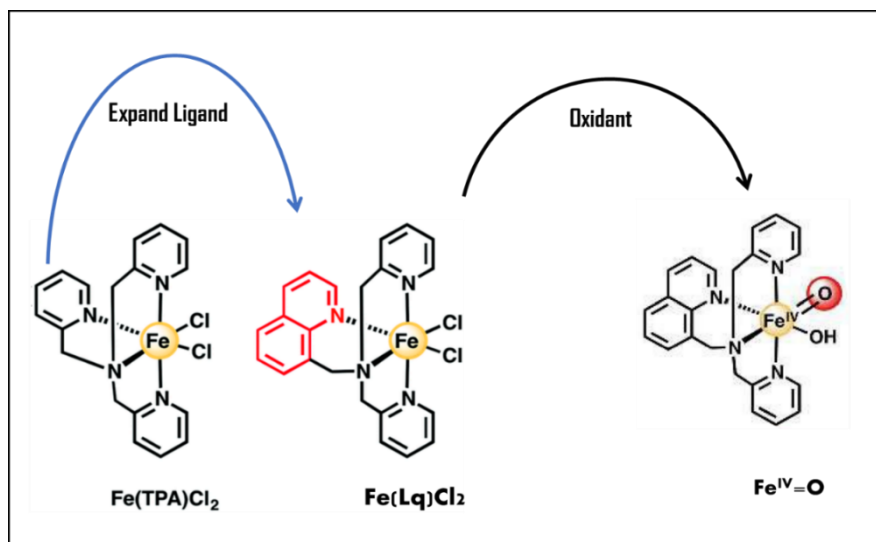


Figure 1.9. Molecular structure of $\text{Fe}(\text{TPA})\text{Cl}_2$ (left) and $\text{Fe}(\text{Lq})\text{Cl}_2$ (right) [151].

Although my dissertation concentrates on single-site catalysts and the patterns of molecular catalysts were selected accordingly, it has to consider the multinuclear Fe complexes also exist and mean a valid alternative to enhance Fe-based WOCs [146,152,153]. However, these will not be discussed here in more detail.

1.11.2. Immobilization of molecular catalysts (heterogeneous catalysis)

The demand for commercial catalysts, avoiding deactivation or decomposition pathways, and more straightforward catalyst lifetime measurements for research purposes call for surface immobilization on electrodes. Cost-efficient and robust materials containing Fe, like layered double hydroxides (NiFe-LDHs, or other mixed metal compounds), are readily available as surface-bound WOCs and, accordingly, extensively studied [124,154–156]. While these are efficient electrocatalysts under fundamental conditions, their application near the neutral pH or under acidic conditions is minimal or not possible at all.

Some molecular catalysts that can operate under non-alkaline conditions, on the other hand, were observed to possess such remarkable affinity for the electrode surface that homogeneous electrocatalysis was unlikely. Instead, these molecular catalysts can be immobilized on oxide surfaces through covalent bonds or *via* non-covalent interactions [112]. As manifested, molecular catalysts have higher catalytic activity and more flexibility in their design, and these advantages give the elasticity to link them with semiconducting materials that are compatible only with neutral or mildly basic electrolytes. Such co-catalysts/semiconductor hybrids would be highly desirable for building PEC systems to advance artificial photosynthesis research. Typical semiconductor metal oxides are TiO₂, WO₃, BiVO₄, etc., because of their availability, straightforward synthesis, and tunable bandgap; besides, another asset in the use of photoanodes is that sacrificial oxidants like CAN, are no longer needed [145]. An economical solution to address an actual model for artificial photosynthesis, is to anchor active catalysts onto suitable electrode support. Thus, for practical application, it is crucial to modify light-harvesting semiconductors' interfacial characteristics through their modification with suitable electrocatalysts [157].

The intended immobilization of molecular catalysts on the electrode surface/semiconductor has become critical to exploit their intrinsic co-catalytic capabilities. Surface confinement, surface attachment, grafting, and surface immobilization are similar terms the studies employed to describe attaching molecular catalysts to an electrode surface [112]. Grafting molecules to the surface

through bridging ligands typically require more synthetic modification steps in the ancillary ligands to introduce anchoring groups [52,92,158].

Reliable and affordable methods usually avoid extensive synthetic modifications. Instead, it is possible to fabricate ad-layers on substrates using DIP, DC, and ED methods. A prosperous method uses DC to graft molecular catalysts of water-insoluble compounds onto electrode surfaces [159]. The DC technique was applied to deposit layers of the active molecular catalyst $[\text{Ru}_2^{\text{II}}(\text{OH})_2(3,6\text{-tBu}_2\text{quinone})_2(\text{btpyan})]^{2+}$, (btpyan=1,8-bis(2,2':6'2'')-terpyridylanthracene) [160]. When deposited onto an indium tin oxide (ITO) electrode, the catalyst layer could electrochemically oxidize H_2O to O_2 . The highest turnover number for molecular catalysts was 6730 under an applied potential of 1.7 V (vs. SCE) and 40-hours of operation.

In recent years, ED has already been considered a surface treatment technique that plays a vital role in the electrochemical synthesis of water-splitting catalysts with excellent performance [161]. ED is an acclaimed method for preparing OER electrodes. In addition to the fact that it can be a simple fabrication process, it also offers a practicable technique for electrodes with very high active site utilization and fast mass transport [162,163]. ED offers a broad scope for control over the catalyst deposition process by managing the amount of charge passed during a deposition. The amount of compound deposited (and hence the film thickness and/or morphology) can be adjusted, allowing nanoscale films to be deposited [164,165]. The control over film thickness is particularly influential in PEC electrodes for OER, where solar irradiation is utilized to force the reaction; thin catalyst films assure that the quantity of light contacting the underlying photo-active substrate is not remarkably attenuated by distribution or absorbance in the co-catalyst coating. Also, ED advances significant scope for modifying the morphology of the layers produced through the variation of potential during deposition [164]. An example is Zhang *et al.*, who fabricated a thin NiFe film for OER from precursors [166]. The dopant Fe was deployed on Ni by a cathodic-to-anodic CV sequence; the turnover frequency of 8.7 s^{-1} at an overpotential of 329 mV is outstanding among heterogeneous OER catalysts.

A tailored assembly can also be achieved through self-assembly and surface precipitation of precursors for molecular electrocatalysts, immobilization *via* physical confinement, and electrostatic, non-covalent immobilization, especially by layer-by-layer (LbL) assembling methods [157]. One also needs to consider that a slight change in the reaction conditions may significantly affect both the stability of WOCs and the operating mechanism [89,167–169].

In a heterogeneous system of the TAML water-oxidation reaction, Fe^{III}-TAML immobilized on carbon black/Nafion carbon-based electrodes has been published as an effective OER electrocatalyst (Figure 1.10a). However, an electrocatalytic version of the TAML readily produced O₂ with much higher TONs than the homogeneous predecessors, thus revealing that immobilization can result in more robust catalysts. The Fe^{III/IV} oxidation process occurred at 720 mV (vs Ag/AgCl) and pH= 9-11 prior to the onset of OER at ~1 V at a constant current of 5 mA with an estimated TOF of 0.081 s⁻¹ over 50 min. The empirical Faradaic efficiency was ~45%, no doubt that evolved O₂ can leak from the reaction cell due to the partial pressure of O₂ in the cell being more significant than that of ambient air [170].

In 2014, Bartlett and co-workers published covalent anchoring of a phosphonate-derivatized complex, Fe(tebppmcn)Cl₂ (tebppmcn = tetraethyl-*N,N'*-bis(2-methylpyridyl-4-phosphonate)-*N,N'*-dimethylcyclohexyldiamine) (Fig. 1.10b) to WO₃ photoelectrodes[171]. This combination enhanced the rate of photoelectrochemical OER on WO₃ by 60% in comparison to bare WO₃, and there was no need for a sacrificial oxidant. A molecular Fe complex immobilized onto WO₃ over FTO and linked with phosphonic acid-modified tris(2-picoly)amine (TPA) ligand was used in a photoelectrochemical cell. In this case, assembling the photoanode consisted of the deposition of WO₃ onto FTO *via* hydrothermal synthesis, followed by the dipping of the electrode itself in a methanol solution containing the Fe complex overnight at room temperature in the dark.

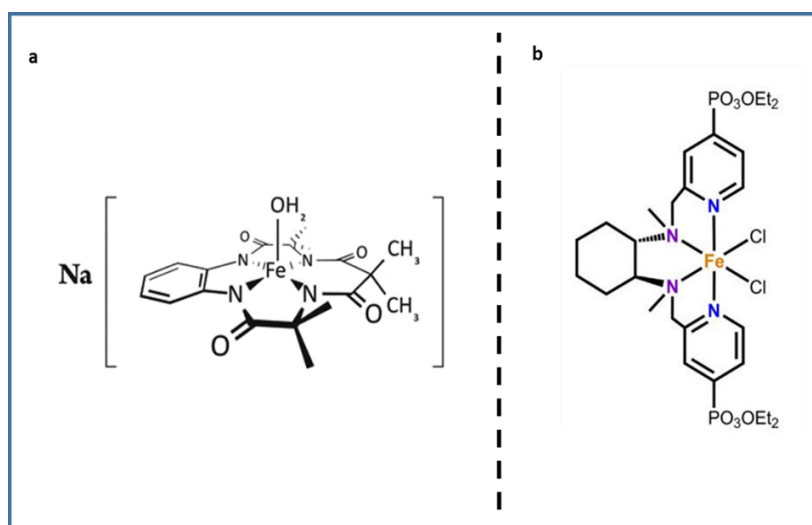


Figure 1.10. a) Fe^{III}-TAML (prototype) activator, b) iron complex Fe(tebppmcn)Cl₂.

UV-Vis spectrum confirmed the appearance of the catalyst grafting with the absorbance in the 400–450 nm region. Importantly, this anode was combined with a Ni(II)-bis(diphosphine)

molecular catalyst immobilized on TiO₂ as a hybrid cathode in a complete, noble-metal free PEC water splitting cell [175]. At pH 3, this hybrid anode displayed a well-characterized increase in activity and selectivity for O₂ evolution instead of the unmodified electrode.

An inexpensive and convenient synthetic strategy toward nanocomposites prepared by Fe(II)phthalocyanine/carbon nitride nanosheet (FePc/CN) were studied by Shi *et al.*, and the results showed that the photocatalytic activity of CN was supported by FePc anchoring, and the electrocatalytic activity of FePc was promoted by CN doping synergistically [172]. Thus, attaching FePc to CN increased the visible-light absorption region of CN. The electron transfer from the excited state FePc to CN obstructed charge carrier recombination and thus improved the photoinduced carrier separation efficiency, leading to enhanced photoelectrocatalytic activity. The electrocatalytic efficacies using mono- and binuclear iron corroles successfully immobilized in Nafion films were also published to act as electrochemical WOCs [173].

The above results are summarized in Table 1.2, where I followed the abbreviations as used in the literature sources. From this brief summary, it is clear that there is a need for further, simple grafting methods and Fe complexes that are compatible with those methods to explore new ways of semiconductor activation towards OER. The increased performance and longevity of co-catalyst/semiconductor hybrids is a goal that can be achieved only by fundamental research in this field.

Table 1.2. Summary of Fe catalysts with ligands* utilized as homogeneous and heterogeneous catalysts for WO.

<i>Homogeneous WOCs</i>				
Catalysts	TOF S ⁻¹	TON	Experimental	Refs.
Fe^{III}-TAMLs	1.3	16	CAN as sacrificial oxidants at pH = 0.7	[142]
biuret-modified Fe^{III}-TAMLs	0.76	220	Chemical: CAN at pH = 1 Photochemical: 50% of 10 mM acetonitrile-borate buffer pH = 8.7, λ _{max} = 440 nm at 30 °C.	[144]
[Fe(L) (CH₃CN)₂]²⁺	0.04	67	at pH = 0.7 using CAN and sodium periodate	[174]
[Fe^{III}(Cl)₂(dpa)]Cl	0.23	-	a CAN solution in nitric acid at pH = 1.	[146]
[Fe^{III}(Cl)₂(ppq)]Cl	2.2	-		
Fe^{III}(dpaq)(H₂O)	0.15	-	propylene carbonate (PC)/H ₂ O mixtures	[147]

Fe(BQEN)(OTf)₂	-	80 ± 10	CAN under an acidic condition, and [Ru(bpy) ₃] ²⁺ as a photosensitizer under basic.	[148]
Fe(BQCN)(OTf)₂	-	20 ± 10		
Fe(mpc)(SO₃CF₃)₂	0.23	360	at pH=1 by Ce ⁴⁺ as the oxidant	[104]
Fe(mep)(SO₃CF₃)₂	0.13	145		
Fe(TPA)Cl₂	0.05	7.5	CAN and 0.1 M HNO ₃ solution	[151]
Fe(L)Cl₂	0.16	3.2		
[Fe(bpy)₂Cl₂] Cl	3.6	95	Ru(bpy) ₃](ClO ₄) ₃ at pH = 8.5 in borate buffer at 23°C	[149]
[Fe(tpy)₂]Cl₂	1.5	19		
Fe(tmc)Br₂	4.6	93		
cis-[Fe(cbc)Cl₂]⁺	-	1030	NaIO ₄ as the oxidant at pH = 1 -7	[175]
cis-[Fe(cyclam)Cl₂]Cl	-	-	0.1 M NaClO ₄ or 0.1 M phosphate buffer (pH= 7.5)	[176]
<i>Heterogeneous WOCs</i>				
Fe^{III}-TAML (prototype)	0.081	-	carbon black/Nafion carbon-based, HNO ₃ (0.1M) at pH =1.	[170]
Fe(tebppmcn)Cl₂	-	-	Na ₂ SO ₄ at pH= 3	[171]
Fe (TPA)	-	-	aqueous Na ₂ SO ₄ (0.1 M) solution at pH =3	[177]
FePc/CN			0.2 M Na ₂ SO ₄ , at pH= 6.6	[172]

*TAML=tetraamido macrocyclic ligand; L = N,N'-dimethyl-N,N'-bis(pyridazin-3-yl-methyl)ethane-1,2-diamine ; BQEN = N,N'-dimethyl-N,N'-bis(8-quinolyl)-ethane-1,2-diamine, BQCN = N,N'-dimethyl-N,N'-bis(8-quinolyl)cyclohexanediamine; mcp=N,N'-dimethyl-N,N'-bis(2-pyridylmethyl)cyclohexane-trans-1,2-diamine; Tf = triflyl; cbc = 4,11-dimethyl-1,4,8,11-tetraazabicyclo[6.6.2]hexadecane; dpaq=2-[bis(pyridine-2-ylmethyl)]amino-N-quinolin-8-yl-acetamide; tebppmcn = tetraethyl N,N'-bis(2-methylpyridyl-4-phosphonate)-N,N'-dimethylcyclohexyldiamine; and TPA= tris(2-picolyl)amine).

2. Aim of the work

2.1. Motivation and preliminary considerations

Facilitating the oxygen evolution reaction (OER) still stands as a significant challenge in solar to chemical energy conversion due to its sluggish kinetics and large overpotential need. Therefore, one of the essential objectives of scientists remains the fabrication of suitable and robust catalysts for OER. Several Ru- and Ir-based WOCs have been reported to combine efficiency with robustness, and these noble metal complexes gave impetus to this research field. Progress with molecular catalysts based on abundant, non-precious, and non-toxic transition metals is incredibly fascinating, because economic and large-scale applications in the future are better based on environmentally friendly and available raw materials. Additionally, the characterization and study of catalysts and their catalytic pathways are crucial in their design. Accordingly, in this Ph.D. thesis, my aims were to study the electrochemical and catalytic properties of homogeneous water oxidation catalysts and their immobilized counterparts based on Fe complexes.

2.2. Aim of the work

My research objective was to select and synthesize some molecular catalysts that were expected to be water-insoluble, stable, and capable of exhibiting high catalytic performance and high affinity for the semiconductor surface. Nevertheless, simple methods suffice for their immobilization. I focused on first-row transition metals; thus, Fe complexes with hydrophobic, robust heterocyclic ligands have been utilized in this work. The primary objective was to evaluate the redox behavior and intrinsic catalytic activity for water oxidation; thus, the Fe complexes were first studied and characterized by electrochemical and spectroscopic methods in homogeneous organic/water mixtures to help select those are potentially capable of OER electrocatalysis.

My second objective was to find simple methods (such as drop-casting, dip-coating, and electrodeposition) for the immobilization of the selected candidates on semiconducting materials in order to fabricate hybrid systems. Model substrate electrodes (ITO or FTO) were used to warrant comparable and repeatable results, and the use of additives like Nafion was avoided as far as possible. In addition to the proposed effect of the heterocyclic ancillary ligands on the OER capabilities, their effect on immobilization and surface stability was an important question to clarify.

3. Experimental

This chapter describes all the materials, procedures, methods, and experimental techniques used in my work discussed in Chapter 4 [52,178,179]. The applied physical techniques to characterize homogeneous and heterogeneous catalysts are also introduced. Finally, the analytical techniques for oxygen detection are also presented.

3.1. Solvents and materials

Acetonitrile (MeCN), methanol, ethanol, acetone, propylene carbonate, and dichloromethane (DCM) were of HPLC grade, purchased from commercial sources, and used without further purification. These solvents were used in synthesis or electrolytes for nonaqueous electrochemical experiments. Tetrabutylammonium perchlorate (TBAP) was purchased from commercial sources and used without further purification. For complex synthesis, the $\text{FeCl}_3 \cdot 6\text{H}_2\text{O}$ and $\text{Fe}(\text{CF}_3\text{SO}_3)_2$ were purchased from Sigma-Aldrich and Strem Chemicals, respectively. Nafion polymer (a commonly used support for molecular electrocatalysts) was purchased from Sigma-Aldrich as a methanolic solution.

3.2. Ligands and complexes

The ligand 2-(2'-pyridyl)benzimidazole (PBI) was purchased from Sigma-Aldrich, while 2-(2'-pyridyl)benzoxazole (PBO) was synthesized following literature procedure [180]. The ligands 1,3-*bis*(2'-thiazolyl), iminoisoindoline (tia-BAIH), and 1,3-*bis*(2'-benzothiazolylimino)isoindoline (btia-BAIH) were synthesized according to known procedures [181].

[Fe(PBI)₃](OTf)₂ (1) (OTf⁻ = trifluoromethyl sulfonate anion). This complex was synthesized according to a published procedure [180]. The PBI ligand (0.29 g, 1.5 mmol) was added to the stirred solution of dry $\text{Fe}^{\text{II}}(\text{CF}_3\text{SO}_3)_2$ (0.18 g, 0.5 mmol) in acetonitrile (10 mL) under an Ar blanketing atmosphere. After 4 hours of stirring at room temperature, the dark-red solution was filtered and layered carefully with an excess amount of diethyl ether under Ar in a Schlenk-tube capped with a rubber septum. After complete diffusion, the solvent and a small amount of a brown powdery precipitate on the bottom of the Schlenk were removed with a cannula. The crystalline product was carefully collected from the wall of the tube, washed with minimal diethyl ether, and dried in a vacuum. Yield: 0.40 g of dark red crystalline product.

[Fe(PBO)₂](OTf)₂ (3) (OTf⁻ = trifluoromethyl sulfonate anion). This complex was synthesized by following the exact same procedure as complex **1**. The orange crystalline product was rinsed

with diethyl ether and dried under a vacuum. Yield: 0.24 g. The UV-vis and FT-IR spectroscopic features and the electrochemical redox properties in MeCN for both **1** and **2** were identical to those reported earlier [182].

[Fe^{III}Cl₂(tia-BAIH)] (3). The compound was synthesized and re-crystallized according to published procedures [180,181]. Under an Ar atmosphere and reflux (*ca.* 72-75°C) temperature, (tia-BAIH) (1.2 g, 4 mmol) and FeCl₃·6H₂O (1.08 g, 4 mmol) were reacted in 30 mL of methanol for 6 hours. The precipitate was filtered off after cooling to room temperature, washed with cold methanol three times, and dried under a vacuum. Yield: 1.4 g of a deep purple microcrystalline solid. The UV-vis and FT-IR spectroscopic features and the electrochemical redox signal in DMF were identical to those reported earlier.

[Fe^{III}Cl₂(btia-BAIH)] (4). This complex was synthesized just like complex **3**, and as it was reported earlier in ref. [183]. Four mmol of FeCl₃·6H₂O was reacted with the btia-BAIH ligand in a 1:1 ratio in refluxing methanol under Ar atmosphere. Yield: 1.2 g of a deep purple-brown microcrystalline solid. The UV-vis and FT-IR spectroscopic features and the electrochemical redox signal in DMF were identical to those reported earlier.

3.3. Electrodes, semiconductor substrates and electrochemical techniques

Electrodes and semiconductor substrates. Glassy carbon electrode (GCE) and boron-doped diamond (BDD) working electrodes were used for *homogeneous electrochemical and electrocatalytic experiments*. For heterogeneous electrochemistry and catalysis (using the immobilized complexes), ITO glass slides (~100 nm thickness) were purchased from PGO GmbH, Germany, or Ossila Ltd., Great Britain. FTO, which can be applied for long periods of OER electrocatalysts, was purchased from Ossila Ltd. Platinum coil (Pt) was used as an auxiliary electrode. The reference electrode was Ag⁺/Ag (0.01 M AgNO₃, 0.1 M TBAP/acetonitrile) for non-aqueous experiments, and Ag/AgCl (3 M KCl) for aqueous experiments. The GCE and BDD (as WEs) were polished with 1 μm diamond suspension, ultrasonicated in MilliQ (ultra-pure) water, and dried using an N₂ stream before use. The ITO and FTO pieces were cleansed before use as described in 3.5.2.

Electrochemical techniques. In voltammetric techniques, nonspontaneous, interfacial charge transfer processes (electron or ion transfer across the electrode/electrolyte solution interface) are driven by an external electrical potential difference in an electrolytic cell [182,183]. The potential difference at the electrolyte/electrode interface of the working electrode was controlled using a

BioLogic SP-150 potentiostat (Seyssinet-Pariset, France) or a Gamry Reference 3000 instrument (USA) in a 3-electrode setup consisting of a working electrode (WE), a counter electrode (CE, separated by a Vycor glass frit, when necessary) and a reference electrode (RE), as shown in Fig. 3.1. The cell was purged with Ar when required.



Figure 3.1. Electrochemical cell, three-electrode setup as used in my experimental work.

Herein, the principal techniques that were applied to investigate electrochemistry of the complexes in non-aqueous solution or immobilized on ITO/FTO (in aqueous solution) will be discussed only briefly, concentrating on the information needed in the context of the study.

In linear sweep voltammetry (LSV), the potential is linearly swept at a constant rate from a starting E_1 to a terminal E_2 potential (Fig. 3.2a). The obtained information essentially depends on the rate of the potential variation with time (scan rate, v) [189]. Fig. 3.2a shows a typical LSV for ferrocene dissolved in MeCN, obtained using a GC working electrode by varying the electrode potential from $E_1 = -0.4$ V to the final potential $E_2 = 0.4$. If the potential is reversed back to E_1 , keeping the same scan rate, it makes a complete cycle, and the technique is called cyclic voltammetry (CV) (see next section for more details), and E_1 and E_2 become the vertex potentials. Both LSV and CV were applied to evaluate the activity of the catalyst for OER. In addition, LSV at slow scan rates (≈ 2 -5 mVs^{-1}) can be used in the Tafel analysis of immobilized catalysts in aqueous electrolytes.

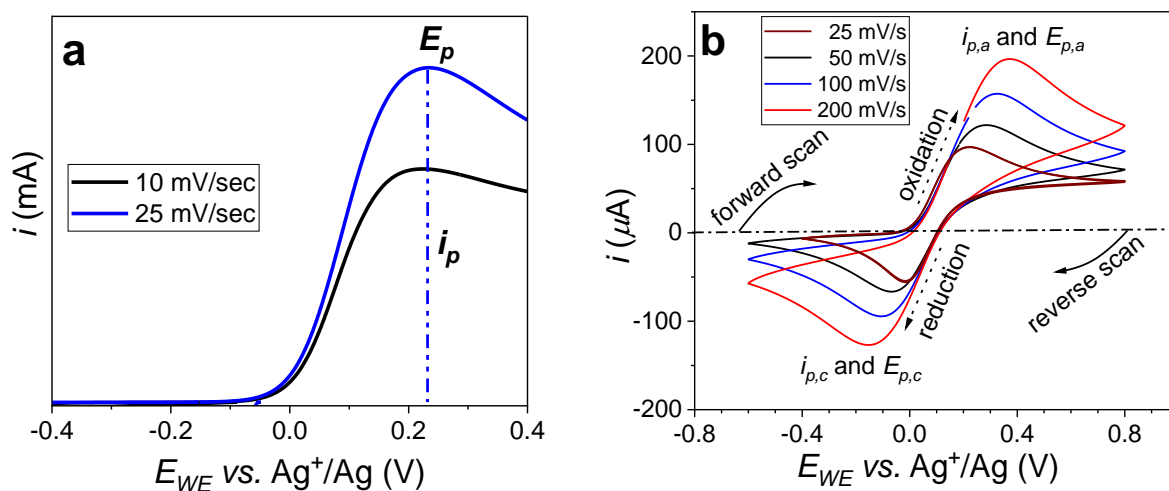


Figure 3.2. a) LSVs recorded at different scan rates of 10 mM ferrocene dissolved in MeCN, i_p is the peak current, and E_p is the peak potential; b) CVs of ferrocene in MeCN, showing the peak currents and peak potentials, recorded on a BDD WE, Pt CE, Ag+/Ag (0.01 M AgNO₃ in CH₃CN) RE, at different scan rates, under Ar, at 25°C.

CV is a popular technique for collecting quantitative and/or qualitative knowledge about electrochemical reactions; one of the principal uses of CV is to investigate the chemical and electrochemical behavior of TM compounds [183,184]. By exploiting the well-understood connection between the scan rate, v , and the thermodynamics and kinetics of electrode reactions, the mechanism of interfacial electron transfer, the kinetics of catalysis, adsorption of redox species, the role of coupled chemical reactions, etc., therefore, it is a leading technique of electrochemical analysis [184–187]. Frequently, to evaluate the stability of the catalyst, multiplied cycles are applied (in addition to chronoamperometric examinations). Potential calibration is essential in nonaqueous electrolytes. Thus, Ferrocene (Fc) is commonly used as an internal standard. Accordingly, throughout this thesis, the potentials in organic electrolytes will be given as V vs Fc⁺/Fc, where the $E_{Fc^+/Fc}$ is regarded as 620 mV vs NHE[188]. Fig. 3.2b shows CV scans with Fc in MeCN in the three-electrode system used during the studies.

By taking the example of Fc, as shown in Fig.3.2, the principles of the CV technique are briefly discussed here. First, a positively ramping potential (forward sweep) is applied between the WE and RE. As the potential increases, Fc within the diffusion layer near the working electrode surface is oxidized, transforming it to Fc⁺. The thickness of the diffusion layer is proportional to the square root of the scan rate ($v^{0.5}$). The passage of the electrons produces an electrical current, the so-called Faradaic current. The current is proportional to concentration and increases linearly with the square

root of the scan rate; the Randles–Sevcik equation gives the peak current for a reversible couple (at 25°C, Eq.3.1):

$$i_p = 2.69 \times 10^5 n^{3/2} AD^{1/2} C v^{1/2} \quad \text{Eq. 3.1}$$

Where n is the number of electrons, A is the electrode area (cm^2), C is the concentration (mol cm^{-3}), D is the diffusion coefficient (cm^2s^{-1}), and v is the scan rate (Vs^{-1}).

At the vertex potential, the reverse scan starts, and Fc^+ close to the working electrode surface is reduced, converting it back to Fc , generating an electrical current is defined as negative. Scanning the potential in both directions affords us to examine the reversibility, electrochemical-chemical reaction sequences, diffusion constant, and redox potentials for electrochemical reactions in a simple way.

CV has been beneficial in the electrodeposition of catalytic thin films onto conductive substrates. The number of cycles determining the mass loading and the redox properties of the catalyst depends on the scan rate and the vertex potentials. The anodic $E_{p,a}$ and cathodic $E_{p,c}$ peak potentials and the corresponding $i_{p,a}$ and $i_{p,c}$ current peaks can be acquired at different scan rates. CV was also applied to investigate the catalyst and substrate concentration dependence and kinetic isotope effect (KIE) [184].

Square wave voltammetry (SWV) is a potentiostatic technique that significantly reduces the capacitive current, thus making the detection of compounds at sub-mM concentration levels possible, which offers some advantages to standard techniques like CV and LSV. In SWV, the continuous potential ramp in CV is replaced with a staircase potential-time function: a staircase-shaped potential sequence is added to a linearly ramping polarization of the electrode [193]. In the SWV experiment, the working electrode's potential is stepped through a series of forward and reverse pulses from an initial potential to a final potential. The square amplitude determines the forward step, and the reverse step is determined by subtracting the square increment from the square amplitude. The main features of the method are the scan increment ΔE (SH in mV) by which the potential is increased in each step, the potential pulse amplitude (PH in mV) that is added to the base potential then quickly reversed, and the duration of each potential step (PW in ms). The current is measured at the end of each pulse, and their difference is plotted; thus, the capacitive (or charging) current contribution is diminished, profoundly improving the sensitivity and quality of the voltammetric data and allowing for a better resolution of overlapping peaks. Therefore, LSV,

CV, and SWV were applied to identify the redox transitions of the complexes in organic solutions and evaluate the activity of the catalysts for OER.

Controlled-potential electrolysis (CPE), also known as potentiostatic coulometry, measures the current response to an applied potential. Thus, chronoamperometry CA can be defined as an electrochemical technique in which the potential set to the working electrode is stepped. The resulting CA is a current from Faradaic processes transpiring at the electrode (caused by the potential step) controlled as a time function [189]. Cottrell's equation (Eq.3.2) gives the current in a reversible redox reaction as a function of time passed after setting a high potential step [190].

$$i = \frac{zFAC\sqrt{D_o}}{\sqrt{\pi t}} \quad \text{Eq.3.2}$$

Where z is the number of electrons transferred in the redox reaction, F is the Faraday constant (96,485 Cmol⁻¹), A denotes the electrode surface area (cm²), and C and D are the concentration (mol cm⁻³) and diffusion constant (cm²s⁻¹), respectively, of the electroactive species in the solution. CPE is also used in closed cells to generate enough amounts of hydrogen and oxygen to be detected by a suitable technique like gas chromatography (GC).

Electrochemical impedance spectroscopy (EIS) is a powerful technique that allows the analysis of the kinetics of electrochemical reactions and describes the properties of the electrode/electrolyte interfaces at which these reactions occur. EIS is applied to verify the electrical response of chemical systems to an alternating perturbation of the equilibrium state in a non-destructive way. The most common and standard approach of EIS is to measure impedance (Z) by applying a single-frequency voltage or current at a time to the interface and measuring the phase-shift and amplitude, or real (Re) and imaginary (Im) parts, of the resulting current using either analog circuit fitting or fast Fourier transform analysis. Frequency can vary from 1 mHz to 1 MHz. Small-signal perturbation at each frequency $\nu(t) = E\sin(\omega t)$, involving the single frequency $\nu = \omega/2\pi$, and the resulting steady-state current $i(t) = i\sin(\omega t + \Theta)$ is measured, where Θ is the phase difference between the voltage and the current. In real systems, a combination of resistive (R), capacitive (C), and inductive elements (L) are present, Θ is non-zero, and the relation between system properties and response to periodic voltage or current excitation is complex. Impedance takes phase differences into account; thus, it can be expressed as a vector in an orthogonal system of the Re (a) and an Im (b) axes components: $Z = a + bj$, where $j \equiv \sqrt{-1} \equiv \exp(j\pi/2)$. Impedance $Z(\omega) = Z' + jZ''$ is a vector quantity and can be plotted in the plane with rectangular coordinates $\text{Re}(Z) \equiv Z' =$

$|Z|\cos(\Theta)$ and $\text{Im}(Z) \equiv Z'' = |Z|\sin(\Theta)$ with a phase angle $\Theta = \tan^{-1}(Z''/Z')$ and the modulus $|Z| = [(Z')^2 + (Z'')^2]^{1/2}$ [191]. The most general plotting is that of Z'' against Z' (Nyquist plot) or $\log|Z|$ against $\log \omega$ (Bode plot). Throughout my work, Nyquist plots proved to be sufficient to be fitted with simple Randles circuits (see Fig4.26, Chapter 4) from which the solution resistance (R_s), the charge transfers resistance (R_{ct}), and the capacitance of the inhomogeneous surfaces represented a constant phase element (CPE) could be extracted that satisfactorily described the electrodeposited surfaces. The electrode setup was the same as for CV or SWV techniques.

EIS was applied to evaluate the critical parameters of the modified FTO or ITO working electrodes immersed in the aqueous electrolyte. To obtain the Nyquist plots, EIS was performed at 1.25 V vs. Ag/AgCl. The curves were evaluated by a Randles equivalent circuit fitted to the experimental data points. This circuit has been used repeatedly to fit transition metal-based systems under OER conditions [192]. R_1 , CPE, and R_2 correspond to the solution and electrode ohmic resistance, a constant phase element, and charge transfer resistance in the equivalent circuit. This was the simplest model to fit reasonably well our experimental data. The fitting was carried out with the EIS Spectrum Analyser 1.0 software. CPE represents the inhomogeneity on the surface of the electrodes that causes non-ideality of the double-layer capacitance (C_{dl}) at the solid/electrolyte interface. In CPE, there is a pre-exponential factor (P) to represent the value of a 'non-ideal capacity' for CPE and the exponent (n), which is an 'ideality factor' ranging from 0 to 1 (ideal capacitor, where P becomes C_{dl}).

The evaluation parameters for the performance of electrocatalysts (overpotential, exchange current density, Tafel slope, Faraday efficiency, turnover numbers, and frequency) were experimentally determined. Appendix (A) briefly introduces kinetic parameters that are generally (and also in this work) utilized to evaluate electrocatalysts' performance.

3.4. Electrocatalytic investigations

3.4.1. Homogeneous electrocatalysis

All experiments in the nonaqueous medium were done under Ar blanketing atmosphere unless stated otherwise. The complexes $[\text{Fe}(\text{PBI})_3](\text{OTf})_2$ (**1**) and $[\text{Fe}(\text{PBO})_2(\text{OTf})_2]$ (**2**) [52] were dissolved in MeCN, the catalyst concentration was varied between 0.01 and 0.2 mM, and water was added in 0–1.9 M concentration to the solution. All potential values and the corresponding figures in Chapter 4 are reported vs the Fc^+/Fc redox couple. The complex $[\text{Fe}^{\text{III}}\text{Cl}_2(\text{tia-BAI})]$ (**3**) [193] was dissolved in MeCN or acetone, and water was added in 0–3 M concentration.

[Fe^{III}Cl₂(btia-BAIH)] (**4**) was dissolved in dichloromethane under Ar, and water was mixed with acetone and added to the solution [179]. The kinetic isotope effect (KIE) was determined using D₂O (99.95%). All experiments employed a standard three-electrode setup, including a GCE or BDD as WEs (polished and conditioned before use), Pt auxiliary electrode, and Ag⁺/Ag (0.01 M AgNO₃, 0.1 M TBAP/acetonitrile) reference electrode. All potential values homogeneous studies are reported versus the ferrocenium/ferrocene (Fc⁺/Fc) redox couple. The redox potential of Fc, that is, E_{fc} has been measured under the conditions of each experiment. The reported potential values are: $E \text{ (V vs. Fc}^+/\text{Fc)} = E \text{ (V vs. Ag}^+/\text{Ag)} - E_{fc}$.

3.4.2. Heterogeneous electrocatalysis

Different electrochemical techniques were applied to characterize the immobilized complexes, including LSV, CV, EIS, and CA. Low surface roughness FTO (20×15 mm, 600 nm thickness, 6-9 Wδ-1, 34.8 nm RMS) and ITO (20×15 mm, 100 nm thickness, 20 Wδ-1, 1.8 nm RMS) coated glass slides of uniform size were used as standard model electrodes, which were modified with thin films of the complexes as described in the followings. These modified electrodes were set as WE in a three-electrode setup (Pt aux. and Ag/AgCl ref.) in a small cell, and the electrochemical behavior was compared to that of the unmodified ITO or FTO under the same conditions. ITO or FTO coated glass slides were cleaned with ethanol in an ultrasonic bath for 20 min, then rinsed with deionized water and dried with dry N₂ gas. All experiments were conducted in 0.2 M borate buffer at pH 8.2(1) for better comparison.

Deposition of the complexes on semiconductors (ITO, or FTO). Different procedures (DIP, DC, and ED) were applied to immobilize the complexes on a semiconductor surface. These were used to fabricate active catalytic layers of the complexes on the surface of ITO, or FTO [179]. Herein, I list all methods used, as shown in Fig. 3.3 (Methods **A-D**). Methods (**A-C**) include DC and DIP with/no Nafion, whereas method (**D**) shows the ED method.

Drop-casting (DC): the same procedure in method (**A**) was used for complexes [Fe(PBI)₃](OTf)₂ and [Fe(PBO)₂](OTf)₂ dissolved in methanol in 6 mM concentration. As shown in Fig. 3.4, small portions of the solutions (50–150 μL) were evenly layered onto ITO using a micro-syringe. For these two complexes, methanol was evaporated at room temperature and, after that, dried for 30 min using an infrared lamp to provide evenly distributed catalyst films (Fig. 3.4) [52]. The same procedure was repeated with Nafion and complex [Fe(PBI)₃](OTf)₂ in methanol to prepare complex/Nafion/ITO composite films, but no significant difference was observed in comparison

with the complex/ITO sample[52]. Method (C) was followed to produce Nafion/substrate electrode for reference [179].

This procedure was used for $[\text{Fe}^{\text{III}}\text{Cl}_2(\text{tia-BAI})]$, dissolved in methanol in 3 mM concentration. Small aliquots (50–200 μL) were evenly layered onto ITO using a micro-syringe. The solvent was evaporated, and the solid was dried by infrared heating for 30 min (Fig. 3.5) [193].

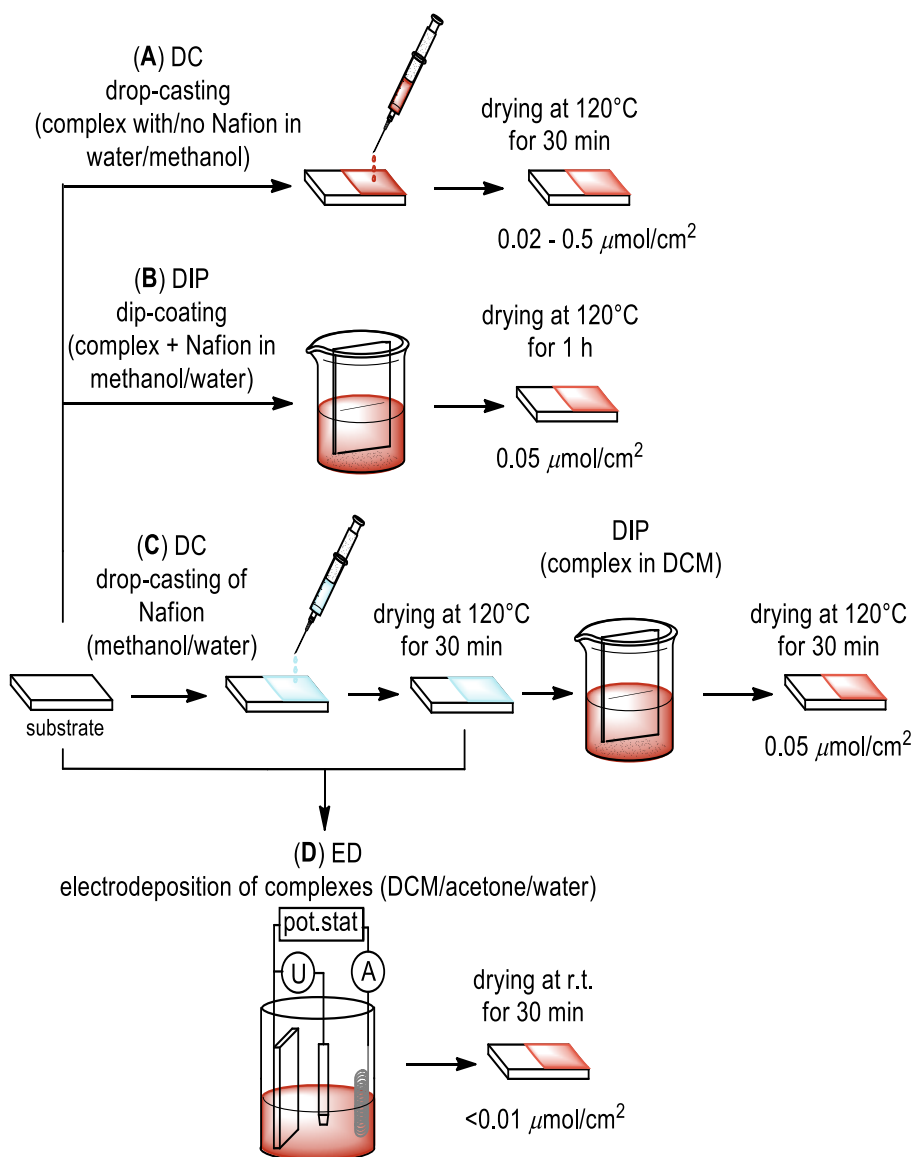


Figure 3.3 Schematic presentation of the different deposition methods [179].

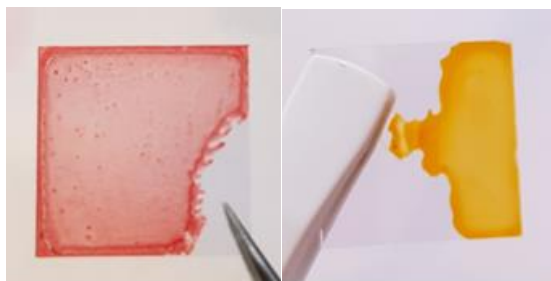


Figure 3.4. Typical drop-casted samples of $[\text{Fe}(\text{PBI})_3](\text{OTf})_2/\text{ITO}$ (left, before use in long term CPE) and $[\text{Fe}(\text{PBO})_2(\text{OTf})_2]/\text{ITO}$ (right, to be used for CV experiments) [52].

Dip-coating (DIP): method (B) was used for complex $[\text{Fe}(\text{PBI})_3](\text{OTf})_2$ was dissolved in methanol with or without adding Nafion (5 wt% in water/methanol) to reach a final concentration of 0 or 0.4 wt% for Nafion and 0.4–6.0 mM for the complex. With complex $[\text{Fe}(\text{PBO})_2(\text{OTf})_2]$ (0.4–10.0 mM), the concentration of Nafion was varied between 0 and 0.8 wt% to obtain different composite films. The ITO pieces were dipped into the coating solutions for 1 min, then kept at room temperature for 30 min, and finally heated for 30 min at 90–110°C [52]. A similar procedure could be applied for $[\text{Fe}^{\text{III}}\text{Cl}_2(\text{tia-BAI})]$ [179].



Figure 3.5. Typical appearance of a drop-casted $[\text{Fe}^{\text{III}}\text{Cl}_2(\text{tia-BAI})]/\text{ITO}$ sample [193].

Electrodeposition (ED): Due to the poor solubility of $[\text{Fe}^{\text{III}}\text{Cl}_2(\text{btia-ind})]$ in methanol, we developed method (D). The deposition was performed using a three-electrode configuration containing FTO or ITO, Pt, and Ag^+/Ag (0.01 M AgNO_3 , 0.1 M TBAP/MeCN), as working, counter, and reference electrodes, respectively. The solution consisted of 0.8 mM of $[\text{Fe}^{\text{III}}\text{Cl}_2(\text{tia-BAI})]$, or $[\text{Fe}^{\text{III}}\text{Cl}_2(\text{btia-BAI})]$ in dichloromethane and a mixture of 500 μL acetone and 54 μL MilliQ water. ED was conducted by CV at 100 mV/s, turning potentials of -0.4 V and 1.7 V vs Fc^+/Fc , for a total of 20 cycles. The surface concentration of the deposited complex was determined

from the current peak integral after the final cycle by presuming a $1e^-$ Fe(III)/Fe(II) transition ($z = Q/F$). The electrodes could be dried at room temperature after rinse [179].

3.5. Physical characterization

The following techniques include molecular spectroscopic and surface analysis methods that provide different types of information about the samples' complexes and surfaces.

3.5.1. Scanning electron microscopy (SEM) and energy-dispersive X-ray spectroscopy (EDX)

SEM can obtain the surface image *via* the interaction of a focused electron beam with the top 2-3 μm surface depth of samples. Topology, morphology, and crystallinity are all readily visible by SEM. The extraordinary depth of field often allows three-dimensional imaging shapes [194,195]. EDX is an analytical method for identifying and quantifying elemental compositions on the surface, which can be combined with SEM for elemental analysis at the sub-micrometer resolution. The electron beam brings atoms to the surface in the excited state, and specific wavelengths of X-rays are emitted. The elements emit at characteristic wavelengths, thus allowing their semi-quantitative detection [195]. During our studies, all experiments were done on a Thermo Scientific Scios2 dual beam system equipped with an Oxford X-maxn 20 SDD EDX (typically 5 keV beam energy and process time of 6 was applied, the dead time was below 50%, further details are found in figure captions).

3.5.2. X-ray photoelectron spectroscopy (XPS)

XPS is based on the photoelectric effect that can detect all elements except hydrogen. It provides information on the material surface's elemental composition and chemical oxidation state. A radiation beam of sufficient energy hitting the sample on the substrate creates photoelectrons. By measuring the kinetic energy (E_{kin}), one can calculate binding energies (E_B) since the irradiation is done at a fixed wavelength. Characteristic E_B -s of elements irradiated with a monochromatic X-ray (Mg K_α at 1.25 keV or Al K_α at 1.49 keV) occur as emission peaks in electron count *vs.* E_B plots. When a film-deposited substrate is irradiated, the X-ray photons interact with the inner electron shell of atoms in a thin surface layer (<3 nm). Photon energy of the X-ray is transferred to an electron in the inner shell, enabling a photoelectron to escape from the sample. An analyzer measures the E_{kin} of the photoelectron, which allows the calculation of E_B . Knowledge of E_B allows identification of the element. Chemical bonds between elements shift E_B to higher or lower values. This shift in E_B provides structural information [195].

Surface compositions of the film deposited on the ITO or FTO electrodes in our studies were determined by a KRATOS XSAM 800 XPS instrument equipped with an atmospheric reaction chamber. Al K α characteristic X-ray line, 40 eV pass energy (energy steps 0.1 eV), and FAT mode were applied for recording the XPS lines of the Fe 2p and 3p, O 1s, Sn 3d, In 3d, N 1s, C 1s, B 1s, F 1s, S 2p, and Na 1s photoelectrons, and the C 1s binding energy at 284.8 eV was used as a reference for charge compensation. The surface ratio of the elements can be calculated from the integral intensities of the XPS lines using sensitivity factors provided by the manufacturer.

3.5.3. Ultraviolet-visible spectrophotometry

Ultraviolet-visible (UV-vis) absorption spectroscopy was applied to detect dissolved molecular species. UV-vis spectroscopy can be used in the qualitative and quantitative determination of the soluble species which have absorbance in this spectral region (typically intramolecular electronic excitations that will be discussed in Chapter 4). It is commonly employed to characterize molecular catalysts in solution based on the characteristic absorptions. Spectra were recorded on an Agilent Cary 60 spectrophotometer using $l = 0.2\text{-}1.0$ cm quartz cuvettes or immersion probes.

3.6. Quantitative analysis of O₂

3.6.1. Optical oxygen sensor

An Ocean Optics NeoFox optical probe, after 2-point calibration (*i.e.*, exposed to argon, 0% O₂ and air, 20.9% O₂), was immersed into the stirred electrolyte in a temperature-regulated (Julabo F-25), double jacketed cell at 25.0(1)°C before the electrolysis experiments. The short response time of the probe allowed for real-time detection of produced O₂ at the beginning of CA experiments near the electrode, typically in the first 30 minutes, until saturation occurred.

3.6.2. Gas chromatography analysis of the headspace gas

Gas chromatography (GC) separated and quantified volatile compounds without decomposition [196]. In GC, the separation of the sample constituents is based on the different degrees of interaction between each component and a nonvolatile stationary phase while they pass through a packed column driven by the flow of carrier gas (He is the most popular carrier gas in use). Different types of detectors are used, depending on the sample, such as flame-ionization detector (FID), thermal-conductivity detector (TCD), and barrier ionization discharge detector (BID), which latter we used. The BID is a universal detector with a sensitivity 100 times larger than a TCD and

offers a much more stable baseline. The BID detector generates a 17.7 eV helium plasma ionizing almost all compounds except the Ne.

Our analysis to detect the O₂ evolution started with taking samples from the headspace of the air-tight electrochemical cell using a calibrated 200 μL micro-syringe and feeding them into the injection gate of the Shimadzu GC 2010 Tracera gas chromatograph, equipped with a BID detector. The sample is introduced into a 6.0 He carrier gas flow that is also the plasma gas. The in-and outlet pipes were connected to a homemade He-dilution loop, including an injector unit, a circulating micro-pump, and a 4-stand valve to close the circle with He gas. The optimized sampling parameters were the following: carrier gas: helium, 50 mL/min total flow rate, 40 mL/min DCG flow rate, 3 mL/min purge flow rate, oven program: T_{col. start} = 35°C (3 min), ΔT_{ramp} = 15°C min⁻¹ T_{col. end} = 160°C (10 min) T_{det.} = 250°C.

To evaluate the amount of O₂, calibration was performed using a gas mixture of H₂, O₂, N₂, and CO₂ in known concentrations ranging from 0.98 n/n% up to 78.17 n/n%. Using this calibration, the areas of the detected peaks were correlated with the gas components in the headspace of the electrochemical cell. Faradaic efficiency could be obtained using Equation (3.3):

$$FE\% = (n_{product} / \Sigma Q) \times 100\% = [(n_{product} \times F \times z) / \Sigma Q] \times 100\% \quad \text{Eq.3.3}$$

Faradaic efficiency is one of the most critical characteristics of an electrocatalytic system. Where n_{product} is the moles of O₂ evolved, F is the Faraday constant, and z is the number of electrons. ΣQ can be derived from the CPE current. In an ideal system, ΣFE% is close to 100%. However, values below 100% can be measured if gas leakage occurs or the dissolved O₂ in the buffer solution is not accounted for parasitic processes consume part of the charges.

4. Results and discussion

As presented in the literature overview in Chapter One, Fe complexes are especially interesting for application in water oxidation catalysis. This chapter gives a comprehensive overview of my studies on selected Fe complexes and their utilization as water oxidation catalysts (WOCs).

In the first subchapter (Part I), I concentrated on comparing electrochemical characterization and electrocatalytic properties of two selected, water-insoluble Fe(II) complexes bearing homolog, non-symmetric, bidentate ligands, 2-(2'-pyridyl) benzimidazole (PBI) in $[\text{Fe}(\text{PBI})_3](\text{OTf})_2$ (**1**, $\text{OTf}^- = \text{trifluoromethyl sulfonate anion}$) and 2-(2'-pyridyl)benzoxazole (PBO) in $[\text{Fe}(\text{PBO})_2(\text{OTf})_2]$ (**2**). These complexes were grafted on ITO surface with two different standard methods and, in this immobilized form, thoroughly studied as WOCs.

In the second subchapter (Part II), I discussed the structurally characterized $[\text{Fe}^{\text{III}}\text{Cl}_2(\text{tia-BAI})]$ complex ($\text{tia-BAI}^- = 1,3\text{-bis}(2'\text{-thiazolylimino})\text{isoindolate}(-)$) acting as a precursor to immobilized ad-layers on ITO by simple drop-casting. The enhanced electrocatalytic OER performance and good stability are discussed in context with the water-insolubility and ligand exchangeability of the $\text{Fe}^{\text{III}}(\text{tia-BAI})^{2+}$ assembly.

In the last subchapter (Part III), a simple electrodeposition method (ED) is presented that allows immobilization of the $[\text{Fe}^{\text{III}}\text{Cl}_2(\text{BAI})]$ precursor complexes bearing aromatic NN'N pincer ligands from a suitable water/organic mixture, and this method is compared to other standard methods like drop-casting and dip-coating.

- **The chapter relies on the following published, peer-reviewed papers:**

- I.** S. M. Al Zuraiji, T. Benkó, L. Illés, M. Németh, K. Frey, A. Sulyok, J. S. Pap: *J. Catal.* 381 (2020) 615-625. <https://doi.org/10.1016/j.jcat.2019.12.003>
- II.** S. M. Al Zuraiji, D. Lukács, M. Németh, K. Frey, T. Benkó, L. Illés, J. S. Pap: *Reactions* 1 (2021) 16–36. <https://doi.org/10.3390/reactions1010003>
- III.** S. M. Al Zuraiji, T. Benkó, K. Frey, Z. Kerner, J. S. Pap: *Catalysts* 11 (2021) 577. <https://doi.org/10.3390/catal11050577>

Part (I)

4.1. Immobilization and characterization of water-insoluble Fe(II) complexes as water oxidation catalysts utilizing hydrophobic NN' bidentate ligands

In this study, my role was to synthesize two water-insoluble Fe(II) complexes made with the non-symmetric, bidentate ligands, 2-(2'-pyridyl)benzimidazole (PBI) in $[\text{Fe}(\text{PBI})_3](\text{OTf})_2$ (**1**, $\text{OTf}^- =$ trifluoromethyl sulfonate anion) and 2-(2'-pyridyl)benzoxazole (PBO) in $[\text{Fe}(\text{PBO})_2(\text{OTf})_2]$ (**2**) based on a published procedure [180], and compare the electrochemical and electrocatalytic properties of these complexes. CV in water/acetonitrile mixture indicated considerable activity for both compounds; however, only **1** acted as a homogeneous catalyst. The hydrophobic ligands allowed for a simple immobilization of **1** and **2** by the DC and DIP methods on ITO. Long-term CPE showed that both **1**/ITO and **2**/ITO advance electrocatalytic O_2 evolution in borate buffer at pH 8.3 but differently. SEM-EDX, XPS, and re-dissolution tests suggested that the Fe remains complex with PBI during electrolysis as a nano-porous film. In contrast, the PBO complex in **2**/ITO undergoes a rapid decomposition yielding a mineralized form that is responsible for catalysis.

4.1.1. Selection of the complexes based on preliminary examples

Several WOCs have been designed, investigated, and applied during the last few decades, varying from small molecules to heterogeneous materials [197]. The last decade has proved the capability of Fe-based catalysts to be effective in water oxidation [198]. Iron (Fe) has experienced widespread applications in dioxygen activation by high-valence intermediates, motivating studies to apply Fe-based molecular catalysts in water oxidation [199]. In the analogy to Ru- and Ir-based catalysts, some Fe-based molecular WOCs have been reported as molecular catalysts using CAN as a sacrificial chemical oxidant [143,200]. A sacrificial chemical oxidant is usually applied in homogeneous catalysis in an acidic aqueous solution to oxidize the soluble catalyst to a state that, in turn, can oxidize water to liberate O_2 , electrons, and protons [201]. However, the highly acidic conditions can induce ligand dissociation, leading either to catalyst deactivation or a derived molecular species that are catalysts by themselves [201–204]. It is thus well justified to consider chemical modifications of the ligands and gain more reliable knowledge by developing improved catalysts, which may lead to the transcription into practical applications [201].

TM complexes bearing tetradentate N-donor ligands, especially those with pyridyl donor groups, have been widely utilized in catalytic oxidations due to their durability and synthetic variability.

Recently, a series of Fe(II) complexes with 4N ligands were reported to outperform the TAML complexes, reaching TONs up to 1000 in catalytic OER [202]. The reaction was driven by the sacrificial reagent CAN. In a later study by Codolà *et al.*, different complexes were investigated in their ligand topology and showed drastically different activities in acidic media [205]. Hetterscheid and co-workers explored that Fe complexes were capable of electrocatalysis with various tetradentate ligands like cyclam, cyclamacetate [206], and *N,N*-bis(2,2-bipyrid-6-yl)amine [207]. As mentioned before, molecular WOCs are easier to investigate under operational conditions and represent an excellent platform for clearly illustrating reaction mechanisms to define structure-activity correlations at the molecular level. However, one may always expect decomposition [92]. Most importantly, for true single-site catalysts, it has been concluded that a metal center with two labile sites in a *cis* position is required in order to coordinate two neighboring water molecules. Thus, the structure of the ancillary ligand has significant control over the reactivity of high-valent metal-oxo intermediates produced during PCETs, which is also manifested in the control of side reactions. Indeed, alterations to the ligand can completely improve or negatively affect the catalytic capacities [197,208]. Further, a structurally durable and oxidatively stable organic ligand is necessary under the harsh reaction conditions of WOCs [209], even though electrocatalysis can be operated under near-neutral conditions, where hydrolytic ligand dissociation may be suppressed. Last but not least, for the development of highly efficient Fe-based molecular WOCs in (photo)electrocatalysis that can benefit from the advantages of these molecular units, their immobilization on semiconducting materials would be the next logical step.

These considerations have led to the utilization of the non-symmetric, readily available bidentate ligands, *i.e.*, 2-(2'-pyridyl)benzimidazole (PBI) in [Fe(PBI)₃](OTf)₂ (**1**, OTf⁻ = trifluoromethyl sulfonate anion) and 2-(2'-pyridyl)benzoxazole (PBO) in [Fe(PBO)₂](OTf)₂ (**2**) [180](Fig.4.1). The ligands have been reported to influence the reactivity against H₂O₂ in acetonitrile depending on the heteroatom present in the heterocycle PBO or PBI. Importantly, electrochemical and ¹H-NMR proof supported that ligand exchange may occur in the presence of trace (or added) water in MeCN solution, even though the ligands strongly disfavor the dissolution of the solid complexes in water. On this basis, I first studied the redox behavior of complexes **1** and **2** in MeCN and water/MeCN mixtures.

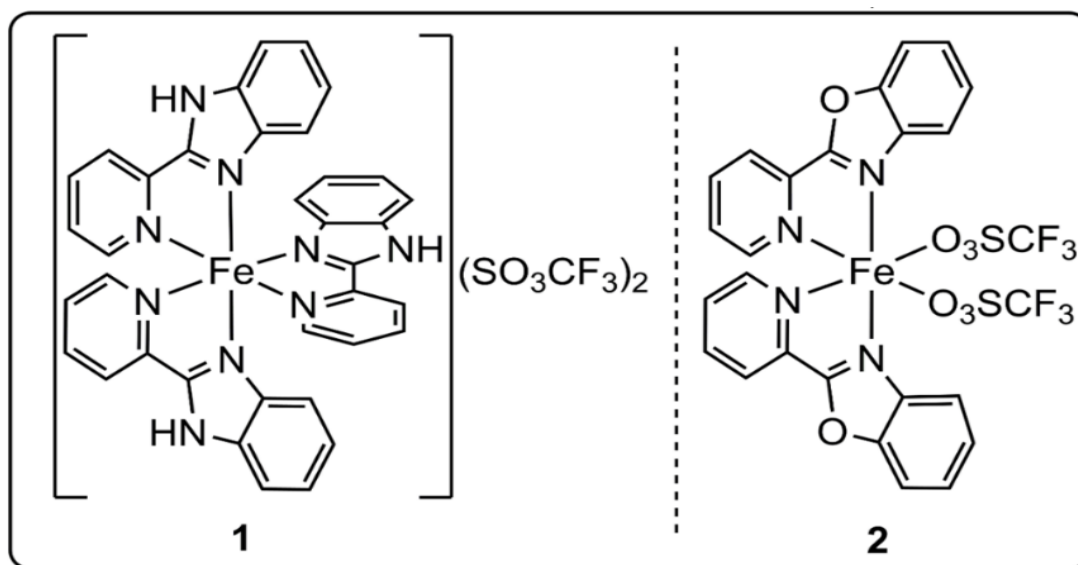


Figure 4.1. The molecular structure of the precursor Fe(II) complexes was utilized for water oxidation in this study.

4.1.2. Synthesis of complexes **1** and **2** and their redox properties in homogeneous water/acetonitrile mixture

The non-symmetrical NN' ligands PBI and PBO react spontaneously with Fe(II) triflate in dry MeCN under an inert atmosphere. With PBI, the red *tris*-chelate complex **1**, while with PBO, the neutral, orange *bis*-chelate complex **2** is formed in high yield (Fig. 4.1). In its solid state, complex **1** shows Fe–N bond lengths typical for low spin complexes (~ 2.0 Å), while **2** is high spin, exhibiting Fe–N bond lengths above 2.15 Å according to single-crystal structural analyses [210,211]. I synthesized these compounds according to the reported procedures and obtained similar yields of the spectroscopically confirmed crystalline products. According to the planned utilization of the complexes in water oxidation, I first investigated their redox behavior in acetonitrile without (Fig. 4.2a) or with added water (Figs.4.2b) to trace the expected ligand exchange reactions. Following the earlier observations, even trace amounts of water (*i.e.*, some equivalents typically present in acetonitrile stored under air) cause a cathodic shift in the oxidation potential and irreversibility of the otherwise quasi-reversible Fe(III)/Fe(II) redox couple characteristic for **1** [210]. Importantly, it was pointed out earlier that complex **1** in MeCN exhibits a paramagnetically broadened ^1H NMR spectrum typical of high spin Fe(II) complexes, which indicates rapid ligand exchange with a trace amount of water present. Consequently, I observed this oxidation at *ca.* +0.4 V vs. Fc^+/Fc (Fig. 4.2b, inset), and the addition of water caused a cathodic shift in its potential (Fig. 4.2b inset, indicated with blue arrow). This shows the preference of Fe(III)

for two aqua over an N, N'-ligand in accordance with the strikingly similar behavior of other Fe(II) complexes containing N₄ ligands [212]. In **1**, the configuration of the PBI ligands is expectedly *OC-6-21 (mer)* as indicated by the structure of the homolog low spin Fe(II) complex with 2-(2'-pyridyl)-*N*-methylbenzimidazole(MePBI)[210] and that of the [Fe^{II}(PBI)₃](ClO₄)₂·CH₃CN·H₂O [211].

As water molecules may induce the dissociation of a PBI ligand and occupy the two available sites in *cis*-positions; thus, upon electrochemical oxidation to Fe(III) (Scheme 4.1), a preferred arrangement for efficient water oxidation catalysis can be achieved (note that ligand exchange was viable in the presence H₂O₂, or para-substituted pyridine ligands [210]).

An irreversible wave of larger amplitude appeared roughly at +1.25 V *vs.* Fc⁺/Fc (Fig. 4.2a, inset). Notice that [Fe^{IV}(N4Py)(O)]²⁺ (containing the neutral pentadentate ligand N4Py) was successfully generated by bulk electrolysis in water/MeCN at a similar potential (> +1.3 V *vs.* Fc⁺/Fc) starting from [Fe(N4Py)(CH₃CN)₂]²⁺ [213]. The Fe(III) to Fe(IV) oxidation seems to be a valid assignment in our case, too, which would provide [(PBI)₂Fe^{IV}(OH₂)(O)]²⁺. Since there is no other visible oxidation peak between the catalytically enhanced current and this oxidation of the complex, the Fe(III) to Fe(IV) assignment would mean that the latter oxidation state is responsible for the catalysis. However, in similar complexes to **1a** (Scheme 4.1), which had neutral N₄ ligands and allowed *cis*-diaquo coordination, the (L^{N₄})Fe^{IV}(OH₂)(O) motif was associated with the resting state in the CAN excess-driven catalytic cycle [205,214–216]. This form yielded (L^{N₄})Fe^V(O)(OH) through PCET, for which the potential was calculated to be roughly +1.7 V *vs.* NHE at pH=1 by computational methods [216]. This Fe(V) species was suggested to participate in a water nucleophilic attack. Based on these facts, moreover, the 2.3-times higher current passed at +1.25 V than at +0.4 V (Fig. 4.2a, inset, the scan rate is 50 mV/s), indicating a two-electron, or two energetically leveled one-electron transitions, we tentatively assigned this oxidation to [(PBI)₂Fe^V(OH)(O)]²⁺ (**1a^{ox}**), stabilized by the negatively charged *cis*-ligand (Scheme 4.1).

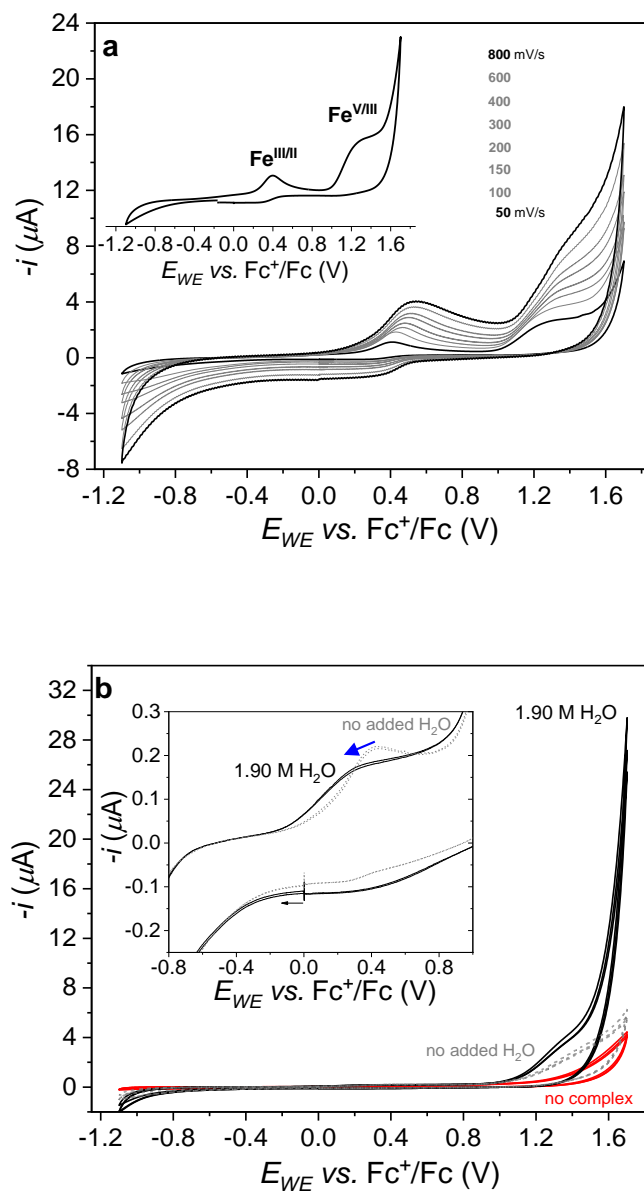
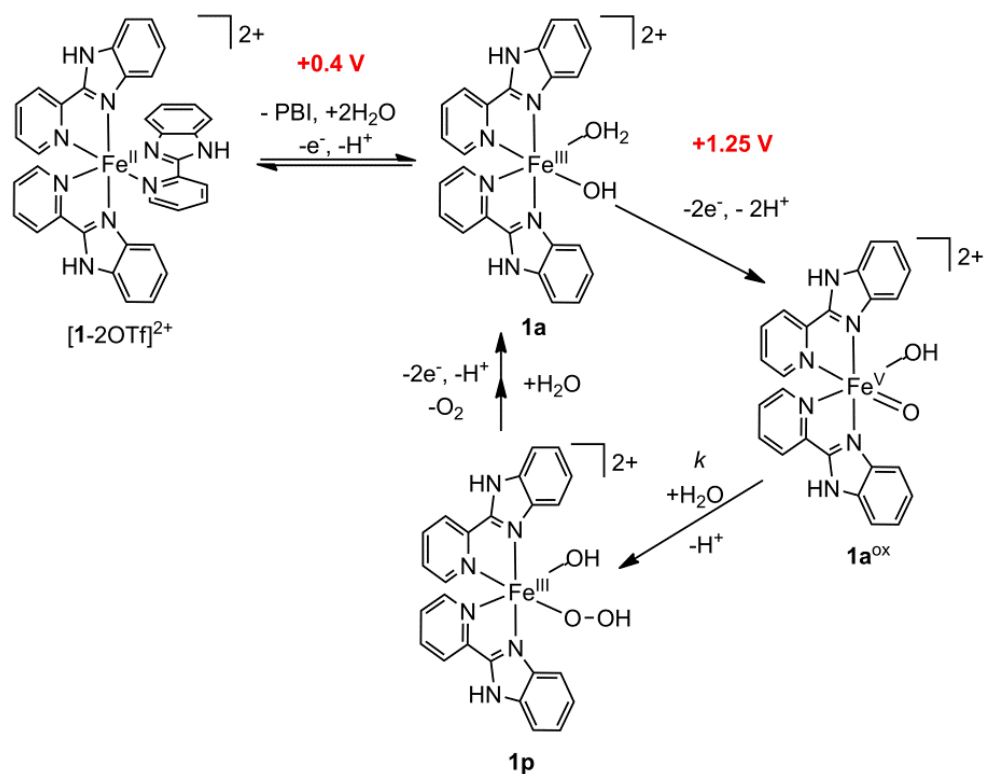


Figure 4.2. a) CVs of **1** (0.04 mM) at different scan rates, inset: magnified view of the 50 mV/s CV scan with the proposed peak assignments; b) **1** with no added water (in grey), in the presence of added H_2O (1.90 M, in black), and with water only (1.90 M, in red), at $\nu = 100$ mV/s. Inset: blown-up view of the potential range, where the Fe^{III}/Fe^{II} transition undergoes cathodic shift (blue arrow) upon the addition of H_2O . All experiments were carried out in MeCN, 0.1 M TBAP, BDD working electrode, 25°C, under Ar.



Scheme 4.1. Proposed mechanism for molecular water oxidation with complex **1a** (potentials are vs. Fc^+/Fc).

High excess of water over **1** drastically enhanced the current at above the potential where **1a^{ox}** was generated (Fig. 4.3b), and it remained so over several CV scans indicating an electrocatalytic event. The above facts indicate that this process should involve water molecules and **1a^{ox}**. This assumption was supported by the concentration dependence in water and **1** (see also the oxygen evolution measurements using the heterogenized complex in the next section).

The excess current over $+1.2 \text{ V vs. Fc}^+/\text{Fc}$ was proportional to the concentration of the complex (Fig. 4.3a). The current was negligibly low when only water was present, as shown by the CV curves in red in Figs: 4.2 b and 4.3a (the same applied to the free ligand). At above *ca.* 0.05 mM concentration of **1**, a slight deviation from linearity occurred in the current associated with substrate depletion near the electrode surface [217]. The square of the catalytic current at $+1.7 \text{ V vs. Fc}^+/\text{Fc}$ (I_{cat}^2) was linear dependent on the concentration of water (Fig. 4.3b).

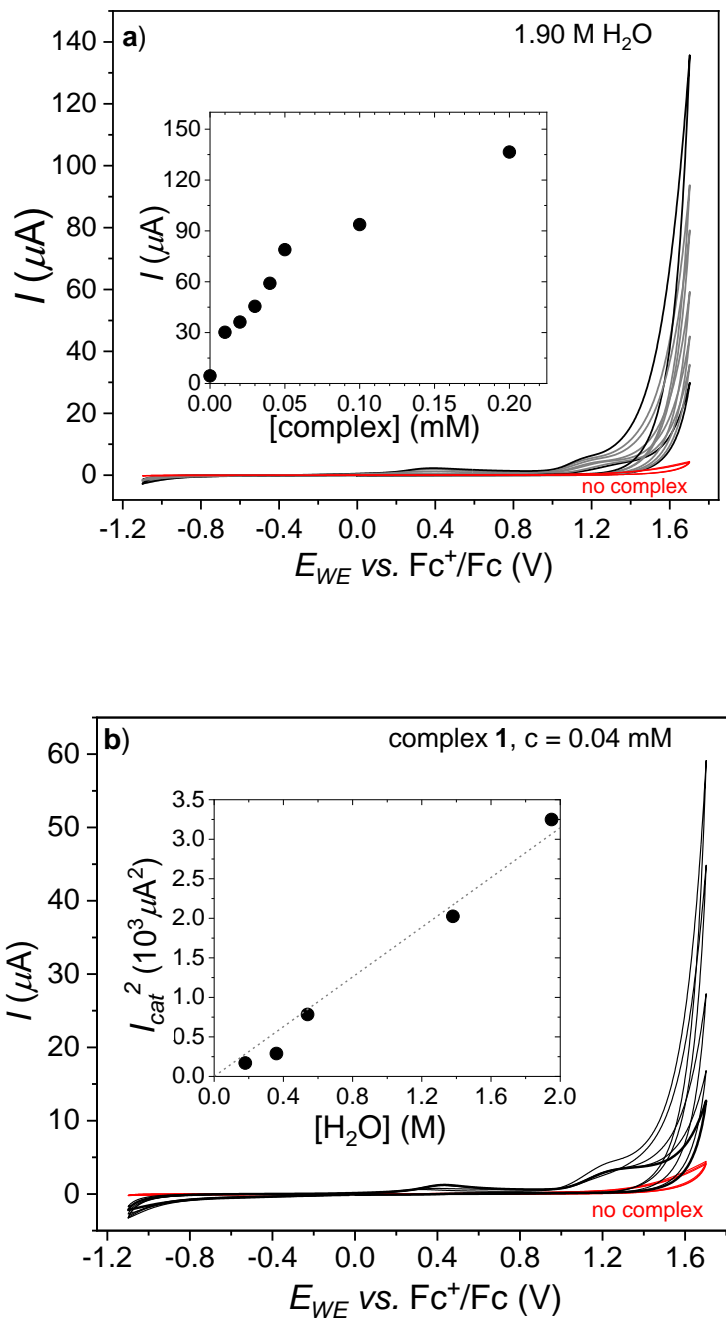


Figure 4.3. a) CVs of **1** (0.01-0.2 mM), in the presence of 1.90 M water, inset: current at +1.7 V vs. Fc⁺/Fc plotted against catalyst concentration; b) **1** (0.04 mM) with different amounts of added water and, when no complex is added (red curve). Inset: square of the current at +1.7 V vs. Fc⁺/Fc, plotted against added water. All experiments in MeCN, at $\nu = 100$ mV/s, (0.1M TBAP), BDD working electrode, Pt aux. Electrode and non-aqueous Ag⁺/Ag ref. el.

The dependence of I_{cat} (catalytic current) on $[1]$ and $[H_2O]$ is in line with the rate law in Equation 4.1, considering the proposed mechanism in Scheme 4.1, since $[1a^{ox}]$ should correlate with the initially added $[1]$. The expression of I_{cat} by Equation 4.2 applied under high substrate excess[217] in the exponential growth region of I_{cat} explains why the linear dependence of I_{cat}^2 on $[H_2O]$ as plotted in Fig. 4.3b indicates first order in the water substrate. This suggests a bulk water molecule participation in the rate-limiting step that is thus considered as a bimolecular reaction between $1a^{ox}$ and H_2O .

$$reaction\ rate = k_{cat}[1a^{ox}] = k[1a^{ox}][H_2O] \quad Eq.\ 4.1$$

$$I_{cat} = nFA[1](k_{cat}D_1)^{0.5} = nFA[1](k[H_2O]D_1)^{0.5} \quad Eq.\ 4.2$$

In Eqs. 4.1 and 4.2, k_{cat} is the catalytic rate constant (s^{-1}), k is the second-order rate constant for the reaction between $1a^{ox}$ and H_2O ($M^{-1}s^{-1}$), n is the number of electrons transferred (for water oxidation, $n = 4$), F is the Faraday constant ($96,485\ Cmol^{-1}$), A is the geometric area of the working electrode (cm^2), and D_1 is the diffusion coefficient of the catalyst (cm^2s^{-1}). This rate law suggests a single site mechanism for water oxidation like it was proposed for the iron complexes of general formula $[Fe(X)_2(L^{N4})]$ [202,205,214–216], or $[Fe^{III}(dpaq)(H_2O)]^{2+}$ with a pentadentate N-donor ligand [218].

By performing CV with deuterium oxide, a kinetic isotope effect ($KIE = I_{cat}^2(H_2O) / I_{cat}^2(D_2O) = k_{cat}(H_2O)/k_{cat}(D_2O)$) of 2.0 could be calculated (Fig. 4.4) that is consistent with a rate-limiting, multiple-site electron-proton transfer (MS-EPT) step, possibly with bulk water as the proton acceptor [208]. In contrast to the above observation, an apparent lack of KIE was concluded for catalysts utilizing CAN as an oxidant [215]. In the case of systems bearing N4 ligands, an $Fe^{IV}(O)(\mu-O)-Ce^{IV}$ core was evidenced in the resting state adduct, which produced $Fe^V(O)(OH)$ following an inner sphere electron transfer mechanism [205,214]. According to the suggested mechanism, this species reacts with H_2O in the rate-determining step providing $Fe^{III}(OOH)(OH_2)$, and only a minor reorganization of the O–H bonds takes place consistent with the lack of KIE [215]. Based on all this, it is feasible to propose that the attack of a water molecule at the oxo-ligand results in intermediate **1p** (Scheme 4.1), most likely assisted by an H-bonding interaction with the second, hydroxide ligand of $1a^{ox}$. Based on detailed computational work, the possible role

of the adjacent hydroxyl ligand in binding and orienting the incoming water molecule has been previously discussed by Lloret-Fillol *et al.* [216].

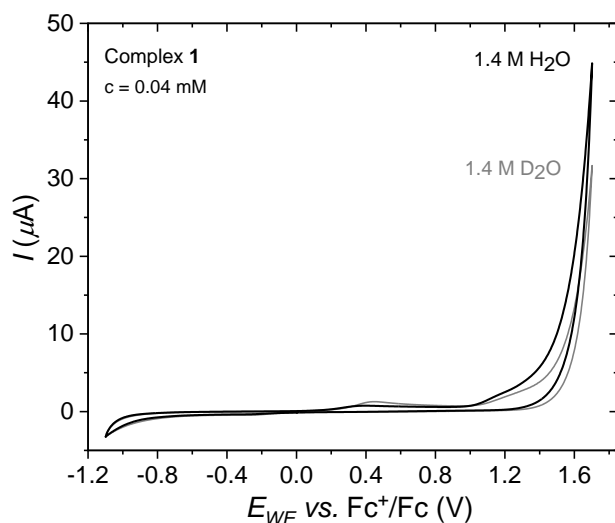
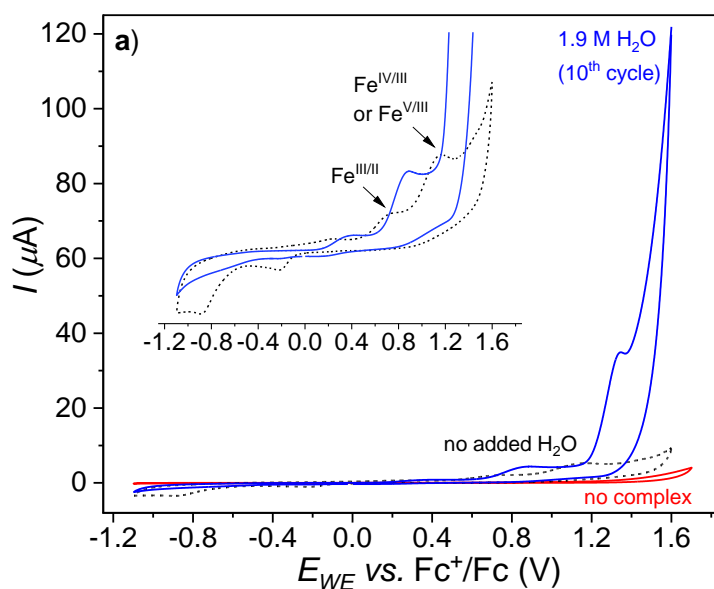


Figure 4.4. CVs of **1** (0.04 mM) in H₂O(D₂O)/acetonitrile (0.1 M TBAP), $\nu = 100$ mV/s, BDD working electrode, Pt aux. electrode and non-aqueous Ag⁺/Ag reference electrode.

Following the rate-limiting step, the oxidation of **1p** is proposed to affect the peroxide ligand resulting in facile O₂ release and H₂O coordination, which means re-entering the catalytic cycle by re-forming **1a**. Note that **1** was shown to react with H₂O₂ to give a green product identified as a μ -peroxido-diiron(III) species with a considerable lifetime at room temperature. Its oxidation potential was more positive by *ca.* 0.4 V than that of **1** [210], which means that it is lower by roughly 0.6 V than the onset potential of the catalytic process. This observation supports that a proposed peroxide species from the O–O bond formation step should undergo rapid oxidation during electrocatalysis due to the high thermodynamic driving force.

Importantly, returning to the ferrous state is unlikely during electrocatalysis, and thus, the proposed mechanism involves **1a** as the resting state. As will be discussed later (see chapter 4.1.3), Fe(III) could be detected on the surface of immobilized samples by XPS. In addition, successful re-dissolution tests in acetonitrile on used samples together with the CV and UV-vis results indicated that the molecular nature of the ad-layer is preserved, and changes in the UV-vis spectra could be associated with the occurrence of Fe(III).

In contrast to **1**, the Fe(III)/Fe(II) redox couple of **2** is irreversible and occurs at +0.75 V vs. Fc⁺/Fc (Fig. 4.5a, dashed CV curve, inset) that has been associated with the electron-withdrawing nature of O compared with NH in the corresponding ligands [210]. Further oxidation at +1.16 V vs. Fc⁺/Fc can be tentatively associated with oxidation to the Fe(IV) or Fe(V) state. The single-crystal structure of complex **2** confirmed the OC-6-33 configuration of the donor atoms, as shown in Fig. 4.1, and Fe–N(O) bond distances longer than 2.15 Å in the solid-state that is typical of high spin Fe(II) complexes. The two triflate ligands can readily exchange with water molecules (or acetonitrile in the absence of water); moreover, the high spin Fe(II) center should be unstable towards hydrolysis. The addition of water to the solution of **2** resulted in high anodic currents indicating a catalytic event (Fig. 4.5a and b). However, the current drops drastically from one cycle to another, and the overall landscape changes entirely in the low current regime, too (Fig. 4.5b). If the cycling is started in the cathodic direction, the original peaks for **2** in acetonitrile cannot be observed anymore; instead, some current peaks suggest the presence of surface-adsorbed species. This indicates that the high spin complex **2** is unstable and may hydrolyze in the presence of water.



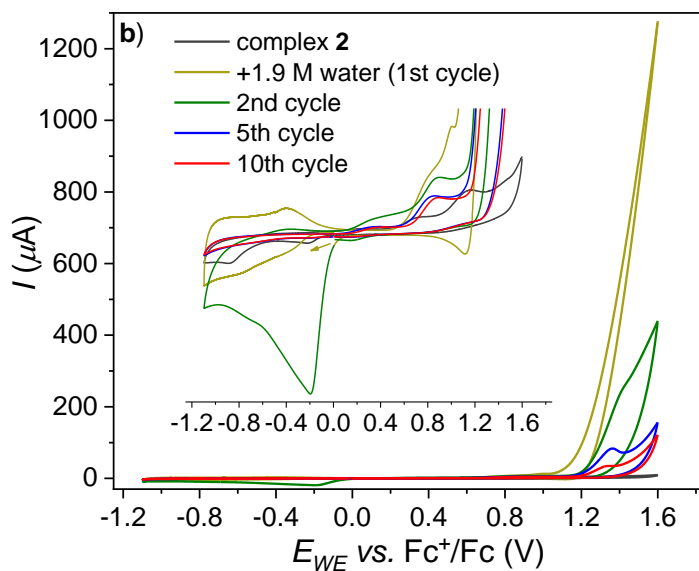


Figure 4.5. a) CVs of **2** (0.04 mM) in MeCN (0.1M TBAP), in the presence or absence of 1.90 M H₂O, $\nu = 100$ mV/s; b) CVs of **2** (0.08 mM) in MeCN (0.1 M TBAP), in the presence or absence of 1.90 M H₂O and, when no complex is added (red curve), $\nu = 100$ mV/s (BDD working electrode, 25°C, under Ar).

Indeed, slow precipitation of a fine solid product occurred in samples with added water. After passing through the positive potentials, re-dissolution peaks occurred at *ca.* +1.1 and -0.2 V *vs.* Fc⁺/Fc that can be rendered to decomposition products at the surface. After 10 cycles, no more changes occurred, and two current peaks can be detected at +0.4 and +0.9 V *vs.* Fc⁺/Fc, besides the catalytic current. Due to the complexity of the processes, I did not attempt to explain the chain of events in more detail. However, the processes cannot be regarded as homogeneous, especially considering the results from the immobilized samples of **2**, as presented in chapter 4.1.3.

Despite the analog structure and NN' binding mode of the PBI and PBO ligands, the behavior of the two complexes under water oxidation conditions is strikingly different. This difference can be associated with the electron-withdrawing nature of O in PBO compared with NH in PBI, making PBI a stronger donor (as also reflected in the respective high *vs.* low spin electron configuration of the isolated Fe(II) complexes). Specifically, a supposed [(PBO)₂Fe^{III}(OH₂)(OH)]²⁺ and other oxidation products from **2** are expectedly degradation-prone due to the weaker donor PBO, which would be a plausible explanation for the non-homogeneous behavior in water/acetonitrile; moreover, for the mineralization of the deposited complex on the ITO surface (see the next section).

4.1.3. Immobilization of complexes **1** and **2** on ITO

Immobilizing the two complexes onto ITO-coated glass was carried out by scalable and straightforward methods (see the experimental work, chapter 3, section 3.4). Complexes **1** and **2** are water-insoluble, thanks to the ancillary bidentate ligands. I hypothesized that hydrophobic interactions would keep the surface-deposited complexes on the ITO electrode in an aqueous buffer during electrolysis. Also, it was presumed that the ligand exchange reactions observed in water/MeCN mixtures would occur at the solid-liquid interface upon contact of the layered ITO with the aqueous phase, which would allow carrying forward the catalytic activity of the molecular units.

According to the first procedure (see chapter 3, section 3.4), ITO pieces were dipped into methanol solutions of the complexes. With this method, thin layers were expected upon drying. The modified electrodes' performance was compared to plain ITO in borate buffer at pH 8.3. CV showed increased currents above +1.2 V *vs.* Ag/AgCl (3M KCl) as the concentration of **1** increases in the dip-coating solution (Fig. 4.6a). The same trend could be observed in CA currents at +1.4 V *vs.* Ag/AgCl (Fig. 4.6b).

However, the addition of Nafion (as support) had no significant effect on the steady currents. In the case of **2**, the concentration of the dip-coating solution did not affect the catalytic current (Fig. 4.7). Notably, the current was very low on plain ITO under identical conditions, both in CV and CA experiments (Figs. 4.6b & 4.7). Although these experiments demonstrated the successful addition of the complexes as modifiers to ITO, the solubility of the complexes in methanol set an upper limit to the layer; moreover, at high concentrations, the ad-layer showed patchy distribution on the surface.

On the other hand, drop-casting is a relatively controllable and convenient way to fabricate **1**/ITO and **2**/ITO (see chapter 3, Fig. 3.4) that can be tested for more extended periods of CA. In this case, the volume of the drop-casted solution of **1** or **2** in methanol can be adjusted to yield a different surface concentration of the corresponding complex. With a series of **1**/ITO, CV currents increased proportionally as the amount of **1** changed from 0.26 to 0.78 μmol on a 1.56(14) cm^2 ITO surface (Fig. 4.8a).

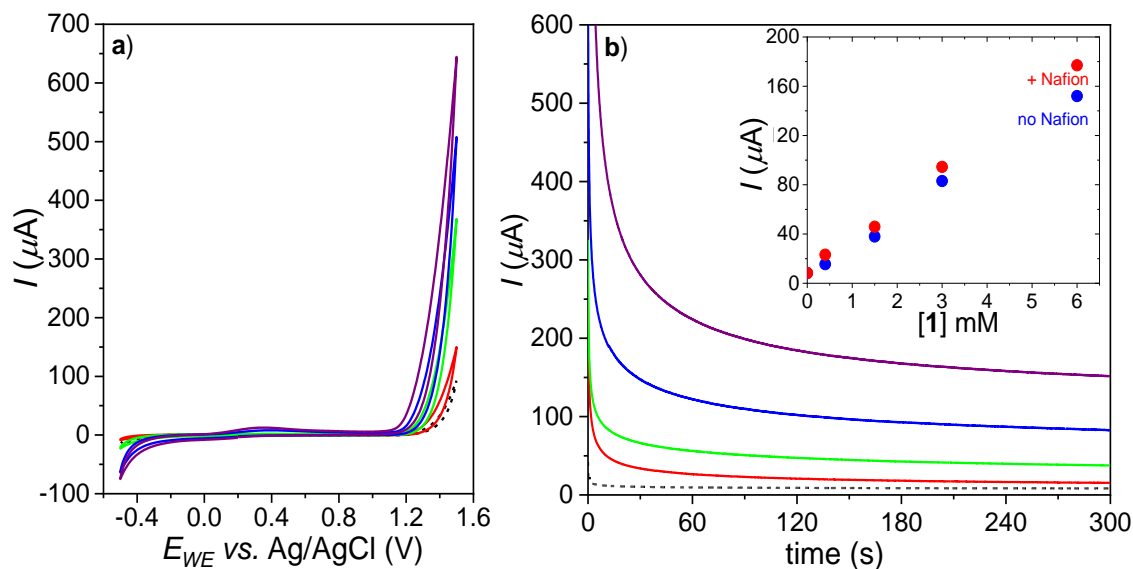


Figure 4.6. (a) CVs with **1**/ITO prepared by dip-coating from solutions containing **1** in different concentrations (0.4, 1.5, 3.0, and 6.0 mM); (b) comparison of chronoamperometry tests with the dip-coated ITO electrodes at +1.4 V. Inset of (b): current after 5 minutes of CA as a function of the complex concentration in the coating solution with or without added Nafion (for details see the Experimental Section). Conditions: 0.2 M borate buffer, pH 8.3, $\nu = 100$ mV/s, Pt aux. and Ag/AgCl ref. electrode.

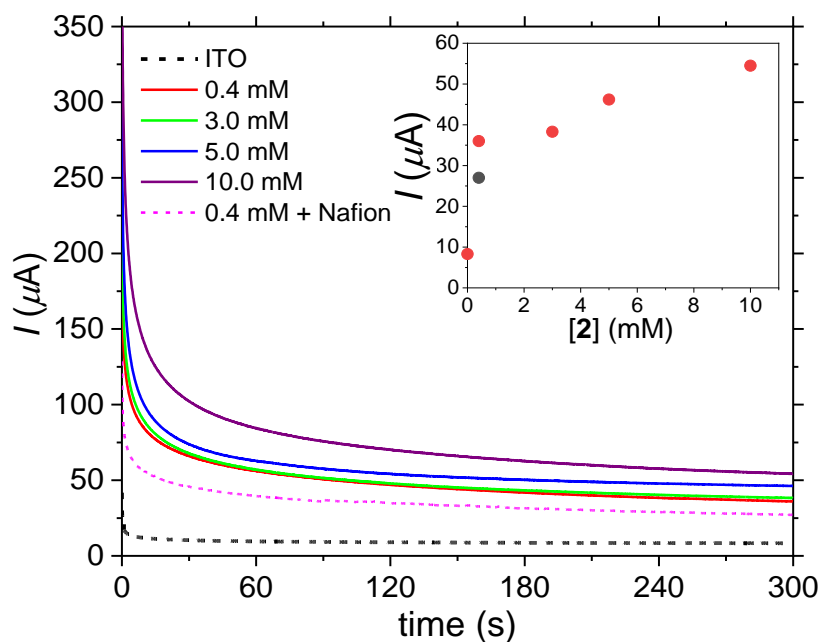


Figure 4.7. Comparison of CA tests with dip-coated **2**/ITO from solutions of **2** in different concentration (0, 0.4, 3.0, 5.0 and 10.0 mM), in 0.2 M borate buffer, pH 8.3, +1.4 V, Pt aux. and Ag/AgCl ref. el. Inset: current after 5 minutes of CA as a function of the complex concentration in the coating solution (black point) or without added Nafion.

Over multiple CV scans (apart from an initial drop), the current was unchanged, indicating an electrochemically activated proportion of the catalyst derived from **1** under the conditions of the experiment. The oxidation peak at +0.8 V vs. Ag/AgCl was assigned as the Fe(III)/Fe(II) transition of this form that is followed by a catalytically enhanced Faraday current with an onset potential of +1.2 V (similar characteristics were observed in the water/MeCN solution).

On the reverse scan, a reduction can be observed at +0.02 V vs. Ag/AgCl, which can be associated with the coordination of water molecules. The nearly 800 mV separation from the Fe(III)/Fe(II) oxidation may originate from the increased stability of the Fe(III) state in the presence of aqua ligands. The low reversibility on both sides suggests rapid ligand exchange, resulting in an electrochemical-chemical-electrochemical (ECE) mechanism. Notice that the aqua ligands have enough driving force to dissociate from the complex when reduced to the Fe(II) upon cathodic polarization. However, it is uncertain which ligands can compete for the empty sites.

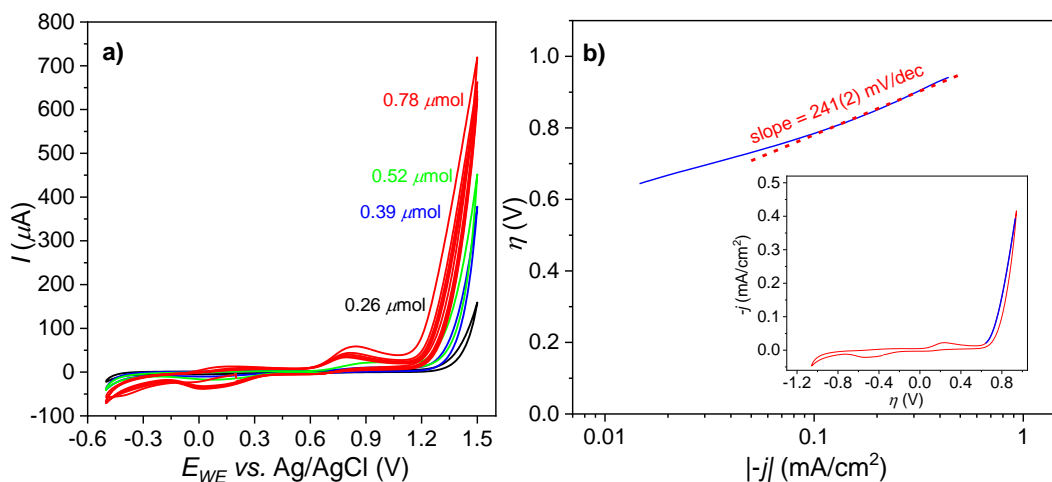


Figure 4.8. (a) CV of drop-casted **1**/ITO in 0.2 M borate buffer (pH 8.3, $\nu = 100$ mV/s, Pt aux. separated with Vycor frit and Ag/AgCl ref. electrode); (b) Tafel plot from the blue segment of the 5th CV scan, which is shown in the inset).

The overpotential calculated from the 5th CV scan ($\eta = E_{WE} + E(\text{Ag/AgCl}) - E^\circ(\text{O}_2/\text{H}_2\text{O}) + 0.059\text{pH}$, no iR compensation) at $j = -0.1$ mA/cm² is +0.78 V and the Tafel slope is 241(2) mV/dec (Fig. 4.8b) that signals considerable energy barrier for the catalysis.

Longer-term CPE experiments were performed at +1.2 V vs. Ag/AgCl in a different cell, where the Nafion membrane separated the counter electrode compartment. After saturating the electrolyte, the evolved gas diffuses from the solution causing an apparent decline from the $[\text{O}_2]$ calculated for

100% Faraday efficiency. The almost instant O₂ evolution could be confirmed with an optical oxygen sensor immersed near the 1/ITO surface (Appendix B, Fig. A.4.1). During the first 15 minutes, the evolved O₂ corresponded to ~100% Faraday efficiency, and the color of the layer changed from brick-red to dark-red (Fig. 4.11, inset). However, the current remained steady for over 2 hours, during which time ~6 C (corresponds to 62.2 μmol of electrons) passed (Fig. 4.9), and bubble formation was continuous (plain ITO gave negligible current, see Fig. 4.9).

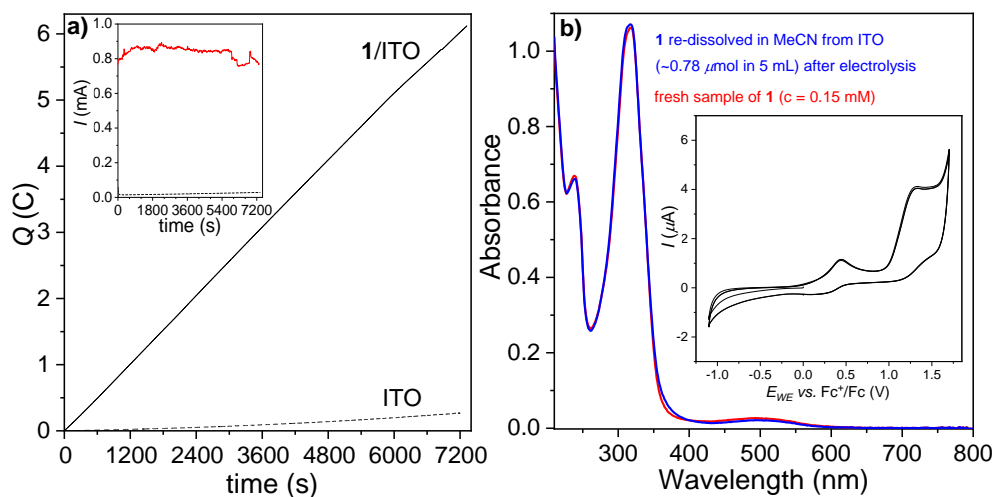


Figure 4.9. (a) The passed charge during CPE using 1/ITO and plain ITO (dashed line) at +1.2 V vs. Ag/AgCl for 2 hours in 0.2 M borate buffer, at pH 8.3. The inset shows the corresponding current vs. time plot; b) UV-vis spectrum of the solid re-dissolved in acetonitrile from 1/ITO after electrolysis and comparison to a fresh sample of **1**. Inset: CV of the same re-dissolved sample.

The oxygen evolution was also confirmed and quantified by gas chromatography analysis of a headspace sample after 100 minutes of electrolysis at +1.4 V vs. Ag/AgCl (Fig. 4.10). In this experiment, 0.52 μmol of **1** was spread over ~1.68 cm² of which ~1.5 cm² was immersed in the solution; thus, roughly 0.46 μmoles of **1** were in contact with the electrolyte. After passing 13.22 C of charge (corresponding to 137 μmoles of electrons, or 34.25 μmol O₂), 33.4 μmol O₂ could be detected by GC. This means an overall turnover number (TON) of 73 within 100 minutes by 98% Faraday efficiency at $\eta = 0.86$ V, corresponding to a TOF of 0.012 s⁻¹ based on the detected product.

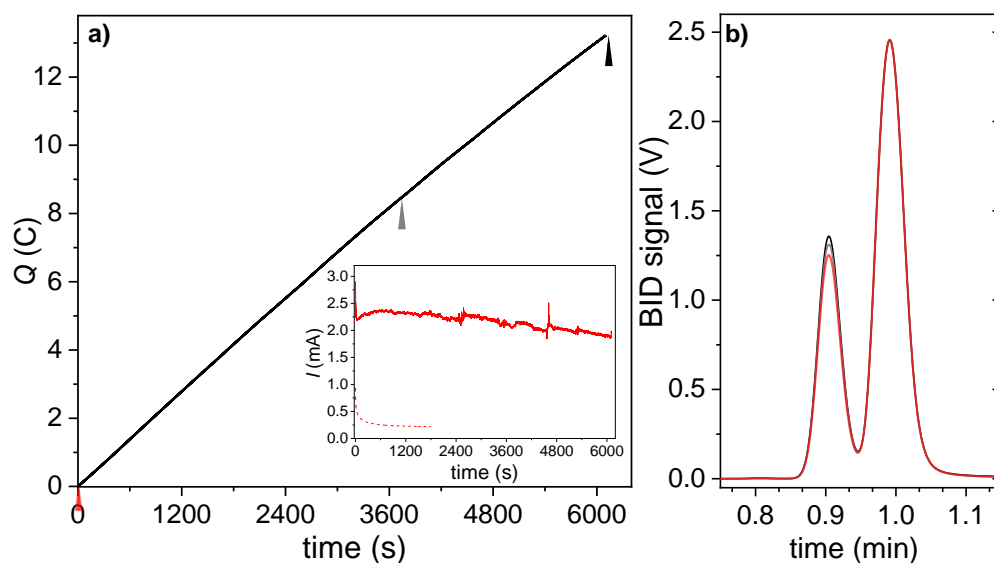


Figure 4.10. a) Passed charge upon CPE with **1**/ITO (drop-casted, $0.52 \mu\text{mol}$), conditions: 0.2 M, borate buffer, pH 8.3, +1.4 V vs. Ag/AgCl, Pt counter el. separated by a Nafion membrane, and inset: current (the dashed line represents the current on a neat ITO); b) gas chromatograms of headspace samples taken at the start (red), after 60 (grey), and after 100 minutes (black) of electrolysis, the peak of O_2 comes first, N_2 second, the cell was filled with artificial air of known composition, for results see the text.

The surface morphology of a freshly prepared **1**/ITO electrode and after its use in electrolysis for 2 hours at +1.2 V vs. Ag/AgCl was analyzed by scanning electron microscopy (SEM) (inset pictures in Fig. 4.11a and 4.11b, respectively). The composition was analyzed by EDX (Fig. 4.11a, and 4.11b, respectively) and XPS, as shown in Tables 4.1 and 4.2 (Appendix B, Figs. A.4.2 and A.4.3). The surface morphology of the freshly prepared **1**/ITO (Fig. 4.11a, insets) showed cracks in the layer, but otherwise, the surface is relatively featureless, *e.g.*, no smaller pores could be seen. The elemental composition by EDX reflected the expected C, N, and Fe for the complex cation and the F, O, and S from the triflate counter ion (Fig. 4.11). The color of the complex exposed to CPE became darker (Fig. 4.11b, inset). Others observed a similar color change for the low spin $[\text{Fe}(\text{phen})_3](\text{NCS})_2$ after its transformation to the high spin $[\text{Fe}(\text{phen})_2(\text{NCS})_2]$ in the solid phase [219]. In the case of **1**, the color change may also indicate ligand exchange that would be consistent with the formation of **1a**.

The surface of the layer was cracked, and the layer structure was porous, with pore sizes in the 100 nm range. This porous structure may be responsible for the high durability and good catalytic performance since it helps to channel O_2 bubbles from the surface.

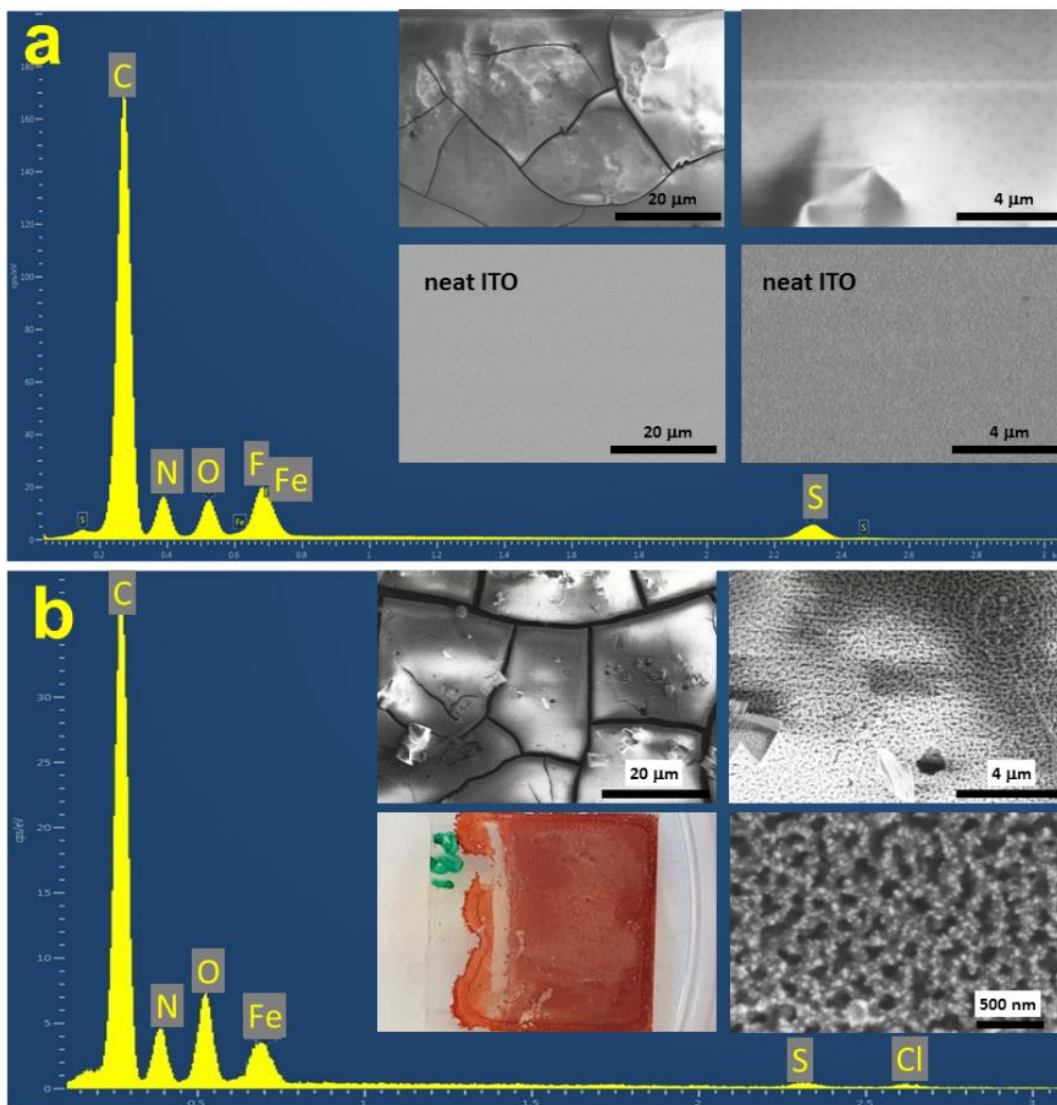


Figure 4.11. (a) EDX spectrum of a freshly prepared **1**/ITO sample, inset: SEM pictures of the sample and the neat ITO surface at $\times 2000$ and $\times 10,000$ magnification; (b) EDX spectrum of **1**/ITO after electrolysis (for experimental details, see Fig. 4.9), inset: photo and SEM pictures of the used electrode at $\times 2000$, $\times 10,000$ and $\times 50,000$ magnifications. Experimental conditions for SEM: 2 kV beam accelerating voltage, 0.10 nA probe current, Everhart-Thornley detector, operation for secondary electron, 6.4 mm working distance. The detection mode was optimized for a horizontal plane with a short working distance.

The C, N, Fe, O, and S significant components in the EDX spectrum (Fig. 4.11b) are consistent with the elementary constitution of the complex. Two significant differences may be highlighted. The first O content has increased, which is reasonable regarding the sample being exposed to water for an extended period; moreover, it is consistent with the proposed **1a** form. The second difference is the lowered F and S content, indicating that the triflate is partly dissolved upon electrolysis. A

more detailed analysis of the used **1**/ITO was done by XPS that revealed the presence of Fe, C, N, O, S, and F in the surface layer (Appendix B, Fig. A4.2), beside Sn and In, in qualitative agreement with the elemental composition of **1a**.

In comparison with the surface composition of the as-prepared **1**/ITO, the O/Fe ratio is higher, while the N and C content is lower in the used sample (Table 4.1). The calculated surface composition for the used sample is Fe/C/N = 1/20.6/3.8 (Table 4.1, for **1a** with two ancillary ligands 1/(2×12)/(2×3) would be expected); this indicates that the surface is enriched in Fe. This also represents the as-prepared sample suggesting that the immediate surface layer contains a complex form with an equal PBI to Fe ratio. This is probably a minor accompanying equilibrium form layered on **1** upon drying from its methanol solution.

Table 4.1. XPS surface composition of as-prepared, drop-casted **1**/ITO and **2**/ITO and after 2 h, or 30 min of CPE, respectively at +1.2 V vs. Ag/AgCl.

surface atomic ratio (at.%) on as-prepared samples								
	Fe	F	O	Sn	In	N	C	S
1 /ITO	4.0	n.d.	17.6	<0.1	0.4	13.7	64.3	0.6
2 /ITO	4.1	n.d.	29.3	<0.1	0.3	5.0	61.3	n.d.
surface atomic ratio (at.%) on used samples								
	Fe	F	O	Sn	In	N	C	S
1 /ITO	3.0	2.4	20.2	0.1	0.5	11.5	61.8	0.6
2 /ITO	7.8	-	53.6	0.1	0.7	2.0	35.8	-

The Fe(2p) peaks do not exhibit apparent satellite features revealing the high spin state. However, the peaks are broad and somewhat asymmetric; moreover, the splitting between them, $\Delta = \text{Fe}(2p_{3/2}) - \text{Fe}(2p_{1/2}) = 13.9 \text{ eV}$ (Appendix B, Fig. A.4.3, for data, see Table 4.2), falls in the range reported for high spin complexes with increased spin-orbit coupling, for example $[\text{Fe}(\text{phen})_2(\text{NCS})_2]$ that has been examined as a powder on ITO support [219], or other spin-crossover complexes [220,221]. In conclusion, I believe that Fe(III) is found in the surface layer. Interestingly, the as-prepared sample shows features for the surface Fe-content (Appendix B, Table 4.2) that also

suggest Fe(III) in considerable proportion. However, the Δ value is lower (13.7 eV), and the Fe(II) content is ~40%. Consequently, in the case of this immobilized system, the presence of Fe(III) cannot be associated with only **1a** to the analogy with the proposed homogeneous catalytic cycle.

Table 4.2. XPS binding energy and chemical state of the elements at the surface of drop-casted **1**/ITO and **2**/ITO samples after 2 h, or 30 min of CPE at +1.2 V vs. Ag/AgCl, respectively.^aThe corresponding Fe 2p energy data for as-prepared samples are given in parenthesis.

elements / component peak	Binding energy (eV)	Chemical state
1/ITO		
Fe 2p 1	710.4 (710.7)	Fe(III)
Fe 2p 2	724.3 (724.4)	
Fe 3p	56.5	
N 1s	397.8	N _{hc}
	399.5	Fe-N _{hc}
2/ITO		
Fe 2p 1	710.6 (710.3)	Fe(III)
Fe 2p 2	724.6 (723.9)	
Fe 3p	56.3	
N 1s	~397	N _{hc}
	399.4	Fe-N _{hc}

^athis modified electrode has been analyzed by SEM-EDX, and the complex was re-dissolved in acetonitrile

The ancillary ligand PBI contains N atoms in two environments, i.e., a non-coordinated NH heterocyclic group (N_{hc}) and two coordinated Fe(N_{hc}) donor groups in a 2:1 ratio. The detailed analysis of the N 1s peak in the used sample tells about the Fe-N interaction. Indeed, the N 1s peak fitting reveals two components at 399.5 and 397.8 eV binding energy in a ~2:1 ratio (Appendix B, Fig. A.4.3). The component at higher binding energy can be associated with the coordinated N donor atoms, while the component at lower binding energy with the non-coordinated N_{hc} atoms. This is consistent with the fact that the electron density shared in the dative bond is expected to

increase the binding energy of the 2p electrons. Based on these findings, one can surmise that the upper layer of the complex coating detected by XPS consists of a Fe(III) complex form with higher iron content than **1a**, possibly exhibiting only one PBI ligand per Fe. Since XPS informs only about the upper proportion of the layer (which should be separated from the ITO electrode), the contribution of this component to the catalysis is hard to judge, but it cannot be excluded.

After surface analysis, the drop-casted layer of **1** was re-dissolved in acetonitrile. The UV-vis absorption spectrum of the solution fits well with that of a freshly prepared one with **1** (Fig. 4.9b). The intra-ligand charge transfer band at 316 nm is identical to that of the fresh sample, showing no sign of ligand degradation or considerable dissolution during electrolysis. The metal-to-ligand charge transfer (MLCT) band at 497 nm is also present, but it is lower by 19% in intensity. This might be attributed in part to metal ion loss upon electrocatalysis, but it is more likely that some of the complexes are present in a high spin $[\text{Fe}(\text{PBI})_2(\text{X})_2]^{2+}$ form, where X is a solvent ligand, exhibiting no MLCT band. Likewise, according to the XPS findings, it cannot be ruled out that some of the complexes are in the ferric state. Three ligands surround the Fe(II) center in the original complex. However, one of the ligands is proposed to be exerted during water oxidation.

UV-vis measurements in acetonitrile with added ligand to a re-dissolved sample (used in electrolysis at +1.2 V vs. Ag/AgCl for 2 h) showed a somewhat regained intensity of the MLCT band at 497 nm (Fig. 4.12) that is characteristic for the original complex. This suggests that after electrolysis $[\text{Fe}(\text{PBI})_3]^{2+}$ can be re-formed to some extent, which may appear surprising considering the presence of Fe(III) in the surface layer. On the other hand, as discussed earlier, in the added layer, only a part of the solid complex is expected to be in contact with both the electrode support and the solvent, which is necessary to trigger catalysis. Another part remains aqua-coordinated Fe(II), capable of accepting the added PBI ligand, which puts our observations into a complementary relation. The CV scan of the re-dissolved sample also confirms that during electrolysis, most of the complex remains in a form that reproduces the electrochemical features of the original complex in acetonitrile (Fig. 4.9b, inset).

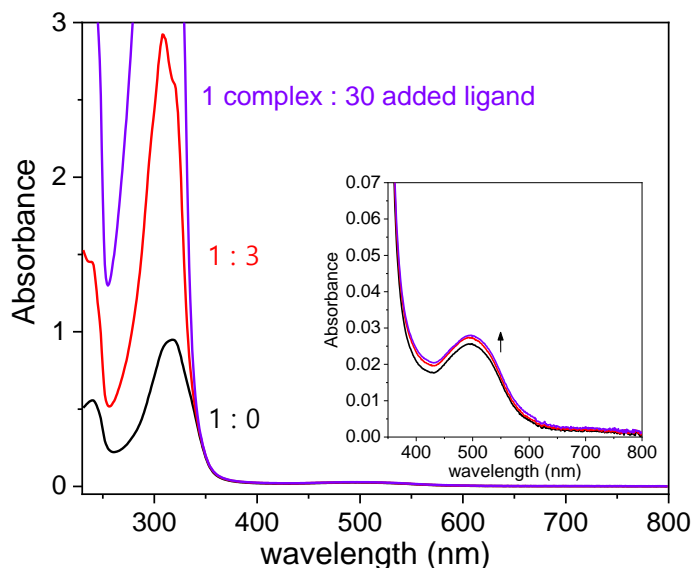


Figure 4.12. UV-vis spectra of a sample re-dissolved in acetonitrile from **1**/ITO after 2 hours of controlled potential electrolysis at +1.2 V vs. Ag/AgCl, with different amounts of added PBI ligand to the solution. The increased absorbance near 300 nm is due to the intraligand CT band from the added free ligand. The numbers indicate the complex: added ligand ratios. The inset shows the magnified MLCT region of the identical spectra.

Complex **2** shows a vastly different electrochemical behavior in drop-casted samples prepared analogously to **1**/ITO samples. This is not surprising if one regards the instability of **2** toward hydrolysis in water/acetonitrile. The SEM pictures show a compact layer of the solid complex on ITO (Fig. 4.13a, insets). The elemental composition by EDX reflects the expected C, N, Fe, F, O, and S from the complex with coordinated triflate anions (Fig. 4.13a). CV scans with **2**/ITO working electrodes, which contain increasing loads of the complex spread over a 1.0(1) cm² area, exhibit lowering currents in the high positive potential range (Fig. 4.13c), which can be attributed to an insulating effect of the non-porous deposit, as clear from the SEM pictures of a used **2**/ITO sample (Fig. 4.13b, insets). In the CV scans, the features indicate mineralization to iron oxide [222] that is also supported by the EDX spectrum, which shows O and Fe predominantly on the surface and only the very low presence of N and C, in sharp contrast with the as-prepared **2**/ITO (Fig. 4.13). The dominance of mineralization is also underlined by XPS (Tables 4.1 and 4.2 and Appendix B, Figs. A.4.2 and A.4.3), which detected increased Fe and O concentration on the surface and significantly lowered concentration for C and N.

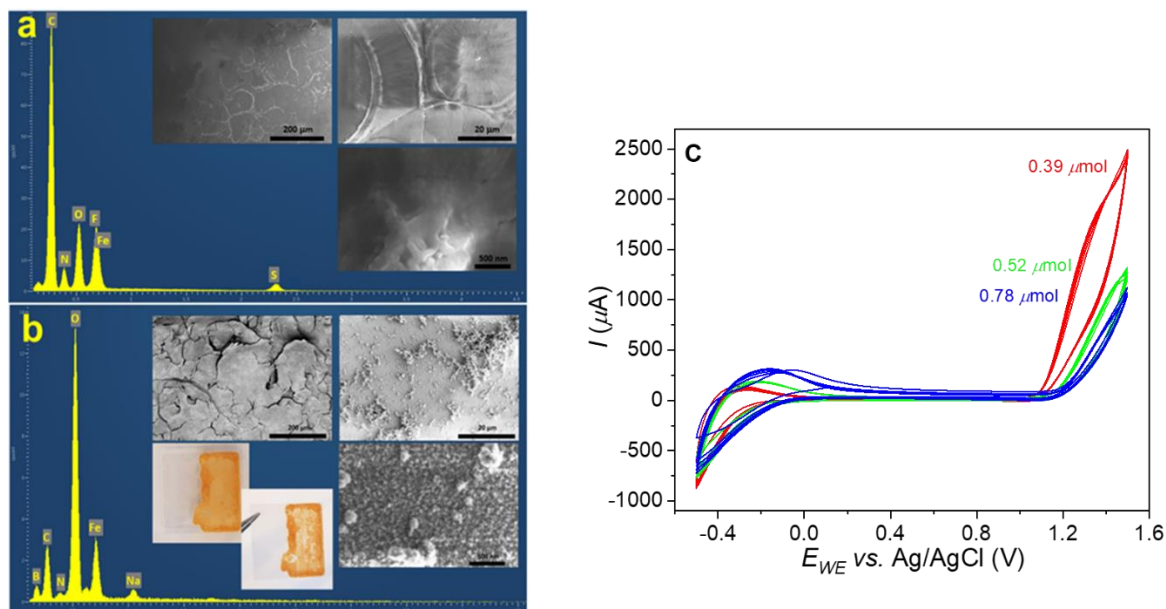


Figure 4.13. (a) EDX spectrum of an as-prepared **2**/ITO sample, inset: SEM pictures of the sample and the neat ITO surface at $\times 2000$ and $\times 10,000$ magnification; (b) SEM pictures at different magnifications and EDX spectrum of **2**/ITO after electrolysis at +1.2 V vs. Ag/AgCl for 30 minutes in 0.2 M borate buffer, at pH 8.3. The photos show the layer before (on the left) and after (on the right) electrolysis. Experimental conditions for SEM: 5 kV beam accelerating voltage, 0.10 nA probe current, Everhart-Thornley detector, operation for secondary electron, 7.0 mm working distance. The detection mode was optimized for a horizontal plane with a short working distance. c) CVs of **2**/ITO made with different drop-casted amounts of the complex (0.2 M borate buffer, pH 8.3, $\nu = 100$ mV/s, Pt aux. and Ag/AgCl ref. electrode).

EDX and XPS detected B and Na in the used sample that seems to be participating elements in the oxide material. Note that the **2**/ITO working electrode also produced oxygen. However, the impermeable deposit peeled off from ITO, and its physical durability was poor (Fig. 4.13b shows SEM-EDX analysis results after only 30 minutes of CPE at +1.2 V vs. Ag/AgCl); moreover, the solid could not be re-dissolved in acetonitrile. These findings underline again that **2** (with its oxidized derivatives) is not a molecular catalyst of water oxidation.

Part (II)

4.2. Immobilization and characterization of water-insoluble Fe(III) complexes as water oxidation catalysts using hydrophobic pincer ligand

I synthesized the five-coordinate $[\text{Fe}^{\text{III}}\text{Cl}_2(\text{tia-BAI})]$ complex (**3**, $\text{tia-BAI}^- = 1,3\text{-bis}(2'\text{-thiazolylimino})\text{isoindolate}(-)$) according to a known procedure [181]. Concerning the previous study, **3** is isomerized into two electrochemically active equilibrium species when dissolved in *N,N*-dimethylformamide, attributed to the exchange of chloride to solvent upon reduction due to the more labile ferrous species [181]. Based on the known ligand exchange behavior of **3**, I studied this complex (i) in the potentially non-coordinating solvent acetone (miscible with water) with and without adding water in order to clarify the redox properties and explore homogeneous catalysis, (ii) in methanol, because it is a suitable solvent for simple immobilization purposes by drop-casting on ITO electrodes.

Before and after electrolysis, the complex/ITO assembly was analyzed by SEM, EDX, and XPS. Surface analysis and re-dissolution of the complex layer after long-term CPE supported that an immobilized molecular catalyst is responsible for catalysis, and de-activation occurs by depletion of the metal. As an outcome, the complex with the pincer ligand can be considered a potential pre-catalyst for water oxidation by producing the active form through the exchange of chloride ligands to water molecules.

4.2.1. Selection of the complex based on preliminary results

The activity of Fe complexes is highly responsive to electronic and geometric features due to the occurrence of different oxidation and spin states. Therefore, finding ligand architectures robust enough to favor high-valence states and facilitate WOC remains challenging [133,223]. Furthermore, instead of being dissolved in the electrolyte, catalysts are better applied in an immobilized form on conductive surfaces [224]. The conversion or degradation of homogeneous Fe catalysts due to the oxidation of ligands [206,207] and the question of the homogeneous *vs.* heterogeneous nature of catalysis remain crucial issues from the viewpoint of the application [133]. Although detailed studies are often performed on either homogeneous or heterogeneous systems, the link between the two scenarios would be essential in order to rationalize practical WOCs [133,225].

The results in part I, fueled further investigation of water-insoluble Fe complexes as immobilized molecular WOCs with an ancillary ligand type, which was supposed to be an efficient Fe chelating agent and favor its affinity for the surface. Pincer ligands appeared to serve this aim with their wide versatility applications in organic synthesis and catalysis [226]. The 1,3-*bis*(arylimino)isoindolines (BAIs) are 3N donor ligands that have been utilized in iron complexes exerting oxidative reactivity against organic substrates [181,227]. The tia-BAIH forms the characterized Fe^{III} complex, [Fe^{III}Cl₂(tia-BAI)] (**3**) selectively (Fig. 4.14) that is sufficiently soluble in organic solvents but it is insoluble in water. The exchange of the chloride to aqua ligands may occur upon the addition of water to the solution of the complex in organic solvents leading to electrocatalytic water oxidation. This chapter will discuss that the ancillary ligand indeed allows immobilization of **3** on (ITO) electrode, and the ad-layer acts as a robust electrocatalyst in aqueous buffers.

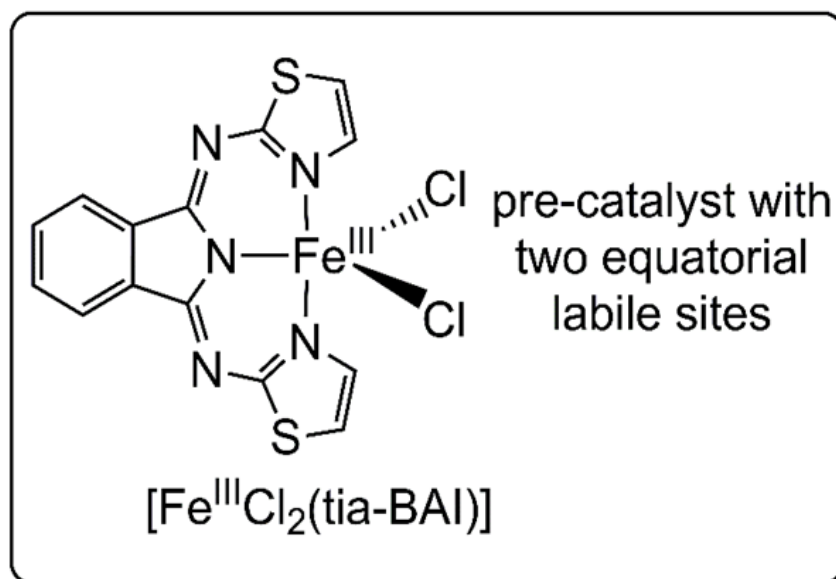


Figure 4.14 The selected Fe^{III} complex **3** with (tia-BAIH) ancillary ligand for WOC.

4.2.2. Structural properties of [Fe^{III}Cl₂(tia-BAI)] (**3**) and its behavior in acetone

The complex was synthesized and characterized earlier as part of a study on Fe^{III} complexes exhibiting dioxygenase-like activity, *e.g.*, capable of incorporating oxygen atoms into a catechol substrate [181]. According to the reported single crystal structure of [Fe^{III}Cl₂(tia-BAI)], the complex is five-coordinate, distorted trigonal bipyramidal with the tridentate, anionic tia-BAI ligand occupying the two apical and one equatorial position in meridional topology [181]. The central pyrrolic nitrogen atom (Fig. 4.14) resides closer to the Fe center than the two thiazole nitrogen atoms (the Fe-N bond distances are 2.019(2) and 2.095(2) Å in avg., respectively). Due to

the greater Lewis basicity of the former, the Fe-Cl distances are equally ~ 2.23 Å, all together in agreement with a high-spin ferric center, in contrast with the homoleptic $[\text{Fe}^{\text{III}}(\text{tia-BAI})_2]^+$ exhibiting shorter bond distances of ~ 1.95 and 2.00 Å, or similar *bis*-BAI $^-$ complexes with low-spin ferric center [228]. Importantly, in the earlier report, two electrochemically responsive species could be detected when **3** was dissolved in *N,N*-dimethylformamide solvent attributed to the exchange of chloride to solvent upon reduction due to the more labile ferrous species [181].

I wished to examine the behavior of **3** in a non-coordinating solvent (miscible with water) to elucidate the redox properties without any disturbance from chemical follow-up reactions. Therefore, the initial electrochemical investigations were performed in acetone. Square wave voltammetry (SWV) of **3** dissolved in acetone by using a boron-doped diamond (BDD) working electrode revealed three predominant redox events (Figure 4.15a). At -0.27 V *vs.* Fc^+/Fc , a fully reversible redox transition was present that could be assigned as the $\text{Fe}^{\text{III/II}}$ transition of **3**. Electrolytic conductivity of acetone with 1 mM complex ($0.1 \mu\text{Scm}^{-1}$) showed no significant increase compared to that of pure acetone ($0.0 \mu\text{Scm}^{-1}$); therefore, this redox transition could be unequivocally associated with the non-dissociated $[\text{Fe}^{\text{III}}\text{Cl}_2(\text{tia-BAI})]$ form; for comparison, the conductivity of the entirely dissociating TBAP at 1 mM concentration is $152 \mu\text{Scm}^{-1}$ under identical conditions.

Another quasi-reversible oxidation peak was present at $+1.23$ V *vs.* Fc^+/Fc (Figure 4.15a) that could be assigned as a ligand-based $1e^-$ oxidation of **3** since the free tia-BAIH ligand also undergoes oxidation at a somewhat lower potential ($+1.13$ V *vs.* Fc^+/Fc , Fig.4.15c). The i_{net} current at $+1.23$ V correlated with that of the $\text{Fe}^{3+/2+}$ transition, and both were linearly dependent on the complex concentration (Figure 4.15a, inset). These observations suggest that both redox events can be associated with **3** and its consecutive $[\text{Fe}^{\text{II}}\text{Cl}_2(\text{tia-BAI})]^-/[\text{Fe}^{\text{III}}\text{Cl}_2(\text{tia-BAI})]^0/[\text{Fe}^{\text{III}}\text{Cl}_2(\text{tia-BAI}^*)]^{1+}$ oxidation states. Finally, $[\text{Fe}^{\text{III}}\text{Cl}_2(\text{tia-BAI}^*)]^{1+}$ underwent the last oxidation step, which was irreversible and found at $+1.43$ V *vs.* Fc^+/Fc (Figure 4.15a). This transition we tentatively associated with the oxidation of the Fe^{III} - to Fe^{IV} -center, which probably triggers a chemical reaction step involving the chloride ligand.

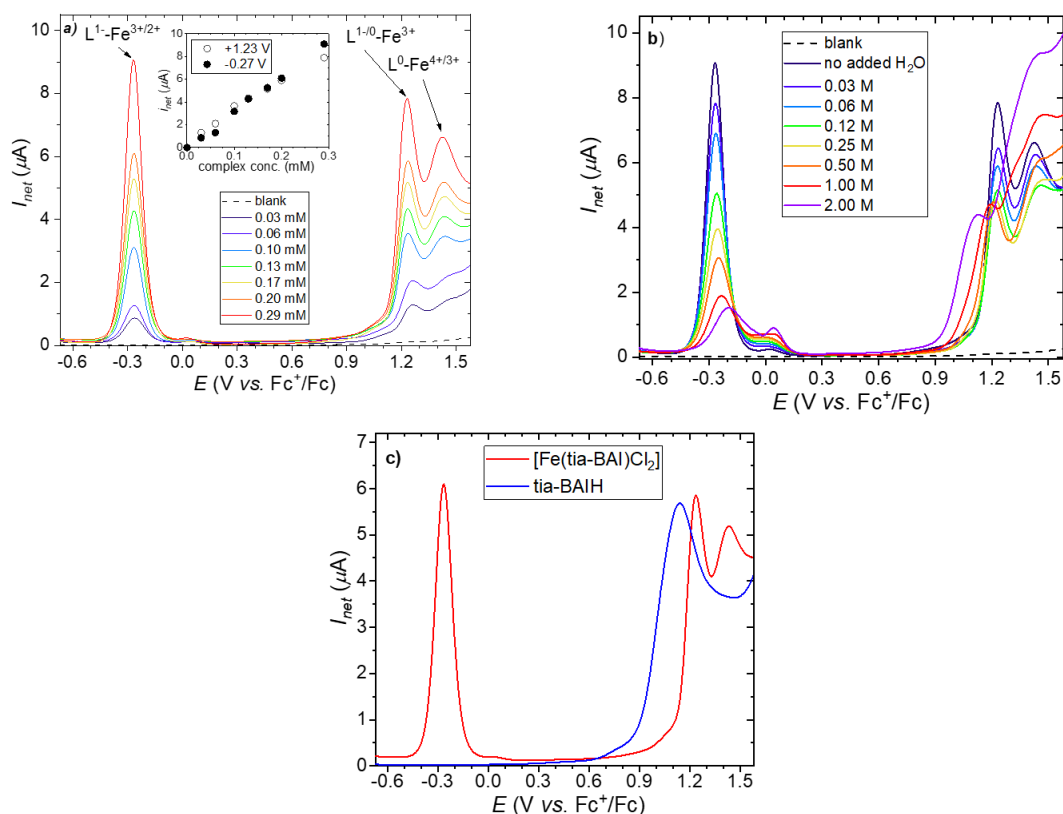


Figure 4.15. (a) SWVs of **3**, dissolved in acetone at different concentrations (L^1 stands for tia-BAl in the assignments of the redox transitions); inset: i_{net} peak currents as a function of complex concentration at -0.27 and +1.23 V vs. Fc^+/Fc ; (b) changes in SWV current peaks upon addition of increasing amounts of water (see the legend) to the solution, $c = 0.29$ mM for **3**. c) SWVs of the tia-BAlH ligand and **3** ($c = 0.2$ mM). WE: BDD, RE: non-aqueous Ag^+/Ag , CE: Pt, Ar atm., 25°C, 0.1 M TBAP, SWV settings: $P_w = 80$ ms ($f = 12.5$ Hz), $P_H = 32$ mV, $S_H = 4$ mV.

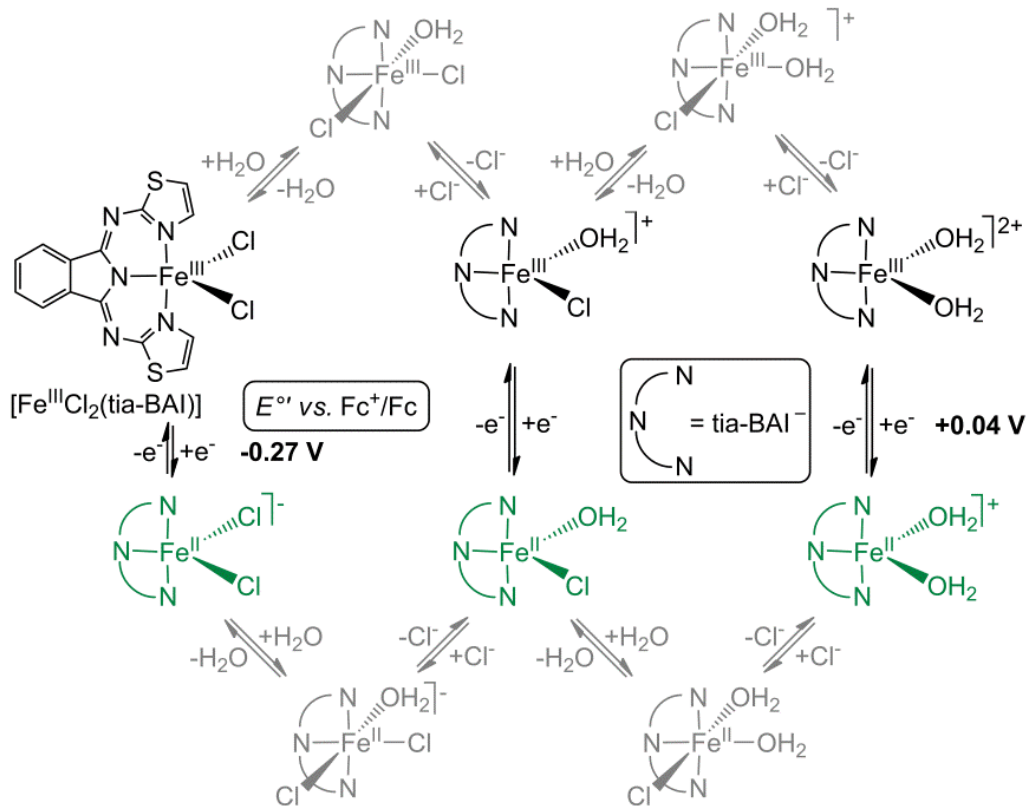
4.2.3. Addition of water to the solution of $[\text{Fe}^{\text{III}}\text{Cl}_2(\text{tia-BAl})]$ in acetone

The above-detailed electrochemical transitions for **3** in acetone suffered fundamental changes when water was added to the solution (Figure 4.15b). All current peaks that were initially present decreased simultaneously as an increasing amount of water were added, roughly up to 0.12 M (Figure 4.15b). A new current peak occurred at above 0 V vs. Fc^+/Fc . The potential (E_{net}) for the new i_{net} current maximum changed with the water/complex ratio. At higher water concentrations (0.12 to 2.0 M), a new current peak could be identified at +0.04 V vs. Fc^+/Fc . Note that increasing the proportion of water to a certain level in the mixture caused slow precipitation of a solid; therefore, investigations were limited to a specific concentration regime. Based on the above

observations, it was assumed that **3** is transformed to $[\text{Fe}^{\text{III}}\text{Cl}(\text{H}_2\text{O})(\text{tia-BAI})]^+$ and $[\text{Fe}^{\text{III}}(\text{H}_2\text{O})_2(\text{tia-BAI})]^{2+}$, or the singly deprotonated $[\text{Fe}^{\text{III}}(\text{OH})(\text{H}_2\text{O})(\text{tia-BAI})]^+$ *via* stepwise Cl^- to H_2O ligand exchange reaction upon addition of water. (The existence of six-coordinate variants with both chloride and aqua ligands could not be excluded. However, the exact evaluation of the solution equilibria and addressing the five- or six-coordinate specification was ambiguous; therefore, in the course of further discussions, only the above assignments are considered for the sake of simplicity. As explained later, from the viewpoint of water oxidation, the absence of chloride and the presence of at least two adjacent coordinated water molecules are the most relevant pieces of information. Although chloride, as an inner-sphere ligand, may have a role in catalysis [229], the investigation of this aspect was beyond the scope of my studies.)

The conductivity of the solution should be sensitive to the presence of ionic species resulting from the proposed ligand exchange. Indeed, when water was added in 3.0 M concentration ($x_{\text{water}} = 0.19$) to the solution of **3** (1 mM), the conductivity increased from 0.1 to $15.6 \mu\text{Scm}^{-1}$ (in contrast, the addition of water to pure acetone caused no change in conductivity). This could be clearly associated with the presence of ionic species, uncoordinated Cl^- , the cationic forms of the aqua complexes, and H_3O^+ that may originate from the acidic proton of the $\text{Fe}^{\text{III}}-\text{OH}_2$ moiety (according to $\text{p}K_a$ values of acetone and water, the latter will be the proton acceptor [230]). However, its value suggested that only a low proportion of Cl^- is dissociated [231] in the ferric state. On the other hand, the complete changes in the $\text{Fe}^{3+/2+}$ current peaks upon water addition in Figure 4.15b indicated that reducing the metal center facilitated ligand exchange and pushed the equilibrium towards aqua-complex formation (Scheme 4.2).

The electronic spectrum of the complex (like the redox transitions detected in SWV) also suffered changes in the presence of added water (Figure 4.16a). In addition to the high-intensity intra-ligand charge transfer (ILCT) bands originating from the $\pi-\pi^*$ transitions of the coordinated BAI at 392, 413, and 441 nm, ligand-to-metal charge transfer (LMCT) bands were also observed above 480 nm with lower intensity. The addition of water resulted in a bathochromic shift in the ILCT bands (solvation); moreover, the LMCT bands were affected, indicating a change in the ligand configuration (the LMCT bands somewhat overlap with the high-intensity ILCT absorptions and therefore occur as the ill-defined shoulder).



Scheme 4.2 Proposed ligand exchange steps leading from $[\text{Fe}^{\text{III}}\text{Cl}_2(\text{tia-BAI})]^{0-}$ to $[\text{Fe}^{\text{III/II}}(\text{H}_2\text{O})_2(\text{tia-BAI})]^{+0}$.

The shift in the isosbestic points (in the vicinity of 420, 440, and 490 nm) indicated the presence of more than two absorbing species in consistency with the proposed $[\text{Fe}^{\text{III}}\text{Cl}(\text{H}_2\text{O})(\text{tia-BAI})]^+$, $[\text{Fe}^{\text{III}}(\text{H}_2\text{O})_2(\text{tia-BAI})]^{2+}$ and/or $[\text{Fe}^{\text{III}}(\text{OH})(\text{H}_2\text{O})(\text{tia-BAI})]^{1+}$ forms in addition to **3**. The addition of the strong acid HClO_4 in the presence of 2 M water in acetone shifted the ILCT bands to lower energy along with some increase in absorbance (Figure 4.16b). The most significant change occurred in the LMCT region around 520 nm as soon as the 1st equiv. of HClO_4 (Figure 4.16b, inset, compare the red and the orange spectra) supporting the occurrence of a $\text{Fe}^{\text{III-L}}$ to $\text{Fe}^{\text{III-LH}}$ protonation step and the associated change in the LMCT band energy. The observations by SWV, electrolytic conductivity, and UV-vis spectrophotometry in a homogeneous solution, the coordination of water to the ferric center can occur *via* the exchange with chloride. Detailed NMR investigations on high-spin five-coordinate Fe^{II} - and Co^{II} -BAI complexes revealed an associative exchange mechanism for the rearrangement of Cl-M-solvent units through a six-coordinate transition state [232]. Accordingly, a similar addition-elimination mechanism can be suggested for

the formation of $[\text{Fe}^{\text{III}}\text{Cl}(\text{H}_2\text{O})(\text{tia-BAI})]^+$ and $[\text{Fe}^{\text{III}}(\text{H}_2\text{O})_2(\text{tia-BAI})]^{2+}$, moreover, for the complex forms involving Fe^{II} (Scheme 4.2).

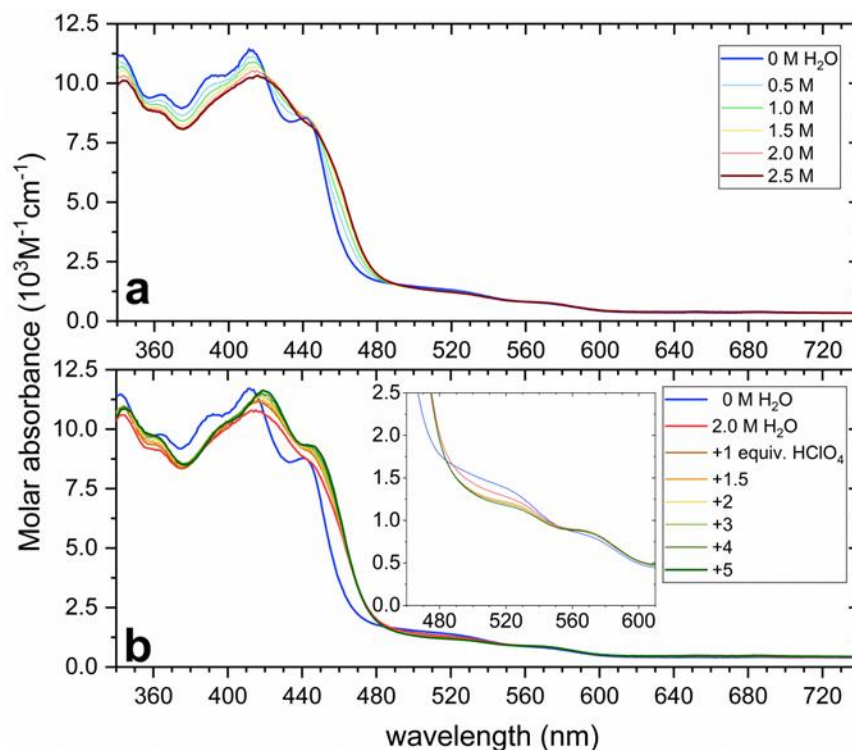


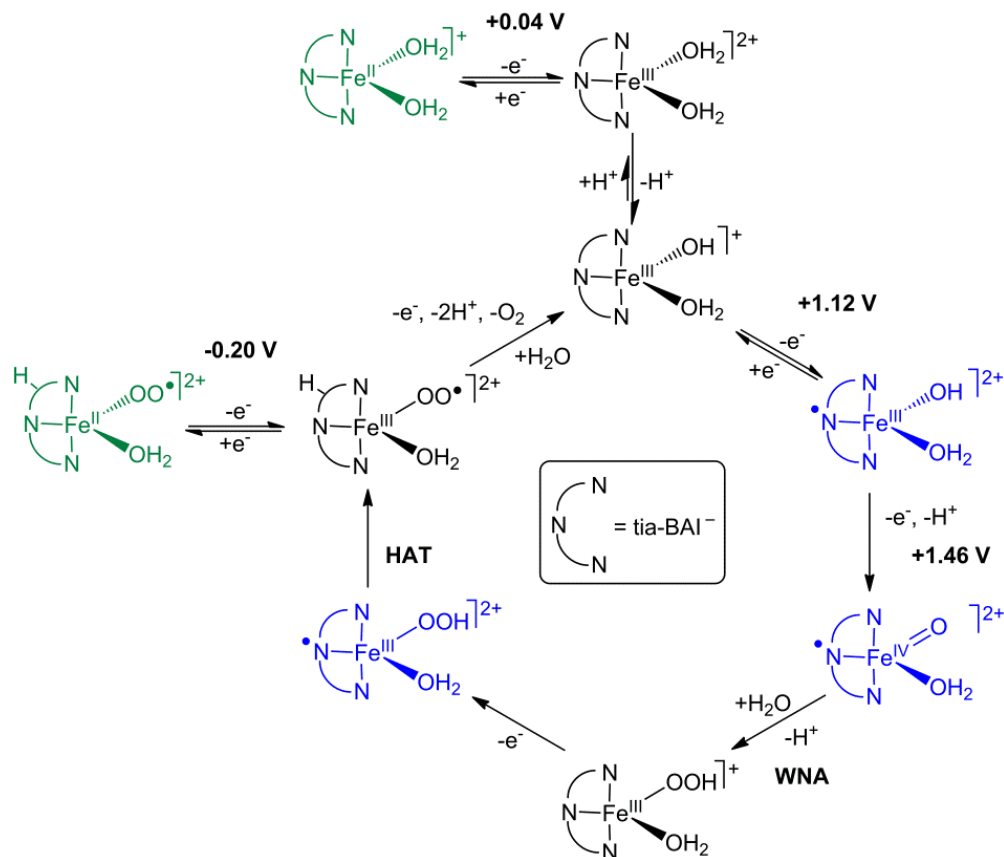
Figure 4.16. (a) UV-visible spectra of **3** in acetone ($l = 1$ cm quartz cuvette) at different concentrations of water; (b) the effect of acid (HClO_4) on the electronic spectrum of the $[\text{Fe}^{\text{III}}\text{Cl}_2(\text{tia-BAI})]^+$ water mixture in acetone (the inset shows the 460-610 nm range magnified). Conditions: $c = 0.2$ mM in 3 mL acetone, 25°C , under air.

4.2.4. Electrocatalytic water oxidation in water/acetone with $[\text{Fe}^{\text{III}}\text{Cl}_2(\text{tia-BAI})]$

The current peaks in SWV at +1.23 V and +1.43 V *vs.* Fc^+/Fc originally present for **3** gradually gave place to new current peaks at +1.12 and +1.46 V *vs.* Fc^+/Fc when water was added to the solution (Figure 4.15b). This could be explained by Cl^- to H_2O ligand exchange (Figure 4.15b). When H_2O is present in higher amounts, it can act as ligand and proton acceptor to furnish predominantly the $[\text{Fe}^{\text{III}}(\text{OH})(\text{H}_2\text{O})(\text{tia-BAI})]^+$ equilibrium form. The current peak at +1.12 *vs.* Fc^+/Fc ($c_{\text{H}_2\text{O}} = 3$ M) thus might come from the ligand-based $1e^-$ oxidation of $[\text{Fe}^{\text{III}}(\text{OH})(\text{H}_2\text{O})(\text{tia-BAI})]^+$ to $[\text{Fe}^{\text{III}}(\text{OH})(\text{H}_2\text{O})(\text{tia-BAI})]^+$ (PCET is also viable for the oxidation of $[\text{Fe}^{\text{III}}(\text{H}_2\text{O})_2(\text{tia-BAI})]^+$ to $[\text{Fe}^{\text{III}}(\text{OH})(\text{H}_2\text{O})(\text{tia-BAI})]^+$). The peak at +1.46 V *vs.* Fc^+/Fc could be associated with subsequent oxidation to $[\text{Fe}^{\text{IV}}(\text{O})(\text{H}_2\text{O})(\text{tia-BAI})]^+$ (Scheme 4.3, on the right).

This species could be thermodynamically competent in the reaction of water nucleophilic attack (WNA). Indeed, cyclic voltammetry in the presence of water revealed a catalytic current at more

positive potentials (*vide infra*, the CVs beyond the +1.3 V potential range of the re-dissolved samples after long term electrolysis producing $[\text{Fe}^{\text{III}}(\text{H}_2\text{O})_2(\text{tia-BAI})]^+$, see section 4.2.2.4, and Fig.4.17). The WNA step, *i.e.*, the chemical reaction between H_2O and $[\text{Fe}^{\text{IV}}(\text{O})(\text{H}_2\text{O})(\text{tia-BAI})]^+$ was proposed to yield $[\text{Fe}^{\text{III}}(\text{OOH})(\text{H}_2\text{O})(\text{tia-BAI})]^+$ by the dissociation of one proton (Scheme 4.3).



Scheme 4.3. Proposed mechanism for the water oxidation electrocatalysis by the $[\text{Fe}^{\text{III}}(\text{H}_2\text{O})_2(\text{tia-BAI})]^+$ active complex form. Intermediates with tia-BAI^- appear in blue. The Fe^{II} -complex in green is the Fe^{II} form of the suspected intermediate detected by CV, as shown in Figure 4.21c (potential values are given vs. Fc).

This step is most likely assisted by H-bonding interaction with the adjacent aqua ligand considering the results of a detailed computational work by Lloret-Fillol *et al.*[216], where the adjacent hydroxide ligand was held responsible for directing the H_2O substrate molecules. By exchanging H_2O to D_2O , a kinetic isotope effect ($\text{KIE} = i_{\text{cat}}^2(\text{H}_2\text{O}) / i_{\text{cat}}^2(\text{D}_2\text{O}) = k_{\text{cat}}(\text{H}_2\text{O}) / k_{\text{cat}}(\text{D}_2\text{O})$) of ~ 1.4 could be estimated based on catalytically enhanced current range ($> +1.3$ V, see Fig.4.17). This KIE value is lower than what we found earlier for **1** exhibiting the proposed ‘ $\text{Fe}^{\text{V}}(\text{O})(\text{OH})$ ’ active species (the KIE was 2.0) [233], and its value indicates a reorganization of the O-H bonds in the

rate-limiting step with bulk water as the proton acceptor [212] (consistently with the proposed WNA step in Scheme 4.3).

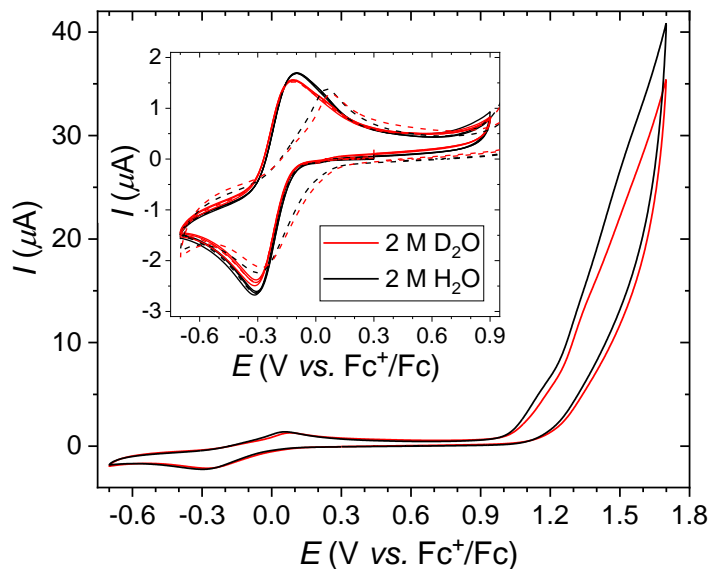


Figure 4.17. Comparison of CVs for **3** in acetone when 2 M of H₂O (black line) or D₂O (red line) is added, inset: CV scans of freshly prepared **3** used in the corresponding experiments (solid lines, *c* = 0.2 mM) and CVs recorded after the addition of H₂O or D₂O (dashed lines, magnified view of the main figure). Setup: BDD working el., non-aqueous Ag⁺/Ag ref. el., Pt counter-el., Ar atm., 25°C, 0.1 M TBAP.

In contrast, KIE was absent for chemically activated catalysts using Ce^{IV} as the oxidant [215]. In the presence of 4N ligands, a Fe^{IV}(O)(μ-O)–Ce^{IV} adduct could be detected, and the Fe^V(O)(OH) active form was generated by an inner sphere electron transfer mechanism [205,214]. This species was suggested to react with H₂O in the rate-determining step resulting in Fe^{III}(OOH)(OH₂); thus, reorganization of the O-H bonds and KIE were minimal [215].

In our case, the further oxidation steps that close the proposed catalytic cycle will be discussed later, considering the heterogenized samples' re-dissolution test and surface analysis. It is to note here that similar results could be achieved in propylene carbonate (PC) or acetonitrile (ACN) solvent since both are miscible with water. However, in the former case, the solubility is lower, while in the latter, the coordination of ACN molecules complicates the analysis of redox transitions.

4.2.5. Drop-casting and characterization of **3** as a solid ad-layer on ITO

The solid pre-catalyst complex is practically insoluble in water fostering its deposition from an organic solvent to ITO/glass and subsequent utilization as an anode for WOC. Simple drop-casting of **1** in methanol was found suitable and convenient to fabricate ad-layers that could be applied in controlled potential electrolysis (CPE) experiments (see also, chapter 3, section 3.4)[52]. Like in our earlier study (Part I), we hypothesized that the self-supporting ad-layer could be formed starting from **3** on ITO, and the exchange of the chloride ligands with solvent molecules observed in water/acetone mixtures could help to graft the catalytic activity of the Fe-(tia-BAI) moieties to the solid electrode-aqueous electrolyte interface.

In the case of **3**, the conductivity of its 1 mM solution in methanol was $83.7 \mu\text{Scm}^{-1}$, indicating the dominance of an ionic Fe^{III} -complex. SWV showed the presence of a single, quasi-reversible $\text{Fe}^{\text{III/II}}$ redox couple at +0.08 V vs. Fc^+/Fc (Figure 4.18). This is similar but not identical to the redox potential found at +0.04 V for the sample re-dissolved from ITO after long term electrolysis (*vide infra*); moreover, what we detected in water/acetone mixtures (Figure 4.15b) and associated with water addition followed by chloride elimination (Scheme 4.2). Therefore, it hints at the existence of a methanol-coordinated complex.

In turn, when copious amounts of water were added to the complex's solution in methanol, the $\text{Fe}^{3+/2+}$ redox couple occurred at +0.04 V vs. Fc^+/Fc (Figure 4.18). This supported the hypothesis of easy access to the aqua-complex in this medium (note that the solvent window of methanol in electrochemistry did not allow investigating the more positive potential region to detect catalysis). Overall, our results suggested that methanol was suitable for DC. According to the solution behavior, the layered crystalline solid from methanol (the SEM pictures are seen in Figure 4.19a) should consist of $[\text{Fe}^{\text{III}}\text{Cl}_{(2-x)}(\text{solvent})_x(\text{tia-BAI})](\text{Cl})_x$ ($x = 1, \text{ or } 2$) species, where H_2O molecules from the aqueous electrolyte can generate the proposed $[\text{Fe}^{\text{III}}(\text{H}_2\text{O})_2(\text{tia-BAI})]^{2+}$ active form. Indeed, this coating was catalytically active and produced O_2 (*vide infra*), while layering from acetone resulted in lower activity, thus underlining the pivotal role of the choice of solvent for DC.

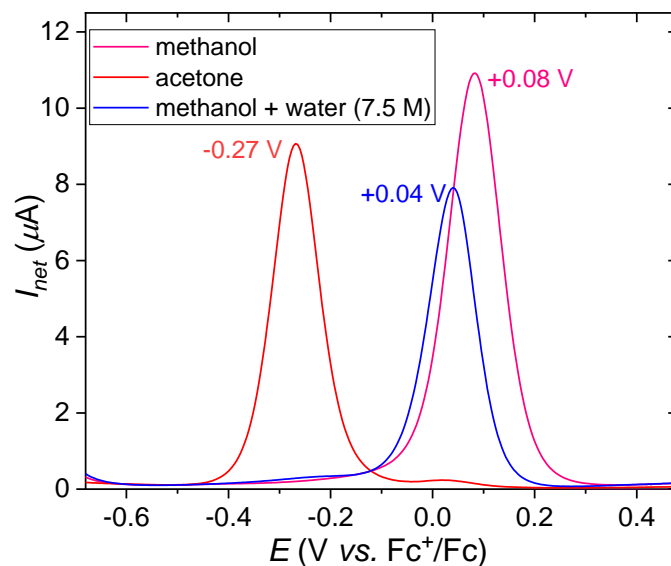


Figure 4.18. SWVs of **3** in acetone (red, $c = 0.29$ mM), methanol (pink, $c = 0.75$ mM) and 3 M water/methanol mixture (blue, $c = 0.75$ mM). WE: BDD, RE: non-aqueous Ag^+/Ag , CE: Pt, Ar atm., 25°C , 0.1 M TBAP, SWV settings: $P_w = 80$ ms ($f = 12.5$ Hz), $P_H = 32$ mV, $S_H = 4$ mV.

The surface morphology of the freshly prepared **3**/ITO electrode ($0.31 \mu\text{mol}$ **3** in $100 \mu\text{L}$ methanol, spread over 2.37 cm^2 ITO, see also chapter 3, Fig. 3.5) was analyzed by SEM, and its composition by EDX (Figure 4.19a) in addition to XPS (see Tables 4.3 and 4.4, and Appendix B, Figs. A4.4 and A4.5). The SEM view of the as-prepared **3**/ITO showed submicron size crystallites attached to the ITO surface in a relatively even distribution.

The SEM picture at $\times 500$ magnification in Figure 4.19a ($50 \mu\text{m}$ scale bar) illustrates a typical arrangement, *i.e.*, areas covered by crystallites directly attached to ITO alternating with thicker, micro-porous layers of crystals (darker patches). The elemental composition by EDX was consistent with the expected presence of C, N, O, S, Cl, and Fe for **3**, or the derived $[\text{Fe}^{\text{III}}\text{Cl}_{2-x}(\text{solvent})_x(\text{tia-BAI})](\text{Cl})_x$ complex and some contribution from In and Si (Fig. 4.19a) originating from the support. The porous structure of the thicker patches was expected to increase the durability of the layer since it might help the O_2 bubbles leaving from the surface.

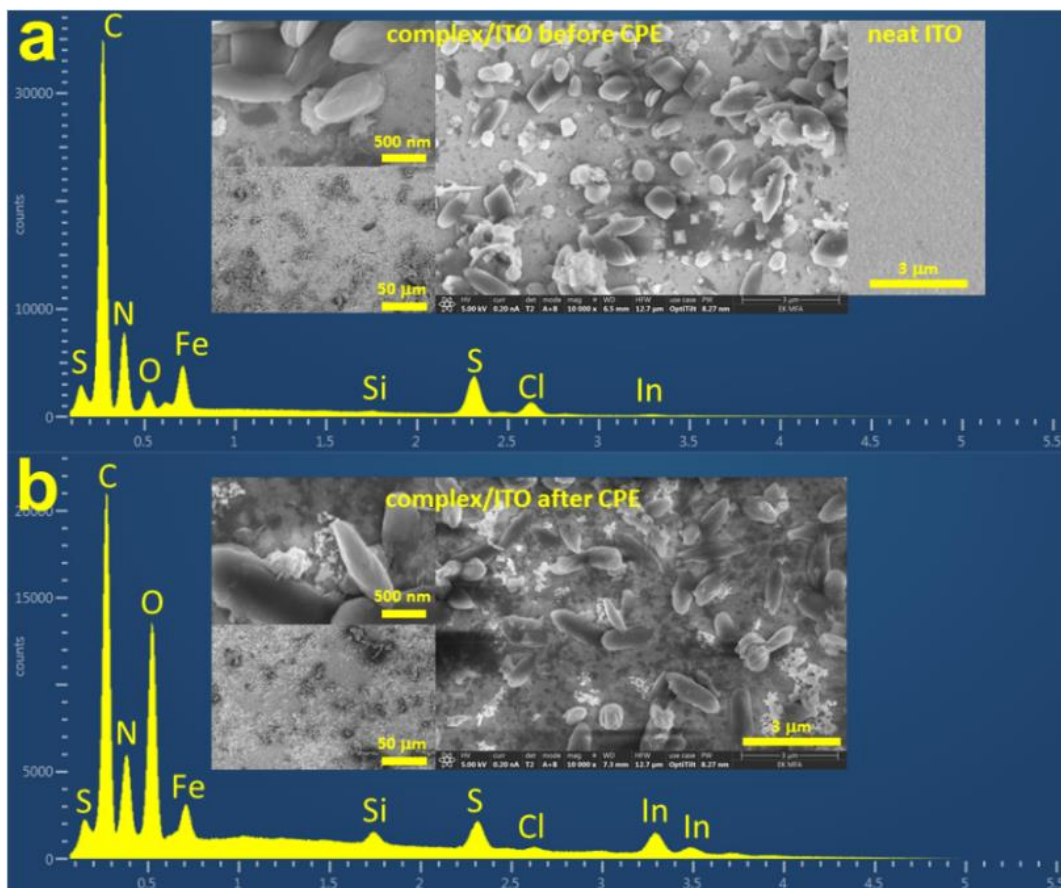


Figure 4.19. (a) EDX spectrum of the as-prepared **3**/ITO ($0.31 \mu\text{mol}$ over 2.37 cm^2), inset: SEM pictures of the sample at $\times 500$, $\times 10,000$, and $\times 50,000$ magnification (and the neat ITO surface at $\times 10,000$); (b) EDX spectrum of the sample after 4.5 h CPE at $+1.4 \text{ V vs. Ag/AgCl}$ in 0.2 M borate buffer (pH 8.3, see Fig. 4.20 and discussion for more details), inset: SEM pictures of the sample at $\times 500$, $\times 10,000$ and $\times 50,000$ magnifications after electrolysis.

The XPS analysis of the as-prepared **3**/ITO sample revealed the chemical composition of the surface layer that can make contact with the liquid phase and was thought to be responsible for electrocatalysis. The surface ratio of the elements (as shown in Table 4.3) confirmed the expected elements for the precursor (Fe, C, N, O, S, and Cl), in addition to Sn and In from ITO. The surface atomic ratios were Fe: C: N: S = 1: 19.5: 5.5: 1.8 (expected, 1: 14: 5: 2 for **3**), indicating that the Fe: tia-BAI ratio is 1: 1, with some excess of C. Although it is tempting to say that excess C originates from methanol molecules coordinated to Fe, XPS likely detected adventitious C. The Fe:Cl ratio was 1.4 (Table 4.3), lower than the expected value of 2 for the original precursor complex. This ratio was indicative of the dissociation of chloride from the coordination sphere and its partial loss.

Table 4.3. XPS surface composition of as-prepared **3**/ITO drop-casted from methanol and the same sample after 4.5 h of CPE at +1.4 V vs. Ag/AgCl.

	surface ratio (at.%)	
	fresh	after CPE
Fe	2.81	2.01
O	12.34	17.15
N	15.53	15.09
C	54.76	53.97
Cl	3.90	0.24
S	5.05	4.86
Sn	0.64	0.68
In	4.97	6.00
<i>N/Fe</i>	5.5	7.5
<i>Cl/Fe</i>	1.4	0.12

Table 4.4. Selected binding energy values from the fitting of XP spectra of a freshly drop-casted **3**/ITO sample and those collected after 4.5 h of CPE at +1.4 V vs. Ag/AgCl in borate buffer at pH 8.3 (in parenthesis). The associated chemical states of the elements are provided.^a

elements / component peak	binding energy (eV)	chemical state
1/ITO		
Fe 2p 1	709.0 (709.6)	Fe ^{III}
Fe 2p 2	711.0 (711.3)	
Fe 2p 3	713.2 (713.0)	
Fe 2p 4	716.4 (716.2)	
Fe 3p	55.6 (55.6)	
N 1s 1	398.9 (399.5)	C=N–C and Fe–N _{hc}

N 1s 2	400.9 (401.1)	C–NH–C
C 1s 1	284.8 (285.4)	
Cl 2p 1	198.5 (198.7)	Cl ⁻
Cl 2p 2	200.1 (200.3)	Cl ⁻
S 2p 1	164.4 (164.9)	S _{tia}
S 2p 2	165.6 (166.1)	S _{tia}

^athe same 3/ITO sample has been analyzed by SEM-EDX, then applied in CPE (Fig. 4.21), and re-analyzed

The Fe 2p peaks exhibited satellite features indicating high-spin Fe^{III} (Appendix B, Fig. A.4.4). The splitting energy, $\Delta = \text{B.E.}(\text{Fe } 2p_{1/2}) - \text{B.E.}(\text{Fe } 2p_{3/2}) = 13.2 \text{ eV}$, was in accordance with a high-spin ferric state with increased spin-orbit coupling [219], or Δ values typically observed for spin-crossover complexes [220,221]. The fitting of the Fe 2p multiplet ('Fe 2p 1-3') and the shake-up satellite ('Fe 2p 4') is illustrated in Figure A.4.4, Appendix B; the selected binding energy data from the fitted component peaks are listed in Table 4.4. The analysis of the Cl 2p peaks (Appendix B, Fig. A.4.4) revealed that only a minor part of the remaining chloride was bound to iron (doublet peaks 'Cl 2p 3-4' in Fig. A.4.4, Appendix B), and the majority of it was uncoordinated (doublet peaks 'Cl 2p 1-2'). This result is in accordance with the outer sphere presence of chloride and the predominance of a $[\text{Fe}^{\text{III}}(\text{solvent})_2(\text{tia-BAI})](\text{Cl})_2$ form.

The N atoms in the ancillary ligand tia-BAI were found in different environments, including uncoordinated exocyclic imine groups (C=N-C) and coordinated heterocyclic donor groups (Fe-N_{hc}). The fitting of the N 1s peak showed two components at 398.9 and 400.9 eV binding energy (Table 4.4. & Fig. A.4.5, Appendix B). The former major component could be assigned as an unresolved mix of the coordinated Fe-N_{hc} donor atoms and the exocyclic C=N-C imine moieties. In metal phthalocyanines (MPc-s), a family of compounds closely related to our complex, it is known that despite their nonequivalence, the 1s core levels of the metal-coordinated and iminic N atoms lie close in energy [234,235]. This typically leads to an unresolved, single N 1s core level peak, like in our case. The minor, blue-shifted peak at ~2 eV higher binding energy could be tentatively associated with some hydrogenated N atoms, based on the DFT calculations by Sarasola *et al.* [235]. This allowed us to presume the occurrence of Fe(tia-BAIH)³⁺ moieties, but a minimal

demetallation of the ligand after its hydrogenation could not be excluded (*vide infra*). The S 2p_{1/2} and S 2p_{3/2} doublet at 164.4 and 165.6 eV, respectively (Appendix B, Fig. A.4.5), were associated with the ligand S_{tia} atoms. According to the presence of a doublet at 167.0 and 168.2 eV (Appendix B, Fig. A.4.5), a small amount of sulfone groups was present, probably formed by the oxidation of the thiazole units at the ITO surface.

4.2.6. Utilization of 3 in water oxidation electrocatalysis as a solid ad-layer on ITO anode

The 3/ITO electrode (0.31 μmol complex spread over 2.37 cm² ITO) was applied in controlled potential electrolysis (CPE) in borate buffer at pH 8.3. The potential was set to +1.4 V vs. Ag/AgCl, the electrolyte was slowly stirred, and the electrolyte containing the counter electrode was connected through a Nafion membrane. Fig. 4.20a shows the current and charge as a function of CPE duration. After an initial drop, the current was steady for *ca.* 1 hour. The ΔQ was ~ 4 C, and bubble formation was continuous in this period. The steady period was followed by a slow drop in the current from 1.7 to 1.2 mA until the stop of CPE after 4.5 hours (the current on plain ITO working electrode was negligible under the same conditions [236]). The evolution of O₂ gas was followed by GC analysis of headspace samples taken after ~ 2 and ~ 4 hours; finally, after stopping CPE (Figure 4.20b, the cell was purged with the air of known composition before CPE). In this experiment, *ca.* 2 cm² of the complex/ITO anode, *i.e.*, 0.26 μmoles of the complex, was immersed into the solution.

After the pass of 24.34 C corresponding to 252 μmoles of electrons (considering a 4e⁻ process and 100% Faraday efficiency, this means 63 μmoles of produced O₂ as theoretical maximum), 50.4 μmol O₂ could be detected by GC from the headspace. Based on GC detection this means an overall turnover number (TON) of 193 and a turnover frequency (TOF) of 0.012 s⁻¹, by 80% Faraday efficiency (Figure 4.20c) at $\eta = 0.86$ V ($\eta = E_{WE} + E(\text{Ag}/\text{AgCl}) - E^\circ(\text{O}_2/\text{H}_2\text{O}) + 0.059\text{pH}$). However, the amount of dissolved O₂ in the electrolyte also increased by 8.9 μmol by the end of CPE (single-point detection before and after CPE by an optical probe [236]), which allowed us to estimate an overall 94% Faraday efficiency, a TON of 228 and a TOF of 0.014 s⁻¹. However, this gave only a lower limit for TON and TOF since not the entire immobilized complex contributed equally to catalysis.

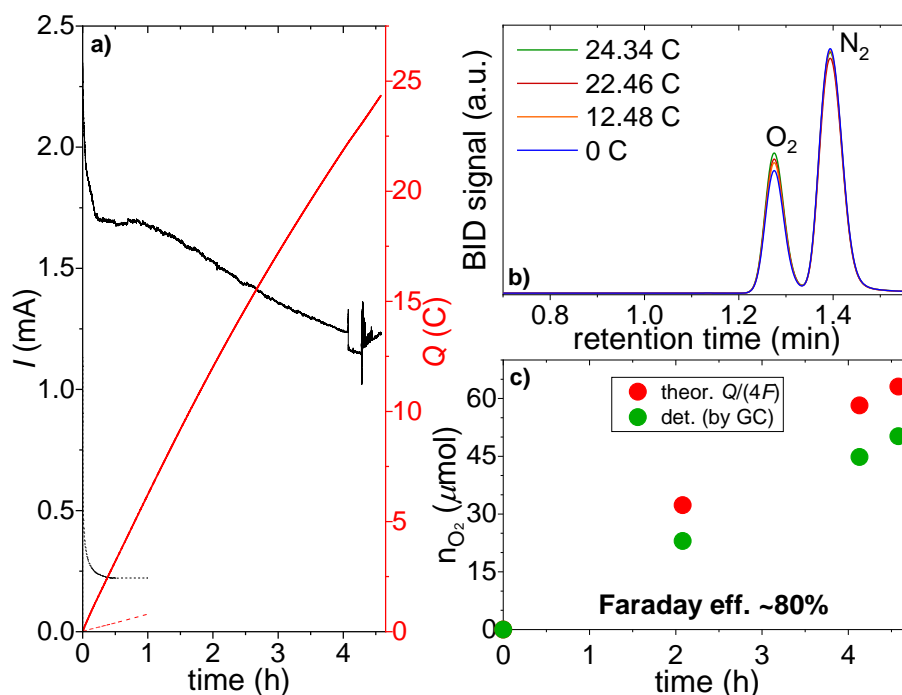


Figure 4.20 (a) Current (black) and charge (red) during controlled potential electrolysis performed at +1.4 V vs. Ag/AgCl for over 4.5 hours in 0.2 M borate buffer, at pH 8.3 by using an ITO working electrode drop-casted with **3** ($0.31 \mu\text{mol}$ over 2.37 cm^2 , $\sim 2 \text{ cm}^2$ was dipped into the electrolyte, dashed lines show the current and charge on pristine ITO), Pt counter electrode separated by a Nafion membrane; (b) gas chromatograms of headspace samples taken at different stages of electrolysis, the peak of O_2 comes first, N_2 second, the cell was filled with the air of known composition; (c) comparison of the theoretical and detected O_2 , for results see the text.

According to the SEM pictures, the surface morphology after CPE showed changes (Fig. 4.19b). Where crystallites remained attached to the ITO surface, areas exhibited similar features on the as-prepared surface. Thicker layers of crystals (darker patches) were also observed, but the original crystallites were missing from some patches. The loss of the crystallites of the catalyst from the ITO support might be partly responsible for the gradual decrease of current in the course of CPE. On the other hand, the composition by EDX (Fig. 4.19b) indicated the almost total absence of Cl^- and an increase in the O-content (along with that of In, which should be the result of the catalyst-free patches). The elemental composition by EDX (Fig. 4.19b) suggested that the outer-sphere counter-ions were almost entirely exchanged from beside the cationic $Fe^{III}(\text{solvent})_2(\text{tia-BAI})$ assemblies. XPS also confirmed that less than 7% of Cl^- remained in the layer, indicating that CPE induced ion exchange in the solid phase.

Interestingly, the proportion and atomic% of elements (C, N, and S) that are characteristic of the tia-BAI ligand barely changed (Table 4.3). This indicated two phenomena, both of which may play an essential role in the course of CPE. First, the lattice energy of the crystalline complex might be supported by strong π -stacking between the tia-BAI ligands that are well-known [237,238], and in our case, it could help stabilize a robust catalyst layer. Second, despite the absence of crystallites in patches (Fig. 4.19b), the unchanged atomic% of C, N, and S in the outermost <3 nm layer (the maximum depth of XPS in our case) indicated the existence of a quasi-monolayer of the complex at the ITO surface. Notably, the atomic% for Fe was lower roughly by 30% than it had been before CPE. We concluded that the primary route of losing the WOC activity should be the leaching of Fe^{3+} ions from the complex, leaving the ligand behind in the solid phase. One more change in the XP spectrum is worth mentioning that may shade the above deactivation mechanism. The blue-shifted peak for the N 1s at 401.1 eV (Table 4.4) associated with hydrogenated N atoms in $\text{Fe}^{\text{III}}(\text{tia-BAIH})^{3+}$ moieties increased in intensity at the expense of the main N 1s peak (Appendix B, Fig. A.4.5). This suggested that demetallation might be induced by a hydrogen atom transfer (HAT) to the ligand as a side-reaction that would be in line with a proposed HAT step of the catalytic mechanism in Scheme 4.3.

A re-dissolution experiment was carried out to analyze the complex layer in more depth after CPE. In this case, CPE was performed in a standard 3-electrode cell at +1.4 V vs. Ag/AgCl, in borate buffer at pH 8.3, with an ITO support drop-casted with 0.35 μmol complex (0.15 $\mu\text{mol}/\text{cm}^2$). Before CPE, a CV scan revealed the $\text{Fe}^{\text{III/II}}$ redox couple for the complex adsorbate at +0.65 V on the anodic and +0.37 V on the cathodic branch, while the onset potential of catalysis occurred at +1.15 V (Fig. 4.21a). (Note that upon multiple scans to turning potentials more negative than the Fe^{III} -to- Fe^{II} reduction, a parallel and proportional decrease occurs in the $\text{Fe}^{\text{III/II}}$ redox peaks and the catalytic current. This indicates that the reduction-oxidation cycle of the iron center accelerates demetallation in the case of the drop-casted complex.)

The duration of CPE was set to ~1.5 h ($\Delta Q \sim 7$ C) to avoid significant demetallation and maximize the chloride dissociation. The 3/ITO was then rinsed with acetone in an ultrasonic bath for 5 minutes. The color of acetone quickly became brownish-yellow, and only a small remnant of the complex coating was visible on the ITO surface. The SWV with a BDD working electrode of the re-dissolved sample ($C_{\text{max}} \sim 0.09$ mM) revealed a single, reversible $\text{Fe}^{\text{III/II}}$ redox transition at +0.04

V vs. Fc^+/Fc (Fig. 4.21b), which matches with the redox peak associated with a proposed $[\text{Fe}^{\text{III}}(\text{H}_2\text{O})_2(\text{tia-BAI})]^{2+}$ in the homogeneous system (Fig. 4.15 and Scheme 4.3).

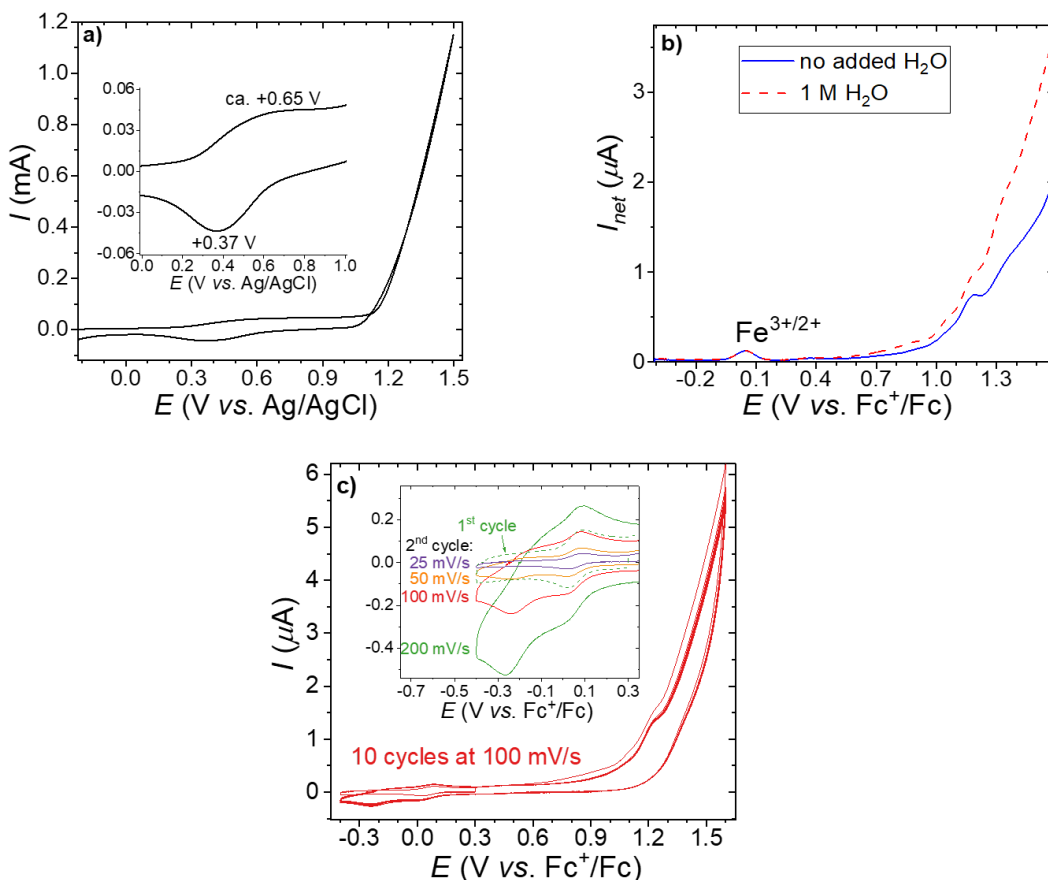


Figure 4.21 (a) First CV scan of **3**/ITO electrode ($0.35 \mu\text{mol}$ complex over 2.37 cm^2 ITO) at 100 mVs^{-1} in 0.2 M borate buffer (pH 8.3), inset: magnified view of the $\text{Fe}^{3+/2+}$ redox couple; (b) SWV of the solid from the same **3**/ITO electrode re-dissolved in acetone after CPE (blue line, $c_{\text{max}} \sim 0.09 \text{ mM}$), and the same sample after addition 1 M of H_2O (dashed red line); (c) CV scans of the same solution as in (b), inset: scan rate dependence of the CV in the potential range of the detected $\text{Fe}^{3+/2+}$ redox couples. Cell setup for (b) and (c): BDD working el., non-aqueous Ag^+/Ag ref. el., Pt counter-el., Ar atm., 25°C , 0.1 M TBAP, SWV settings: $P_w = 80 \text{ ms}$ ($f = 12.5 \text{ Hz}$), $P_H = 32 \text{ mV}$, $S_H = 4 \text{ mV}$.

The current peak at $+1.16 \text{ vs. Fc}^+/\text{Fc}$ and the follow-up wave showed good agreement with the transitions assigned as the ligand-associated $1e^-$ oxidation to $[\text{Fe}^{\text{III}}(\text{OH})(\text{H}_2\text{O})(\text{tia-BAI})]^+$ and concomitant oxidation to $[\text{Fe}^{\text{IV}}(\text{O})(\text{H}_2\text{O})(\text{tia-BAI})]^+$ (Fig. 4.15b and Scheme 4.3). Note that a shoulder preceding the peak at $+1.16 \text{ V}$ indicated the presence of some free ligand and supported our hypothesis of demetallation upon CPE. The addition of water (1 M) to this solution yielded extra current in the electrocatalytic regime (Fig. 4.21b, dashed red curve), thus confirming that the

re-dissolved species was responsible for WOC. The latter fact was also apparent from the multiple-cycle CV recorded at a 100 mVs^{-1} scan rate in the same solution (Fig. 4.21c).

Surprisingly, in addition to the features that were present in the SWV, a reversible redox couple occurred roughly at $-0.2 \text{ V vs. Fc}^+/\text{Fc}$ starting from the 2nd cycle, *i.e.*, after the electrode was polarized through the potential range of electrocatalysis. An enlarged view is shown in the inset of Figure 4.21c of the 1st (dashed green line) and the 2nd cycle of CV recorded at 200 mVs^{-1} (green line). When the scan rate was lower, this reversible feature was absent, and only the $\text{Fe}^{\text{III/II}}$ redox couple could be seen that has been associated with the $[\text{Fe}^{\text{III}}(\text{H}_2\text{O})_2(\text{tia-BAI})]^{2+}$ complex (Figure 4.21c, inset). This suggested that an intermediate species was detected at $-0.2 \text{ V vs. Fc}^+/\text{Fc}$, which was generated in the course of electrocatalysis. Based on its redox potential, we tentatively assigned this transition as the $\text{Fe}^{\text{III/II}}$ redox couple of a proposed intermediate, $[\text{Fe}^{\text{III}}(\text{OO}^\cdot)(\text{H}_2\text{O})(\text{tia-BAIH})]^{2+}$ that might be generated from $[\text{Fe}^{\text{III}}(\text{OOH})(\text{H}_2\text{O})(\text{tia-BAI})]^{2+}$ by a HAT step from the hydroperoxide to one of the uncoordinated iminic N atoms of the tia-BAI ligand, as it is illustrated in Scheme 4.3 (see also the discussion about XPS N 1s binding energy data).

In the proposed mechanism, a concomitant transformation of $[\text{Fe}^{\text{III}}(\text{OO}^\cdot)(\text{H}_2\text{O})(\text{tia-BAIH})]^{2+}$ regenerates $[\text{Fe}^{\text{III}}(\text{H}_2\text{O})_2(\text{tia-BAI})]^{2+}$, thus closing the catalytic cycle with the involvement of an H_2O molecule. We think that detecting a relatively short-lived intermediate was possible because of the depletion of water from the diffusion layer near the BDD electrode. Note that this was only one possible assignment, and further evidence (either experimental or theoretical) would be required to confirm or exclude the existence of the peroxo species.

As a final comment, it has to be noted that upon solvation by water, complex **3** might also rearrange to six-coordinate species, with one Cl^- remaining in the coordination sphere beside the incoming aqua ligands. The five-coordinate $[\text{Fe}^{\text{III}}\text{Cl}(\text{OH}_2)(\text{tia-BAI})]$ could also prevail (Scheme 4.2). Still, the XPS and SEM-EDX result in combination with the electrochemical investigations on the re-dissolved samples after CPE do not support the presence of chloride. The lack of chloride from the used **3**/ITO samples and the single $\text{Fe}^{3+/2+}$ redox peak in SWV (Fig. 4.21b) identical to that resulting from the addition of water to acetone rather suggests $[\text{Fe}^{\text{III}}(\text{H}_2\text{O})_2(\text{tia-BAI})]^{2+}$ as the prevalent species responsible for prolonged water oxidation catalysis.

Part (III)

4.3. Electrodeposition of water-insoluble Fe(III) complexes with pincer ligands as Water Oxidation Catalysts

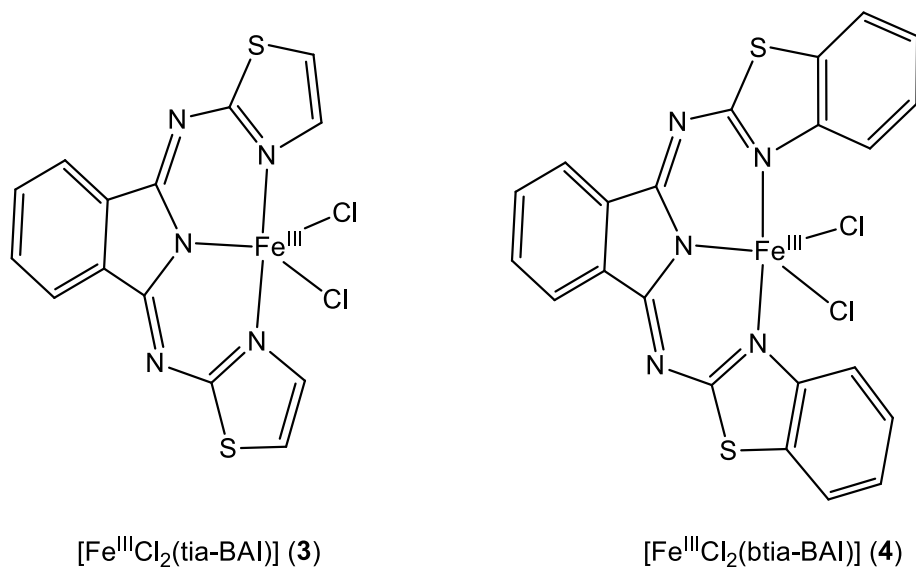
Based on the results from Part II, I decided to investigate further possibilities to immobilize pincer ligand-containing Fe complexes and investigate the influence of the ligand on the WOC activity. I found an immobilization method that was more efficient than deposition techniques such as drop-casting (DC) or dip-coating (DIP) (Chapter 3, section 3.4, for more details). Electrodeposition (ED) methods were used for two Fe(III) complexes prepared with closely related NN’N pincer ligands.

4.3.1. Strategies to enhance the performance of immobilized molecular catalysts

The often-cumbersome covalent grafting of molecular catalysts to electrodes called for other valuable methods to fabricate catalytic films, including DC, DIP, and ED. Relevant strategies focusing on immobilizing the molecular catalysts have become essential. If it can be applied in the case of a specific system, ED can be a desirable method and a unique way to prepare electrodes with functional electrocatalytic properties [163,239–241]. Simplicity, low cost, mild operating conditions, scalability, and manufacturability are common advantages of ED that often warrant robust attachment deposits to the substrate [242]. Moreover, the morphology of the films can also be influenced *via* the applied electrochemical method [164]. Finally, the oxidation state of precursors is an additional option to control the ad-layer formation.

In Part II, the structurally characterized complex **3** [181] has been discussed as a precursor to immobilized ad-layers prepared by simple DC on ITO [178]. This work was inspired by the known coordination chemistry and catalytic oxidation reactions by complexes made with derivatives of tia-BAIH [243–245]. The choice of solvent for the DC of **3** seemed crucial to the OER activity. In addition to the tia-BAI[−] ligand, which warranted good solubility and detailed solution analysis for complex **3** in various organic solvents, other NN’N pincer ligands would be of interest, too. Considering surface deposition, ligand homologs with fused aromatic rings would be desirable to favor surface stability of the ad-layer in the aqueous electrolyte and investigate the ligand oxidation further suggested to play a role in electrocatalytic OER [178]. On the other hand, polycyclics are expected to limit solubility, and thus the effectiveness of the DC technique was found suitable for **3** and some other Fe-complex precursors.

Indeed, we illustrated with the $[\text{Fe}^{\text{III}}\text{Cl}_2(\text{btia-BAI})]$ complex (**4**, $\text{btia-BAI}^- = 1,3\text{-bis}(2'\text{-benzothiazolylimino})\text{isoindolate}(-)$, see Scheme 4.4) [181] the effectiveness of an ED method (section 3.4.2, Fig. 3.3, method **D**) in a case when DC and DIP methods were unsuited to fabricate catalytically active layers due to poor solubility in the obligate solvent mixtures. The layers prepared by ED from complexes **3** and **4** showed better charge transfer properties and stability. Beyond that, ED was the most atom-efficient, additive-free deposition method found so far for this group of compounds. This simple ED method may also represent a viable alternative for other molecular electrocatalysts. Different electrochemical methods were carried out to compare how the deposition method affects the OER performance of the differently fabricated electrodes. The methods (methods A-C) (see chapter 3, section 3.4, Fig. 3.3) were also applied in combination with Nafion, a common additive for the stable deposition of molecular catalysts.



Scheme 4.4. Structure of the BAI⁻ complexes used in Part III.

4.3.2. Structural properties of complexes **3** and **4** and electrodeposition in DCM

Both complexes **3** and **4** were soluble in dichloromethane (DCM), and their electronic absorption spectra were dominated by the very intense intra-ligand charge transfer (ILCT) and the less intense ligand to metal charge transfer (LMCT) bands, as shown in Fig. 4.22a. These features can be related to other known Fe-complexes with BAI ligands [227]. The anionic coordination mode of the BAI ligands was clear from the $\nu(\text{C}=\text{N})$ bands present at 1534 and 1530 cm^{-1} for **3** and **4**, respectively, in the FTIR spectra of the complexes isolated in a pure solid form (Fig. 4.22b) [181,227]. Cyclic

voltammetry revealed a single, fully reversible $\text{Fe}^{\text{III/II}}$ transition at -0.27 V vs. Fc for **3** and $-0.18\text{ V vs. Fc}^+/\text{Fc}$ for **4** (Fig. 4.23a, and the blue SWV inset in Fig. 4.23b), indicating a single complex form in DCM. The zero electrolytic conductivity of the solution ($\sim 0\ \mu\text{S}/\text{cm}$) indicated that no electrolytic dissociation occurred, and the chloride ligands remained coordinated under these conditions maintaining the rigid TBPY-5 geometry around the $\text{Fe}(\text{III})$ center. The difference between the redox potential of **3** and **4** thus can be attributed to the weaker donor strength of the btia-BAI ligand in **4**, since this ligand should force a larger bite angle together with longer $\text{Fe}-\text{N}_{\text{btia}}$ bond distances originating from its steric hindrance.

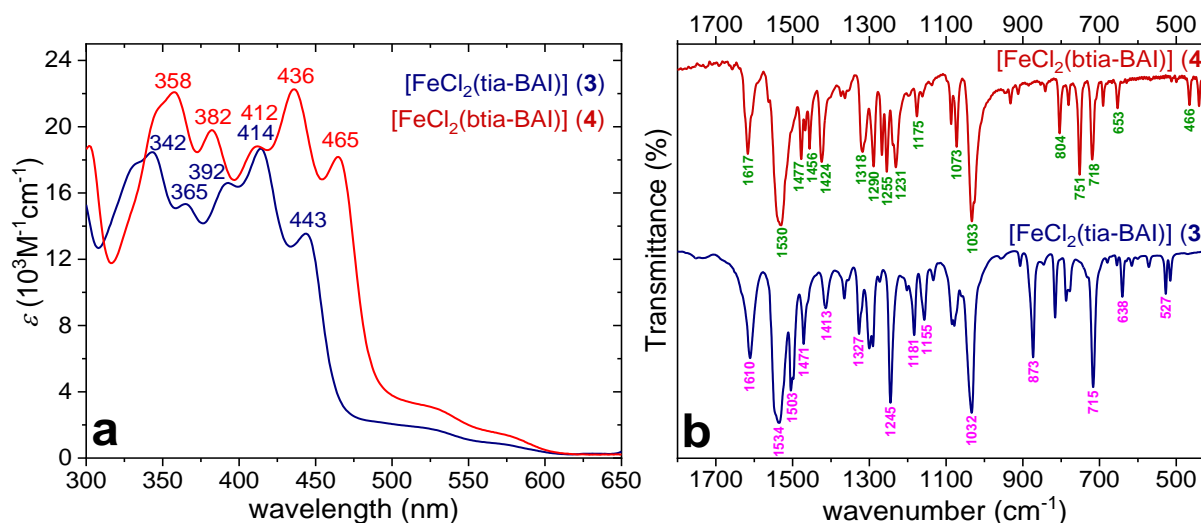


Figure 4.22. (a) UV-visible absorption spectra of **1** and **2** in dry dichloromethane (DCM), the wavelengths for the characteristic ILCT bands are given with numbers; (b) FTIR spectra of **1** and **2** as solid dispersed in KBr pastille.

On the other hand, chloride could dissociate from complex **3**, and eventually, the exchange is traced by the occurrence of new $\text{Fe}^{\text{III/II}}$ redox transitions at more positive potentials in methanol or other organic-aqueous mixtures like water in acetone. This could be exploited to fabricate a self-supported complex at electrode ad-layer that was depleted in Cl^- and showed activity in electrocatalytic OER. The layer made by DC consisted of adsorbed crystallites, in which only some of the complex molecules can participate in catalysis, those, which are close enough to the polarized electrode surface to gain sufficient driving force for the redox events to take place, and at the same time, located near the crystallite surface to get in contact with water molecules. However, in the case of **4**, I could not follow the DC or DIP methods since this compound was practically insoluble in alcohols or other volatile organic solvents that could aid ligand exchange.

I looked for a suitable organic-aqueous mixture that allowed electrochemistry in the presence of water. Since both **3** and **4** were soluble in DCM, a solvent immiscible with water, I added pre-mixed water-acetone aliquots to their solution to achieve a reasonable excess of H₂O in the same phase as the complex (note that under the reaction conditions, drops of an aqueous phase was usually observed on the top of the electrolyte). Cyclic voltammetry (CV) scans of **3** or **4** in DCM mixed with acetone-water were recorded under argon (Figure 4.23a,b, red CVs) using a BDD as a working electrode.

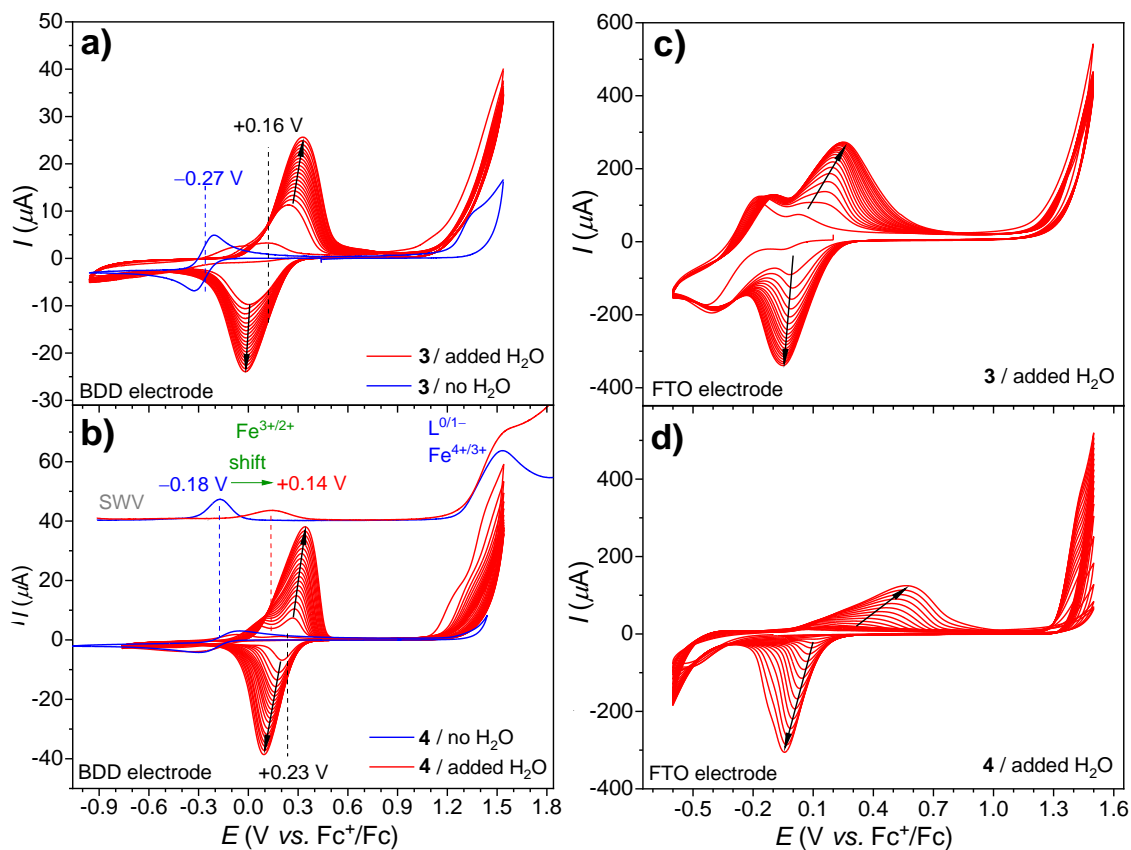


Figure 4.23 (a) CV scans of **3** (0.4 mM) in dry DCM (in blue) or with added H₂O (in red, 3 mmol H₂O in 0.5 mL acetone) on a BDD electrode (0.071 cm²); (b) CV scans of **4** (0.4 mM) under the same conditions as those in (a), inset: SWV showing the potentials of the redox transitions in the two different media; (c) CV scans of complex **3** (0.8 mM) on FTO (1.5 cm²) in DCM with added water (3 mmol of H₂O in 0.5 mL acetone, see also the ED method); (d) CV scans of complex **4** (0.8 mM) under the same conditions as those in (c). Settings: under Ar, $\nu = 100$ mV/s, 20 cycles (red CVs), Pt CE, and Ag⁺/Ag (0.01 M AgNO₃, 0.1 M TBAP/acetonitrile) RE.

Reversible peaks increasing in intensity from cycle to cycle were observed. This behavior indicated the deposition of an electrochemically active compound, while the symmetrical peak shape, a single immobilized isomer with favorable electron transfer kinetics. (Simply immersing the

electrode into the same electrolyte and follow-up CV scan did not show the appearance of the same redox feature. Additionally, when the anodic turning point was lowered below the oxidation starting at +1.1 V vs. Fc⁺/Fc, the increase in the peaks was negligible and reached a maximum after a few cycles, Figure 4.24 below).

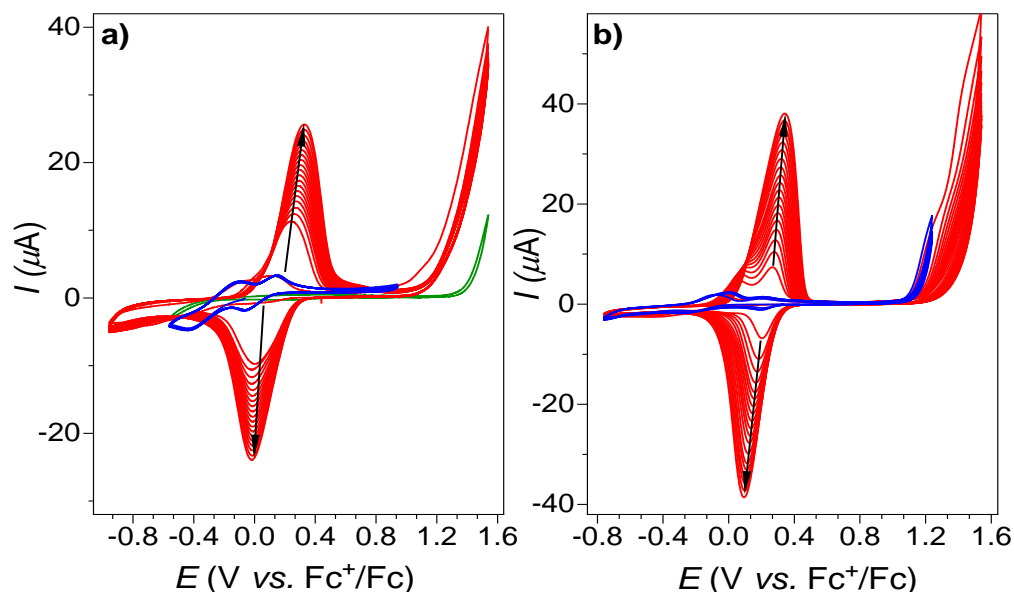


Figure 4.24 (a) CV scans of **3** (0.4 mM) in DCM with added H₂O (3 mmol in 0.5 mL acetone) on a BDD electrode (0.071 cm²); (b) CV scans of **4** (0.4 mM) under the same conditions. Settings: under Ar, $\nu = 100$ mV/s, Pt, and Ag⁺/Ag (0.01 M AgNO₃, 0.1 M TBAP/acetonitrile), as counter, and reference electrodes, respectively. Red curves: 20 cycles in a broader potential range in both cases show that the anodic oxidation above +1.2 V vs. Fc⁺/Fc is required for electrodeposition (compare to the blue CVs, 10 cycles, in a narrower potential range). The green CV was recorded in DCM (10 mL) with added H₂O (3 mmol in 0.5 mL acetone) on a BDD electrode (0.071 cm²) for comparison.

By the 20th cycle, the peak separation was gradually increased, more pronouncedly for **3** (black arrows in Fig. 4.23). At the same time, the capacitive current was nearly unchanged, suggesting a slight increase in the electroactive surface area (see the cathodic branches below -0.5 V in Figs. 4.23a and b). These two facts suggested non-homogeneous deposition yielding unevenly distributed deposits with low specific capacitance. The growing peak separation probably originated from the shifting mean value of the electron transfer constants due to the increasing distance between the deposited compound and the conducting surface with the number of cycles. A plausible morphological explanation would be the thickening of a patchy, non-conducting complex deposit that was indeed observed on ED samples by SEM (section 4.3.2.3).

The half-wave potential, $E_{1/2} = (E_{pa} + E_{pc})/2$ (where E_{pc} is the potential of the cathodic and E_{pa} is the potential of the anodic peak), was found at +0.16 V for the solution made with **3** and +0.23 V vs. Fc⁺/Fc for that of **4** after 20 cycles (black dashed lines in Figs. 4.23a and b). Note that SWV performed on a cleansed BDD electrode revealed a redox transition at +0.14 V for the solution in DCM-acetone-water made with **4** instead of -0.18 V vs. Fc⁺/Fc in dry DCM (Fig. 4.23b, red SWV inset). A similar shift of the reversible Fe^{III/II} potential from -0.27 to +0.04 V vs. Fc⁺/Fc has been associated with chloride-to-aqua ligand substitution in the case of **3** [178], and the same explanation may fit well the anodic potential shift for **4**.

A second, non-symmetrical oxidation peak above +1.5 V vs. Fc⁺/Fc was also apparent in the SWV of **4** in dry DCM (Fig 4.23b, blue SWV) associated with non-separate ligand-based bti-a-BAI[•]/bti-a-BAI⁻ and metal-based Fe^{IV/III} oxidations. Note that the oxidation had been suggested in Part II to generate the (BAI[•])Fe^{IV}=O²⁺ ternary unit that was held responsible for carrying out the water nucleophilic attack (WNA) step [178]. Indeed, when water was present, the catalytic enhancement of this oxidation current was apparent in the case of both complexes (compare blue and red CVs in Fig. 4.23). Finally, based on the excellent match between the $E_{1/2}$ potentials for the product formed by chloride-to-aqua ligand substitution in the homogeneous phase and that of the deposited compound, it was reasonable to conclude that an aqua complex had been deposited starting from **3** or **4**. Efficient ED requires cycling through the anodic potential regime, where the coordinated WOC occurs. Therefore, the participation of a catalytic intermediate occurring only in the close vicinity of the electrode and exhibiting lowered solubility in the applied solvent mixture is likely a scenario for the deposit buildup.

Based on the sharp, reversible, and symmetrical redox peaks for the deposited complex, a single isomeric form was supposed to be present on the surface of BDD. Note that the redox peaks of the chloride precursor complexes were suppressed after the first CV cycles, which might come from a combination of reasons. First, the solution equilibrium produces the aqua complex, and the bulk concentration of **3** and **4** is reduced. However, cycling through the Fe^{III/II} redox transition helps to generate the aqua form by favoring chloride dissociation upon reducing the metal center [178]. This could be clearly seen when the anodic vertex potential was lowered, and only the Fe^{III/II} redox potentials were scanned (Fig. 4.24). However, after deposition commenced, **3** and **4** approached a complex-coated surface that attenuated electron transfer; thus, the redox current was diminished (this also implied that BDD coating should cover the whole surface).

Notably, the same ED method worked on neat or Nafion-coated ITO and FTO electrodes, too. When FTO was immersed in the same mixture as the BDD electrode, a similar redox feature for a surface-adsorbed electroactive species could be observed (Fig. 4.23c and d). The main difference was that the peak separation was greater on FTO (and similarly, on ITO, see Fig. 4.23c and d), mainly due to the anodic shift and broadening of the oxidation current peak, indicating a more sluggish electron transfer kinetics concerning the oxidation of the deposited compound on the oxides compared to that on BDD. This phenomenon was more pronounced for **4** (Fig. 4.23d). As discussed below, these samples from ED experiments were used in a comparison study involving both **3** and **4** immobilized by other methods. Notably, the ED method was reproducible (Fig. 4.25).

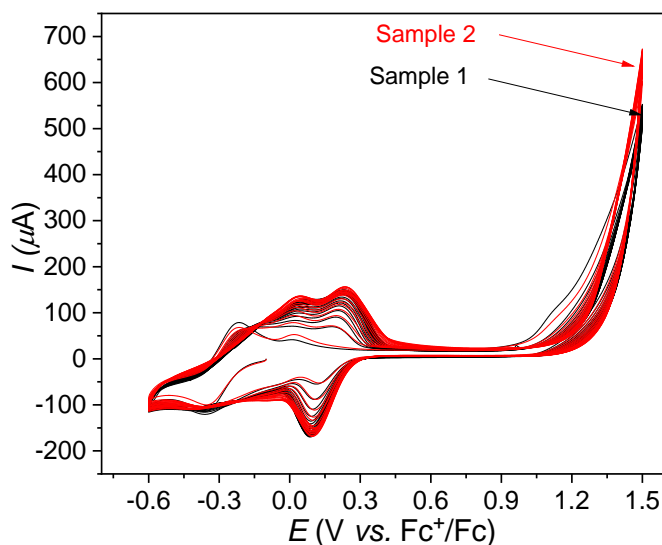


Figure 4.25. Comparison of repeated electrodeposition experiments using complex **3** (0.8 mM) on ITO (1.5 cm²) in DCM with added water (3 mmol in 0.5 mL acetone) illustrates good reproducibility. Settings: under Ar, $\nu=100$ mV/s, 20 cycles, Pt, and Ag⁺/Ag (0.01 M AgNO₃, 0.1 M TBAP/acetonitrile), as counter, and reference electrodes, respectively. See the analogous experiments on FTO in Fig. 4.23c for comparison.

4.3.3. Comparison of the differently immobilized complexes **3** and **4** in water oxidation

The immobilized complexes on ITO, or FTO, were investigated employing linear sweep voltammetry (LSV) at 5 mV/s and electrochemical impedance spectroscopy (EIS). The electrolyte was borate buffer (pH 8.2) since it was found suitable in studies on molecular Fe-based catalysts [178,233]. Its solubility in methanol allowed the addition of **3** to Nafion-coated ITO (or FTO) electrodes by the DC and DIP methods. The same modified surfaces were applied as working electrodes in CA experiments to test their catalytic activity towards the OER (Fig. 4.26a-f,

representative examples). Nafion (Nf) significantly reduced the required amount of complex to create a stable layer on the electrode surface (compared to the DC method discussed in Part II using the complex only, the amount necessary was roughly one order of magnitude lower). The contribution of Nf to the activity was expected to be negligible (indeed, experiments with the DC-Nf/ITO and DIP-Nf/ITO samples made by the DC and DIP methods confirmed this presumption, see Fig. 4.26).

In Fig. 4.26a, LSV curves are shown, where the current density (j , mA/cm²) is plotted against the overpotential ($\eta = E_{WE} - 1.23 + 0.059\text{pH} + E_{ref} - iR$, where $R = R_1$ from EIS). It can be seen that **3**-DC-Nf/ITO was less efficient in the catalysis of OER than **3**-DIP-Nf/ITO (the amount of deployed complex by DIP was calculated from the UV-vis spectroscopic analysis of the complex solution before and after the dipping, suggesting $\Gamma \sim 0.05 \mu\text{mol}/\text{cm}^2$). Tafel plots were constructed from the LSVs (Fig. 4.26b). Slopes were considered at low j to avoid un-subtracted mass-transport contribution [246]. At $j > 10 \mu\text{A}/\text{cm}^2$, the slopes were drastically increased, indicating mass-transport control that may be associated with the inhomogeneous coverage of the electroactive areas by the complex and limited access of water or base to the active sites. With these considerations in mind, the Tafel slope of 68.5(6) mV/dec for **3**-DIP-Nf/ITO would be in tentative consistency with a single-site mechanism and a limiting access of OH⁻ to the active (BAI[•])Fe^{IV}=O²⁺ form [178,246]. However, CA proved that the longer-term stability of this sample was rather poor, and within 15 min, the current was significantly decreased (Fig. 4.26a, inset).

EIS was performed at an overpotential (η) of 0.67 V for all samples to evaluate the electron transfer properties near the OER onset potential for the best performing ED samples, which showed $j \sim 0.1 \text{ mA}/\text{cm}^2$ here. Still, above this current, the Tafel slopes started to increase (Fig. 4.26e). Since I focused on the differences between the ED method compared to others, I adjusted the EIS potential to the ED samples. Electrodes coated with Nf only, *i.e.*, Nf-DC/ITO and Nf-DIP/ITO, were also investigated for reference (Fig. 4.26c). Fig. 4.26c shows the Nyquist plot and fit of the experimental data based on a simple Randles-type equivalent circuit (see inset of Fig. 4.26c) that revealed the smallest charge transfer resistance (R_2) across the electrolyte/electrode interface for **3**-DIP-Nf/ITO (Table 4.1).

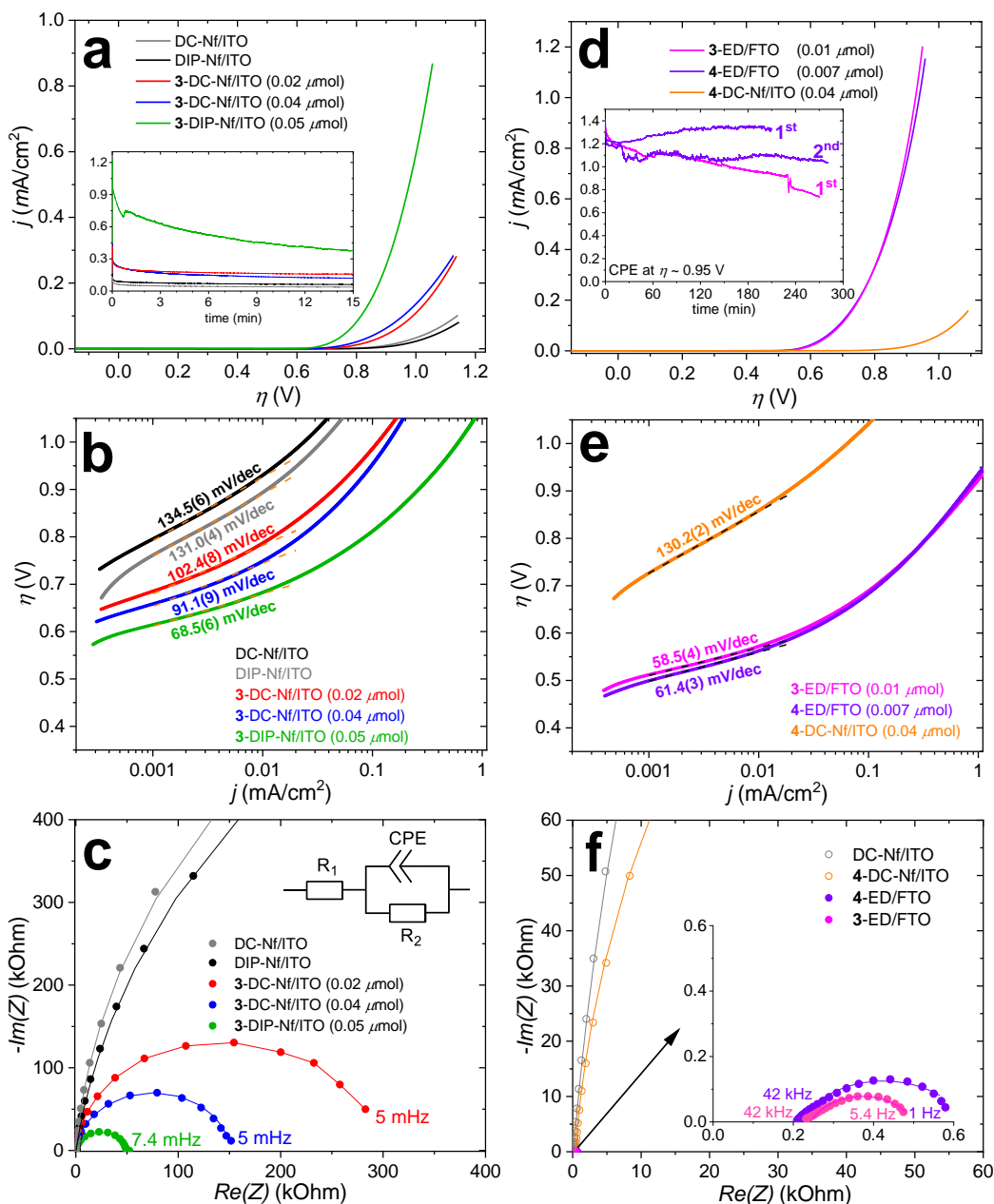


Figure 4.26 (a) LSVs ($\nu = 5$ mV/s) and CPE currents at +1.5 V vs. AgCl/Ag (inset), (b) Tafel plot constructed from LSV, and (c) Nyquist plot (from 200 kHz to as indicated) with fitted equivalent circuits (lines) for complex **3** immobilized by DC or DIP on ITO, and those for the complex-free electrodes. Inset in (c): equivalent circuit for fitting the experimental EIS data, R_1 is the solution + electrode ohmic resistance, R_2 is the charge transfer resistance, and CPE is a constant phase element consisting of a pre-exponential factor P and an exponent (inhomogeneity factor) n ; (d) LSVs of **3** and **4** immobilized by ED, compared to **4** on ITO immobilized by DC. Inset in (d): CPE for the same samples at +1.5 V vs. AgCl/Ag, 1st and 2nd run for the 4-ED@FTO show two consecutive tests with the same electrode; (e) Tafel plot, and (f) Nyquist plot and equivalent circuits (lines) for the same samples as those in (e). Conditions: 0.2 M borate buffer at pH 8.2, Pt auxiliary, and AgCl/Ag reference electrodes.

The lower onset potential observed for **3**-DIP-Nf/ITO with respect to the examined DC samples was in accordance with its smallest Tafel slope and the relatively smaller R_2 . The $n < 1$ value in the CPE component indicated non-ideal behavior due to surface irregularities and complexity in the double-layer structure that could be expected for such combined systems.

Table 4.1 Tafel slopes and fitting parameters of the equivalent circuit to the experimental EIS data.

Sample	Tafel slope (mV/dec)	R_1 (Ω)	R_2 (Ω)	P ($\mu\text{Fs}^{(1-n)}$)	n
3 -DC-Nf/ITO(0.02 μmol)	102.4(8)	61.6(13)	$291(13) \times 10^3$	19.9(4)	0.947(5)
3 -DC-Nf/ITO(0.04 μmol)	91.1(9)	96.4(8)	$151(4) \times 10^3$	19.3(3)	0.952(5)
3 -DIP-Nf/ITO	68.5(6)	121.1(18)	$51(2) \times 10^3$	16.0(4)	0.909(5)
3 -ED/FTO	58.5(4)	242.5(3)	259.5(8)	122.7(6)	0.691(8)
4 -ED/FTO	61.4(3)	211.7(3)	426.5(12)	86.5(3)	0.676(7)
4 -DC-Nf/ITO (0.04 μmol)	130.2(2)	388.6(7)	$53(9) \times 10^3$	21.3(2)	0.964(10)

a Pre-exponential factor P represents a 'non-ideal capacity' for CPE. b 'Ideality factor' ranging from 0 to 1. For details, see the corresponding paragraph in chapter 3, section 3.3.

In sharp contrast to the previously discussed samples, those made by ED (see Figs. 4.23c and d), *i.e.*, **3**-ED/FTO and **4**-ED/FTO, showed distinctly better performance in the OER. Moreover, this method worked equally well for both complexes. The presence of Nf did not cause any notable difference in the OER; therefore, the latter combinations will not be discussed hereafter. Figure 4.26d shows the almost identical LSVs of **3**-ED/FTO and **4**-ED/FTO. A drop-casted sample, **4**-DC-Nf/ITO, was also prepared despite its insolubility in methanol. The recorded LSV is shown in Fig. 4.26d in red, as a contrast to the ED samples. In this case, the LSV current and the other parameters in Fig. 4.26 were identical to those of the DC-Nf/ITO that was prepared without the complex. This clearly showed that complexes insoluble in methanol were unsuitable for the DC method since the ligand exchange reaction to provide the catalytically active form could be complete only in homogeneous precursor solutions but not in a suspension.

The Tafel plot in Fig. 4.26e revealed similar slopes for the electrodes modified by ED compared to that of **3**-DIP-Nf/ITO (Table 4.1). However, at lower overpotential, roughly by 0.1 V. This can be attributed to the more favorable reaction conditions for OER at the reaction centers formed by the ED method. The relatively small charge transfer resistance (R_2) for the **3**-ED/FTO and **4**-ED/FTO were also consistent with this explanation (Fig. 4.26f and Table 4.1).

CPE was performed for several hours to investigate the electrochemical stability and Faradaic efficiency of the modified electrodes. The current vs. time plots at +1.5 V vs. Ag/AgCl ($\eta = 0.95$ V) are shown as inset in Fig. 4.26d. The complex-free Nf-DC/ITO or FTO electrodes exhibited minimal current at this potential (inset of Fig 4.26a). When **4**-ED/FTO was applied as the working electrode, the reaction was stopped after 3.5 h (the 1st run in the inset of Fig. 4.26d), a sample was taken from the headspace, and the evolved O₂ gas was quantified by gas chromatography (for technical details see the chapter 3 and earlier publications [178,233,247]). The overall passed charge was 16.4 C; thus, the theoretical maximum for O₂ was 42.4 μmol ($n = Q/4F$). The produced O₂ was 35.2 μmol , corresponding to a Faradaic efficiency of 83% compared to **3** in the earlier study [178]. Based on the detected O₂, the turnover number (TON) within 3.5 h of electrolysis at $\eta = 0.95$ V is over 5,000, corresponding to a TOF of 0.4 s⁻¹ that indicates good stability especially considering the simplicity of the system. More so, since the sample could be re-used in a new buffer solution in a follow-up CPE experiment for 4.5 h without a noticeable decrease in the current. Note that **3**-ED/FTO containing the tia-BAI ligand (instead of the btia-BAI of **4**) showed over 40% decrease of the initial current (Fig. 4.26d, inset) that was attributed to the partial release of the complex from the surface (and depletion of Fe, as mentioned in Part II). This underlines the advantage of hydrophobic ligand extensions during the design of future catalytic complexes.

4.3.4. Post-catalytic analysis of the ED samples by SEM-EDX

Following their use, in the electrocatalytic OER experiments, the **3**-ED/FTO and **4**-ED/FTO electrodes were investigated by SEM, and the elemental composition was also analyzed by EDX (Figures 4.27a and 4.28a). In the SEM images, the FTO surface is covered by a solid material in patches of random morphology but in even relative distribution on a few hundred μm scale (Figs. 4.27a and 4.28a). The average composition by EDX confirmed the presence of the expected Sn, O, and F for the substrate; however, the peak of F overlapped with that of Fe from the complex, as indicated in Spectrum 7 (EDX inset in Figure 4.28a). The elemental composition of complexes **3** and **4** were also recognizable in the EDX spectra, but Cl was absent. However, the large, bare FTO areas suppressed the C, N, Fe, and S peaks. To gain more information about the composition and morphology of the patches, smaller regions were analyzed by SEM (Figs. 4.27b-c and 4.28b-c), and EDX spectra were collected from selected spots (Spectrum 2 in Fig. 4.27a and Spectrum 10 in Fig. 4.28a). The elemental composition at these spots suggested that the main components are C, N, S, and Fe, but Cl was still absent.

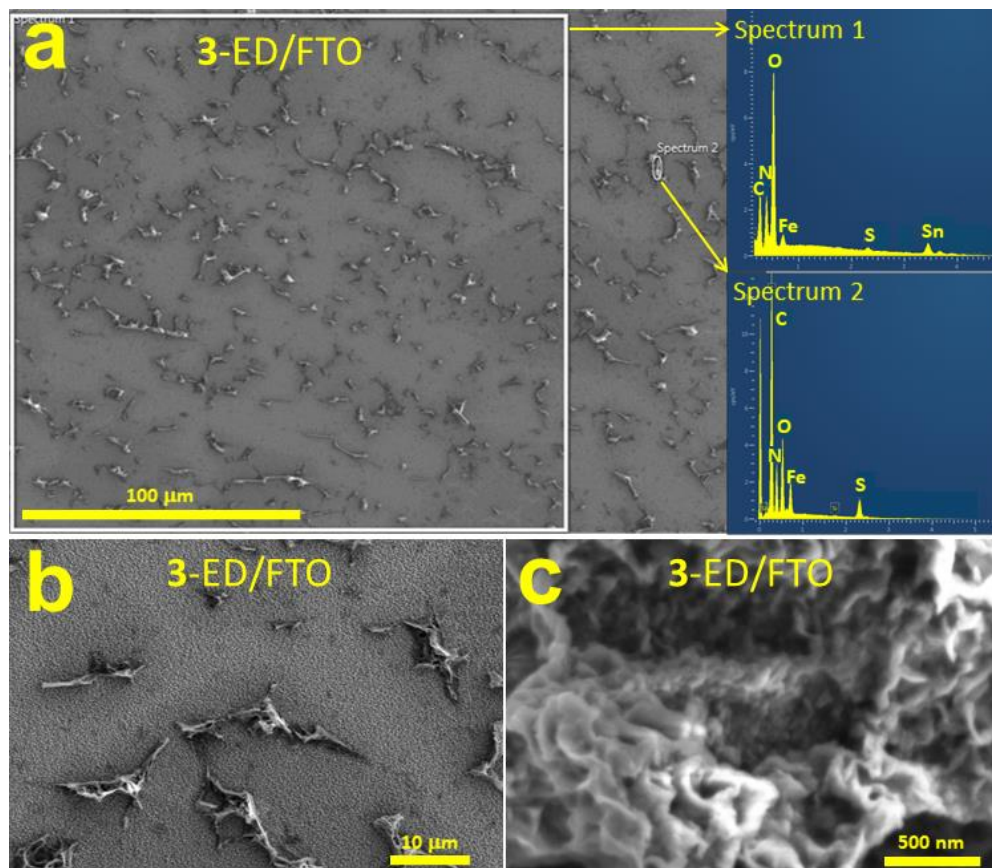


Figure 4.27. (a) SEM image at $\times 500$ magnification of **3-ED/FTO** after 4.5 h of CA at +1.5 V vs. Ag/AgCl in 0.2 M borate buffer at pH 8.2, inset: EDX spectrum of the area in the white frame (Spectrum 1), and from a small spot (Spectrum 2); (b) SEM images at $\times 2,000$; and (c) at $\times 50,000$ magnification (see Fig. 1 and Fig. 3c for further information on this sample).

Note that sulfur is a crucial signature element to the presence of the BAI ligands. The elemental composition is thus concurring with the presence of Fe(tia-BAI) assemblies derived from **3** (the same applies to the presence of Fe(btia-BAI) assemblies in the case of **4-ED/FTO**). SEM-EDX investigations on as-prepared samples revealed similar morphological features and elemental composition to those of the used samples (see Figs. A.4.6 and A.4.7, the analogous SEM-EDX results for **3-ED/ITO** and **4-ED/ITO** are shown in Fig. A.4.8).

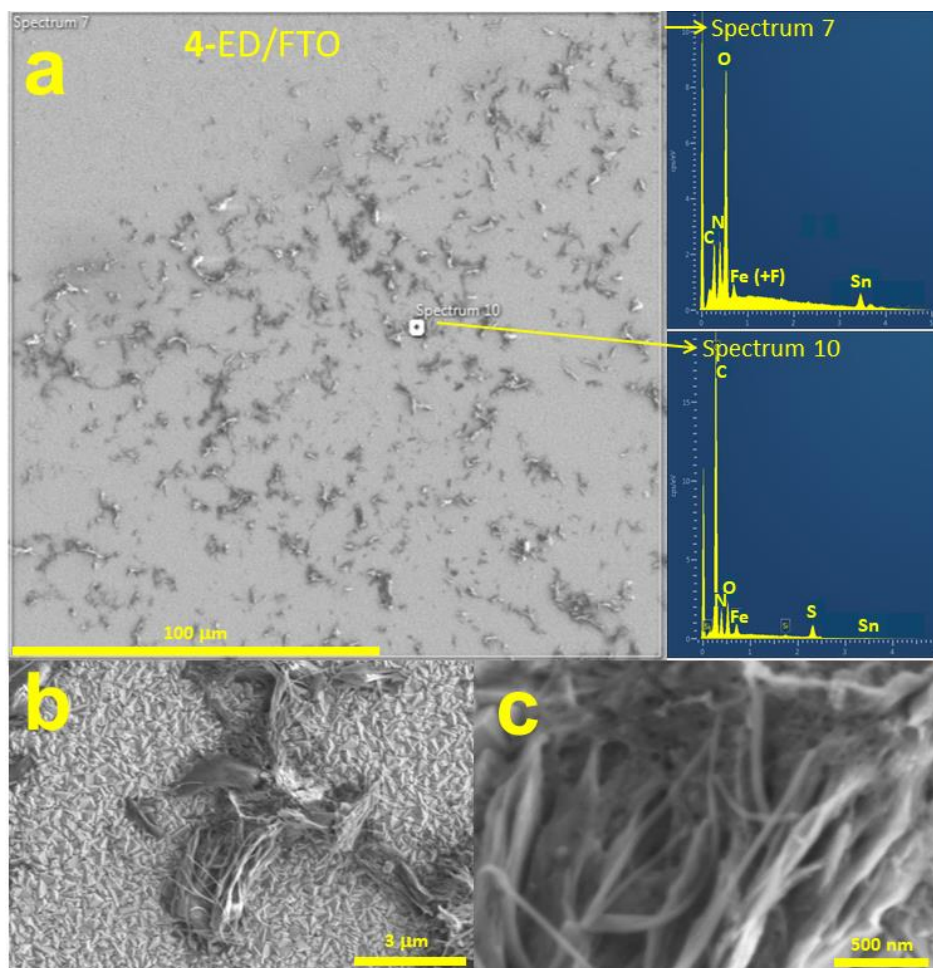


Figure 4.28. (a) SEM image at $\times 500$ magnification of **4-ED/FTO** after 8 h of CA at +1.5 V vs. Ag/AgCl in 0.2 M borate buffer at pH 8.2, inset: EDX spectrum of the area in the white frame (Spectrum 7, and from a small spot (Spectrum 10)); (b) SEM image at $\times 10,000$; and (c) at $\times 50,000$ magnification (see Fig. 1 and Fig. 3d for further information on this sample).

Morphology analysis at larger magnification revealed differences in the fine structures of the two electrodes. In the case of **3-ED/FTO**, typically coral-like deposits could be observed with a scabrous surface (Fig. 4.27c), while the formations on the surface of **4-ED/FTO** entangled fibers were seen (Fig. 4.28c). These differences indicated that the ligand structure has a determinant role in the nanoscale structure of the electrodeposited compounds. Our results suggest that electrolysis does not significantly affect the morphology and elemental composition. However, one must consider the possible effect of drying on the morphology as the original state of the deposit can be altered due to surface tension effects associated with solvent removal (either after the ED treatment or after CA).

5. Conclusions and outlook

Water splitting and fuel cells are technologies that will significantly determine the utilization, conversion, and chemical storage of solar power. Both can be carbon-neutral if operated by solar energy. In water-splitting, water oxidation to O₂ produces electrons and protons for the reduction reaction: proton reduction, to produce H₂, or CO₂ reduction, to generate carbon-based fuels.

Catalysts are vital for efficient oxidation and reduction reactions, ideally facilitating high reaction rates at low kinetic overpotential. In this context, the water oxidation reaction to produce O₂ remains a challenge. Significant efforts have been made to develop homogeneous and heterogeneous catalysts for water oxidation in the past decade. Systematic structural modifications of molecular complexes such as introducing electron-donating or withdrawing substituents on the backbone of the ligand, building protecting groups at locations prone to degradation, and developments in immobilization methods resulted in actual progress in this field.

According to the aims of my Ph.D. dissertation, I joined this field by utilizing ancillary ligands that appeared suitable to promote the immobilization of Fe complexes on various electrode surfaces by exploiting simply secondary interactions instead of covalent linkage. In the following, I highlighted the new scientific findings based on my work and contributed to the progress of the field.

In the first study, two Fe(II) complexes, **1** and **2**, containing non-symmetric, bidentate heterocyclic ligands were examined in electrocatalytic water oxidation as catalyst candidates. The working hypothesis was that two labile coordination sites at *cis*-positions would be available in the presence of the NN' ligands to favor small molecule binding and transformation. It was revealed that complex **2** was hydrolytically unstable in the presence of water, while complex **1** was a relatively robust catalyst both in a homogeneous phase or immobilized on the oxide semiconductor ITO. This could be attributed to the electron-withdrawing nature of O in PBO applied in complex **2**, compared with NH in PBI in complex **1**. *It was demonstrated for the first time that the non-coordinated heteroatoms (or groups) of heterocyclic ligands sufficiently electron-donating to support higher oxidation states of the Fe center could support water oxidation catalysis (Chapter4, Part I).*

Consequently, complex **1** deposited as a solid on ITO (in contrast to **2**) was suitable for longer-term electrocatalysis to produce O₂ without apparent decomposition of the catalyst layer. The kinetic study of complex **1** in homogeneous water/MeCN mixtures indicated a single-site mechanism involving a WNA rate-limiting step. *The catalytically active form of complex 1*

generated by ligand exchange allowing the coordination of two H₂O molecules in cis-positions, followed a WNA mechanism and determined the effectiveness of the immobilized catalyst. It can be clearly concluded that the ancillary ligand controls the favorable geometry, while the applied solvent strongly influences the exchange (Chapter4, Part I).

The work was continued with a Fe^{III} dichloride complex utilizing a heterocyclic pincer ligand, which served as a precursor to the true electrocatalyst, an aqua-complex. Adjacent, labile sites were shown to favor H₂O binding and WOC in the presence of 4N and NN' ligands. In contrast, the tia-BAIH ligand was a rigid, meridional one, so the question emerged about how this configuration would influence catalysis. In addition, due to its easy synthesis, a dichloride precursor has been applied in this case. The electrochemical studies on **3** in homogeneous water/acetone mixture revealed the signatures of Cl⁻ to H₂O ligand exchange, and a molecular mechanism could be proposed for the catalytic cycle. *For the first time, it was shown that the NN'N pincer ligands could behave as redox-active compounds and carry a single electron vacancy stabilized by an extended π -delocalization, thus generating the catalytically active [Fe^{IV}(O)(H₂O)(tia-BAI)]²⁺(Chapter4, Part II).* It was also presumed that it played a role in proton channeling in the course of the follow-up reaction steps (peroxide formation). It has to be underlined that *considering the single-site WNA mechanism and the importance of ligand exchange, the same postulations can be made for the NN' complex I.*

The complex could be grafted to ITO as a model anode from methanol. This solvent promoted ligand exchange in the precursor, thus creating a catalytically active, solid ad-layer. *The solvent effect is more pronounced in the case of the NN'N ligand scaffold. Hence, deciding which solvent to use for drop-casting can be essential for gaining an active immobilized catalyst (Chapter4, Part II).* The water-insolubility of the complex that stems from the coordinated tia-BAI⁻ ligand supported surface attachment and left open sites necessary for WOC; thus, this complex design was found suitable for new molecular catalyst/(photo)anode hybrids. The route of catalyst deactivation appeared to be the demetallation of the complex. The water-insoluble ancillary ligand remained at the electrode, indicating its strong attachment to the surface. *These results confirmed that water-insoluble Fe complexes utilizing hydrophobic ancillary ligands with a two-way effect, i.e., control of the complex stability in the course of catalysis and strong attachment to the surface by secondary interactions, represent a viable general strategy to fabricate molecular catalyst/anode hybrids (Chapter4, Part I, II, III).*

Finally, practically insoluble complexes (as complex 4) in alcohols or other volatile organic solvents make it inconceivable to follow the DC or DIP methods since this strategy could aid ligand exchange; thus, techniques like electrodeposition (ED) were required. Therefore, it was introduced that the simple ED method was a new method that allowed immobilizing $[Fe^{III}Cl_2(BAI)]$ precursors bearing aromatic NN'N pincer ligands from a suitable water/organic mixture (Chapter4, Part III).

The process involved the loss of inner-sphere chlorides leading to the formation of the electrocatalytically active surface deposits. ED presented advantages over DC or DIP of the **3** with Nafion in terms of overpotential and better charge transfer properties. ED also allowed reducing the amount of complex required for long-term operando stability. In the case of **3**, this amount by ED was an order of magnitude lower compared to the self-supported system (prepared by DC of **3** from methanol).

Moreover, for $[Fe^{III}Cl_2(btia-BAI)]$ (**4**), which was practically insoluble in alcohols, making it unsuitable for DC, the ED operated just as well, resulting in a very stable complex-electrode combination that was able to produce O_2 by TON of >5,000 in borate buffer at pH 8.2. The case of complex **4** with the fused aromatic rings in the ligand, aiming at water-insolubility and better surface affinity, illustrates that ED may be a practical immobilization method, even in the case of precursors soluble only in solvents that are practically immiscible with water. **Most importantly, the extension of the molecular structure of the Fe complex by introducing aromatic groups on the periphery of the NN'N polycyclic pincer ligands increases the surface stability of electrodeposited samples.**

Further work with complexes is a strategy that can lead to the atom-efficient and morphology-preserving fabrication of active catalysts at the surface of semiconductors to overcome the sluggish interfacial kinetics and enhance the efficiency of (PEC) water oxidation. Based on literature reviews and results from this work, the development of new and efficient molecular WOCs based on first-row transition metals such as iron is demanded. The utilization of these abundant metals would solve the problem that originates from the scarcity of noble metals if we aim to utilize water splitting on a broader scale. In my dissertation, successful candidates of Fe complexes as molecular catalysts have demonstrated that redox-active ancillary ligands can assist metal centers in obtaining the reactive form. While the stability of the electrodeposited Fe(btia-BAI) complex is remarkable, and to our knowledge, no similar system has been published before; its practical use would be an

unrealistic goal. Despite the new accomplishments, catalysts that can operate at low overpotentials with high catalytic rates and remain stable for tens of thousands of hours are still lacking.

On the other hand, further enhancing the efficiency of molecular WOCs can help better comprehend the details of the reaction mechanism, particularly the catalytically active species, and the rate-determining step. The WOC catalysis presented in this work is also a first step in developing new hybrid co-catalyst/semiconductor systems, where the role of the co-catalyst candidates is to enhance the efficiency of the wished chemical reaction, in our case, water oxidation. According to the current trends, smart nanostructures are appealing to tune the light-harvesting, charge transport, and e^- -transfer properties of semiconductors. However, such nanostructures can be sensitive to post-treatments. The water-insoluble complexes ensure that the metal ion content remains at the surface, and the immobilization does not require complicated or harsh thermal treatment methods that jeopardize the semiconductor's efficiency. The decomposition mechanism of a molecular unit under dark conditions is an essential piece of knowledge prior to any further application. Hence, the focus of my dissertation was placed on effective co-catalyst/semiconductor coupling strategies. The outlook of my work includes the direct utilization of the presented Fe complexes in PEC systems and investigating the real catalytic role or precursor nature of the molecular units under operando conditions. Whichever scenario happens, the applied ancillary ligands are thought to warrant that the metal content will be very efficiently distributed as part of the real co-catalyst on the surface. Therefore, the immobilized complexes discussed above may open new avenues toward novel systems.

6. Scientific results and thesis points

The results of my work are summarized in the following thesis points concerning the ultimate objective of finding Fe-based molecular catalysts for the oxygen-evolving reaction (OER, or water oxidation). I selected known Fe complexes containing non-symmetric NN' bidentate (complexes **1** and **2**) or NN'N pincer ligands (complexes **3** and **4**) and utilized those candidates successfully in water oxidation electrocatalysis as a new application.

1. I demonstrated for the first time that the non-coordinated heteroatoms (or groups) of non-symmetric bidentate heterocyclic ligands sufficiently electron-donating to support higher oxidation states of the Fe center could support water oxidation catalysis.

The strikingly different redox behavior caused by two different, non-symmetrical, heterocyclic bidentate ligands with analog structures and NN' binding mode in the two corresponding complexes highlights a determinant electronic effect of the non-coordinated heteroatoms. The relative electron-withdrawing nature of O in PBO compared with NH in PBI makes the PBI ligand a stronger donor. Therefore, the replacement of a non-coordinated O-atom in the ligand heterocycle (complex **2**) with an NH group (complex **1**) enhances the redox stability. Specifically, oxidation products occurring upon water oxidation catalysis are expectedly degradation-prone in the presence of a weaker donor ancillary ligand like PBO. This leads to a non-homogeneous behavior of **2** in water/acetonitrile, moreover, mineralization of the deposited complex on the ITO surface. Complex **1**, on the other hand, is an efficient precursor to an Fe(PBI)₂ assembly-based molecular catalysis.

2. I confirmed that the catalytically active form involved in water oxidation is generated by ligand exchange in the case of Fe complexes made with non-symmetric NN' bidentate or NN'N pincer ligands. This ligand exchange allows the coordination of H₂O molecules and determines the effectiveness of the immobilized catalyst. The ancillary ligand controls the favorable geometry, while the applied solvent strongly influences the exchange.

In the case of **1** (Fig. 1), the NN' ancillary ligand allows *cis*-diaqua coordination that favors efficient catalysis. In the case of the rigid NN'N pincer ligands (complexes **3** and **4**), two equatorial sites become available for H₂O coordination, leading to the catalytically active form. The presence of water induces the ligand exchange, but the organic solvent is also essential: methanol is preferable over acetonitrile or dichloromethane. The solvent effect is more pronounced in the case of the NN'N ligand scaffold. Consequently, selecting the solvent for drop-casting can be crucial for gaining an active immobilized catalyst.

3. I found that Fe complexes exhibiting tridentate NN'N or bis-bidentate NN' ancillary ligand environments follow the WNA mechanism in mixed water/organic solvent, where the rate-limiting step is the nucleophilic attack of a water molecule at a single Fe center.

Detailed kinetic investigations in water/organic solvent mixtures using complex **1** support single-site catalysis for the electrocatalytic O₂-evolution since the observed rate-dependence is first order in both the H₂O- and the catalyst-concentration. In the case of complex **3**, the electrochemical detection of a proposed peroxidic intermediate also hints at a single-site mechanism. The KIE values in both cases are consistent with a rate-limiting, multiple-site electron-proton transfer WNA step.

4. I discovered that the NN'N pincer ligands could behave as redox-active compounds and carry a single electron vacancy stabilized by an extended π -delocalization.

The free tia-BAIH ligand undergoes oxidation at a similar potential like the Fe^{III} complex formed with it (**3**); therefore, the first 1e⁻ oxidation in the catalytic cycle is assigned as [Fe^{III}(OH)(H₂O)(tia-BAI)]¹⁺ to [Fe^{III}(OH)(H₂O)(tia-BAI[•])]²⁺. This fact implies that a ligand-based 1e⁻ oxidation occurs in **3** and plays a role in water oxidation catalysis.

5. I found that water-insoluble Fe complexes utilizing hydrophobic ancillary ligands with a two-way effect, i.e., control of the complex stability in the course of catalysis and strong attachment to the surface by secondary interactions, represent a viable strategy to fabricate molecular catalyst/anode hybrids.

Controlled potential electrolysis experiments using the drop-casted and dip-coated complex/electrode samples showed that hydrophobic ligands could be utilized to favor a stable surface attachment of the molecular architectures. I performed electrolysis to achieve several turnovers in O₂ production without considerable desorption of the metal-ancillary ligand moieties in the case of complexes **1** and **3**. This strategy is also promising when hybrid molecular co-catalyst/semiconductor carrier photoelectrodes are considered. Importantly, by this strategy, the application of additional immobilizing agents like Nafion can be avoided.

6. I introduced electrodeposition (ED) as a new method for the pincer ligand containing Fe complex precursors that affords a catalytically active, chloride-depleted catalyst coating that is non-homogeneously distributed on ITO and FTO electrodes.

The simple DC and DIP methods can be limited by the solubility of the complex, as complex **4** illustrates. In this case, ED may represent a more atom-efficient immobilization method that is

morphology-preserving with respect to the carrier. The ED method is based on utilizing a chloride precursor complex $[\text{Fe}^{\text{III}}\text{Cl}_2(\text{NN}'\text{N})]$, which is dissolved in an organic electrolyte and undergoes chloride/aqua ligand exchange upon the addition of water. Compared to the amount of the catalyst immobilized by DC and DIP combined with Nafion, lower amounts in samples fabricated by ED are available by at least an order of magnitude that can be just as stable in long-term CPE. SEM analysis of the deposits from **3** and **4** confirmed a patchy distribution of the compound. The charge transfer resistance related to the electrocatalytic OER, determined by EIS, also demonstrates the inhomogeneity of the deposited catalyst and a clear advantage of ED over the DC and DIP carried out using Nafion.

7. I revealed that extending the molecular structure of the Fe complex by introducing aromatic groups on the periphery of the NN'N polycyclic pincer ligands increases the surface stability of electrodeposited samples.

Polycyclic ligands would be beneficial to supporting surface stability of the immobilized complexes in the aqueous electrolyte and further investigate the role of ligand oxidation in electrocatalytic OER. Electrodeposition may be a fruitful immobilization method, even in the case of precursors that are only soluble in solvents that are practically immiscible with water. The example of complex **4** offers the same metal-binding geometry and donor pattern as **3** but contains fused aromatic rings on the periphery to provide a better surface affinity, illustrating that such molecular design enhances the stability of the complex/electrode assembly. This strategy can be beneficial for future co-catalyst/semiconductor hybrids in advanced PEC systems.

7. List of publications

1. **Sahir M. Al-Zuraiji**, Tímea Benkó, Levente Illés, Miklós Németh, Krisztina Frey, Attila Sulyok, József S. Pap: *Utilization of hydrophobic ligands for water-insoluble Fe(II) water oxidation catalysts – Immobilization and characterization*
Journal of Catalysis 381 (2020) 615-625. **IF = 7.920** Cited: 8(5)
2. **Sahir M. Al-Zuraiji**, Dávid Lukács, Miklós Németh, Krisztina Frey, Tímea Benkó, Levente Illés, József S. Pap: *An Iron(III) Complex with Pincer Ligand—Catalytic Water Oxidation through Controllable Ligand Exchange*
Reactions 1 (2020) 16–36. **IF = n.a.** Cited: 4(2)
3. **Sahir M. Al Zuraiji**, Tímea Benkó, Krisztina Frey, Zsolt Kerner, József S. Pap: *Electrodeposition of Fe-Complexes on Oxide Surfaces for Efficient OER Catalysis*
Catalysts 11 (2021) 577. **IF = 4.146.** Cited: 3(2)
4. József S. Pap, **Sahir M. Al-Zuraiji**: *Immobilization and Characterization of Water-insoluble Fe Complexes as Molecular Catalysts For Water Oxidation*
12th ICEEE – 2021 “Global Environmental Development & Sustainability: Research, Engineering & Management,” November 18–19, 2021 RKK – Óbuda University, Budapest, Hungary.
Proceedings book (8 pages), ISBN: 978-963-449-256-6.
5. **Sahir M. Al-Zuraiji**, József S. Pap: *Redox-active ligands in Fe complexes and their use in water oxidation catalysis*
Engineering Symposium at Bánki (ESB 2021), <http://bgk.uni-obuda.hu/esb/2021/>
Proceedings book (6 pages), ISBN:

8. Conference presentations

1. **Sahir M. Al-Zuraiji**, Tímea Benkó, József S. Pap: *Application of water-insoluble Fe(II) complexes with hydrophobic bidentate N-donor ligands in electrocatalytic water oxidation*
European Materials Research Society (E-MRS) Spring Meeting, Materials for Energy, symposium A – Latest advances in solar fuels, <https://www.european-mrs.com/latest-advances-solar-fuels-emrs>
May 27-31, 2019, Nice, France. **(poster A.3.11)**
2. József S. Pap, **Sahir M. Al-Zuraiji**: *Immobilization and Characterization of Water-insoluble Fe Complexes as Molecular Catalysts For Water Oxidation*
The 12th ICEEE-2021 International Annual Conference on “Global Environmental Development & Sustainability: Research, Engineering & Management.”
18th – 19th of November 2021, Budapest – Hungary. **(oral presentation)**
3. József S. Pap, Tímea Benkó, Krisztina Frey, **Sahir M. Al-Zuraiji**, Márta M. Móricz, Shaohua Shen: *How First Row Transition Metal Complexes Can Be Utilized to Improve Water Oxidation in (Photo)Electrocatalytic Hybrid Systems?*
The “5th International Conference on New Photocatalytic Materials for Environment, Energy, and Sustainability” (NPM-5) & The “6th International Conference on Photocatalytic and Advanced Oxidation Technologies for the Treatment of Water, Air, Soil and Surfaces” (PAOT-6)
Proceedings (p. 70), ISBN number: 978-963-306-789-5 **(oral presentation)**

9. References

- [1] Key World Energy Statistics 2020 – Analysis, IEA. <https://www.iea.org/reports/key-world-energy-statistics-2020>.
- [2] M. Rafique, R. Mubashar, M. Irshad, S.S.A. Gillani, M.B. Tahir, N.R. Khalid, A. Yasmin, M.A. Shehzad, A Comprehensive Study on Methods and Materials for Photocatalytic Water Splitting and Hydrogen Production as a Renewable Energy Resource, *J Inorg Organomet Polym.* 30 (2020) 3837–3861. <https://doi.org/10.1007/s10904-020-01611-9>.
- [3] H. Ritchie, M. Roser, Fossil Fuels, Our World in Data. (2017). <https://ourworldindata.org/fossil-fuels>.
- [4] M.I. Hoffert, K. Caldeira, A.K. Jain, E.F. Haites, L.D.D. Harvey, S.D. Potter, M.E. Schlesinger, S.H. Schneider, R.G. Watts, T.M.L. Wigley, D.J. Wuebbles, Energy implications of future stabilization of atmospheric CO₂ content, *Nature.* 395 (1998) 881–884. <https://doi.org/10.1038/27638>.
- [5] N.S. Lewis, D.G. Nocera, Powering the planet: Chemical challenges in solar energy utilization, *Proceedings of the National Academy of Sciences.* 103 (2006) 15729–15735. <https://doi.org/10.1073/pnas.0603395103>.
- [6] J.M. Pearce, Thermodynamic limitations to nuclear energy deployment as a greenhouse gas mitigation technology, *IJNGEE.* 2 (2008) 113. <https://doi.org/10.1504/IJNGEE.2008.017358>.
- [7] S. Styring, Artificial photosynthesis for solar fuels, *Faraday Discuss.* 155 (2012) 357–376. <https://doi.org/10.1039/C1FD00113B>.
- [8] K. Ramalingam, C. Indulkar, Chapter 3 - Solar Energy and Photovoltaic Technology, in: G.B. Gharehpetian, S.M. Mousavi Agah (Eds.), *Distributed Generation Systems*, Butterworth-Heinemann, 2017: pp. 69–147. <https://doi.org/10.1016/B978-0-12-804208-3.00003-0>.
- [9] Z. Wang, R.R. Roberts, G.F. Naterer, K.S. Gabriel, Comparison of thermochemical, electrolytic, photoelectrolytic and photochemical solar-to-hydrogen production technologies, *International Journal of Hydrogen Energy.* 37 (2012) 16287–16301. <https://doi.org/10.1016/j.ijhydene.2012.03.057>.
- [10] M. Roeb, H. Müller-Steinhagen, Concentrating on Solar Electricity and Fuels, *Science.* 329 (2010) 773–774. <https://doi.org/10.1126/science.1191137>.
- [11] B. Zhang, L. Sun, Artificial photosynthesis: opportunities and challenges of molecular catalysts, *Chemical Society Reviews.* 48 (2019) 2216–2264. <https://doi.org/10.1039/C8CS00897C>.
- [12] I. Dincer, C. Acar, Review and evaluation of hydrogen production methods for better sustainability, *International Journal of Hydrogen Energy.* 40 (2015) 11094–11111. <https://doi.org/10.1016/j.ijhydene.2014.12.035>.
- [13] A.C. Nieland, M.R. Shaner, K.M. Papadantonakis, S.A. Francis, N.S. Lewis, A taxonomy for solar fuels generators, *Energy Environ. Sci.* 8 (2014) 16–25. <https://doi.org/10.1039/C4EE02251C>.
- [14] R.J. Cogdell, T.H. Brotsudarmo, A.T. Gardiner, P.M. Sanchez, L. Cronin, Artificial photosynthesis – solar fuels: current status and future prospects, *Biofuels.* 1 (2010) 861–876. <https://doi.org/10.4155/bfs.10.62>.
- [15] M.D. Kärkäs, O. Verho, E.V. Johnston, B. Åkermark, Artificial Photosynthesis: Molecular Systems for Catalytic Water Oxidation, *Chem. Rev.* 114 (2014) 11863–12001. <https://doi.org/10.1021/cr400572f>.

- [16] J. Whitmarsh, Govindjee, The Photosynthetic Process, in: G.S. Singhal, G. Renger, S.K. Sopory, K.-D. Irrgang, Govindjee (Eds.), *Concepts in Photobiology*, Springer Netherlands, Dordrecht, 1999: pp. 11–51. https://doi.org/10.1007/978-94-011-4832-0_2.
- [17] D.G. Nocera, The Artificial Leaf, *Acc. Chem. Res.* 45 (2012) 767–776. <https://doi.org/10.1021/ar2003013>.
- [18] Z. Xu, Y. Jiang, G. Zhou, Response and adaptation of photosynthesis, respiration, and antioxidant systems to elevated CO₂ with environmental stress in plants, *Front. Plant Sci.* 6 (2015). <https://doi.org/10.3389/fpls.2015.00701>.
- [19] C.A. Grimes, O.K. Varghese, S. Ranjan, eds., *Light, Water, Hydrogen*, Springer US, Boston, MA, 2008. <https://doi.org/10.1007/978-0-387-68238-9>.
- [20] V. Krewald, M. Retegan, D.A. Pantazis, Principles of Natural Photosynthesis, *Top Curr Chem.* 371 (2016) 23–48. https://doi.org/10.1007/128_2015_645.
- [21] Y. Umena, K. Kawakami, J.-R. Shen, N. Kamiya, Crystal structure of oxygen-evolving photosystem II at a resolution of 1.9 Å, *Nature.* 473 (2011) 55–60. <https://doi.org/10.1038/nature09913>.
- [22] K.R.S. Onge, Photosynthesis: Light Reactions, in: ELS, American Cancer Society, 2018: pp. 1–8. <https://doi.org/10.1002/9780470015902.a0001311.pub2>.
- [23] M.H. Brown, R.S. Schwartz, Connecting photosynthesis and cellular respiration: Preservice teachers' conceptions, *Journal of Research in Science Teaching.* 46 (2009) 791–812. <https://doi.org/10.1002/tea.20287>.
- [24] C. Herrero, A. Quaranta, W. Leibl, A.W. Rutherford, A. Aukauloo, Artificial photosynthetic systems. Using light and water to provide electrons and protons for the synthesis of a fuel, *Energy Environ. Sci.* 4 (2011) 2353–2365. <https://doi.org/10.1039/C0EE00645A>.
- [25] J.D. Blakemore, R.H. Crabtree, G.W. Brudvig, Molecular Catalysts for Water Oxidation, *Chem. Rev.* 115 (2015) 12974–13005. <https://doi.org/10.1021/acs.chemrev.5b00122>.
- [26] J. Barber, P.D. Tran, From natural to artificial photosynthesis, *J. R. Soc. Interface.* 10 (2013) 20120984. <https://doi.org/10.1098/rsif.2012.0984>.
- [27] V. Balzani, A. Credi, M. Venturi, Photochemical Conversion of Solar Energy, *ChemSusChem.* 1 (2008) 26–58. <https://doi.org/10.1002/cssc.200700087>.
- [28] A. Sartorel, M. Bonchio, S. Campagna, F. Scandola, Tetrametallic molecular catalysts for photochemical water oxidation, *Chem. Soc. Rev.* 42 (2013) 2262–2280. <https://doi.org/10.1039/C2CS35287G>.
- [29] R.L. Purchase, H.J.M. de Groot, Biosolar cells: global artificial photosynthesis needs responsive matrices with quantum coherent kinetic control for high yield, *Interface Focus.* 5 (2015) 20150014. <https://doi.org/10.1098/rsfs.2015.0014>.
- [30] G. Ciamician, The Photochemistry of the Future, *Science.* 36 (1912) 385–394. <https://doi.org/10.1126/science.36.926.385>.
- [31] V. Balzani, A. Credi, M. Venturi, Photochemical Conversion of Solar Energy, *ChemSusChem.* 1 (2008) 26–58. <https://doi.org/10.1002/cssc.200700087>.
- [32] J.R. McKone, N.S. Lewis, H.B. Gray, Will Solar-Driven Water-Splitting Devices See the Light of Day?, *Chem. Mater.* 26 (2014) 407–414. <https://doi.org/10.1021/cm4021518>.
- [33] R.F. Service, Is It Time to Shoot for the Sun?, *Science.* 309 (2005) 548–551. <https://doi.org/10.1126/science.309.5734.548>.
- [34] G.W. Crabtree, N.S. Lewis, Solar energy conversion, *Physics Today.* 60 (2007) 37–42. <https://doi.org/10.1063/1.2718755>.

- [35] P.V. Kamat, Meeting the Clean Energy Demand: Nanostructure Architectures for Solar Energy Conversion, *J. Phys. Chem. C*. 111 (2007) 2834–2860. <https://doi.org/10.1021/jp066952u>.
- [36] C.J. Gagliardi, A.K. Vannucci, J.J. Concepcion, Z. Chen, T.J. Meyer, The role of proton coupled electron transfer in water oxidation, *Energy Environ. Sci.* 5 (2012) 7704–7717. <https://doi.org/10.1039/C2EE03311A>.
- [37] J.H. Alstrum-Acevedo, M.K. Brennaman, T.J. Meyer, Chemical Approaches to Artificial Photosynthesis. 2, *Inorg. Chem.* 44 (2005) 6802–6827. <https://doi.org/10.1021/ic050904r>.
- [38] M.D. Kärkäs, E.V. Johnston, O. Verho, B. Åkermark, Artificial Photosynthesis: From Nanosecond Electron Transfer to Catalytic Water Oxidation, *Acc. Chem. Res.* 47 (2014) 100–111. <https://doi.org/10.1021/ar400076j>.
- [39] T.J. Meyer, The art of splitting water, *Nature*. 451 (2008) 778–779. <https://doi.org/10.1038/451778a>.
- [40] M. Wang, Z. Wang, X. Gong, Z. Guo, The intensification technologies to water electrolysis for hydrogen production – A review, *Renewable and Sustainable Energy Reviews*. 29 (2014) 573–588. <https://doi.org/10.1016/j.rser.2013.08.090>.
- [41] X. Zou, Y. Zhang, Noble metal-free hydrogen evolution catalysts for water splitting, *Chem. Soc. Rev.* 44 (2015) 5148–5180. <https://doi.org/10.1039/C4CS00448E>.
- [42] null Turner, A realizable renewable energy future, *Science*. 285 (1999) 687–689. <https://doi.org/10.1126/science.285.5428.687>.
- [43] K. Zeng, D. Zhang, Corrigendum to “Recent progress in alkaline water electrolysis for hydrogen production and applications” [*Progr Energ Combust Sci* 36 (3) (2010) 307–326], *Progress in Energy and Combustion Science*. 37 (2011) 631. <https://doi.org/10.1016/j.pecs.2011.02.002>.
- [44] E. Fabbri, A. Habereder, K. Waltar, R. Kötz, T.J. Schmidt, Developments and perspectives of oxide-based catalysts for the oxygen evolution reaction, *Catal. Sci. Technol.* 4 (2014) 3800–3821. <https://doi.org/10.1039/C4CY00669K>.
- [45] S. Anantharaj, S.R. Ede, K. Sakthikumar, K. Karthick, S. Mishra, S. Kundu, Recent Trends and Perspectives in Electrochemical Water Splitting with an Emphasis on Sulfide, Selenide, and Phosphide Catalysts of Fe, Co, and Ni: A Review, *ACS Catal.* 6 (2016) 8069–8097. <https://doi.org/10.1021/acscatal.6b02479>.
- [46] R.J. Detz, J.N.H. Reek, B.C.C. van der Zwaan, The future of solar fuels: when could they become competitive?, *Energy Environ. Sci.* 11 (2018) 1653–1669. <https://doi.org/10.1039/C8EE00111A>.
- [47] K.M.K. Yu, I. Curcic, J. Gabriel, S.C.E. Tsang, Recent advances in CO₂ capture and utilization, *ChemSusChem*. 1 (2008) 893–899. <https://doi.org/10.1002/cssc.200800169>.
- [48] H. Wendt, H. Hofmann, V. Plzak, Materials research and development of electrocatalysts for alkaline water electrolysis, *Materials Chemistry and Physics*. 22 (1989) 27–49. [https://doi.org/10.1016/0254-0584\(89\)90030-8](https://doi.org/10.1016/0254-0584(89)90030-8).
- [49] S. Ye, C. Ding, C. Li, Artificial photosynthesis systems for catalytic water oxidation, in: *Advances in Inorganic Chemistry*, Elsevier, 2019: pp. 3–59. <https://doi.org/10.1016/bs.adioch.2019.03.007>.
- [50] H. Yamazaki, A. Shouji, M. Kajita, M. Yagi, Electrocatalytic and photocatalytic water oxidation to dioxygen based on metal complexes, *Coordination Chemistry Reviews*. 254 (2010) 2483–2491. <https://doi.org/10.1016/j.ccr.2010.02.008>.

- [51] C.C.L. McCrory, S. Jung, J.C. Peters, T.F. Jaramillo, Benchmarking Heterogeneous Electrocatalysts for the Oxygen Evolution Reaction, *J. Am. Chem. Soc.* 135 (2013) 16977–16987. <https://doi.org/10.1021/ja407115p>.
- [52] S.M. Al-Zurajji, T. Benkó, L. Illés, M. Németh, K. Frey, A. Sulyok, J.S. Pap, Utilization of hydrophobic ligands for water-insoluble Fe(II) water oxidation catalysts – Immobilization and characterization, *Journal of Catalysis*. 381 (2020) 615–625. <https://doi.org/10.1016/j.jcat.2019.12.003>.
- [53] A.J. Bard, M.A. Fox, Artificial Photosynthesis: Solar Splitting of Water to Hydrogen and Oxygen, *Acc. Chem. Res.* 28 (1995) 141–145. <https://doi.org/10.1021/ar00051a007>.
- [54] S. Kotrel, S. Bräuninger, Industrial Electrocatalysis, in: *Handbook of Heterogeneous Catalysis*, American Cancer Society, 2008: pp. 1936–1958. <https://doi.org/10.1002/9783527610044.hetcat0103>.
- [55] A.J. Bard, L.R. Faulkner, *Electrochemical methods: fundamentals and applications*, 2nd ed, Wiley, New York, 2001.
- [56] B. Malik, S. Anantharaj, K. Karthick, D. K. Pattanayak, S. Kundu, Magnetic CoPt nanoparticle-decorated ultrathin Co(OH)₂ nanosheets: an efficient bi-functional water splitting catalyst, *Catalysis Science & Technology*. 7 (2017) 2486–2497. <https://doi.org/10.1039/C7CY00309A>.
- [57] S. Anantharaj, P.E. Karthik, B. Subramanian, S. Kundu, Pt Nanoparticle Anchored Molecular Self-Assemblies of DNA: An Extremely Stable and Efficient HER Electrocatalyst with Ultralow Pt Content, *ACS Catal.* 6 (2016) 4660–4672. <https://doi.org/10.1021/acscatal.6b00965>.
- [58] R. Matheu, M.Z. Ertem, C. Gimbert-Suriñach, X. Sala, A. Llobet, Seven Coordinated Molecular Ruthenium–Water Oxidation Catalysts: A Coordination Chemistry Journey, *Chem. Rev.* 119 (2019) 3453–3471. <https://doi.org/10.1021/acs.chemrev.8b00537>.
- [59] L. Wu, M. Eberhart, A. Nayak, M.K. Brennaman, B. Shan, T.J. Meyer, A Molecular Silane-Derivatized Ru(II) Catalyst for Photoelectrochemical Water Oxidation, *J. Am. Chem. Soc.* 140 (2018) 15062–15069. <https://doi.org/10.1021/jacs.8b10132>.
- [60] S. Anantharaj, S.R. Ede, K. Karthick, S.S. Sankar, K. Sangeetha, P.E. Karthik, S. Kundu, Precision and correctness in the evaluation of electrocatalytic water splitting: revisiting activity parameters with a critical assessment, *Energy Environ. Sci.* 11 (2018) 744–771. <https://doi.org/10.1039/C7EE03457A>.
- [61] B. Pitschak, J. Mergel, *Electrolytic Processes*, in: J. Töpler, J. Lehmann (Eds.), *Hydrogen and Fuel Cell*, Springer Berlin Heidelberg, Berlin, Heidelberg, 2016: pp. 187–207. https://doi.org/10.1007/978-3-662-44972-1_11.
- [62] F. Ganci, T. Baguet, G. Aiello, V. Cusumano, P. Mandin, C. Sunseri, R. Inguanta, Nanostructured Ni Based Anode and Cathode for Alkaline Water Electrolyzers, *Energies*. 12 (2019) 3669. <https://doi.org/10.3390/en12193669>.
- [63] A. Cho, Energy’s Tricky Tradeoffs, *Science*. 329 (2010) 786–787. <https://doi.org/10.1126/science.329.5993.786>.
- [64] T. Hisatomi, J. Kubota, K. Domen, Recent advances in semiconductors for photocatalytic and photoelectrochemical water splitting, *Chem. Soc. Rev.* 43 (2014) 7520–7535. <https://doi.org/10.1039/C3CS60378D>.
- [65] G. Thuillier, M. Hersé, D. Labs, T. Foujols, W. Peetermans, D. Gillotay, P.C. Simon, H. Mandel, The Solar Spectral Irradiance from 200 to 2400 nm as Measured by the SOLSPEC Spectrometer from the Atlas and Eureka Missions, *Solar Physics*. 214 (2003) 1–22. <https://doi.org/10.1023/A:1024048429145>.

- [66] A. Djafour, M. Matoug, H. Bouras, B. Bouchekima, M.S. Aida, B. Azoui, Photovoltaic-assisted alkaline water electrolysis: Basic principles, *International Journal of Hydrogen Energy*. 36 (2011) 4117–4124. <https://doi.org/10.1016/j.ijhydene.2010.09.099>.
- [67] M. Khzouz, E.I. Gkanas, *Hydrogen Technologies for Mobility and Stationary Applications: Hydrogen Production, Storage and Infrastructure Development*, IntechOpen, 2020. <https://doi.org/10.5772/intechopen.91676>.
- [68] Ibrahim Dincer, Anand S. Joshi, *Solar Based Hydrogen Production Systems*, 2013. <https://doi.org/10.1007/978-1-4614-7431-9>.
- [69] D. Lukács, Ł. Szyrwił, J.S. Pap, Copper Containing Molecular Systems in Electrocatalytic Water Oxidation—Trends and Perspectives, *Catalysts*. 9 (2019) 83. <https://doi.org/10.3390/catal9010083>.
- [70] A. Fujishima, K. Honda, Electrochemical Photolysis of Water at a Semiconductor Electrode, *Nature*. 238 (1972) 37–38. <https://doi.org/10.1038/238037a0>.
- [71] P. Dias, A. Mendes, Hydrogen Production from Photoelectrochemical Water Splitting, in: R.A. Meyers (Ed.), *Encyclopedia of Sustainability Science and Technology*, Springer, New York, NY, 2017: pp. 1–52. https://doi.org/10.1007/978-1-4939-2493-6_957-1.
- [72] Zhebo Chen, Huyen Dinh., Eric Miller, *Photoelectrochemical Water Splitting*, 1st ed., Springer-Verlag New York, n.d. <https://www.springer.com/gp/book/9781461482970>.
- [73] P. Arunachalam, A.M. Al Mayouf, Chapter 28 - Photoelectrochemical Water Splitting, in: S. Mohapatra, T.A. Nguyen, P. Nguyen-Tri (Eds.), *Noble Metal-Metal Oxide Hybrid Nanoparticles*, Woodhead Publishing, 2019: pp. 585–606. <https://doi.org/10.1016/B978-0-12-814134-2.00028-0>.
- [74] A.G. Tamirat, J. Rick, A.A. Dubale, W.-N. Su, B.-J. Hwang, Using hematite for photoelectrochemical water splitting: a review of current progress and challenges, *Nanoscale Horiz.* 1 (2016) 243–267. <https://doi.org/10.1039/C5NH00098J>.
- [75] K. Sivula, F. Le Formal, M. Grätzel, Solar Water Splitting: Progress Using Hematite (α -Fe₂O₃) Photoelectrodes, *ChemSusChem*. 4 (2011) 432–449. <https://doi.org/10.1002/cssc.201000416>.
- [76] B.S. Kalanoor, H. Seo, S.S. Kalanur, Recent developments in photoelectrochemical water-splitting using WO₃/BiVO₄ heterojunction photoanode: A review, *Materials Science for Energy Technologies*. 1 (2018) 49–62. <https://doi.org/10.1016/j.mset.2018.03.004>.
- [77] S.M. Thalluri, L. Bai, C. Lv, Z. Huang, X. Hu, L. Liu, Strategies for Semiconductor/Electrocatalyst Coupling toward Solar-Driven Water Splitting, *Advanced Science*. 7 (2020) 1902102. <https://doi.org/10.1002/advs.201902102>.
- [78] J.M. Spurgeon, J.M. Velazquez, M.T. McDowell, Improving O₂ production of WO₃ photoanodes with IrO₂ in acidic aqueous electrolyte, *Phys. Chem. Chem. Phys.* 16 (2014) 3623–3631. <https://doi.org/10.1039/C3CP55527E>.
- [79] M.V. de Voorde, *Hydrogen Production and Energy Transition*, Walter de Gruyter GmbH & Co KG, 2021.
- [80] H.B. Gray, Powering the planet with solar fuel, *Nat Chem*. 1 (2009) 7. <https://doi.org/10.1038/nchem.141>.
- [81] A.J. Bard, M.A. Fox, Artificial Photosynthesis: Solar Splitting of Water to Hydrogen and Oxygen, *Accounts of Chemical Research*. 28 (1995) 141–145. <https://doi.org/10.1021/ar00051a007>.
- [82] A. Singh, L. Spiccia, Water oxidation catalysts based on abundant 1st row transition metals, *Coordination Chemistry Reviews*. 257 (2013) 2607–2622. <https://doi.org/10.1016/j.ccr.2013.02.027>.

- [83] H.-Y. Su, Y. Gorlin, I. C. Man, F. Calle-Vallejo, J. K. Nørskov, T. F. Jaramillo, J. Rossmeisl, Identifying active surface phases for metal oxide electrocatalysts: a study of manganese oxide bi-functional catalysts for oxygen reduction and water oxidation catalysis, *Physical Chemistry Chemical Physics*. 14 (2012) 14010–14022. <https://doi.org/10.1039/C2CP40841D>.
- [84] M. Wiechen, M. M. Najafpour, S. I. Allakhverdiev, L. Spiccia, Water oxidation catalysis by manganese oxides: learning from evolution, *Energy & Environmental Science*. 7 (2014) 2203–2212. <https://doi.org/10.1039/C4EE00681J>.
- [85] S. Jung, C.C. L. McCrory, I. M. Ferrer, J. C. Peters, T. F. Jaramillo, Benchmarking nanoparticulate metal oxide electrocatalysts for the alkaline water oxidation reaction, *Journal of Materials Chemistry A*. 4 (2016) 3068–3076. <https://doi.org/10.1039/C5TA07586F>.
- [86] R.D.L. Smith, M.S. Prévot, R.D. Fagan, Z. Zhang, P.A. Sedach, M.K.J. Siu, S. Trudel, C.P. Berlinguette, Photochemical Route for Accessing Amorphous Metal Oxide Materials for Water Oxidation Catalysis, *Science*. 340 (2013) 60–63. <https://doi.org/10.1126/science.1233638>.
- [87] H. Jin, J. Wang, D. Su, Z. Wei, Z. Pang, Y. Wang, In situ Cobalt–Cobalt Oxide/N-Doped Carbon Hybrids As Superior Bifunctional Electrocatalysts for Hydrogen and Oxygen Evolution, *J. Am. Chem. Soc.* 137 (2015) 2688–2694. <https://doi.org/10.1021/ja5127165>.
- [88] C.C.L. McCrory, S. Jung, I.M. Ferrer, S.M. Chatman, J.C. Peters, T.F. Jaramillo, Benchmarking Hydrogen Evolving Reaction and Oxygen Evolving Reaction Electrocatalysts for Solar Water Splitting Devices, *J. Am. Chem. Soc.* 137 (2015) 4347–4357. <https://doi.org/10.1021/ja510442p>.
- [89] M.D. Kärkäs, O. Verho, E.V. Johnston, B. Åkermark, Artificial Photosynthesis: Molecular Systems for Catalytic Water Oxidation, *Chem. Rev.* 114 (2014) 11863–12001. <https://doi.org/10.1021/cr400572f>.
- [90] B. Zhang, L. Sun, Artificial photosynthesis: opportunities and challenges of molecular catalysts, *Chem. Soc. Rev.* 48 (2019) 2216–2264. <https://doi.org/10.1039/C8CS00897C>.
- [91] J.-W. Wang, C. Hou, H.-H. Huang, W.-J. Liu, Z.-F. Ke, T.-B. Lu, Further insight into the electrocatalytic water oxidation by macrocyclic nickel(II) complexes: the influence of steric effect on catalytic activity, *Catal. Sci. Technol.* 7 (2017) 5585–5593. <https://doi.org/10.1039/C7CY01527E>.
- [92] S. Berardi, S. Drouet, L. Francàs, C. Gimbert-Suriñach, M. Guttentag, C. Richmond, T. Stoll, A. Llobet, Molecular artificial photosynthesis, *Chem. Soc. Rev.* 43 (2014) 7501–7519. <https://doi.org/10.1039/C3CS60405E>.
- [93] P. Garrido-Barros, C. Gimbert-Suriñach, R. Matheu, X. Sala, A. Llobet, How to make an efficient and robust molecular catalyst for water oxidation, *Chem. Soc. Rev.* 46 (2017) 6088–6098. <https://doi.org/10.1039/C7CS00248C>.
- [94] A. Coehn, M. Gläser, Studien über die Bildung von Metalloxyden I. Über das anodische Verhalten von Kobalt- und Nickel-Lösungen, *Zeitschrift Für Anorganische Chemie*. 33 (1902) 9–24. <https://doi.org/10.1002/zaac.19020330105>.
- [95] A. Badreldin, A.E. Abusrafa, A. Abdel-Wahab, Oxygen-Deficient Cobalt-Based Oxides for Electrocatalytic Water Splitting, *ChemSusChem*. 14 (2021) 10–32. <https://doi.org/10.1002/cssc.202002002>.
- [96] S.W. Gersten, G.J. Samuels, T.J. Meyer, Catalytic oxidation of water by an oxo-bridged ruthenium dimer, *J. Am. Chem. Soc.* 104 (1982) 4029–4030. <https://doi.org/10.1021/ja00378a053>.

- [97] V. Charles, A.O. Anumah, K.A. Adegoke, M.O. Adesina, I.P. Ebuka, N.A. Gaya, S. Ogwuche, M.O. Yakubu, Progress and challenges pertaining to the earthly-abundant electrocatalytic materials for oxygen evolution reaction, *Sustainable Materials and Technologies*. 28 (2021) e00252. <https://doi.org/10.1016/j.susmat.2021.e00252>.
- [98] A. Damjanovic, A. Dey, J.O. Bockris, Electrode Kinetics of Oxygen Evolution and Dissolution on Rh, Ir, and Pt-Rh Alloy Electrodes, *J. Electrochem. Soc.* 113 (1966) 739. <https://doi.org/10.1149/1.2424104>.
- [99] L. Wang, L. Duan, Y. Wang, M.S.G. Ahlquist, L. Sun, Highly efficient and robust molecular water oxidation catalysts based on ruthenium complexes, *Chem. Commun.* 50 (2014) 12947–12950. <https://doi.org/10.1039/C4CC05069J>.
- [100] J. Creus, R. Matheu, I. Peñafiel, D. Moonshiram, P. Blondeau, J. Benet-Buchholz, J. García-Antón, X. Sala, C. Godard, A. Llobet, A Million Turnover Molecular Anode for Catalytic Water Oxidation, *Angewandte Chemie International Edition*. 55 (2016) 15382–15386. <https://doi.org/10.1002/anie.201609167>.
- [101] L.-H. Zhang, S. Mathew, J. Hessels, J.N.H. Reek, F. Yu, Homogeneous Catalysts Based on First-Row Transition-Metals for Electrochemical Water Oxidation, *ChemSusChem*. 14 (2021) 234–250. <https://doi.org/10.1002/cssc.202001876>.
- [102] R. Matheu, M.Z. Ertem, C. Gimbert-Suriñach, X. Sala, A. Llobet, Seven Coordinated Molecular Ruthenium–Water Oxidation Catalysts: A Coordination Chemistry Journey, *Chem. Rev.* (2019). <https://doi.org/10.1021/acs.chemrev.8b00537>.
- [103] A. Savini, A. Bucci, G. Bellachioma, L. Rocchigiani, C. Zuccaccia, A. Llobet, A. Macchioni, Mechanistic Aspects of Water Oxidation Catalyzed by Organometallic Iridium Complexes, *European Journal of Inorganic Chemistry*. 2014 (2014) 690–697. <https://doi.org/10.1002/ejic.201300530>.
- [104] J.L. Fiol, Z. Codolà, I. Garcia-Bosch, L. Gómez, J.J. Pla, M. Costas, Efficient water oxidation catalysts based on readily available iron coordination complexes, *Nature Chem.* 3 (2011) 807–813. <https://doi.org/10.1038/nchem.1140>.
- [105] C. Costentin, M. Robert, J.-M. Savéant, Update 1 of: Electrochemical Approach to the Mechanistic Study of Proton-Coupled Electron Transfer, *Chem. Rev.* 110 (2010) PR1–PR40. <https://doi.org/10.1021/cr100038y>.
- [106] A. Wang, J. Li, T. Zhang, Heterogeneous single-atom catalysis, *Nat Rev Chem*. 2 (2018) 65–81. <https://doi.org/10.1038/s41570-018-0010-1>.
- [107] X. Liu, H. Jia, Z. Sun, H. Chen, P. Xu, P. Du, Nanostructured copper oxide electrodeposited from copper(II) complexes as an active catalyst for electrocatalytic oxygen evolution reaction, *Electrochemistry Communications*. 46 (2014) 1–4. <https://doi.org/10.1016/j.elecom.2014.05.029>.
- [108] J. Li, R. Güttinger, R. Moré, F. Song, W. Wan, G.R. Patzke, Frontiers of water oxidation: the quest for true catalysts, *Chem. Soc. Rev.* 46 (2017) 6124–6147. <https://doi.org/10.1039/C7CS00306D>.
- [109] X. Liu, S. Inagaki, J. Gong, Heterogeneous Molecular Systems for Photocatalytic CO₂ Reduction with Water Oxidation, *Angew. Chem. Int. Ed.* 55 (2016) 14924–14950. <https://doi.org/10.1002/anie.201600395>.
- [110] L. Han, S. Dong, E. Wang, Transition-Metal (Co, Ni, and Fe)-Based Electrocatalysts for the Water Oxidation Reaction, *Advanced Materials*. 28 (2016) 9266–9291. <https://doi.org/10.1002/adma.201602270>.

- [111] C.C.L. McCrory, S. Jung, J.C. Peters, T.F. Jaramillo, Benchmarking Heterogeneous Electrocatalysts for the Oxygen Evolution Reaction, *J. Am. Chem. Soc.* 135 (2013) 16977–16987. <https://doi.org/10.1021/ja407115p>.
- [112] R.M. Bullock, A.K. Das, A.M. Appel, Surface Immobilization of Molecular Electrocatalysts for Energy Conversion, *Chem. Eur. J.* 23 (2017) 7626–7641. <https://doi.org/10.1002/chem.201605066>.
- [113] I. Funes-Ardoiz, P. Garrido-Barros, A. Llobet, F. Maseras, Single Electron Transfer Steps in Water Oxidation Catalysis. Redefining the Mechanistic Scenario, *ACS Catal.* 7 (2017) 1712–1719. <https://doi.org/10.1021/acscatal.6b03253>.
- [114] J. Li, C. A. Triana, W. Wan, D.P.A. Saseendran, Y. Zhao, S. E. Balaghi, S. Heidari, G. R. Patzke, Molecular and heterogeneous water oxidation catalysts: recent progress and joint perspectives, *Chemical Society Reviews.* 50 (2021) 2444–2485. <https://doi.org/10.1039/D0CS00978D>.
- [115] X. Yang, Y. Wang, C.M. Li, D. Wang, Mechanisms of water oxidation on heterogeneous catalyst surfaces, *Nano Res.* (2021). <https://doi.org/10.1007/s12274-021-3607-5>.
- [116] S. Fierro, T. Nagel, H. Baltruschat, C. Comninellis, Investigation of the oxygen evolution reaction on Ti/IrO₂ electrodes using isotope labelling and on-line mass spectrometry, *Electrochemistry Communications.* 9 (2007) 1969–1974. <https://doi.org/10.1016/j.elecom.2007.05.008>.
- [117] I.C. Man, H.-Y. Su, F. Calle-Vallejo, H.A. Hansen, J.I. Martínez, N.G. Inoglu, J. Kitchin, T.F. Jaramillo, J.K. Nørskov, J. Rossmeisl, Universality in Oxygen Evolution Electrocatalysis on Oxide Surfaces, *ChemCatChem.* 3 (2011) 1159–1165. <https://doi.org/10.1002/cctc.201000397>.
- [118] J. Hessels, R.J. Detz, M.T.M. Koper, J.N.H. Reek, Rational Design Rules for Molecular Water Oxidation Catalysts based on Scaling Relationships, *Chemistry – A European Journal.* 23 (2017) 16413–16418. <https://doi.org/10.1002/chem.201702850>.
- [119] L.A. De Faria, J.F.C. Boodts, S. Trasatti, Electrocatalytic properties of ternary oxide mixtures of composition Ru_{0.3}Ti_(0.7-x)Ce_xO₂: oxygen evolution from acidic solution, *J Appl Electrochem.* 26 (1996) 1195–1199. <https://doi.org/10.1007/BF00243745>.
- [120] H. Dau, C. Limberg, T. Reier, M. Risch, S. Roggan, P. Strasser, The Mechanism of Water Oxidation: From Electrolysis via Homogeneous to Biological Catalysis, *ChemCatChem.* 2 (2010) 724–761. <https://doi.org/10.1002/cctc.201000126>.
- [121] A. Badruzzaman, A. Yuda, A. Ashok, A. Kumar, Recent advances in cobalt based heterogeneous catalysts for oxygen evolution reaction, *Inorganica Chimica Acta.* 511 (2020) 119854. <https://doi.org/10.1016/j.ica.2020.119854>.
- [122] F. Song, X. Hu, Exfoliation of layered double hydroxides for enhanced oxygen evolution catalysis, *Nat Commun.* 5 (2014) 4477. <https://doi.org/10.1038/ncomms5477>.
- [123] D. Zhou, P. Li, X. Lin, A. McKinley, Y. Kuang, W. Liu, W.-F. Lin, X. Sun, X. Duan, Layered double hydroxide-based electrocatalysts for the oxygen evolution reaction: identification and tailoring of active sites, and superaerophobic nanoarray electrode assembly, *Chem. Soc. Rev.* 50 (2021) 8790–8817. <https://doi.org/10.1039/D1CS00186H>.
- [124] L.-J. Zhou, X. Huang, H. Chen, P. Jin, G.-D. Li, X. Zou, A high surface area flower-like Ni–Fe layered double hydroxide for electrocatalytic water oxidation reaction, *Dalton Transactions.* 44 (2015) 11592–11600. <https://doi.org/10.1039/C5DT01474C>.
- [125] D.E. Hall, Ni (OH)₂ - Impregnated Anodes for Alkaline Water Electrolysis, *J. Electrochem. Soc.* 130 (1983) 317. <https://doi.org/10.1149/1.2119702>.

- [126] S. Klaus, Y. Cai, M.W. Louie, L. Trotochaud, A.T. Bell, Effects of Fe Electrolyte Impurities on Ni(OH)₂/NiOOH Structure and Oxygen Evolution Activity, *J. Phys. Chem. C.* 119 (2015) 7243–7254. <https://doi.org/10.1021/acs.jpcc.5b00105>.
- [127] D. Friebel, M.W. Louie, M. Bajdich, K.E. Sanwald, Y. Cai, A.M. Wise, M.-J. Cheng, D. Sokaras, T.-C. Weng, R. Alonso-Mori, R.C. Davis, J.R. Bargar, J.K. Nørskov, A. Nilsson, A.T. Bell, Identification of Highly Active Fe Sites in (Ni,Fe)OOH for Electrocatalytic Water Splitting, *J. Am. Chem. Soc.* 137 (2015) 1305–1313. <https://doi.org/10.1021/ja511559d>.
- [128] G. Abellán, J.A. Carrasco, E. Coronado, J. Romero, M. Varela, Alkoxide-intercalated CoFe-layered double hydroxides as precursors of colloidal nanosheet suspensions: structural, magnetic and electrochemical properties, *J. Mater. Chem. C.* 2 (2014) 3723–3731. <https://doi.org/10.1039/C3TC32578D>.
- [129] Y. Zhang, B. Cui, C. Zhao, H. Lin, J. Li, Co–Ni layered double hydroxides for water oxidation in neutral electrolyte, *Phys. Chem. Chem. Phys.* 15 (2013) 7363–7369. <https://doi.org/10.1039/C3CP50202C>.
- [130] M.W. Kanan, D.G. Nocera, In Situ Formation of an Oxygen-Evolving Catalyst in Neutral Water Containing Phosphate and Co²⁺, *Science.* 321 (2008) 1072–1075. <https://doi.org/10.1126/science.1162018>.
- [131] M. Dincă, Y. Surendranath, D.G. Nocera, Nickel-borate oxygen-evolving catalyst that functions under benign conditions, *PNAS.* 107 (2010) 10337–10341. <https://doi.org/10.1073/pnas.1001859107>.
- [132] C. Bolm, J. Legros, J. Le Paih, L. Zani, Iron-Catalyzed Reactions in Organic Synthesis, *Chem. Rev.* 104 (2004) 6217–6254. <https://doi.org/10.1021/cr040664h>.
- [133] Md.A. Asraf, H.A. Younus, M. Yusubov, F. Verpoort, Earth-abundant metal complexes as catalysts for water oxidation; is it homogeneous or heterogeneous?, *Catalysis Science & Technology.* 5 (2015) 4901–4925. <https://doi.org/10.1039/C5CY01251A>.
- [134] A.R. McDonald, L. Que, High-valent nonheme iron-oxo complexes: Synthesis, structure, and spectroscopy, *Coordination Chemistry Reviews.* 257 (2013) 414–428. <https://doi.org/10.1016/j.ccr.2012.08.002>.
- [135] J. Hohenberger, K. Ray, K. Meyer, The biology and chemistry of high-valent iron–oxo and iron–nitrido complexes, *Nature Communications.* 3 (2012) 720.
- [136] X. Huang, J.T. Groves, Beyond ferryl-mediated hydroxylation: 40 years of the rebound mechanism and C–H activation, *J Biol Inorg Chem.* 22 (2017) 185–207. <https://doi.org/10.1007/s00775-016-1414-3>.
- [137] I. Bauer, H.-J. Knölker, Iron Catalysis in Organic Synthesis, *Chem. Rev.* 115 (2015) 3170–3387. <https://doi.org/10.1021/cr500425u>.
- [138] A. Fürstner, Iron Catalysis in Organic Synthesis: A Critical Assessment of What It Takes To Make This Base Metal a Multitasking Champion, *ACS Cent. Sci.* 2 (2016) 778–789. <https://doi.org/10.1021/acscentsci.6b00272>.
- [139] Z. Codolà, I. Garcia-Bosch, F. Acuña-Parés, I. Prat, J.M. Luis, M. Costas, J. Lloret-Fillol, Electronic Effects on Single-Site Iron Catalysts for Water Oxidation, *Chem. Eur. J.* 19 (2013) 8042–8047. <https://doi.org/10.1002/chem.201301112>.
- [140] P. Pelosin, M. Gil-Sepulcre, P. Garrido-Barros, D. Moonshiram, J. Benet-Buchholz, C. Gimbert-Suriñach, A. Llobet, Analysis of the Active Species Responsible for Water Oxidation Using a Pentanuclear Fe Complex, *IScience.* 23 (2020) 101378. <https://doi.org/10.1016/j.isci.2020.101378>.

- [141] T.J. Collins, TAML Oxidant Activators: A New Approach to the Activation of Hydrogen Peroxide for Environmentally Significant Problems, *Acc. Chem. Res.* 35 (2002) 782–790. <https://doi.org/10.1021/ar010079s>.
- [142] W.C. Ellis, N.D. McDaniel, S. Bernhard, T.J. Collins, Fast Water Oxidation Using Iron, *J. Am. Chem. Soc.* 132 (2010) 10990–10991. <https://doi.org/10.1021/ja104766z>.
- [143] T. Liu, B. Zhang, L. Sun, Iron-Based Molecular Water Oxidation Catalysts: Abundant, Cheap, and Promising, *Chemistry – An Asian Journal*. 14 (2019) 31–43. <https://doi.org/10.1002/asia.201801253>.
- [144] C. Panda, J. Debgupta, D. Díaz Díaz, K.K. Singh, S. Sen Gupta, B.B. Dhar, Homogeneous Photochemical Water Oxidation by Biuret-Modified Fe-TAML: Evidence of FeV(O) Intermediate, *J. Am. Chem. Soc.* 136 (2014) 12273–12282. <https://doi.org/10.1021/ja503753k>.
- [145] C. Casadevall, A. Bucci, M. Costas, J. Lloret-Fillol, Water oxidation catalysis with well-defined molecular iron complexes, in: *Advances in Inorganic Chemistry*, Elsevier, 2019: pp. 151–196. <https://doi.org/10.1016/bs.adioch.2019.03.004>.
- [146] L.D. Wickramasinghe, R. Zhou, R. Zong, P. Vo, K.J. Gagnon, R.P. Thummel, Iron Complexes of Square Planar Tetradentate Polypyridyl-Type Ligands as Catalysts for Water Oxidation, *J. Am. Chem. Soc.* 137 (2015) 13260–13263. <https://doi.org/10.1021/jacs.5b08856>.
- [147] M.K. Coggins, M.-T. Zhang, A.K. Vannucci, C.J. Dares, T.J. Meyer, Electrocatalytic Water Oxidation by a Monomeric Amidate-Ligated Fe(III)–Aqua Complex, *J. Am. Chem. Soc.* 136 (2014) 5531–5534. <https://doi.org/10.1021/ja412822u>.
- [148] D. Hong, S. Mandal, Y. Yamada, Y.-M. Lee, W. Nam, A. Llobet, S. Fukuzumi, Water Oxidation Catalysis with Nonheme Iron Complexes under Acidic and Basic Conditions: Homogeneous or Heterogeneous?, *Inorg. Chem.* 52 (2013) 9522–9531. <https://doi.org/10.1021/ic401180r>.
- [149] G. Chen, L. Chen, S.-M. Ng, W.-L. Man, T.-C. Lau, Chemical and Visible-Light-Driven Water Oxidation by Iron Complexes at pH 7–9: Evidence for Dual-Active Intermediates in Iron-Catalyzed Water Oxidation, *Angewandte Chemie International Edition*. 52 (2013) 1789–1791. <https://doi.org/10.1002/anie.201209116>.
- [150] S. Fukuzumi, Y.-M. Lee, W. Nam, Kinetics and mechanisms of catalytic water oxidation, *Dalton Trans.* 48 (2019) 779–798. <https://doi.org/10.1039/C8DT04341H>.
- [151] B. Yang, Q.-Q. Yang, X. Jiang, B. Chen, C.-H. Tung, L.-Z. Wu, Tracking the FeIV(O) intermediate and O–O bond formation of a nonheme iron catalyst for water oxidation, *Chem. Commun.* 53 (2017) 9063–9066. <https://doi.org/10.1039/C7CC04814A>.
- [152] M.M. Najafpour, A.N. Moghaddam, D.J. Sedigh, M. Hołyńska, A dinuclear iron complex with a single oxo bridge as an efficient water-oxidizing catalyst in the presence of cerium(IV) ammonium nitrate: new findings and current controversies, *Catal. Sci. Technol.* 4 (2013) 30–33. <https://doi.org/10.1039/C3CY00644A>.
- [153] M. Okamura, M. Kondo, R. Kuga, Y. Kurashige, T. Yanai, S. Hayami, V.K.K. Praneeth, M. Yoshida, K. Yoneda, S. Kawata, S. Masaoka, A pentanuclear iron catalyst designed for water oxidation, *Nature*. 530 (2016) 465–468. <https://doi.org/10.1038/nature16529>.
- [154] Z. Cai, D. Zhou, M. Wang, S.-M. Bak, Y. Wu, Z. Wu, Y. Tian, X. Xiong, Y. Li, W. Liu, S. Siahrostami, Y. Kuang, X.-Q. Yang, H. Duan, Z. Feng, H. Wang, X. Sun, Introducing Fe²⁺ into Nickel–Iron Layered Double Hydroxide: Local Structure Modulated Water Oxidation Activity, *Angewandte Chemie International Edition*. 57 (2018) 9392–9396. <https://doi.org/10.1002/anie.201804881>.

- [155] M. Gong, Y. Li, H. Wang, Y. Liang, J.Z. Wu, J. Zhou, J. Wang, T. Regier, F. Wei, H. Dai, An Advanced Ni–Fe Layered Double Hydroxide Electrocatalyst for Water Oxidation, *J. Am. Chem. Soc.* 135 (2013) 8452–8455. <https://doi.org/10.1021/ja4027715>.
- [156] C. Kuai, Y. Zhang, D. Wu, D. Sokaras, L. Mu, S. Spence, D. Nordlund, F. Lin, X.-W. Du, Fully Oxidized Ni–Fe Layered Double Hydroxide with 100% Exposed Active Sites for Catalyzing Oxygen Evolution Reaction, *ACS Catal.* 9 (2019) 6027–6032. <https://doi.org/10.1021/acscatal.9b01935>.
- [157] S. Bae, J.-E. Jang, H.-W. Lee, J. Ryu, Tailored Assembly of Molecular Water Oxidation Catalysts on Photoelectrodes for Artificial Photosynthesis: Tailored Assembly of Molecular Water Oxidation Catalysts on Photoelectrodes for Artificial Photosynthesis, *European Journal of Inorganic Chemistry*. (2019). <https://doi.org/10.1002/ejic.201801328>.
- [158] C. Gao, J. Wang, H. Xu, Y. Xiong, Coordination chemistry in the design of heterogeneous photocatalysts, *Chemical Society Reviews*. 46 (2017) 2799–2823. <https://doi.org/10.1039/C6CS00727A>.
- [159] R. Brimblecombe, G.C. Dismukes, G.F. Swiegers, L. Spiccia, Molecular water-oxidation catalysts for photoelectrochemical cells, *Dalton Trans.* (2009) 9374–9384. <https://doi.org/10.1039/B912669D>.
- [160] T. Wada, K. Tanaka, Reversible Bond Formation and Cleavage of the Oxo Bridge of $[\text{Ru}_2(\mu\text{-O})(\text{dioxolene})_2(\text{btpyxa})]^{3+}$ [btpyxa = 2,7-Di-tert-butyl-9,9-dimethyl-4,5-bis(2,2':6',2''-terpyrid-4'-yl)xanthene] Driven by a Three-Electron Redox Reaction, *European Journal of Inorganic Chemistry*. 2005 (2005) 3832–3839. <https://doi.org/10.1002/ejic.200500141>.
- [161] R. Li, Y. Li, P. Yang, D. Wang, H. Xu, B. Wang, F. Meng, J. Zhang, M. An, Electrodeposition: Synthesis of advanced transition metal-based catalyst for hydrogen production via electrolysis of water, *Journal of Energy Chemistry*. 57 (2021) 547–566. <https://doi.org/10.1016/j.jechem.2020.08.040>.
- [162] Z. Yan, H. Liu, Z. Hao, M. Yu, X. Chen, J. Chen, Electrodeposition of (hydro)oxides for an oxygen evolution electrode, *Chem. Sci.* 11 (2020) 10614–10625. <https://doi.org/10.1039/D0SC01532F>.
- [163] K. Zhang, Z. Yan, J. Chen, Electrodeposition Accelerates Metal-Based Batteries, *Joule*. 4 (2020) 10–11. <https://doi.org/10.1016/j.joule.2019.12.012>.
- [164] I. Roger, M.D. Symes, First row transition metal catalysts for solar-driven water oxidation produced by electrodeposition, *J. Mater. Chem. A*. 4 (2016) 6724–6741. <https://doi.org/10.1039/C5TA09423B>.
- [165] C. Fan, D.L. Piron, Electrodeposition as a means of producing large-surface electrodes required in water electrolysis, *Surface and Coatings Technology*. 73 (1995) 91–97. [https://doi.org/10.1016/0257-8972\(94\)02373-5](https://doi.org/10.1016/0257-8972(94)02373-5).
- [166] W. Zhang, Y. Wu, J. Qi, M. Chen, R. Cao, A Thin NiFe Hydroxide Film Formed by Stepwise Electrodeposition Strategy with Significantly Improved Catalytic Water Oxidation Efficiency, *Advanced Energy Materials*. 7 (2017) 1602547. <https://doi.org/10.1002/aenm.201602547>.
- [167] R.H. Crabtree, Resolving Heterogeneity Problems and Impurity Artifacts in Operationally Homogeneous Transition Metal Catalysts, *Chem. Rev.* 112 (2012) 1536–1554. <https://doi.org/10.1021/cr2002905>.
- [168] V. Artero, M. Fontecave, Solar fuels generation and molecular systems: is it homogeneous or heterogeneous catalysis?, *Chem. Soc. Rev.* 42 (2013) 2338–2356. <https://doi.org/10.1039/C2CS35334B>.

- [169] M.D. Kärkäs, B. Åkermark, Water oxidation using earth-abundant transition metal catalysts: opportunities and challenges, *Dalton Transactions*. 45 (2016) 14421–14461. <https://doi.org/10.1039/C6DT00809G>.
- [170] E.L. Demeter, S.L. Hilburg, N.R. Washburn, T.J. Collins, J.R. Kitchin, Electrocatalytic Oxygen Evolution with an Immobilized TAML Activator, *J. Am. Chem. Soc.* 136 (2014) 5603–5606. <https://doi.org/10.1021/ja5015986>.
- [171] B.M. Klepser, B.M. Bartlett, Anchoring a Molecular Iron Catalyst to Solar-Responsive WO₃ Improves the Rate and Selectivity of Photoelectrochemical Water Oxidation, *J. Am. Chem. Soc.* 136 (2014) 1694–1697. <https://doi.org/10.1021/ja4086808>.
- [172] T. Shi, H. Li, L. Ding, F. You, L. Ge, Q. Liu, K. Wang, Facile Preparation of Unsubstituted Iron(II) Phthalocyanine/Carbon Nitride Nanocomposites: A Multipurpose Catalyst with Reciprocally Enhanced Photo/Electrocatalytic Activity, *ACS Sustainable Chem. Eng.* 7 (2019) 3319–3328. <https://doi.org/10.1021/acssuschemeng.8b05366>.
- [173] W. Sinha, A. Mahammed, N. Fridman, Z. Gross, Water Oxidation Catalysis by Mono- and Binuclear Iron Corroles, *ACS Catalysis*. 10 (2020) 3764–3772. <https://doi.org/10.1021/acscatal.9b05382>.
- [174] W.A. Hoffert, M.T. Mock, A.M. Appel, J.Y. Yang, Incorporation of Hydrogen-Bonding Functionalities into the Second Coordination Sphere of Iron-Based Water-Oxidation Catalysts, *European Journal of Inorganic Chemistry*. 2013 (2013) 3846–3857. <https://doi.org/10.1002/ejic.201201499>.
- [175] P. Tan, H.-K. Kwong, T.-C. Lau, Catalytic oxidation of water and alcohols by a robust iron(III) complex bearing a cross-bridged cyclam ligand, *Chem. Commun.* 51 (2015) 12189–12192. <https://doi.org/10.1039/C5CC02868J>.
- [176] K.G. Kottrup, D.G.H. Hettterscheid, Evaluation of iron-based electrocatalysts for water oxidation – an on-line mass spectrometry approach, *Chem. Commun.* 52 (2016) 2643–2646. <https://doi.org/10.1039/C5CC10092E>.
- [177] T.E. Rosser, M.A. Gross, Y.-H. Lai, E. Reisner, Precious-metal free photoelectrochemical water splitting with immobilised molecular Ni and Fe redox catalysts, *Chem. Sci.* 7 (2016) 4024–4035. <https://doi.org/10.1039/C5SC04863J>.
- [178] S.M. Al-Zurajji, D. Lukács, M. Németh, K. Frey, T. Benkó, L. Illés, J.S. Pap, An Iron(III) Complex with Pincer Ligand—Catalytic Water Oxidation through Controllable Ligand Exchange, *Reactions*. 1 (2020) 16–36. <https://doi.org/10.3390/reactions1010003>.
- [179] S.M. Al-Zurajji, T. Benkó, K. Frey, Z. Kerner, J.S. Pap, Electrodeposition of Fe-Complexes on Oxide Surfaces for Efficient OER Catalysis, *Catalysts*. 11 (2021) 577. <https://doi.org/10.3390/catal11050577>.
- [180] J.S. Pap, A. Draksharapu, M. Giorgi, W.R. Browne, J. Kaizer, G. Speier, Stabilisation of μ -peroxido-bridged Fe(III) intermediates with non-symmetric bidentate N-donor ligands, *Chem. Commun.* 50 (2014) 1326–1329. <https://doi.org/10.1039/C3CC48196D>.
- [181] T. Váradi, J.S. Pap, M. Giorgi, L. Párkányi, T. Csay, G. Speier, J. Kaizer, Iron(III) Complexes with Meridional Ligands as Functional Models of Intradiol-Cleaving Catechol Dioxygenases, *Inorganic Chemistry*. 52 (2013) 1559–1569. <https://doi.org/10.1021/ic302378r>.
- [182] F. Scholz, Voltammetric techniques of analysis: the essentials, *ChemTexts*. 1 (2015) 17. <https://doi.org/10.1007/s40828-015-0016-y>.
- [183] J. Wang, *Analytical Electrochemistry: Wang/Analytical Electrochemistry*, Third Edition, John Wiley & Sons, Inc., Hoboken, NJ, USA, 2006. <https://doi.org/10.1002/0471790303>.

- [184] N. Elgrishi, K.J. Rountree, B.D. McCarthy, E.S. Rountree, T.T. Eisenhart, J.L. Dempsey, A Practical Beginner's Guide to Cyclic Voltammetry, *J. Chem. Educ.* 95 (2018) 197–206. <https://doi.org/10.1021/acs.jchemed.7b00361>.
- [185] A.J. Bard, L.R. Faulkner, *Electrochemical methods: fundamentals and applications*, 2nd ed, Wiley, New York, 2001.
- [186] K.J. Lee, N. Elgrishi, B. Kandemir, J.L. Dempsey, Electrochemical and spectroscopic methods for evaluating molecular electrocatalysts, *Nat Rev Chem.* 1 (2017) 1–14. <https://doi.org/10.1038/s41570-017-0039>.
- [187] V. Mirceski, S. Skrzypek, L. Stojanov, Square-wave voltammetry, *ChemTexts.* 4 (2018) 17. <https://doi.org/10.1007/s40828-018-0073-0>.
- [188] V.V. Pavlishchuk, A.W. Addison, Conversion constants for redox potentials measured versus different reference electrodes in acetonitrile solutions at 25°C, *Inorganica Chimica Acta.* 298 (2000) 97–102. [https://doi.org/10.1016/S0020-1693\(99\)00407-7](https://doi.org/10.1016/S0020-1693(99)00407-7).
- [189] B. Rezaei, N. Irannejad, Chapter 2 - Electrochemical detection techniques in biosensor applications, in: A.A. Ensafi (Ed.), *Electrochemical Biosensors*, Elsevier, 2019: pp. 11–43. <https://doi.org/10.1016/B978-0-12-816491-4.00002-4>.
- [190] D.H. Evans, M.J. Kelly, Theory for double potential step chronoamperometry, chronocoulometry, and chronoabsorptometry with a quasi-reversible electrode reaction, *Anal. Chem.* 54 (1982) 1727–1729. <https://doi.org/10.1021/ac00248a016>.
- [191] E. Barsoukov, J.R. Macdonald, eds., *Impedance spectroscopy: theory, experiment, and applications*, 2nd ed, Wiley-Interscience, Hoboken, N.J, 2005.
- [192] R. Beltrán-Suito, V. Forstner, J.N. Hausmann, S. Mebs, J. Schmidt, I. Zaharieva, K. Laun, I. Zebger, H. Dau, P.W. Menezes, M. Driess, A soft molecular 2Fe–2As precursor approach to the synthesis of nanostructured FeAs for efficient electrocatalytic water oxidation, *Chem. Sci.* 11 (2020) 11834–11842. <https://doi.org/10.1039/D0SC04384B>.
- [193] S.M. Al-Zurajji, D. Lukács, M. Németh, K. Frey, T. Benkó, L. Illés, J.S. Pap, An Iron(III) Complex with Pincer Ligand—Catalytic Water Oxidation through Controllable Ligand Exchange, *Reactions.* 1 (2020) 16–36. <https://doi.org/10.3390/reactions1010003>.
- [194] X. Wu, F. Li, B. Zhang, L. Sun, Molecular complexes in water oxidation: Pre-catalysts or real catalysts, *Journal of Photochemistry and Photobiology C: Photochemistry Reviews.* 25 (2015) 71–89. <https://doi.org/10.1016/j.jphotochemrev.2015.07.002>.
- [195] S. Ebnesajjad, Chapter 4 - Surface and Material Characterization Techniques, in: S. Ebnesajjad (Ed.), *Surface Treatment of Materials for Adhesive Bonding (Second Edition)*, William Andrew Publishing, Oxford, 2014: pp. 39–75. <https://doi.org/10.1016/B978-0-323-26435-8.00004-6>.
- [196] H.M. McNair, J.M. Miller, N.H. Snow, *Basic gas chromatography*, 2019. <https://search.ebscohost.com/login.aspx?direct=true&scope=site&db=nlebk&db=nlabk&AN=2220863>.
- [197] J. Li, C. A. Triana, W. Wan, D.P.A. Saseendran, Y. Zhao, S. E. Balaghi, S. Heidari, G. R. Patzke, Molecular and heterogeneous water oxidation catalysts: recent progress and joint perspectives, *Chemical Society Reviews.* 50 (2021) 2444–2485. <https://doi.org/10.1039/D0CS00978D>.
- [198] L.-H. Zhang, S. Mathew, J. Hessels, J.N.H. Reek, F. Yu, Homogeneous Catalysts Based on First-Row Transition-Metals for Electrochemical Water Oxidation, *ChemSusChem.* n/a (n.d.). <https://doi.org/10.1002/cssc.202001876>.
- [199] S. Bang, Y.-M. Lee, S. Hong, K.-B. Cho, Y. Nishida, M.S. Seo, R. Sarangi, S. Fukuzumi, W. Nam, Redox-inactive metal ions modulate the reactivity and oxygen release of

- mononuclear non-haem iron(III)–peroxo complexes, *Nature Chemistry*. 6 (2014) 934–940. <https://doi.org/10.1038/nchem.2055>.
- [200] A. R. Parent, R. H. Crabtree, G. W. Brudvig, Comparison of primary oxidants for water-oxidation catalysis, *Chemical Society Reviews*. 42 (2013) 2247–2252. <https://doi.org/10.1039/C2CS35225G>.
- [201] A. Singh, L. Spiccia, Water oxidation catalysts based on abundant 1st row transition metals, *Coordination Chemistry Reviews*. 257 (2013) 2607–2622. <https://doi.org/10.1016/j.ccr.2013.02.027>.
- [202] J.L. Fillol, Z. Codolà, I. Garcia-Bosch, L. Gómez, J.J. Pla, M. Costas, Efficient water oxidation catalysts based on readily available iron coordination complexes, *Nature Chemistry*. 3 (2011) 807–813. <https://doi.org/10.1038/nchem.1140>.
- [203] W.C. Ellis, N.D. McDaniel, S. Bernhard, T.J. Collins, Fast Water Oxidation Using Iron, *J. Am. Chem. Soc.* 132 (2010) 10990–10991. <https://doi.org/10.1021/ja104766z>.
- [204] U. Hintermair, S.M. Hashmi, M. Elimelech, R.H. Crabtree, Particle Formation during Oxidation Catalysis with Cp* Iridium Complexes, *J. Am. Chem. Soc.* 134 (2012) 9785–9795. <https://doi.org/10.1021/ja3033026>.
- [205] Z. Codolà, I. Gamba, F. Acuña-Parés, C. Casadevall, M. Clémancey, J.-M. Latour, J.M. Luis, J. Lloret-Fillol, M. Costas, Design of Iron Coordination Complexes as Highly Active Homogenous Water Oxidation Catalysts by Deuteration of Oxidation-Sensitive Sites, *J. Am. Chem. Soc.* 141 (2019) 323–333. <https://doi.org/10.1021/jacs.8b10211>.
- [206] K.G. Kottrup, D.G.H. Hettterscheid, Evaluation of iron-based electrocatalysts for water oxidation – an on-line mass spectrometry approach, *Chem. Commun.* 52 (2016) 2643–2646. <https://doi.org/10.1039/C5CC10092E>.
- [207] K.G. Kottrup, S. D’Agostini, P.H. van Langevelde, M.A. Siegler, D.G.H. Hettterscheid, Catalytic Activity of an Iron-Based Water Oxidation Catalyst: Substrate Effects of Graphitic Electrodes, *ACS Catalysis*. 8 (2018) 1052–1061. <https://doi.org/10.1021/acscatal.7b03284>.
- [208] D.R. Weinberg, C.J. Gagliardi, J.F. Hull, C.F. Murphy, C.A. Kent, B.C. Westlake, A. Paul, D.H. Ess, D.G. McCafferty, T.J. Meyer, Proton-Coupled Electron Transfer, *Chemical Reviews*. 112 (2012) 4016–4093. <https://doi.org/10.1021/cr200177j>.
- [209] B. Zhang, L. Sun, Ru-bda: Unique Molecular Water-Oxidation Catalysts with Distortion Induced Open Site and Negatively Charged Ligands, *J. Am. Chem. Soc.* 141 (2019) 5565–5580. <https://doi.org/10.1021/jacs.8b12862>.
- [210] J.S. Pap, A. Draksharapu, M. Giorgi, W.R. Browne, J. Kaizer, G. Speier, Stabilisation of μ -peroxido-bridged Fe(III) intermediates with non-symmetric bidentate N-donor ligands, *Chem. Commun.* 50 (2014) 1326–1329. <https://doi.org/10.1039/C3CC48196D>.
- [211] H.-L. Xia, S. Ardo, A.A. Narducci Sarjeant, S. Huang, G.J. Meyer, Photodriven Spin Change of Fe(II) Benzimidazole Compounds Anchored to Nanocrystalline TiO₂ Thin Films, *Langmuir*. 25 (2009) 13641–13652. <https://doi.org/10.1021/la9022213>.
- [212] W.A. Hoffert, M.T. Mock, A.M. Appel, J.Y. Yang, Incorporation of Hydrogen-Bonding Functionalities into the Second Coordination Sphere of Iron-Based Water-Oxidation Catalysts, *European Journal of Inorganic Chemistry*. 2013 (2013) 3846–3857. <https://doi.org/10.1002/ejic.201201499>.
- [213] M.J. Collins, K. Ray, L. Que, Electrochemical Generation of a Nonheme Oxoiron(IV) Complex, *Inorganic Chemistry*. 45 (2006) 8009–8011. <https://doi.org/10.1021/ic061263i>.

- [214] Z. Codolà, L. Gómez, S.T. Kleespies, L. Que Jr, M. Costas, J. Lloret-Fillol, Evidence for an oxygen evolving iron–oxo–cerium intermediate in iron-catalysed water oxidation, *Nature Communications*. 6 (2015) 5865.
- [215] Z. Codolà, I. Garcia-Bosch, F. Acuña-Parés, I. Prat, J.M. Luis, M. Costas, J. Lloret-Fillol, Electronic Effects on Single-Site Iron Catalysts for Water Oxidation, *Chemistry - A European Journal*. 19 (2013) 8042–8047. <https://doi.org/10.1002/chem.201301112>.
- [216] F. Acuña-Parés, Z. Codolà, M. Costas, J.M. Luis, J. Lloret-Fillol, Unraveling the Mechanism of Water Oxidation Catalyzed by Nonheme Iron Complexes, *Chemistry - A European Journal*. 20 (2014) 5696–5707. <https://doi.org/10.1002/chem.201304367>.
- [217] E.S. Rountree, B.D. McCarthy, T.T. Eisenhart, J.L. Dempsey, Evaluation of Homogeneous Electrocatalysts by Cyclic Voltammetry, *Inorganic Chemistry*. 53 (2014) 9983–10002. <https://doi.org/10.1021/ic500658x>.
- [218] M.K. Coggins, M.-T. Zhang, A.K. Vannucci, C.J. Dares, T.J. Meyer, Electrocatalytic Water Oxidation by a Monomeric Amidate-Ligated Fe(III)–Aqua Complex, *J. Am. Chem. Soc.* 136 (2014) 5531–5534. <https://doi.org/10.1021/ja412822u>.
- [219] E.C. Ellingsworth, B. Turner, G. Szulczewski, Thermal conversion of [Fe(phen)₃](SCN)₂ thin films into the spin crossover complex Fe(phen)₂(NCS)₂, *RSC Advances*. 3 (2013) 3745. <https://doi.org/10.1039/c3ra22534h>.
- [220] L. Li, A.R. Craze, R. Akiyoshi, A. Tsukiashi, S. Hayami, O. Mustonen, M.M. Bhabhade, S. Bhattacharyya, C.E. Marjo, Y. Wang, L.F. Lindoy, J.R. Aldrich-Wright, F. Li, Direct monitoring of spin transitions in a dinuclear triple-stranded helicate iron(II) complex through X-ray photoelectron spectroscopy, *Dalton Transactions*. 47 (2018) 2543–2548. <https://doi.org/10.1039/C7DT04190J>.
- [221] A. Pronschinske, R.C. Bruce, G. Lewis, Y. Chen, A. Calzolari, M. Buongiorno-Nardelli, D.A. Shultz, W. You, D.B. Dougherty, Iron(ii) spin crossover films on Au(111): scanning probe microscopy and photoelectron spectroscopy, *Chemical Communications*. 49 (2013) 10446. <https://doi.org/10.1039/c3cc44904a>.
- [222] H. Bülter, G. Denuault, S. Mátéfi-Tempfli, M. Mátéfi-Tempfli, C. Dosche, G. Wittstock, Electrochemical analysis of nanostructured iron oxides using cyclic voltammetry and scanning electrochemical microscopy, *Electrochimica Acta*. 222 (2016) 1326–1334. <https://doi.org/10.1016/j.electacta.2016.11.108>.
- [223] Z. Codolà, I. Garcia-Bosch, F. Acuña-Parés, I. Prat, J.M. Luis, M. Costas, J. Lloret-Fillol, Electronic Effects on Single-Site Iron Catalysts for Water Oxidation, *Chemistry - A European Journal*. 19 (2013) 8042–8047. <https://doi.org/10.1002/chem.201301112>.
- [224] L. Wu, A. Nayak, J. Shao, T.J. Meyer, Crossing the bridge from molecular catalysis to a heterogenous electrode in electrocatalytic water oxidation, *Proc Natl Acad Sci USA*. 116 (2019) 11153–11158. <https://doi.org/10.1073/pnas.1902455116>.
- [225] P. Garrido-Barros, C. Gimbert-Suriñach, D. Moonshiram, A. Picón, P. Monge, V.S. Batista, A. Llobet, Electronic π -Delocalization Boosts Catalytic Water Oxidation by Cu(II) Molecular Catalysts Heterogenized on Graphene Sheets, *Journal of the American Chemical Society*. 139 (2017) 12907–12910. <https://doi.org/10.1021/jacs.7b06828>.
- [226] M.A.W. Lawrence, K.-A. Green, P.N. Nelson, S.C. Lorraine, Review: Pincer ligands—Tunable, versatile and applicable, *Polyhedron*. 143 (2018) 11–27. <https://doi.org/10.1016/j.poly.2017.08.017>.
- [227] R. Csonka, G. Speier, J. Kaizer, Isoindoline-derived ligands and applications, *RSC Advances*. 5 (2015) 18401–18419. <https://doi.org/10.1039/C4RA15379K>.

- [228] A. Scheja, D. Baabe, D. Menzel, C. Pietzonka, P. Schweyen, M. Bröring, Spin Crossover and Valence Tautomerism in Neutral Homoleptic Iron Complexes of Bis(pyridylimino)isoindolines, *Chemistry – A European Journal*. 21 (2015) 14196–14204. <https://doi.org/10.1002/chem.201501551>.
- [229] B. Das, A. Orthaber, S. Ott, A. Thapper, Iron Pentapyridyl Complexes as Molecular Water Oxidation Catalysts: Strong Influence of a Chloride Ligand and pH in Altering the Mechanism, *ChemSusChem*. 9 (2016) 1178–1186. <https://doi.org/10.1002/cssc.201600052>.
- [230] R. Semino, M.P. Longinotti, Excess protons in water-acetone mixtures. II. A conductivity study, *The Journal of Chemical Physics*. 139 (2013) 164510. <https://doi.org/10.1063/1.4826464>.
- [231] W.J. Geary, The use of conductivity measurements in organic solvents for the characterisation of coordination compounds, *Coordination Chemistry Reviews*. 7 (1971) 81–122. [https://doi.org/10.1016/S0010-8545\(00\)80009-0](https://doi.org/10.1016/S0010-8545(00)80009-0).
- [232] M. Kruck, D.C. Sauer, M. Enders, H. Wadepohl, L.H. Gade, Bis(2-pyridylimino)isoindolato iron(ii) and cobalt(ii) complexes: Structural chemistry and paramagnetic NMR spectroscopy, *Dalton Transactions*. 40 (2011) 10406. <https://doi.org/10.1039/c1dt10617a>.
- [233] S.M. Al-Zuraiji, T. Benkó, L. Illés, M. Németh, K. Frey, A. Sulyok, J.S. Pap, Utilization of hydrophobic ligands for water-insoluble Fe(II) water oxidation catalysts – Immobilization and characterization, *Journal of Catalysis*. 381 (2020) 615–625. <https://doi.org/10.1016/j.jcat.2019.12.003>.
- [234] L. Floreano, A. Cossaro, R. Gotter, A. Verdini, G. Bavdek, F. Evangelista, A. Ruocco, A. Morgante, D. Cvetko, Periodic Arrays of Cu-Phthalocyanine Chains on Au(110), *The Journal of Physical Chemistry C*. 112 (2008) 10794–10802. <https://doi.org/10.1021/jp711140e>.
- [235] A. Sarasola, M. Abadía, C. Rogero, A. Garcia-Lekue, Theoretical Insights into Unexpected Molecular Core Level Shifts: Chemical and Surface Effects, *The Journal of Physical Chemistry Letters*. 8 (2017) 5718–5724. <https://doi.org/10.1021/acs.jpcclett.7b02583>.
- [236] S.M. Al-Zuraiji, T. Benkó, L. Illés, M. Németh, K. Frey, A. Sulyok, J.S. Pap, Utilization of hydrophobic ligands for water-insoluble Fe(II) water oxidation catalysts – Immobilization and characterization, *Journal of Catalysis*. 381 (2020) 615–625. <https://doi.org/10.1016/j.jcat.2019.12.003>.
- [237] J.S. Pap, V. Bányai, D.S. Szilvási, J. Kaizer, G. Speier, M. Giorgi, Influence of meridional N₃-ligands on supramolecular assembling and redox behavior of carboxylatocopper(II) complexes, *Inorganic Chemistry Communications*. 14 (2011) 1767–1772. <https://doi.org/10.1016/j.inoche.2011.08.005>.
- [238] J.S. Pap, B. Kripli, V. Bányai, M. Giorgi, L. Korecz, T. Gajda, D. Árus, J. Kaizer, G. Speier, Tetra-, penta- and hexacoordinate copper(II) complexes with N₃ donor isoindoline-based ligands: Characterization and SOD-like activity, *Inorganica Chimica Acta*. 376 (2011) 158–169. <https://doi.org/10.1016/j.ica.2011.06.001>.
- [239] Z. Yan, H. Liu, Z. Hao, M. Yu, X. Chen, J. Chen, Electrodeposition of (hydro)oxides for an oxygen evolution electrode, *Chemical Science*. 11 (2020) 10614–10625. <https://doi.org/10.1039/D0SC01532F>.
- [240] G.H.A. Therese, P.V. Kamath, Electrochemical Synthesis of Metal Oxides and Hydroxides, *Chem. Mater*. 12 (2000) 1195–1204. <https://doi.org/10.1021/cm990447a>.

- [241] H. Iwami, M. Okamura, M. Kondo, S. Masaoka, Electrochemical Polymerization Provides a Function-Integrated System for Water Oxidation, *Angewandte Chemie International Edition*. (2020). <https://doi.org/10.1002/anie.202015174>.
- [242] I.M. Dharmadasa, J. Haigh, Strengths and Advantages of Electrodeposition as a Semiconductor Growth Technique for Applications in Macroelectronic Devices, *J. Electrochem. Soc.* 153 (2005) G47. <https://doi.org/10.1149/1.2128120>.
- [243] B. Kripli, G. Baráth, É. Balogh-Hergovich, M. Giorgi, A.J. Simaan, L. Párkányi, J.S. Pap, J. Kaizer, G. Speier, Correlation between the SOD-like activity of hexacoordinate iron(II) complexes and their Fe³⁺/Fe²⁺ redox potentials, *Inorganic Chemistry Communications*. 14 (2011) 205–209. <https://doi.org/10.1016/j.inoche.2010.10.023>.
- [244] G. Martić, J.T. Engle, C.J. Ziegler, Complexes of 1,3-bis(2-thiazolylimino)isoindoline with middle and late first row transition metals, *Inorganic Chemistry Communications*. 14 (2011) 1749–1752. <https://doi.org/10.1016/j.inoche.2011.08.001>.
- [245] M.B. Meder, L.H. Gade, Coordination Chemistry of 1,3-Bis(2-pyridylimino)- and 1,3-Bis(2-thiazolylimino)soindole Copper Complexes: Investigation of Their Catalytic Behavior in Oxidation Reactions, *Eur. J. Inorg. Chem.* 2004 (2004) 2716–2722. <https://doi.org/10.1002/ejic.200400012>.
- [246] T. Shinagawa, A.T. Garcia-Esparza, K. Takanabe, Insight on Tafel slopes from a microkinetic analysis of aqueous electrocatalysis for energy conversion, *Sci Rep.* 5 (2015) 13801. <https://doi.org/10.1038/srep13801>.
- [247] D. Lukács, M. Németh, Ł. Szyrwił, L. Illés, B. Pécz, S. Shen, J.S. Pap, Behavior of a Cu-Peptide complex under water oxidation conditions – Molecular electrocatalyst or precursor to nanostructured CuO films?, *Solar Energy Materials and Solar Cells*. 201 (2019) 110079. <https://doi.org/10.1016/j.solmat.2019.110079>.
- [248] M. Tahir, L. Pan, F. Idrees, X. Zhang, L. Wang, J.-J. Zou, Z.L. Wang, Electrocatalytic oxygen evolution reaction for energy conversion and storage: A comprehensive review, *Nano Energy*. 37 (2017) 136–157. <https://doi.org/10.1016/j.nanoen.2017.05.022>.
- [249] J. Wang, F. Xu, H. Jin, Y. Chen, Y. Wang, Non-Noble Metal-based Carbon Composites in Hydrogen Evolution Reaction: Fundamentals to Applications, *Advanced Materials*. 29 (2017) 1605838. <https://doi.org/10.1002/adma.201605838>.
- [250] N.-T. Suen, S.-F. Hung, Q. Quan, N. Zhang, Y.-J. Xu, H.M. Chen, Electrocatalysis for the oxygen evolution reaction: recent development and future perspectives, *Chem. Soc. Rev.* 46 (2017) 337–365. <https://doi.org/10.1039/C6CS00328A>.
- [251] J. Hou, Y. Wu, B. Zhang, S. Cao, Z. Li, L. Sun, Rational Design of Nanoarray Architectures for Electrocatalytic Water Splitting, *Advanced Functional Materials*. 29 (2019) 1808367. <https://doi.org/10.1002/adfm.201808367>.
- [252] H. Bandal, K.K. Reddy, A. Chaugule, H. Kim, Iron-based heterogeneous catalysts for oxygen evolution reaction; change in perspective from activity promoter to active catalyst, *Journal of Power Sources*. 395 (2018) 106–127. <https://doi.org/10.1016/j.jpowsour.2018.05.047>.
- [253] V. Charles, A.O. Anumah, K.A. Adegoke, M.O. Adesina, I.P. Ebuka, N.A. Gaya, S. Ogwuche, M.O. Yakubu, Progress and challenges pertaining to the earthly-abundant electrocatalytic materials for oxygen evolution reaction, *Sustainable Materials and Technologies*. 28 (2021) e00252. <https://doi.org/10.1016/j.susmat.2021.e00252>.
- [254] C. Costentin, S. Drouet, M. Robert, J.-M. Savéant, Turnover Numbers, Turnover Frequencies, and Overpotential in Molecular Catalysis of Electrochemical Reactions.

- Cyclic Voltammetry and Preparative-Scale Electrolysis, *J. Am. Chem. Soc.* 134 (2012) 11235–11242. <https://doi.org/10.1021/ja303560c>.
- [255] H. Lee, X. Wu, L. Sun, Copper-based homogeneous and heterogeneous catalysts for electrochemical water oxidation, *Nanoscale*. 12 (2020) 4187–4218. <https://doi.org/10.1039/C9NR10437B>.
- [256] T. Shinagawa, A.T. Garcia-Esparza, K. Takanabe, Insight on Tafel slopes from a microkinetic analysis of aqueous electrocatalysis for energy conversion, *Scientific Reports*. 5 (2015) 13801. <https://doi.org/10.1038/srep13801>.
- [257] A. Kudo, Y. Miseki, Heterogeneous photocatalyst materials for water splitting, *Chem. Soc. Rev.* 38 (2009) 253–278. <https://doi.org/10.1039/B800489G>.
- [258] H. Vrubel, T. Moehl, M. Grätzel, X. Hu, Revealing and accelerating slow electron transport in amorphous molybdenum sulphide particles for hydrogen evolution reaction, *Chem. Commun.* 49 (2013) 8985–8987. <https://doi.org/10.1039/C3CC45416A>.
- [259] A.P. Umpierre, E. de Jesús, J. Dupont, Turnover Numbers and Soluble Metal Nanoparticles, *ChemCatChem*. 3 (2011) 1413–1418. <https://doi.org/10.1002/cctc.201100159>.
- [260] J. Hagen, *Industrial Catalysis: A Practical Approach*, John Wiley & Sons, 2015.

Appendix (A)

Evaluation parameters for the performance of electrocatalysts

It is necessary to study some indispensable parameters that define the effectiveness of electrocatalysts. Generally addressing, the electrochemical analyses are presented in a three-electrode system, which is employed to assess the two half reaction activities (HER and OER), consisting of the working electrode (anode for OER and cathode for HER), reference electrode, and auxiliary electrode (counter electrode) as it is shown in the Experimental work (Chapter 3). Exhaustively, many reviews have reported the benchmarking methods to evaluate the activity of various electrocatalysts [248–251]. Specific parameters are essential for insightful information concerning the electrochemical reaction mechanism. Herein, we present a brief introduction to kinetic parameters that are generally utilized to evaluate the performance of electrocatalysts:

A. Overpotential (η)

In brief expression, The overpotential (η) represents the driving force of a reaction and is defined as the additional potential, beyond the thermodynamic requirement, needed to drive a reaction at a specific rate[185]. The catalytic current is normalized concerning the geometric surface area of the electrode[252]. (η) is one of the significant standard parameters to evaluate the performance of electrocatalysts. It reflects the difference between the applied potential E (actual electrode voltage needed to drive the reaction) and the potential theoretical need (potential under equilibrium conditions) E_{eq} , as shown in Equation A.1.1:

$$\eta = E - E_{eq} \quad \text{Eq. A. 1.1}$$

In concise expression, the (η) can be defined as the additional potential required to drive an electrochemical reaction from its reversible potential (where reversible potentials for HER and OER are 0 and 1.23 V *vs* NHE, respectively). The η is the most crucial factor in assessing the performance of electrocatalysts and is generally related to a value that must be applied to accomplish a specified current density. Thus, one can calculate the overpotential for the OER as $\eta_{\text{OER}} = E - 1.23 \text{ V}$ and the HER as $\eta_{\text{HER}} = E - 0 \text{ V}$ [60,249]. A lower overpotential for an electrocatalyst means reducing the kinetic energy barrier for the electrochemical reaction [250]. It is also noted that different current densities can be achieved at various overpotential values, and by relying on this note, it is essential to declare the current density of the read overpotential [253].

In homogeneous catalysis, the two significant activity parameters are the onset overpotential (η_o) and overpotential at 1 mA cm⁻² (η_i); these two parameters. η is commonly obtained via employing linear sweep voltammetry (LSV) or cyclic voltammetry (CV) curves by carefully choosing the experimental conditions [254]. In heterogeneous catalysis, η_o and η_i at a specific current density are also often defined, but especially at higher current densities, the IR drop caused by the electrolyte (ohmic resistance) should be considered. Equation A.1.2 can calculate the overpotential for heterogeneous catalysts [253]. Additionally, pH associated with overpotential is driven mainly by the Nernst equation, which only shows the equilibrium potential shift induced by the pH gradient:

$$\eta = E_{app} - IR - E_{O_2/H_2O} + 0.059pH \quad \text{Eq. A. 1.2}$$

Where E_{app} is the applied potential, IR is the potential loss caused by the electrolyte resistance. The potential applied for the OER may supply to the oxidation of the electrocatalyst itself [49]. The OER includes elementary steps that undergo different acidic or alkaline media mechanisms. The OER reaction could occur in multiple conditions across the pH range depending on the specific cell.

B. Faradaic efficiency (FE)

Faradaic efficiency describes electrons' efficiency in catalyzing the desired electrochemical reaction versus undesired reactions such as electrode redox [251]. FE is the amount of evolved oxygen O₂ (product) divided by the theoretical maximum according to the current passed during the electrolysis. It is a significant activity parameter in water splitting electrolysis that indicates the selectivity of the catalyst under study [45]. FE for OER can be obtained by calculating the total amount of charge Q (C) passed through the cell and the total amount of O₂ produced n_{O_2} (mol); see Equation A.1.3.

$$\text{Faradaic efficiency} = n_{O_2} / (Q / 4F) \quad \text{Eq. A. 1.3}$$

where F is the Faraday constant = 96,485 C/mol.

The total charge can be obtained from integrating the measured current during electrolysis. The total amount of O₂ produced can be measured by using gas chromatography (GC), optical oxygen sensor, rotating ring disc electrode (RRDE), or Clark electrode [255]. Notably, the Faraday efficiency should ideally be 100% [250]. As the overpotential need increases, unwanted side

reactions may lower FE (this is typically the case). Accordingly, the decreasing overpotential should be considered as the superiority task of electrocatalyst design [251].

C. Tafel analysis and exchange current density

Tafel analysis is an essential method to evaluate an electrocatalyst by profit information on the inherent kinetics of the electrocatalyst [256]. The Tafel equation in its original form is an empirical formula stating that the logarithm of the current density is linearly proportional to the applied potential ($\eta = a + b \log j$). The Tafel slope (b) may carry information on the rate-determining steps involved in electrocatalysis, and it can be associated with the reaction mechanism of electrocatalysts (in case the whole kinetics is known). It is also suitable for comparing the activity of different catalysts [256]. The Tafel slope explains the current density (j) and the overpotential (η) relationship. The same relationship can be deduced from the Butler–Volmer equation (Equation A.1.4) [55]:

$$j = j_o \left[\exp\left(\frac{\alpha_a n FE}{RT}\right) \eta + \exp\left(\frac{\alpha_c n FE}{RT}\right) \eta \right] \quad \text{Eq. A. 1.4}$$

Where α_a and α_c anodic and cathodic charge transfer coefficient is a specific material property for a given electrochemical reaction, at high overpotentials, the overall current is attributed to either the anodic or the cathodic process, while the other process is negligible; thus, the Butler–Volmer equation simplifies and transformed to the Tafel equation, (Equation A.1.5).

$$j = j_o \exp\left(\frac{\alpha_a n FE}{RT}\right) \eta \quad \text{Eq. A. 1.5}$$

By taking the logarithm function, Eq. 1.5 can be re-written as Equation A.1.6, where the exchange current density (j_o) and Tafel slope (b) can be calculated [55].

$$\eta = b \log \frac{j}{j_o} \quad \text{Eq. A. 1.6}$$

Figure A.1.1 shows how the overpotential need can be plotted against the logarithm of the anodic current. The exchange current (i_o) is another indicator to evaluate the electrocatalytic kinetics, which can be calculated at intercepts at $\eta = 0$ (see Fig. A.1.1). Exchange current (i_o) reflects the inherent activity of electrocatalysts at equilibrium potential or the intrinsic bonding/charge transferring interactions between electrocatalyst and reactant [251].

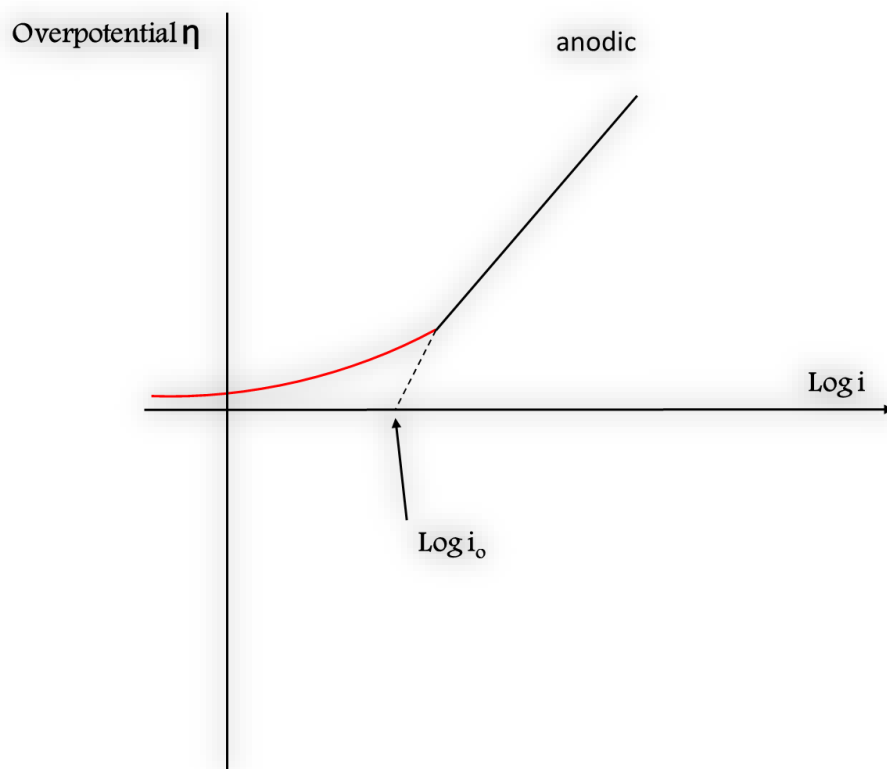


Figure A.1.1. Tafel plot for an anodic process.

A sizable value of i_0 and a slight Tafel slope indicate an excellent purposed electrocatalyst reaction [66,257]. In practice, Tafel slopes are estimated from slow polarization curves replotted as overpotential vs $\log(j)$, or, from the impedance data, the linear fitting of $\log(R_{ct})$ vs overpotential, in which R_{ct} represents the charge transfer resistance in the equivalent circuit fitted in impedance spectrum [249,258].

D. Turnover frequency (TOF) and Turnover number (TON)

The intrinsic rate of a catalytic reaction is also known as turnover frequency (TOF) [259]. For a fair comparison of the catalytic activity, the number of exposed active sites on the catalyst should be indicated by the TOF, which translates as the number of reactant molecules transformed per catalytic site over a unit of time, as shown in Eqs. (A.1.7, and A.1.8). The higher value of TOF implies a better electrocatalytic activity [49,253].

$$TOF = \frac{j \times A}{z \times F \times n}$$

Eq. A. 1. 7

Where j is the current density at a particular overpotential (mA cm^{-2}), A is the working electrode area, F is the Faraday constant, z is the number of transferred electrons, and n is the number of moles of the active materials. Eq.A.1.8 shows another form to calculate the TOF for heterogeneous OER electrocatalysts [248]:

$$TOF = \frac{\text{No. of evolved O}_2 \text{ molecules}}{\text{No. of active sites} \times \text{time}} \quad \text{Eq. A. 1.8}$$

It is challenging to achieve the specific TOF value because not all catalytic sites are involved in catalytic reactions due to the various experimental designs and catalyst loading, making it difficult to estimate the molar number (n) [251]. However, TOF still represents an influential role in electrocatalytic activity comparison between different electrocatalysts.

TON is a dimensionless number and a significant value to evaluate the stability of the catalysts. It can be defined as the amount of product converted from the reactant per mol of the effective catalyst (catalytic site) [259,260]. TON for water oxidation can be calculated by Equation A.1.9:

$$TON = \frac{\text{No. of evolved O}_2 \text{ molecules}}{\text{No. of active sites}} \quad \text{Eq. A. 1.9}$$

Significantly, stability is an essential parameter for assessing electrocatalysts in practical application. Usually, the stability can be measured by carrying out a chronoamperometry experiment by reading the current change vs reaction time at fixed potential or by carrying out a chronopotentiometry experiment by potential variation and fixing the current density [251]. Finally, the higher review of the parameters clearly shows that determining the catalytic activity of an OER electrocatalyst is not a simple duty. Three or more of the parameters must be achieved while examining the activity of the electrocatalyst.

Appendix (B)

Part(I)

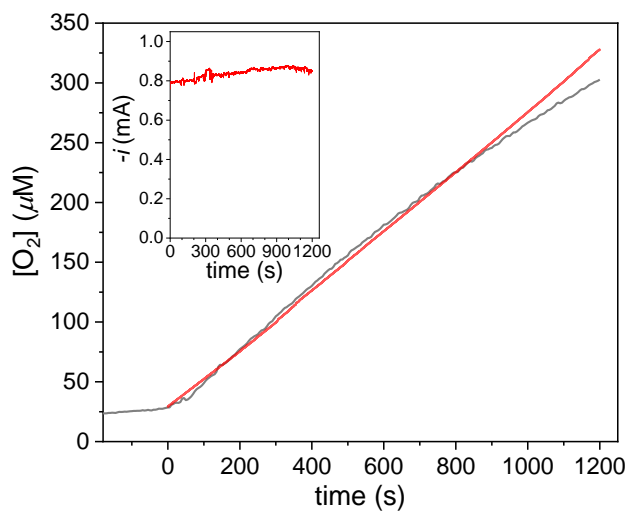


Figure A.4.1. An increase in the oxygen concentration was followed with an optical probe (NeoFox, immersed in the electrolyte near the working electrode) during electrolysis with 1/ITO (drop-casted, $0.78 \mu mol$), conditions: 0.2 M borate buffer, pH 8.3, +1.2 V vs. Ag/AgCl. The red line represents the expected increase in O_2 concentration based on 100% Faradaic efficiency as calculated from the electrolysis current shown in the inset.

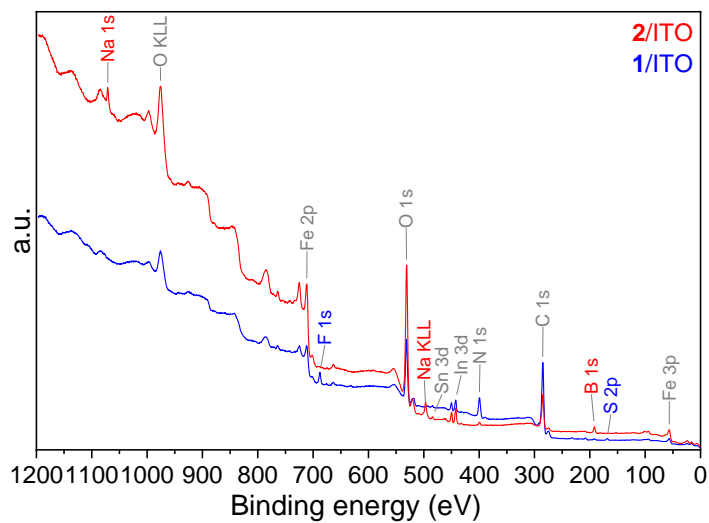


Figure A.4.2. XP spectra of 1/ITO and 2/ITO after electrolysis.

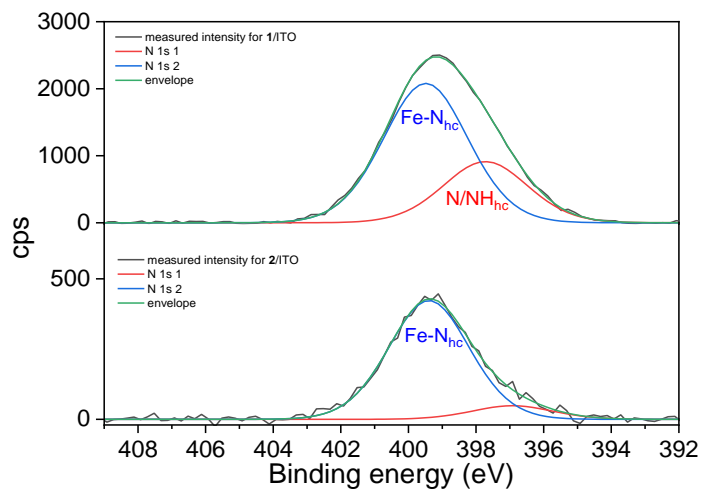
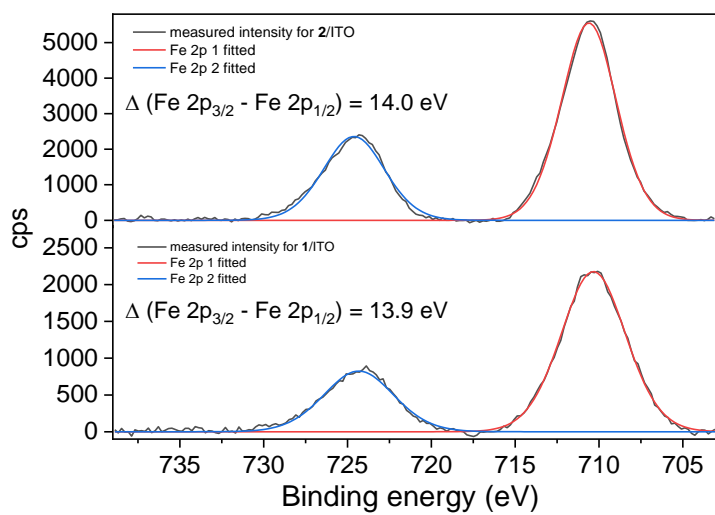


Figure S4.3. XP spectra and fitting of 1/ITO and 2/ITO used in CPE in the Fe and N binding energy region.

Part II

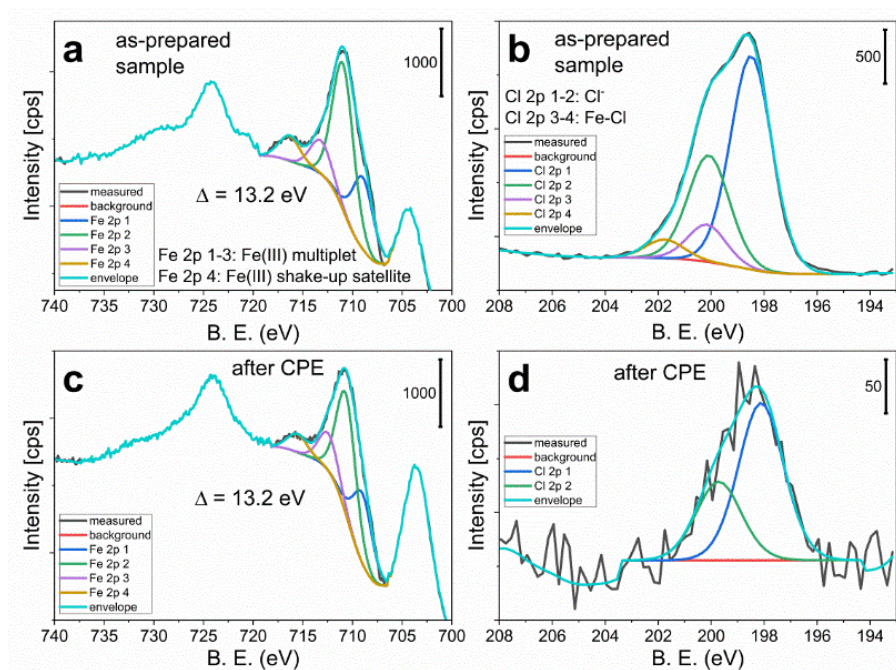


Figure A.4.4 (a) The Fe 2p and (b) the Cl 2p binding energy region of XP spectra of the as-prepared 3/ITO with the fitted components; (c) and (d) the corresponding spectra after CPE.

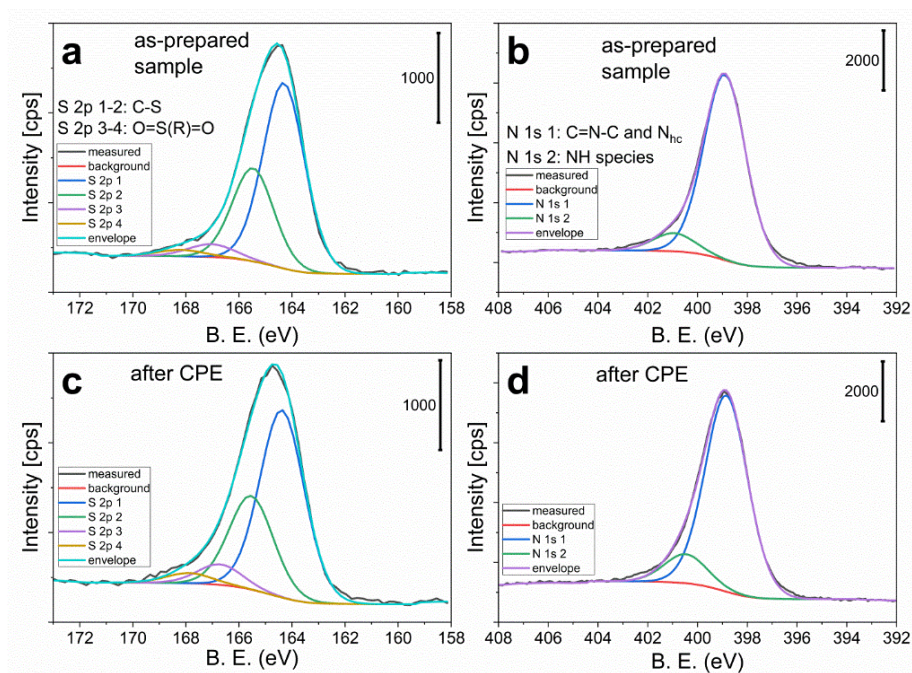


Figure A.4.5 (a) The S 2p and (b) the N 1s binding energy region of XP spectra of the as-prepared 3/ITO with the fitted components; (c) and (d) the corresponding spectra after CPE

Part (III)

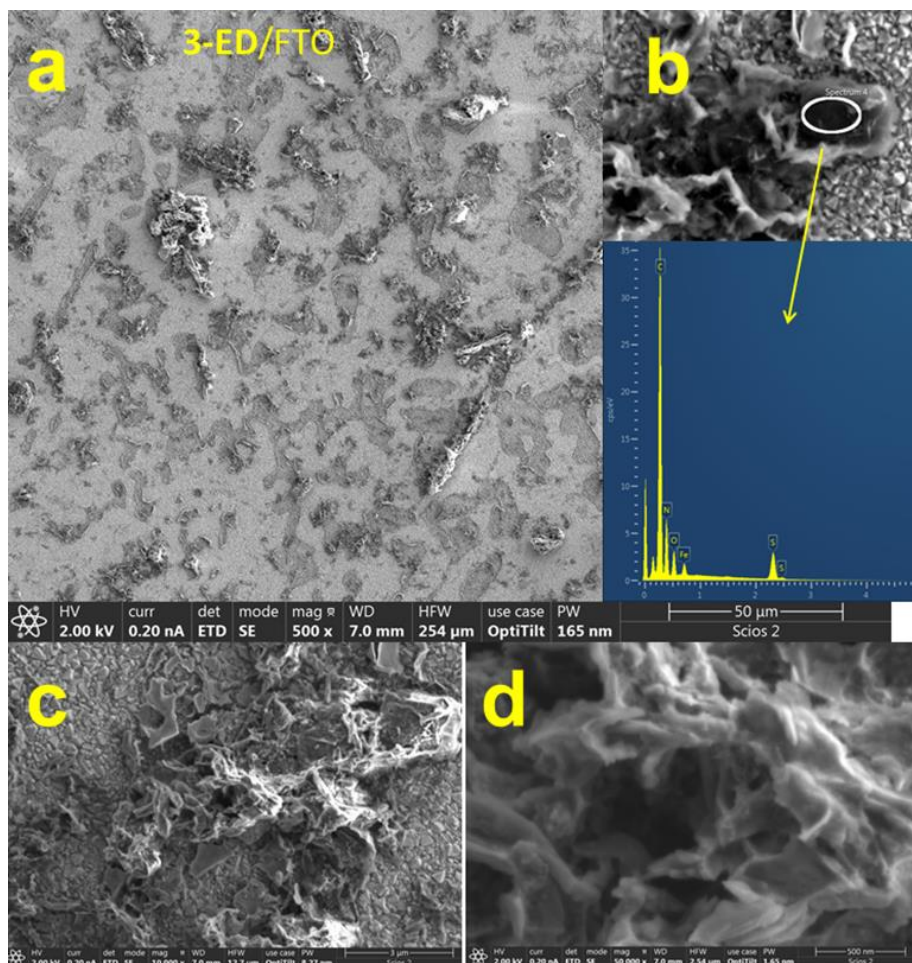


Figure A.4.6 (a) SEM image of 3-ED@FTO as-prepared and cleansed with MilliQ water to remove salt residues, (b) EDX spectrum of the area within the white circle; (c-d) SEM images at different magnifications (see the footers for experimental settings).

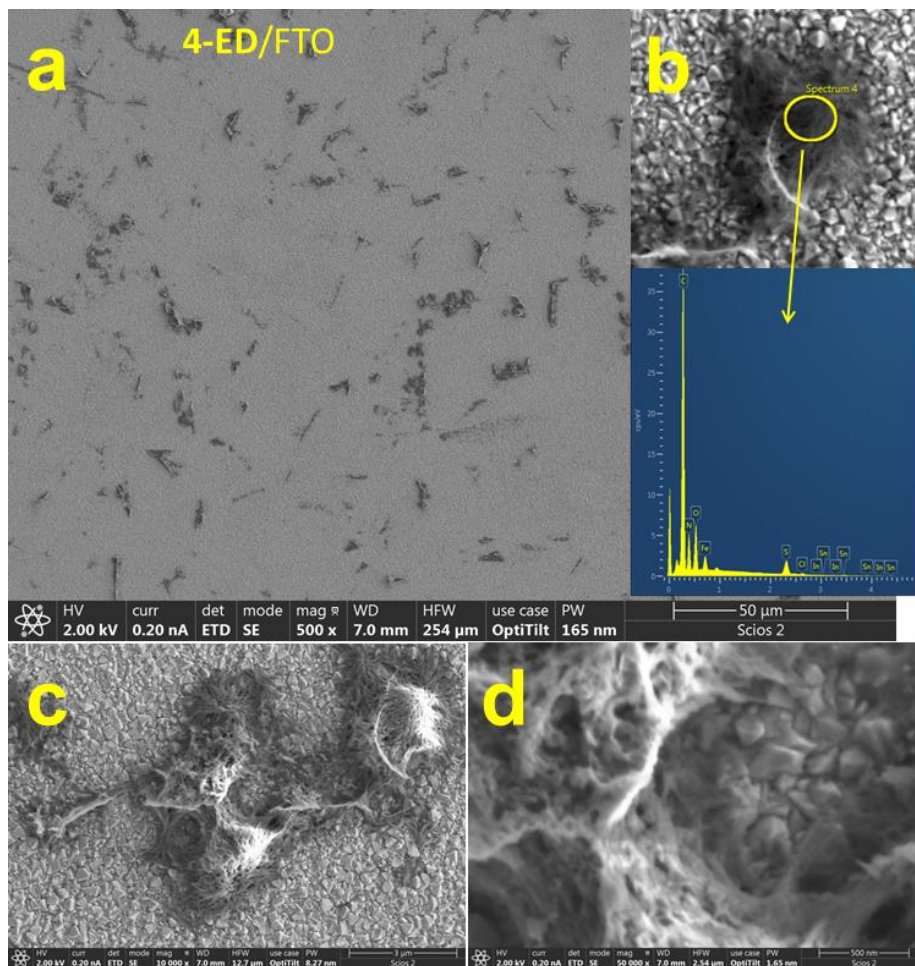


Figure A.4.7 (a) SEM image of 4-ED@FTO as-prepared and cleansed with MilliQ water to remove salt residues, (b) EDX spectrum of the area within the white circle; (c-d) SEM images at different magnifications (see the footers for experimental settings).

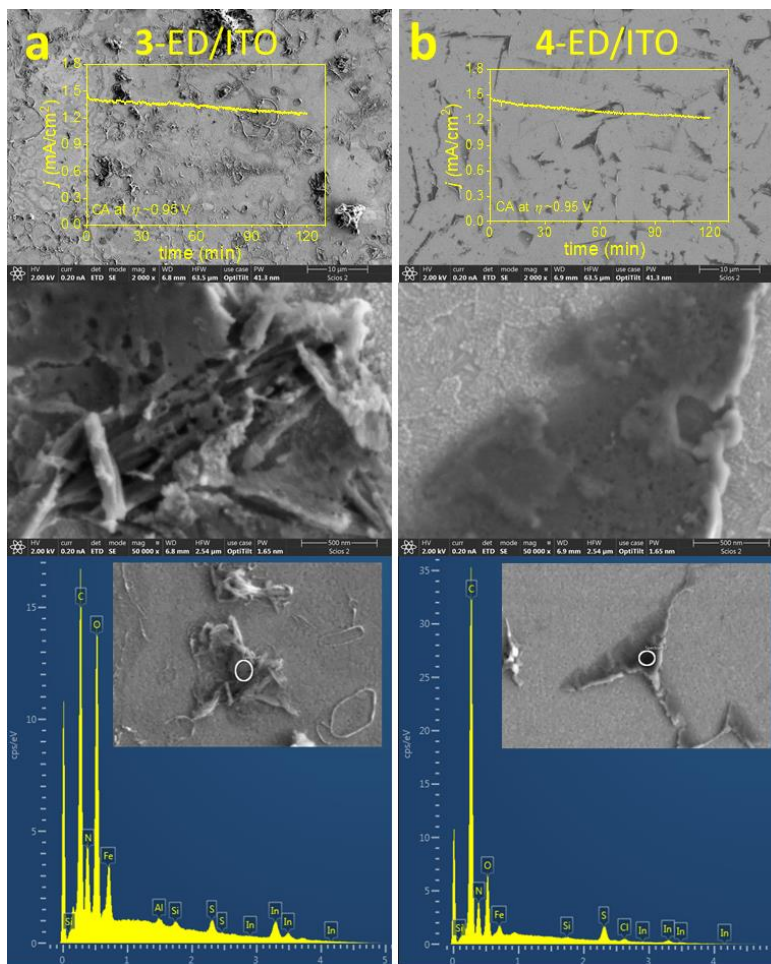


Figure A.4.8 (a) SEM images at different magnifications and EDX spectrum of **3-ED@ITO** as-prepared and cleansed with MilliQ water to remove salt residues, (b) SEM images at different magnifications, and EDX spectrum of **4-ED@ITO** as-prepared (see the footers for experimental settings). Insets on the top: CA currents at +1.5 V vs. AgCl/Ag by using these electrodes.